

University of Southampton Research Repository

Copyright © and Moral Rights for this thesis and, where applicable, any accompanying data are retained by the author and/or other copyright owners. A copy can be downloaded for personal anon-commercial research or study, without prior permission or charge. This thesis and the accompanying data cannot be reproduced or quoted extensively from without first obtaining permission in writing from the copyright holder/s. The content of the thesis and accompanying research data (where applicable) must not be changed in any way or sold commercially in any format or medium without the formal permission of the copyright holder/s.

When referring to this thesis and any accompanying data, full bibliographic details must be given, e.g.

Thesis: J. Williams (2025) "The Role of Particle Characteristics in Determining Transfer Efficiency of the Biological Carbon Pump", University of Southampton, School of Ocean and Earth Science, PhD Thesis, pagination.

Data: J. Williams (2025) The Role of Particle Characteristics in Determining Transfer Efficiency of the Biological Carbon Pump. URI [dataset]

University of Southampton

Faculty of Environmental and Life Sciences

School of Ocean and Earth Science

The Role of Particle Characteristics in Determining Transfer Efficiency of the Biological Carbon Pump

by

Jack Rees Williams

ORCID ID 0000-0002-7177-6020

Thesis for the Degree of Doctor of Philosophy

May 2025

University of Southampton Abstract

Faculty of Environmental and Life Sciences
School of Ocean and Earth Science
Thesis for the Degree of Doctor of Philosophy

The Role of Particle Characteristics in Determining Transfer Efficiency of the Biological Carbon Pump

by

Jack Rees Williams

The Biological Carbon Pump (BCP) exerts a major control on atmospheric CO_2 . Through the surface production, subsequent transfer to depth and remineralisation of organic carbon, the BCP acts to maintain atmospheric CO_2 approximately 120-200 ppm lower than they would otherwise be. The size of the remineralised carbon pool stored in the deep ocean- out of contact with the atmosphere- is strongly influenced by the efficiency with which sinking organic carbon reaches the deep ocean: the "transfer efficiency" of the BCP. Yet despite the importance of transfer efficiency, the importance of the many factors governing transfer efficiency remain unclear.

One group of factors believed to be highly important in determining transfer efficiency are the characteristics of sinking organic particles. In this thesis I examine the influence of several particle characteristics such as size, biomineral ballast content, and morphology on particle sinking velocities and transfer efficiency, combining a meta-analysis, shipboard Marine Snow Catcher (MSC) deployments, and in situ imaging methods.

Particle size alone is shown to represent a poor predictor for particle sinking velocities and transfer efficiencies for in situ particles, in contrast with a common paradigm that has been largely informed from ex-situ measurements. This result highlights the importance of incorporating additional particle morphological information (such as compactness), with particular implications for the estimation of fluxes for in situ imaging methods which are increasingly used to study the BCP. I also show that particulate organic carbon (POC) is more efficiently transferred to depth than biogenic silica at several sites in the subpolar Southern Ocean, suggesting diatoms may not always efficiently transfer carbon to depth and that added density due to biomineral ballast may be compensated by ecological processes. This result highlights the need to move away from a binary view of biomineral ballasting and to characterise the conditions that determine the balance between biomineral ballasting and sometimes counteracting effects of ecological processes. Lastly, I present measurements from a field trial of a novel Marine Snow Catcher design, a tool to safely and swiftly sample marine particles with minimal alteration- currently essential to the calibration of in situ image-based methods of flux estimation. Collectively, results presented in this thesis serve to highlight the need to incorporate additional ecological information and particle characteristics to improve mechanistic understanding of BCP efficiency, accurately model fluxes, and estimate fluxes from in situ image datasets.

Table of Contents	3
Table of Tables	8
Table of Figures	9
List of Accompanying Materials	11
Research Thesis: Declaration of Authorship	12
Acknowledgements	13
Chapter 1 Introduction	14
1.1 The Global Carbon Cycle	14
1.2 The Ocean's Role in the Global Carbon Cycle	15
1.2.1 Ocean Carbon Pumps	15
1.2.2 The Biological Carbon Pump	16
1.3 BCP Metrics and Parameterisations	18
1.4 Drivers of POC flux attenuation	21
1.4.1 Particle Properties Influencing Carbon Flux Attenuation	21
1.4.1.1 Particle size	
1.4.1.2 Chemical composition	22
1.4.1.3 Particle type	
1.4.2 Ecosystem Properties and Processes Influencing Carbon Fluxes	
1.5 Future Changes to the BCP	
1.6 Tools for Measuring POC Fluxes	
1.6.1 Marine Snow Catchers	
1.6.2 Optical Flux Measurements	
1.7 Recent developments in BCP research	
1.8 Thesis Aims, Outline, and Hypotheses	32
Chapter 2 In Situ Particle Measurements Deemphasize the Role of Size	in
Governing the Sinking Velocity of Marine Particles	35
2.1 Abstract	35

2.2	Inti	roduction	1	.35
	2.2.1	The The	oretical Basis for Size-Based Methods	. 38
2.3	Em	pirical Ev	ridence on the Size-Sinking Velocity Relationship	.39
	2.3.1	Methods	S	. 39
		2.3.1.1	Data compilation	. 40
		2.3.1.2	Sinking Velocity/Particle Characteristic Analyses	. 40
		2.3.1.3	Methodological comparison	. 41
	2.3.2	Discuss	ion	. 42
		2.3.2.1	Ex Situ Versus in Situ: Methodological Compromises	. 44
2.4	An	Outlook f	or the Use of In Situ Methods	.46
Cha	pter :	3 Ineffic	cient transfer of diatoms through the subpolar Southern	
_		Ocea	n twilight zone	48
3.1	Abs	stract		.48
3.2	Inti	oduction	l	.49
3.3	Me	thods		.52
	3.3.1	Net Prim	nary Production	. 52
	3.3.2	Particula	ate molar ratios	. 52
	3.3.3	Marine S	Snow Catchers (MSCs)	. 53
		3.3.3.1	MSC biogeochemical analysis	. 53
		3.3.3.2	MSC concentrations and fluxes	. 54
		3.3.3.3	Flux attenuation coefficients (b-values)	. 57
		3.3.3.4	$V_{ extit{fast}}$ sensitivity analysis	. 58
	3.3.4	Uncerta	inties, limitations, and caveats	. 59
3.4	Res	sults and	Discussion	.60
	3.4.1	Preferen	ntial Losses of BSi Relative to POC	. 60
	3.4.2	Reconci	ling Twilight Zone and Deep Ocean Measurements	. 62
	3.4.3	Spatiote	mporal Variation Obscures Nuanced Plankton Ecology	. 65

Chapter	Patterns of Marine Snow Morphology and Sinking Throughout the		
	Atlantic Ocean 68		
4.1 Abs	stract68		
4.2 Int	oduction69		
4.3 Ma	terials and Methods70		
4.3.1	Sample acquisition		
4.3.2	Unsupervised morphological classification71		
4.3.3	Data analyses		
	4.3.3.1 Particle properties		
	4.3.3.2 Depth bin comparisons		
4.3.4	NMDS analyses74		
	4.3.4.1 Environmental variables		
4.4 Res	sults75		
4.4.1	Particle morphotype classifications		
4.4.2	Latitudinal and vertical trends in particle distribution and morphology 77		
4.4.3	Patterns in particle morphology associated with particle transfer 78		
4.4.4	4.4.4 Broad scale particle transfer and transformation 80		
4.4.5	4.4.5 The influence of diel vertical migration		
4.5 Dis	cussion83		
4.5.1	Vertical changes in particle morphology83		
4.5.2	Deep changes in particle morphology84		
4.5.3	Productivity and particle compactness		
4.5.4	Morphological changes: transfer or transformation?		
4.5.5	Outlook for large scale studies into particle morphology		
Chapter	5 A Tool for the Collection of Water Samples and Sampling of		
	Marine Particulates with Minimal Particle Alteration: A Novel		
	Marine Snow Catcher Design 89		
5.1 Δh	stract 80		

5.2 Inti	roduction	90
5.3 Ma	terials and procedures	91
5.3.1	Materials	91
	5.3.1.1 Structure of MSC Yuki	92
	5.3.1.2 Key structural differences to Mk1 MSC model	93
5.3.2	Procedures	95
	5.3.2.1 Pre-deployment	95
	5.3.2.2 Deployment and post-deployment	96
	5.3.2.3 Improvements to ease and safety of deployment	96
5.3.3	General maintenance	97
5.4 Ass	sessment	98
5.4.1	Flow modelling simulations	98
5.4.2	Field trials: MSC version comparison	Э0
5.4.3	Shore-based variability study10	Э6
5.5 Dis	cussion10	07
5.5.1	Future improvements10	37
5.5.2	Insight and applications	38
Chapter (6 Conclusions and Synthesis11	10
6.1 Key	y findings11	10
6.1.1	Particle size, morphology, and sinking velocity	11
6.1.2	Diatoms and particle ballasting in the Southern Ocean 17	12
	6.1.2.1 Balancing ballast and decoupling processes	13
6.1.3	A new tool for sampling particles without alteration	13
6.2 Fut	ture outlook11	14
6.2.1	Models and in situ flux estimation	14
Appendix	x A Inefficient transfer of diatoms through the subpolar Southern	
•	Ocean twilight zone11	17
A.1 Bio	geochemical setting and bloom progression of study sites1	17

A.2	Total sinking flux profiles	120
A.3	DY111 molar ratios: MSC, SAPS, Niskin CTD measurements	121
A.4	Influence of v _{fast} on export efficiencies	122
A.5	Location of our study in relation to Fay & McKinley Biomes	124
A.6	Surface particle back-trajectories	126
A.7	Torres-Valdes et al. sediment trap b-values	126
A.8	BSi:POC particulate molar ratios profiles during the CUSTARD and COMIC	S
	projects	128
A.9	Temporal changes to molar ratios during sinking	128
A.10	Projected deep molar ratios and comparison with previous measurements	S
		130
A.11	Vfast sensitivity analysis	132
Appe	ndix B Patterns of Marine Snow Morphology and Sinking Throughout t	he
• •	Atlantic Ocean	
B.1	Appendix Tables	127
		137
B.2	Appendix Figures	
	Appendix Figures ndix CA Novel Marine Snow Catcher Design	141
Appe		141 146
Appe C.1	ndix CA Novel Marine Snow Catcher Design	141 146 146
Appe C.1	ndix CA Novel Marine Snow Catcher Design	141 1 46 1 46 146
Appe C.1	ndix CA Novel Marine Snow Catcher Design	141 146 146 146
C.1	ndix CA Novel Marine Snow Catcher Design Supplementary Discussion C.1.1 Discrepancies in trends between POC and Chlorophyll C.1.2 Day-to-day variability in chlorophyll profiles	141 146 146 146 146
C.2	ndix CA Novel Marine Snow Catcher Design Supplementary Discussion C.1.1 Discrepancies in trends between POC and Chlorophyll C.1.2 Day-to-day variability in chlorophyll profiles Supplementary Methods	141 146 146 146 147

Table of Tables

Table of Tables

Table 1.1 Particle properties and particle alteration processes32
Table 5.1 List of MSC deployments from field trials101
Table A.1 Back-calculated export efficiencies123
Table A.2: <i>b</i> -values and statistical outputs of linear models used to calculate <i>b</i> -values 132
Table B.1 Morphological properties used to create PCA morphospace137
Table B.2 Environmental parameters used in NMDS multiple regression
Table B.3 Outputs from linear models between T100 and mean particle properties 139
Table B.4 Depth boundaries for "control", "DVM", and "deep" depth strata140
Table C.1 MSC concentrations and fluxes from field trials
Table C.2 MSC concentrations and fluxes from shore-based trials151

Table of Figures

Table of Figures

Figure 1.1: The global carbon cycle1
Figure 1.2: Schematic depicting process and biota involved in the Biological Carbon Pump 1
Figure 1.3 The "Martin curve" (Martin et al., 1987) showing the attenuation of fluxes with depth in the North Pacific.
Figure 1.4: Examples of detrital marine particles and faecal pellets2
Figure 1.5 Examples of future feedbacks that may influence the Biological Carbon Pump 2
Figure 2.1 Schematic illustrating factors posed to influence particle sinking velocity3
Figure 2.2 Boxplot comparing the proportion of variance in sinking velocity explained by particle characteristics4
Figure 2.3 (a) Particle size (equivalent spherical diameter [ESD]) against sinking velocity for all particles in this study4
Figure 3.1 Study region and Net Primary Production (NPP) at the study sites5
Figure 3.2 Flux attenuation coefficients for Chl, BSi and POC6
Figure 3.3 Comparison of projected deep molar ratios with previous measurements
Figure 4.1 Map depicting the locations of 27 pre-dawn stations7
Figure 4.2 Assignation of marine snow into morphological groups via Principal Component Analysis (PCA)7
Figure 4.3 (a) Numerical proportions of marine snow morphologies across the entire transect and with depth
Figure 4.4 Linear regression between maximum particle number concentration in the upper 150 m of each profile, at a depth z, and the number concentration at depth z ₁₀₀ , 100 m beneath the maximum concentration7
Figure 4.5 Distribution of total particle abundance efficiencies and particle abundance efficiencies for each particle morphology8
Figure 4.6 Non-metric multidimensional scaling (NMDS) ordination of particle community
composition 8

Table of Figures

Figure 4.7 Non-metric multidimensional scaling (NMDS) ordination of particle community
composition83
Figure 5.1 Base section of MSC Yuki92
Figure 5.2 Closure mechanisms of MSC Yuki93
Figure 5.3 Schematic illustrating structural differences between the MSC designs94
Figure 5.4 Key steps during preparation of MSC Yuki for deployment97
Figure 5.5 Simulation of flow fields fields through MSCs
Figure 5.6 Time-zero and top fraction concentrations measured by Mk1 and Yuki MSCs 102
Figure 5.7 CTD chlorophyll fluorescence profiles with MSC time-zero Chlorophyll concentrations superimposed
Figure 5.8 MSC measured fluxes of Chlorophyll and Particulate Organic carbon (POC) 105
Figure 5.9 Boxplots showing variability in replicates of particle concentrations106
Appendix Figure A.1 Progression of bloom state in Pacific sector and at Atlantic P3 station 119
Appendix Figure A.2 Total fluxes of Chl, BSi, and POC at each station120
Appendix Figure A.3 Molar ratios of BSi:POC at Pacific sector stations from MSC, SAPS, CTD.121
Appendix Figure A.4 Location of study sites in relation to Fay & McKinley biomes124
Appendix Figure A.5 Surface particle back-trajectories
Appendix Figure A.6 Sediment trap fluxes from Torres-Valdes et al. (2014) 127
Appendix Figure A.7 BSi:POC molar ratios throughout mesopelagic in both sectors
Appendix Figure A.8 Comparison of our projected molar ratios with previous measurements 132
Appendix Figure B.1 Summary outputs from PCA analysis
Appendix Figure B.2 Key variability contributing to variation in principal component axes 141
Appendix Figure B.3 Boxplots showing distribution of particle perimeter for each cluster 142
Appendix Figure B.4 Contributions of particle morphologies to biovolume across the transect
Appendix Figure B.5 Profiles of particle concentration at "High Transfer efficiency" stations . 143

List of Accompanying Materials

Appendix Figure B.6 Contour plot depicting interaction between mean particle brightness, mean
particle area, and T100 residuals144
Appendix Figure B.7 Examples of identification of "control", "DVM", "deep" depth strata 144
Appendix Figure B.8 Depth boundaries for "control", "DVM", "deep" depth strata across
transect145
Appendix Figure C.1 CTD Chlorophyll fluorescence profiles from successive days

List of Accompanying Materials

Chapter 2: Supplementary Data Tables S2.1, S2.2, and S2.3 are available as Supplementary Material at: https://doi.org/10.1029/2022GL099563

Chapter 3: Supplementary Data Tables S3.1, S3.2, S3.3, S3.4, and S3.5 are available in Supplementary Tables 1-5 at: https://doi.org/10.1038/s41561-024-01602-2

Chapter 4: Supplementary Data Tables S4.1, S4.2, and S4.3 are available in https://doi.org/10.5258/SOTON/D3424. CTD data is available from the British Oceanographic Data Centre (BODC) via the DOI doi:10.5285/fe044ed6-9b79-6023-e053-6c86abc09d9e. ADCP data is available from the British Oceanographic Data Centre (accession number: RVS230087), licensed under the Open Government Licence.' UVP particle vignettes will be made available on Ecotaxa under a DOI following submission of Williams et al. (in prep.) and Couret et al. (in prep).

Research Thesis: Declaration of Authorship

Research Thesis: Declaration of Authorship

Print name: JACK WILLIAMS

Title of thesis: The Role of Particle Characteristics in Determining Transfer Efficiency of the Biological

Carbon Pump

I declare that this thesis and the work presented in it are my own and has been generated by me

as the result of my own original research.

I confirm that:

1. This work was done wholly or mainly while in candidature for a research degree at this

University;

2. Where any part of this thesis has previously been submitted for a degree or any other

qualification at this University or any other institution, this has been clearly stated;

3. Where I have consulted the published work of others, this is always clearly attributed;

4. Where I have quoted from the work of others, the source is always given. With the exception

of such quotations, this thesis is entirely my own work;

5. I have acknowledged all main sources of help;

6. Where the thesis is based on work done by myself jointly with others, I have made clear

exactly what was done by others and what I have contributed myself;

7. Parts of this work have been published as:

Williams, J.R. and Giering, S.L.C., 2022. In situ particle measurements deemphasize the role of

size in governing the sinking velocity of marine particles. Geophysical Research Letters, 49(21),

p.e2022GL099563.

Williams, J.R. et al., 2024. Inefficient transfer of diatoms through the subpolar Southern Ocean

twilight zone. Nature Geoscience, 18(1), pp. 72–77. Available at:

https://doi.org/10.1038/s41561-024-01602-2.

12

Acknowledgements

I'd like to express my sincere gratitude to Sari Giering. I'm sure many supervisors are knowledgeable- but equally sure that few have such great people skills, are so enthusiastic, supportive, and patient, and make the PhD slog such fun. Certainly, few are cool enough to talk running and kitesurfing every week. I could not have wished for a better supervisor, nor a better role model in science. Thank you.

To Mark Moore, thank you for your support and wisdom from my undergrad to now. Regardless of whether I was sometimes absent as a supervisee for long periods, I could always count on your support and wisdom when I needed it. To Chelsey Baker, thank you for so much help from the undergrad to now, and for being so generous with your time that you were an unofficial supervisor at times. To Adrian Martin, thank you for your encouragement and support, for your always sound advice, and for making a very green young student feel valued amongst the real scientists of the CUSTARD project.

To all the scientists involved in CUSTARD and COMICS, thank you for your support and allowing me to stand on the shoulders of your great work.

To the ANTICS team: Will Major, Marika Takeuchi, Zonghua Liu, Mojtaba Masoudi, Amanda Elineau, María Couret: what a team! Thanks for helping me out whether on land or at sea, it's been so good knowing there's a whole team of great scientists I can call on. Can't wait to become a non-student member of the team for a while.

I need to thank my fellow NOC PhD'ers and pals for keeping me sane and making the whole experience such fun. Special thanks to Millie, Joe, Emily, Andres, Cordelia, Mark, Anna, Ruth for all the wonderful times whether that be on rocks, bikes, sat on the kitchen floor. And, for dealing with a stinky bike trailer kept in the garden. To Pete, Mark, Dave, Tom C, for sharing the moments of peace sat under dark skies at Lepe. To Matt Walker- we did it! Huuuuuhhhh!!

To my parents, thank you for always believing in me, supporting me in every endeavour, for being role models for who I want to be. To Jamie, for always bringing me a smile and a laugh, and being someone I'm so proud to call bruv. To Zuzka, I'm so grateful for your love and support, and to *Diretmus argenteus* for bringing someone so amazing into my life.

Chapter 1 Introduction

1.1 The Global Carbon Cycle

Carbon (C) plays a crucial role for life on earth. It serves as the basic building block for organic molecules found in living organisms (Calvin and Benson 1948), and in its gaseous form (CO_2) acts a greenhouse gas, regulating global climate (Ledley et al. 1999; Kump et al. 2003). The ocean comprises the second-largest reservoir of carbon on earth after the lithosphere (solid earth), containing approximately 38,000 Pg C (Falkowski et al. 2000; Devries 2022), and is the largest actively cycling reservoir of carbon on earth (Falkowski et al. 2000). This massive size (holding almost 50 times more carbon than the atmosphere) and relatively rapid exchange of this reservoir with the atmosphere make the ocean the dominant natural control on atmospheric CO_2 on timescales of decades to millennia (Falkowski et al. 2000; Devries 2022).

During the Holocene epoch (beginning 11,700 years ago) and prior to the start of the industrial revolution (~1780), atmospheric CO₂ had remained relatively constant at around 280 ppm (Pongratz et al. 2009; Ciais et al. 2013; Devries 2022). Flows of carbon into and out of the atmosphere were tightly coupled, with atmospheric CO₂ concentrations regulated by exchange with the vast and nearly unchanging ocean reservoir (Devries 2022). Since the onset of the industrial revolution, however, human activities have perturbed the equilibrium from steady state, releasing carbon from the lithospheric reservoir into the atmosphere (Ciais et al. 2013) (Figure 1.1). This perturbation has resulted in an input of 700±75 Pg C between 1750 and 2019 (Canadell et al. 2023), resulting in a concurrent increase in global temperature of around 1 °C over the same period (Millar et al. 2017). The ocean reservoir has taken up around 230±60 Pg C over the course of the industrial era, equivalent to 30% of total emissions (Canadell et al. 2023), highlighting the ocean's vital role in mitigating the effects of anthropogenic emissions on the climate system.

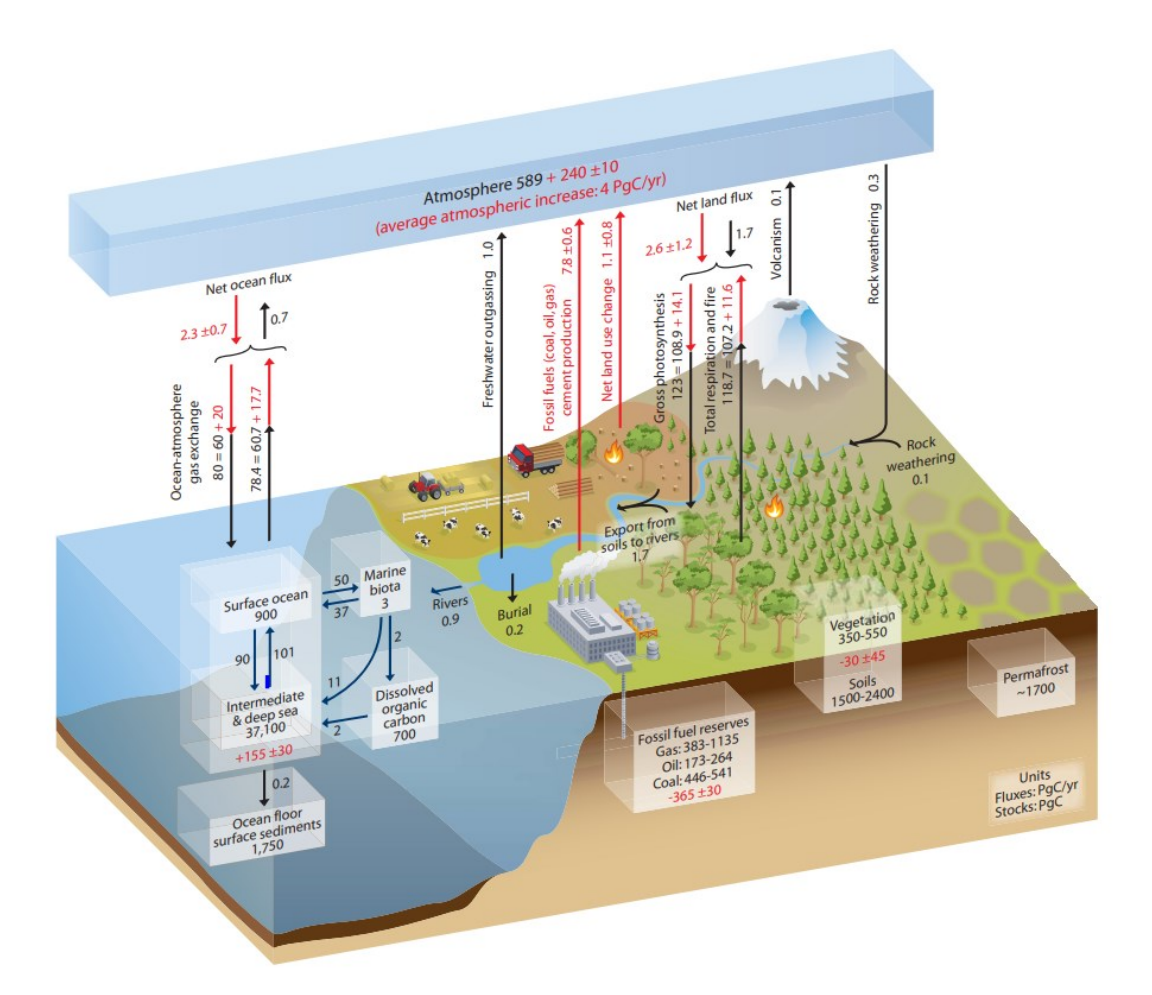


Figure 1.1: The global carbon cycle, depicting reservoir mass and exchange fluxes between reservoirs. Within reservoirs, black text depicts reservoir mass or "carbon stocks" (PgC) within each reservoir prior to the onset of the industrial period (~1750), with red numbers indicating anthropogenic perturbations to the size of these stocks. Black text next to arrows show the size of exchange fluxes (PgC/yr) between reservoirs, with red text indicating anthropogenic perturbations to these exchange fluxes. Figure reproduced from Ciais et al. (2013).

1.2 The Ocean's Role in the Global Carbon Cycle

1.2.1 Ocean Carbon Pumps

Carbon is sequestered in the ocean via two main pumps: the physical or "solubility" pump, and the "Biological Carbon Pump" (BCP). The solubility pump is driven by differences in CO_2 solubility in warm and cold water coupled to the ocean's overturning circulation (Volk and Hoffert 1985), which results in the dissolution of CO_2 into cold polar and subpolar waters and subsequent sinking of this CO_2 laden water to the deep ocean (Volk and Hoffert 1985; Iversen 2023). By contrast, the BCP (described in 1.2.2 in more detail below) describes the surface production of, transfer to depth, and deep remineralisation of organic carbon (Volk and Hoffert

1985). The transfer of carbon to depth via the BCP is dominated by the passive sinking of organic particles (Boyd et al. 2019; Buesseler et al. 2020), but in recent years the importance of other "particle injection pumps" (both biologically and physically mediated) have also been recognised (Boyd et al. 2019; Buesseler et al. 2020). For instance, both the daily (Bianchi et al. 2013; Steinberg & Landry, 2017) and seasonal (Jónasdóttir et al. 2015) vertical migrations of metazoans in the mesopelagic can result in the active transport of carbon out of the surface ocean, and injection of carbon at depth. Physical subduction due to mesoscale eddies (Lévy et al. 2013, Omand et al. 2015), large-scale frontal subduction (Lévy et al. 2013), or mixed-layer shallowing (Dall'Olmo et al. 2016) may also drive the transfer of carbon out of the surface ocean. Particle injection pumps together may sequester almost as much carbon as passive sinking of organic particles (Boyd et al. 2019; Buesseler et al. 2020).

By transporting carbon from the surface ocean to the deep ocean, ocean carbon pumps act to maintain a vertical gradient in dissolved inorganic carbon (DIC) throughout the world's oceans. Although 90% of DIC held within the ocean results from chemical equilibration of the ocean with the pre-industrial atmosphere via the solubility pump (Devries 2022), the BCP dominates the transfer of DIC from the surface to the deep ocean in the present-day ocean (Sarmiento and Gruber 2006). The BCP accounts for approximately 70% of the vertical gradient in DIC, with the solubility and carbonate pumps accounting for the remaining 30% (Sarmiento and Gruber 2006). As such, the BCP exerts a major control on atmospheric CO_2 . Ocean-atmosphere model experiments estimate the BCP to maintain atmospheric CO_2 concentrations ~200 ppm lower than it would otherwise be (Maier-Reimer et al. 1996; Parekh et al. 2006a), though these experiments likely overestimate this effect by 30 - 50% as they neglect feedbacks with the terrestrial biosphere (Oschlies 2009).

1.2.2 The Biological Carbon Pump

The fate of carbon cycled through the biological carbon pump has major implications both for ocean ecosystems and global climate. The exact magnitude of global marine primary production remains uncertain both from remote-sensing (38.8 – 52.1 Pg C yr⁻¹, Behrenfeld et al., 2005; Kulk et al., 2020) and model-based estimates (21.6 – 57.3 Pg C yr⁻¹, Séférian et al., 2020), but it is well-established that only a small fraction (10-18 %, Nowicki et al. 2022) of carbon fixed in the upper ocean is exported from the upper mixed layer, or transferred to the deep ocean seafloor (1%, Ducklow et al. 2001; Iversen 2023) (Figure 1.2b). Only a relatively small fraction of the organic matter exported from the surface ocean is transferred to the seafloor because heterotrophs consume much of it as it sinks (Giering et al. 2014). Sinking fluxes of photosynthetically-derived organic carbon from the surface ocean is the primary energy source for midwater biota (Giering et al. 2014), and-aside from deep sea ecosystems sustained by

chemoautotrophy- the primary energy source for deep sea benthic communities (Billett et al. 1983; Smith et al. 2001) (Figure 1.2a).

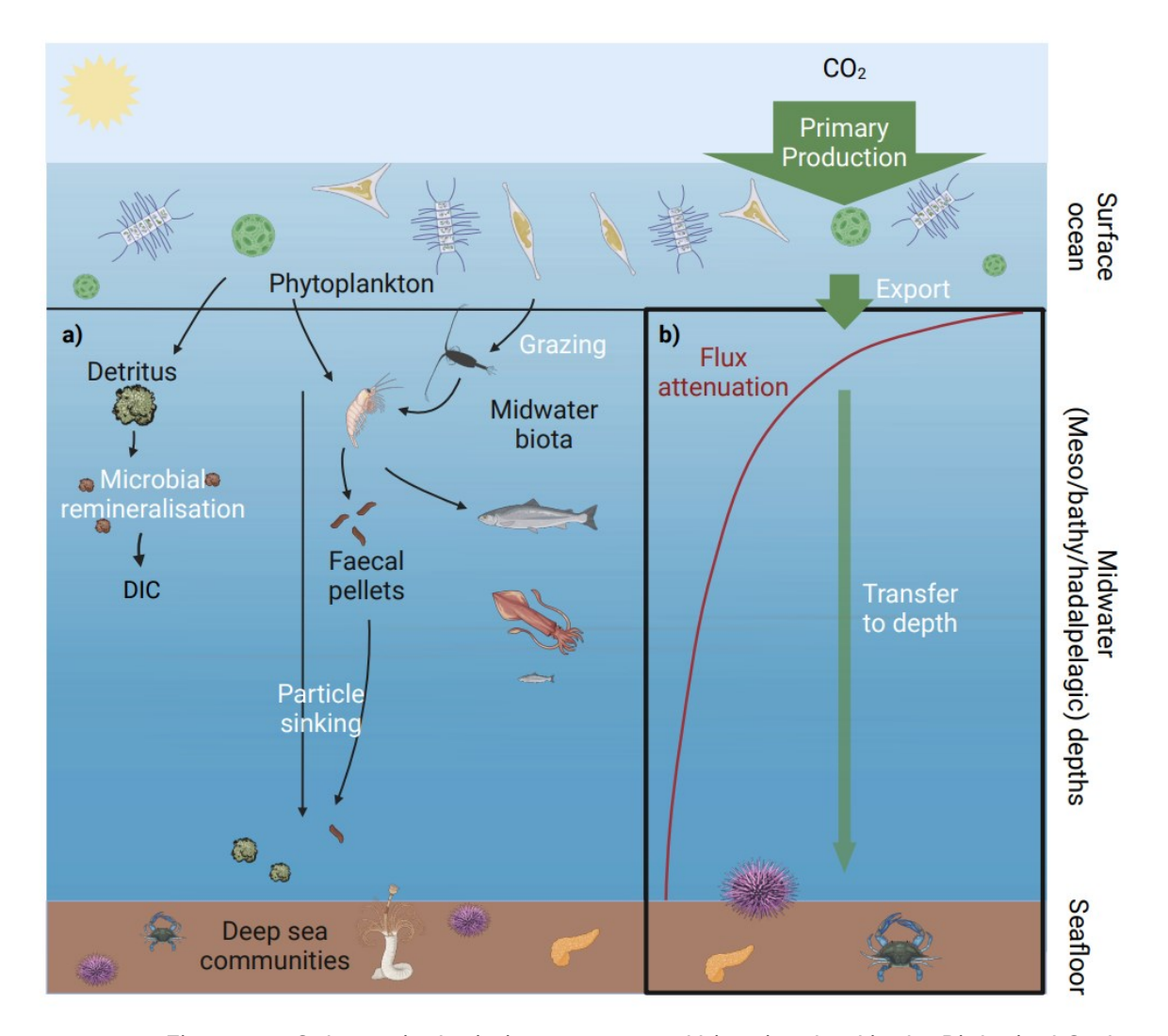


Figure 1.2: Schematic depicting process and biota involved in the Biological Carbon Pump. Panel (a) depicts how organic material formed by phytoplankton in the surface ocean may be utilised by midwater and deep-sea communities for energy, how particles may be repackaged into detritus and faecal pellets, and how organic material is taken up by heterotrophic grazers and microbes. Subpanel (b) depicts the characteristic flux attenuation curve resulting from flux losses depicted in panel (a), with key steps involved in the Biological Carbon Pump (primary production, export, transfer to depth) depicted by green arrows. Produced with Biorender.

The fate of carbon cycled through the BCP also has major impacts on the air-sea carbon partitioning, and therefore on global climate (Kwon et al. 2009). Deeper remineralisation of organic carbon results in a longer residence time of carbon in the deep ocean, with carbon remineralised in deep water masses held out of contact with the atmosphere for timescales of centuries to millennia (Devries et al. 2012). The size of the remineralised carbon pool sequestered away from the atmosphere in the deep ocean is in turn dependent on the residence

time of remineralised carbon (Sanders et al. 2016). As a result, small changes in the depth of carbon remineralisation can have major implications for concentrations of atmospheric CO_2 : modelling suggests a 24 m deepening in the global remineralisation depth (z^*) of organic carbon could decrease atmospheric CO_2 by 10 - 27 ppm (Kwon et al. 2009).

1.3 BCP Metrics and Parameterisations

The role of the BCP in global carbon cycling and in supplying energy to marine ecosystems makes accurately describing, constraining, and understanding the BCP of fundamental importance. Heterotrophic consumption of sinking particulate fluxes results in the characteristic decay shape of sinking flux profiles as they attenuate with depth (Figure 1.2b). Numerous parameterizations have been used to assess flux attenuation and relate sinking particulate fluxes to depth, perhaps the most widely used relationship (Cael and Bisson 2018; Wiedmann et al. 2020) being the "Martin's *b*" power-law function (Martin et al. 1987) (Equation 1.1; Figure 1.3):

$$F_z = F_{z0} * (z/z_0)^{-b} \tag{1.1}$$

where F_z is the flux at a given depth (z) below a reference depth z_0 , usually the export depth, F_{z0} is the flux at the export reference depth, and b is the flux attenuation coefficient calculated as the log-log-slope. Using direct flux measurements from six stations in the North Pacific, Martin et al. assessed the degree of carbon flux attenuation with depth by fitting a power law function to their data. The resulting average b-value of 0.86 described by Martin et al. has since been used to parameterise the flux of carbon sinking from the surface ocean to deep ocean (Primeau 2006; Henson et al. 2012), and the power law function is to this day widely used to describe and compare flux attenuation throughout time and space (Buesseler et al. 2007b; Wiedmann et al. 2020; Bach et al. 2023). Recent studies have highlighted that b varies greatly globally and seasonally (Lutz et al. 2002; Kwon et al. 2009; de Melo Viríssimo et al. 2022), yet in general, a b-value of 0.86 appears to be a reasonable approximation globally (Stolpovsky et al. 2018).

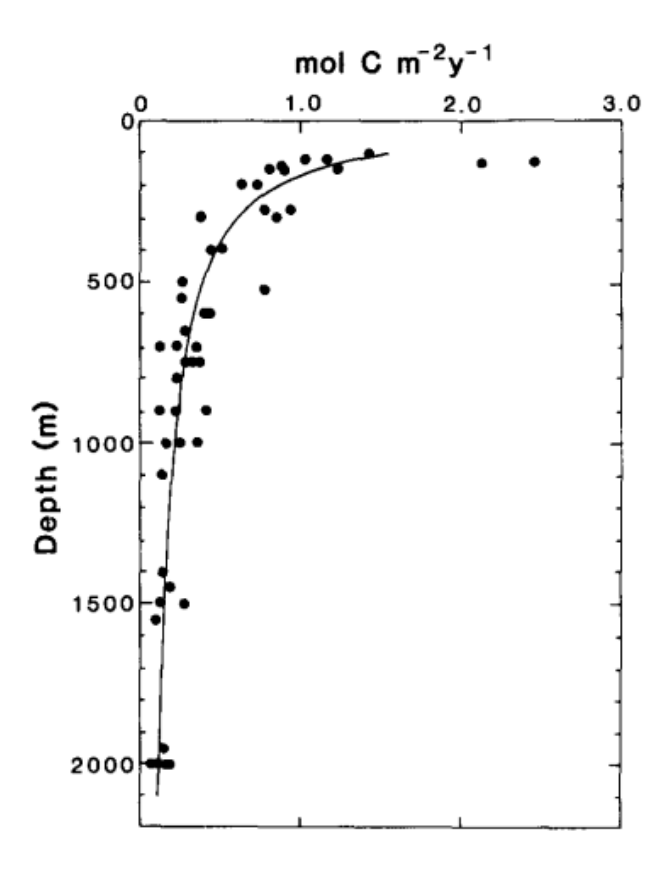


Figure 1.3 The "Martin curve" (Martin et al., 1987) showing the attenuation of fluxes with depth in the North Pacific. The fitted line is derived from the power law function expressed in equation 1.1 and use the exponent *b* of 0.86.

Despite its widespread uptake, use of the Martin curve to model POC flux attenuation has a number of limitations. It is empirically derived rather than mechanistically based, and thus does not allow for projected alterations of BCP efficiencies under future climates scenarios (Martin et al. 1987; Boyd et al. 2015; Buesseler et al. 2020). It is also highly sensitive to the choice of reference depth used (Buesseler and Boyd 2009).

Numerous other flux parameterizations have also been proposed, with the most commonly used and basic alternative an exponential fit (equation 1.2):

$$F_z = F_0 * e^{-kz/v}$$
 (1.2)

where F_z is flux at a given depth, F_0 flux at export depth, z the distance below the reference depth, and k and v are remineralisation rate and sinking velocity respectively. The exponential fit is mechanistically based and relates fluxes to depth via first-order kinetics, and thus can be tuned to represent ecosystem changes in response to climate forcings (Boyd and Trull 2007; Cael and Bisson 2018). Yet, the exponential model assumes constant sinking speed and remineralisation with depth, which often results in underestimation of fluxes at depth (Gloege et al. 2017); the Martin curve implicitly assumes either increasing sinking velocity or decreasing remineralisation rates with increasing depth, better representing deep fluxes (Gloege et al.

2017). In addition, though models incorporating ecological processes may provide better mechanistic models of flux attenuation, detailed and high-resolution measurements are often unavailable (Estapa et al. 2019; Wiedmann et al. 2020), and so the lack of mechanistic basis underpinning the Martin curve can be another advantage in this regard. Regardless of the flux parameterization used, extrapolating fluxes beyond the depth range of flux measurements has the potential to introduce large uncertainties into flux estimations (Cael and Bisson 2018). Differing processes influencing flux attenuation throughout the water column mean the use of a single attenuation coefficient for the whole water column may not accurately reflect attenuation occurring of different depth ranges (Henson et al. 2023).

Numerous definitions are also widely used to simplify and describe the loss processes within the BCP. The most consistently used would be "export efficiency" and "transfer efficiency". "Export efficiency", or "e-ratio", describes the fraction of organic carbon produced by primary production that is exported from the upper ocean (often taken to mean mixed layer, euphotic zone, or upper 100 m) (Laws et al. 2000). It can be expressed as both a ratio and a percentage (e.g. 1 or 100% means export is equal to primary production). Quasi-instantaneous estimates of export efficiency typically range from close to 0 to 0.8, but due to time lags between production and export, export ratios >1 have sometimes been reported (Henson et al. 2011; Henson et al. 2015). Export efficiency is now known to vary both seasonally, especially at high latitudes (Baumann et al. 2013; Henson et al. 2015), and globally (Henson et al. 2011).

"Transfer efficiency" describes the proportion of exported material transferred "to depth" (Buesseler et al. 2007b), though application of the term has not always been used consistently and thus needs to be defined during each use. The metric has been used both to describe the efficiency with which fluxes are transferred to 100 m below a reference depth (often referred to as T100) (Buesseler et al. 2007b; Buesseler and Boyd 2009; Buesseler et al. 2020), and also to describe the efficiency of transfer to the "deep" ocean, using a threshold such as 1000 m or 2000 m (Francois et al. 2002; Henson et al. 2012; Weber et al. 2016). In each case, a transfer efficiency of 1 or 100% means fluxes at the chosen reference depth are equal to fluxes exported from the upper ocean. Transfer efficiency varies globally, but which regions display higher and lower transfer efficiencies are a matter of debate (Henson et al. 2012; Le Moigne et al. 2012; Weber et al. 2016). Direct observations of transfer efficiency in the mesopelagic (~100 – 1000 m) remain scarce (Weber et al. 2016), especially considering the limitations of deploying sediment traps in the mesopelagic (Buesseler et al. 2007a; Lamborg et al. 2008); processes in the mesopelagic have often therefore been inferred from flux measurements deeper in the water column (>1,000 m). Together, export and transfer efficiency describe the overall efficiency of the BCP and the depth distribution over which sinking fluxes are remineralised.

1.4 Drivers of POC flux attenuation

Carbon flux attenuation within the BCP is ultimately determined by the balance between particle sinking rates and remineralisation rates (Marsay et al. 2015). Higher sinking velocities provide a shorter time window over which carbon can be remineralised, hence resulting in a greater proportion of carbon being transferred to depth. Conversely, higher remineralisation rates result in more rapid attenuation of sinking carbon fluxes and remineralisation at shallower depths. Both particle sinking and remineralisation rates are influenced by physical properties of particles such as particle size, porosity, and chemical composition (Bach et al. 2019; Anderson et al. 2023) which in turn are dependent on higher-level ecosystem traits and processes, for example phytoplankton community structure or particle repackaging by zooplankton (Belcher et al. 2016b; Briggs et al. 2020). Ultimately, a mechanistic understanding of how these tiered processes shape losses of sinking particulate fluxes is critical for understanding BCP function. Below, I outline some particle properties, followed by ecosystem properties, commonly held to be important in regulating BCP function.

1.4.1 Particle Properties Influencing Carbon Flux Attenuation

1.4.1.1 Particle size

Particle size is a fundamental particle property posed by both theory and empirical studies to control particle sinking velocities (Gibbs 1985; Laurenceau-Cornec et al. 2015b). Equations based on Stokes's Law (equation 1.3) have been widely used in models (Aumont et al. 2015; Cael et al. 2021b) and more recently to calculate fluxes from in situ particle image datasets (Guidi et al. 2008):

$$w = (\rho_p - \rho_f) \frac{gD^2}{18\mu}$$
 (1.3)

where w is the sinking velocity of a sphere (m s⁻¹), ρ_p and ρ_f are the sphere and fluid densities (kg m⁻³), g is the acceleration due to gravity (9.81 m s⁻²), D is the sphere diameter (m) ,and μ is the fluid dynamic viscosity in kg m⁻¹s⁻¹. Under Stokes Law, particle sinking velocity scales with the square of particle diameter, yet it is known that that for marine particles, porosity increases with increasing particle size (Logan and Wilkinson 1990; Laurenceau-Cornec et al. 2015b). The importance of size in governing sinking velocity is still currently a matter of debate, however; recent studies have challenged the importance of size as a sole predictor of particle size (Iversen and Lampitt 2020; Laurenceau-Cornec et al. 2020), yet the use of size-based parameterisations of vertical carbon fluxes in biogeochemical models (Yool et al. 2013; Aumont et al. 2015) and to estimate fluxes from in situ image datasets (Guidi et al. 2008; Fender et al.

2019; Kiko et al. 2020) remain common.

Particle size has also been posed to influence remineralization rates, with smaller particles displaying higher surface area (on which heterotrophic microbes may colonise) relative to particle volume (Omand et al. 2020; Anderson et al. 2023).

1.4.1.2 Chemical composition

Chemical composition also plays a major role in dictating both particle sinking and remineralisation rates. According to Stokes's Law (Equation 1.3), particles' excess density $(
ho_p -
ho_f)$ is also directly proportional to particle sinking velocity, making the density of chemical constituents which comprise a particle an important control on sinking velocities. One famous and widely employed hypothesis is the "ballast hypothesis", wherein the fluxes of dense biominerals (e.g. calcium carbonate, silicate, lithogenic material) are associated with more efficient transfer of organic carbon fluxes to the deep ocean (Armstrong et al. 2001; Klaas and Archer 2002). Ballast biominerals have been posed to increase sinking rates through imparting greater excess density, thus decreasing the period over which particles are exposed to degradation (Ploug et al. 2008; Iversen and Ploug 2010), or alternatively may physically protect organic material from remineralisation (Hedges et al. 2001). In recent years, several studies have failed to find differences in remineralisation rates between ballast-associated and non-ballasted particles (Ploug et al. 2008; Iversen and Ploug 2010), and hence the sinking velocity-based mechanism seems more likely. Despite a mechanistic underpinning which has led to widespread representation of the ballast hypothesis in biogeochemical models (Yool et al. 2013; Stock et al. 2014; Giering et al. 2017; Henson et al. 2022), the validity of the ballast hypothesis and how broadly it is applicable in the field remains a matter of debate. The ballast hypothesis initially grew out of correlations observed in deep (< 1000 m) sediment trap data, with studies examining the influence of ballast minerals often necessarily incubating particles ex situ (Ploug et al. 2008; Iversen and Ploug 2010; Iversen and Robert 2015). The importance of the ballast hypothesis in the upper ocean is disputed (Thomalla et al. 2008; Sanders et al. 2010) and global analyses provide conflicting results on whether diatoms (dominant, BSi-ballasted phytoplankton) are associated with carbon transfer to the deep ocean (Le Moigne et al. 2012; Le Moigne et al. 2014; Wiedmann et al. 2020).

Biomineral ballast aside, the presence of "biological glues" such as transparent exopolymeric (TEP) substances may also influence sinking velocities directly through reducing excess densities of particles (Engel and Schartau 1999). Chemical composition can also influence particle remineralisation- particles containing more labile compounds will be remineralised more rapidly than those containing refractory compounds (Bendtsen et al. 2015).

1.4.1.3 Particle type

Particle type also plays a major role in determining the balance between sinking and remineralisation rates. Different particle types can vary in characteristics which influence sinking velocity and remineralisation rates, for instance size, chemical composition, or porosity. Whilst not strictly a particle characteristic, distinguishing different particle types provides a means of visual classification and a means to group particles of a certain size, shape, density, and composition. The two particle types that dominate sinking fluxes are phytodetrital aggregates and faecal pellets (Turner 2002; Laurenceau-Cornec et al. 2015a).

Phytodetrital aggregates (Figure 1.4a) are an important component of sinking fluxes. Individual phytoplankton cells typically display sinking rates between 1 - 10 m d⁻¹ (Turner 2002), yet collisions between cells can allow for the formation of larger phytodetrital aggregates (Burd and Jackson 2009) with sinking velocities that span three orders of magnitude (~1 – ~1000 m d⁻¹) (Turner 2002; Laurenceau-Cornec et al. 2015b; Iversen and Lampitt 2020). The term "marine snow" is often used to refer to phytodetrital aggregates (Figure 1.4a-b), but the term is used inconsistently, sometimes referring to any aggregate (including faecal aggregates) > 0.5 mm in size (Alldredge and Gotschalk 1988), sometimes to all sinking marine particles (Trudnowska et al. 2021).

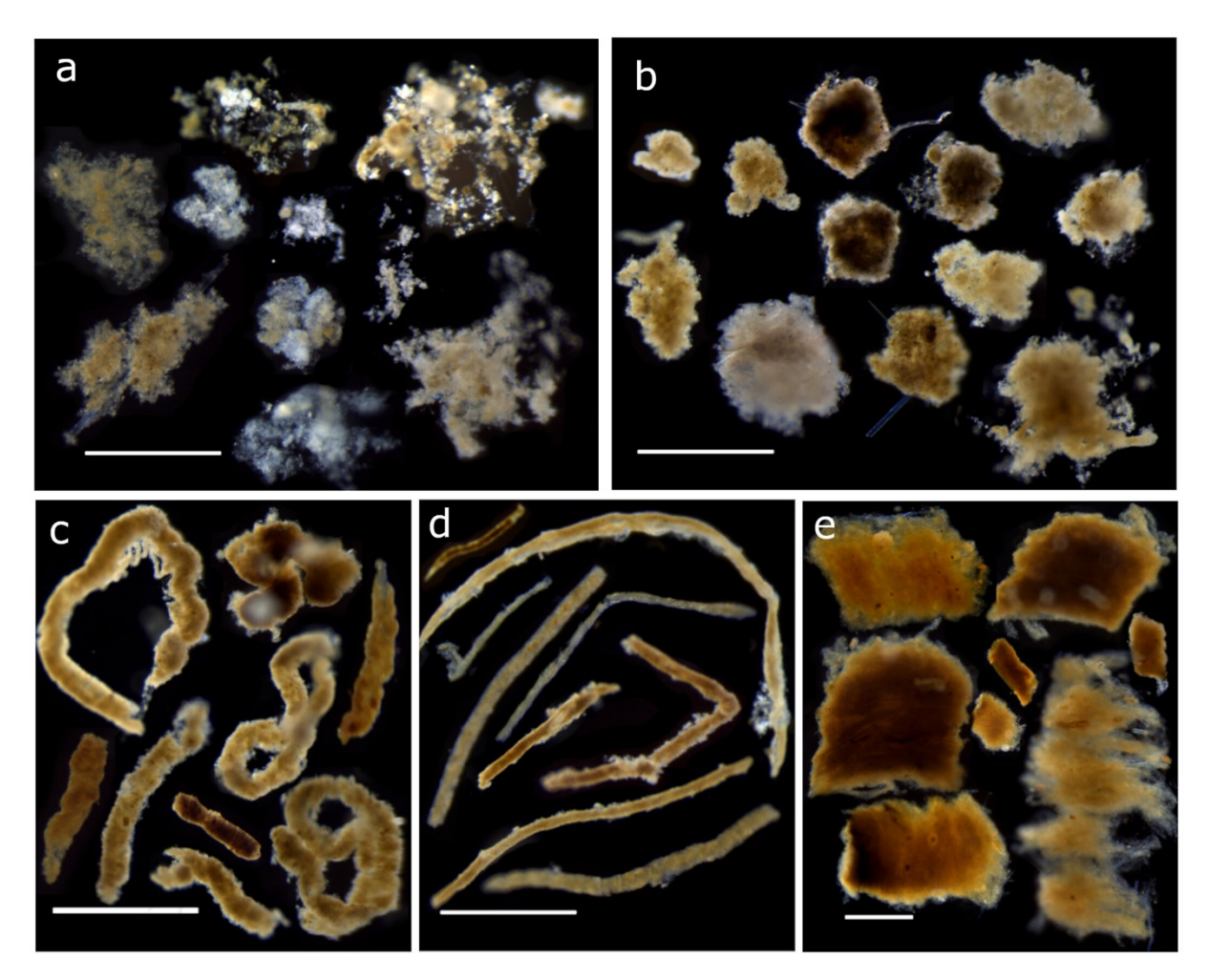


Figure 1.4: Examples of detrital marine particles and faecal pellets. (a) phytodetrital aggregates; (b) detritus; (c-e) faecal pellets, which together dominate sinking particulate fluxes. Reproduced from (Durkin et al. 2021).

Faecal pellets of zooplankton grazers comprise the other major component of sinking fluxes. Through grazing on phytoplankton, organic carbon can also be repackaged into dense, rapidly-sinking (5 – 2700 m d⁻¹) (Turner 2002) faecal pellets, which can efficiently transfer carbon to depth. Faecal pellets can originate from a variety of grazers, such as salps, copepods, pteropods, larvaceans, krill, amphipods, and crustacean nauplii (Belcher et al. 2017), and thus vary in their size and morphology (Figure 1.4c-e, (Wilson et al. 2013). Temporal and spatial variation in ecosystem structure, in particular zooplankton abundance, means the contribution of faecal pellets to total sinking fluxes varies greatly- dominating fluxes in some regions and times of year, and scarcely contributing in others (Laurenceau-Cornec et al. 2015a). As well as being dense and tightly compacted, faecal pellets typically contain more refractory material relative to phytodetrital aggregates (Wilson et al. 2008), and so may be more slowly remineralised.

Whilst faecal pellets or phytodetrital aggregates typically dominate, diverse particle types such as krill exuviae and carcasses (Cavan et al. 2019; Manno et al. 2020), or larvacean houses (Robison et al. 2005) can also represent important contributions to sinking fluxes.

1.4.2 Ecosystem Properties and Processes Influencing Carbon Fluxes

Ecosystem properties and structure play a major role in shaping the strength of the BCP, ultimately determining the abundance, properties, and fate of organic particles. Primary production and phytoplankton community composition are two fundamental ecosystem traits which largely determine the amount of organic carbon available to be transferred out of the surface ocean via the BCP (Doney et al. 2024), as well as influencing food chain structure (Ward et al. 2012; Stukel et al. 2024), and chemical composition of particles, since different phytoplankton types have different stoichiometries (Francois et al. 2002; Leblanc et al. 2009).

Empirical and mechanistic models have previously parameterised a positive relationship between primary production and export efficiency (Laws et al. 2000; Dunne et al. 2005), yet recent global and biome-scale analyses have observed an inverse relationship between primary production and export efficiency, driven by ecosystem structure and decoupling between primary production and upper ocean remineralisation (Maiti et al. 2013; Henson et al. 2019). Zooplankton community structure has also been shown to play a key role in determining particle properties and fate, and by extension, BCP efficiency. On the one hand, zooplankton can decrease the efficiency of carbon transfer to depth by consuming and remineralising particulate organic carbon (Steinberg et al. 2008; Mayor et al. 2014), or by fragmenting or loosening sinking particles, decreasing their sinking velocity (Mayor et al. 2014; Briggs et al. 2020). Conversely, zooplankton can repackage particles into densely compacted faecal pellets (Belcher et al. 2017), resulting in more rapid sinking and efficient transfer, or even actively inject faecal pellets at depth (see Particle injection pumps in section 1.2.1). Many aspects of zooplankton community structure are only recently gaining recognition for their importance in shaping sinking carbon fluxes (for instance the role of Rhizaria (Lampitt et al. 2023); many other factors are known to be important but as yet are poorly constrained and understood (Henson et al. 2022). Better understanding how planktonic ecosystems influence particle properties will in turn lead to an improved mechanistic understanding of the BCP.

Abiotic aspects of ecosystems can also influence sinking carbon fluxes. Water temperature exerts both an indirect effect on particle sinking velocities through the decrease in viscosity resulting from increased water temperatures (Taucher et al. 2014), and directly influences rates of particle remineralisation (Bidle et al. 2002). Temperature also influences dissolved oxygen concentrations; low oxygen concentrations are thought to increase BCP efficiency through a

reduction in oxic remineralisation (Laufkötter et al. 2017) and a decrease in fragmentation due to zooplankton exclusion in oxygen minimum zone cores (Cavan et al. 2017b).

Despite a sound mechanistic understanding of how temperature influences sinking and remineralisation rates, global analyses disagree as to the validity of using water temperature as a globally valid predictor for BCP flux attenuation ("b") or transfer efficiency (Henson et al. 2012; Marsay et al. 2015; Wiedmann et al. 2020). Studies disputing the use of temperature as a valid predictor of b claim that ecosystem and community structure are more valid predictors of b, highlighting a need to better characterise and understand the role of ecosystem processes in dictating BCP efficiency (Henson et al. 2012; Wiedmann et al. 2020; Henson et al. 2024).

1.5 Future Changes to the BCP

Given the myriad of physical and ecological factors involved in regulating BCP magnitude and efficiency, the BCP's response to increasing atmospheric CO₂ remains highly uncertain (Henson et al. 2022; Henson et al. 2024). Climate change and co-occurring changes such as deoxygenation and ocean acidification are predicted to result in positive feedbacks between some processes involved in the BCP, and negative or uncertain feedbacks in others (Figure 1.5, (Henson et al. 2022)).

The unclear importance of certain processes involved in the BCP, coupled with uncertainty in the response of these processes to climate feedbacks, means that the most recent CMIP6 (Coupled Model Intercomparison Project Phase 6) global models do not even agree on the sign of change of several key BCP metrics such as NPP (Tagliabue et al. 2021), export efficiency (Henson et al. 2022), and transfer efficiency (Wilson et al. 2022). Improving mechanistic understanding of these processes driving the BCP is critical to reducing uncertainty in future projections of the BCP under future climate scenarios.

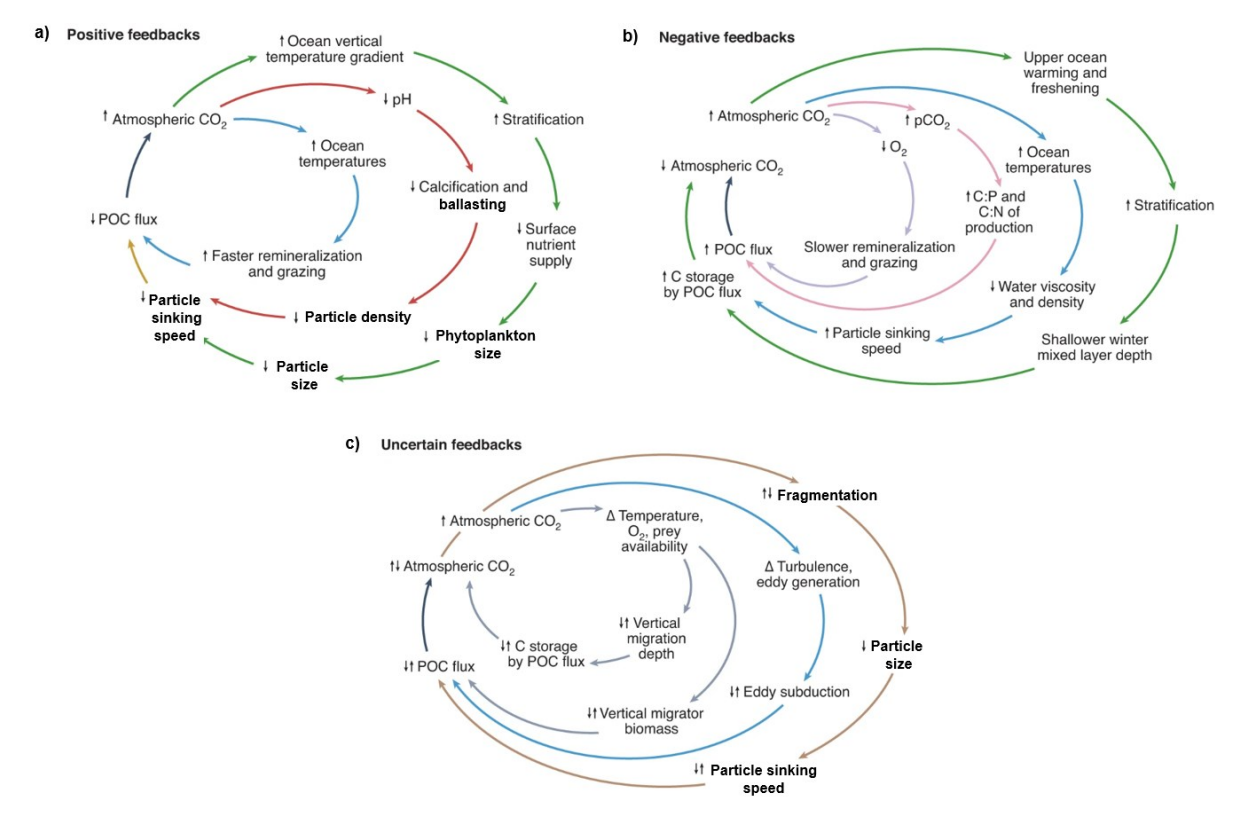


Figure 1.5 Examples of future feedbacks that may influence the Biological Carbon Pump. (a) Positive feedbacks; (b) negative feedbacks; (c) uncertain feedbacks on the Biological Carbon Pump that may arise from increases in atmospheric CO_2 and associated changes to ocean pH, global temperature, and ocean oxygenation. Feedback processes relating to particle characteristics that are discussed in this thesis are highlighted in bold. Adapted from (S. A. Henson et al., 2022).

1.6 Tools for Measuring POC Fluxes

There are a number of methods used to study particles, both suspended and sinking in the ocean—each with its own advantages, disadvantages, biases, and uncertainties. Understanding these biases and features of sampling apparatus is useful in interpreting the data they collect.

Sediment traps were perhaps one of the first and most widely adopted methods for the collection and measurement of sinking particulate fluxes (McDonnell et al. 2015). Traps typically consist of a collection cup or cups and a funnel above the cup to increase collection area, and have traditionally been deployed on moorings (McDonnell et al. 2015) to offer qualitative and quantitative estimates of sinking particle fluxes (Giering et al. 2020a). Such deployments on moorings serve as useful tools for collecting fixed-point time-series measurements of particulate fluxes, yet also suffer from numerous drawbacks and biases. These drawbacks of the original sediment trap design have led to a diversity of designs and deployment strategies to combat these issues. One bias associated with original trap designs are hydrodynamic biases arising from current flow around a tethered trap, which can reduce

collection efficiency by at least a factor of two (Buesseler et al. 2000; Buesseler et al. 2007a). To remedy this issue, neutrally buoyant, Lagrangian traps (Buesseler et al. 2000; Lampitt et al. 2008) have been developed to move with currents, yet such traps may only be deployed over the course of an oceanographic cruise and thus have limited temporal coverage (Giering et al. 2020a). Other developments include the use of gels to prevent amalgamation of particles and preserve individual particles for analysis (Jannasch et al. 1980; Flintrop et al. 2018), modifications to prevent zooplankton "swimmer" contamination (Peterson et al. 1993). Traps typically require the use of preservatives such as formaldehyde to prevent sample degradation, but this complicates downstream molecular analyses; alternative fixatives have been developed to preserve RNA or DNA for downstream molecular analysis of individual particles (Baumas et al. 2024).

An alternative approach to estimate POC fluxes and investigate particle cycling in the upper ocean can come through the use of radioactive pair tracers, such as ²³⁴Th/²³⁸U and ²¹⁰Po/²¹⁰Pb (Bacon et al. 1976; Verdeny et al. 2009). In the absence of particle movement, parent and daughter radionuclides would be in equilibrium, but differences in particle reactivity lead to a scavenging of the daughter radionuclides, and removal from the upper ocean (Verdeny et al. 2009). Vertical profiles of radionuclide activity are then typically converted into fluxes via a onedimensional steady-state model; fluxes are then used to estimate POC fluxes using a POC/radionuclide conversion (Buesseler et al. 1992; Le Moigne et al. 2014). Additionally, bulk particle sinking velocities can also be calculated from radioactive pair-disequilibria (Villa-Alfageme et al. 2016, Villa-Alfageme et al. 2023). Whilst the effect of swimmer flux is negligible for radionuclide fluxes (Buesseler et al. 2008), the half-life of commonly used radionuclides (234Th, 24.1 days; 210Po, 138.4 days) means fluxes estimated using radionuclides typically integrate over weeks or months, and thus are limited in their resolution (Verdeny et al. 2009). They may also be strongly influenced by non-steady state dynamics or advection (Ceballos-Romero et al. 2018; Roca-Martí and Puigcorbé 2024). Further, flux estimates are critically dependent on the radionuclide/POC conversion, which exhibits considerable temporal and spatial variation (Thomalla et al. 2006; Buesseler et al. 2007a; Puigcorbé et al. 2020). Largevolume particle collection using in situ pumps is the most common approach to determine this ratio, and the importance of constraining the radionuclide/POC ratio means that radionuclidebased approaches to estimate POC flux are typically limited to the duration of single oceanographic cruises.

1.6.1 Marine Snow Catchers

Marine Snow Catchers (MSCs) are a sampling method that have been used to study bulk particulate fluxes, partition between suspended-slow-sinking, and fast-sinking pools (Baker et

al. 2017; Cavan et al. 2017b; Giering et al. 2017; Duret et al. 2019), and enable microscale studies of individual particles (Belcher et al. 2016b; Flintrop et al. 2018). Described in detail by (Riley et al. 2012), the MSC is essentially a large (typically 100 L) settling column with two terminal apertures. The MSC is deployed at its target depth using a messenger, before recovery to deck, where an initial "time-zero" sample is taken. Over the course of a designated settling period, typically two hours, a concentration gradient develops within the MSC owing to the passive sinking of particles in the column. Following the settling period, samples may be taken from the upper, lower and often an absolute bottom "tray" section of the MSC, to determine sinking fluxes from the concentration gradient established throughout the MSC and to examine differences in gene expression between suspended, slow-sinking, and fast-sinking particle pools.

As well as being able to distinguish between suspended, slow-sinking, and fast-sinking particles, MSCs enable a range of measurements to be made either on these particle groups or on individual particles, such as sinking velocity measurements, particle morphology measurements, particle-associated microbial respiration, chemical (stoichiometric, isotopic, lipid) composition, and molecular measurements. They do not face the same hydrodynamic biases influencing trapping efficiency as tethered sediment traps in the upper 1,000m (Gardner 1980; Gardner 1985; Buesseler et al. 2007a) (though see disadvantages below) and thus are useful instruments for high vertical resolution, Eulerian time series measurements focused in the mesopelagic and epipelagic.

Whilst MSCs offer instantaneous flux measurements, permitting high-resolution temporal studies, the ship-based nature of their deployment also limits their temporal coverage. A number of assumptions also have the potential to introduce uncertainty into MSC flux measurements, namely that (i) particles are homogenously mixed throughout the MSC; (ii) that alteration to sinking particles during the settling period is negligible; and (iii) that particles are relatively unaltered during sampling, and thus reflective of marine particles in situ. Whilst the MSC was designed to minimise turbulent flow into the MSC and enable rapid flushing (flow-through) of the MSC during deployment (Lampitt et al. 1993; Riley et al. 2012), turbulent flow into the MSC has not been quantified, and small mistakes in the preparation of the MSC for deployment have the potential to result in misfires or prevent accurate measurements. For instance, incorrect positioning of the release on the wire can result in the central plunger which closes the MSC sitting lower than optimal, narrowing the inlet for water inflow into the MSC. A winch operator is also required to lift the MSC during set-up and sampling of the MSC, whilst safety is also a concern in connecting the MSC base section to the main MSC, whilst the MSC body is suspended by the winch. In spite of these shortcomings and practical difficulties, MSCs

are nonetheless an effective tool for direct, high-resolution flux measurements in the upper ocean, and can be useful for the calibration of flux measurements from imaging technologies.

1.6.2 Optical Flux Measurements

The advent of in situ imaging technologies has opened the door to a new age in the study of the Biological Carbon Pump (Giering et al. 2020a). As with all of the technologies listed above, they are limited in their vertical resolution to the number of targeted depth deployments and, unless tethered to one location, generally limited in their temporal coverage to the length of a research cruise. The development of optical technologies is now enabling the study of the biological carbon pump in unprecedented resolution, and-through deployment on autonomous vehicleswith spatial coverage of the ocean far surpassing that possible from oceanographic research vessels (Giering et al. 2020a). In addition, the ability to observe marine particles in situ minimises the likelihood of particle alteration during sampling and processing, ensuring particles are as reflective as possible of true behaviour in situ.

The range of approaches and insights that can be gained from using optical methods are manifold. Bulk optical properties, such as optical backscatter or beam attenuation, can be used to estimate particle concentration (Cetinić et al. 2012), which, when combined with an optical property/carbon content ratio and a sinking velocity, can yield flux estimates (Briggs et al. 2011; Briggs et al. 2020). Particle size distributions obtained through particle imaging approaches can be used to estimate fluxes if sinking velocities can be estimated for each size class (McDonnell and Buesseler 2010), or particle size spectra can be related directly to fluxes using an empirical relationship which incorporates sinking velocity and particle mass as functions of size (Guidi et al. 2008; Iversen et al. 2010). These approaches typically require calibration with simultaneous deployments of sediment traps or other direct flux measurements.

Optical approaches can also yield mechanistic insights besides measurements of POC fluxes. Particle imaging techniques offer insights into particle properties which influence BCP efficiency, such as size, type, shape, and abundance (Giering et al. 2020a), whilst size spectra can offer insights into particle transformations and the processes causing them (Burd and Jackson 2009; Takeuchi et al. 2019).

In spite of the many advantages of optical methods, they also have their drawbacks. Since they do not make direct measurements of sinking fluxes, they are critically dependent on assumptions used to convert from particle concentration to POC (or other measurement, e.g. BSi) concentration, and from particle size to sinking velocity. Relationships used to relate particle size or optical backscatter to POC can vary with time, space, and depth, potentially

introducing a large source of uncertainty to flux estimates from in situ optical methods (Iversen et al. 2010; Cetinić et al. 2012).

1.7 Recent developments in BCP research

Over the last 10-15 years, a wealth of breakthroughs has led to the development of new methodologies, and the recognition of new processes involved in the BCP. One such group of processes are "particle injection pumps" (Boyd et al. 2019), which describe additional physical or biological mechanisms acting in concert with the passive sinking of organic particles to transfer carbon to depth. Examples of physical pumps include physical subduction by mesoscale eddies (Omand et al. 2015) or large-scale frontal subduction (Lévy et al. 2013), and mixed layer shallowing (Dall'Olmo et al. 2016) as mechanisms driving carbon transfer from the surface ocean. Biological particle injection pumps include both the daily (Cavan et al. 2015; Steinberg & Landry, 2017) and seasonal ontogenetic migrations (Jónasdóttir et al. 2015) of metazoans from the surface into the mesopelagic, releasing carbon at depth and allowing it to bypass remineralisation that would be experienced during passive particle sinking. Many of these processes have been known for decades (Spall, 1995; Steinberg et al. 2000), but only recently has their collective importance to carbon sequestration been highlighted, which may be almost equal to the passive sinking of organic particles (Boyd et al. 2019).

As well as their role in delivering carbon to depth via particle injection pumps, the major role of zooplankton in shaping attenuation of sinking particulate fluxes is becoming clear. Whilst the majority of particle remineralization in the mesopelagic zone has been modelled to be carried out by microbes (Giering et al. 2014), several studies have determined that the majority of particle flux attenuation in the twilight zone may, in fact, be driven by zooplankton (Stukel et al. 2019; Van der Jagt et al. 2020, Bressac et al. 2024). Whilst zooplankton can enhance flux to depth via active transport of faecal pellets (Cavan et al. 2015; Hernandez-Leon et al. 2024) and repackaging material into dense faecal pellets (Steinberg et al. 2008; Steinberg and Landry, 2017), they also act to fragment sinking particles (Stukel et al. 2019; Briggs et al. 2020), potentially to stimulate microbial growth and the production of labile organic compounds at depth (Mayor et al. 2014). This fragmentation appears to drive the majority of zooplankton flux attenuation (Briggs et al. 2020; Bressac et al. 2024), and so zooplankton community structure is critical in determining the balance between processes which facilitate efficient transfer to depth and processes attenuating sinking fluxes.

Recognising the role of ecological complexity at the level of individual particles is likewise an emergent topic in BCP research. Driven in part by the proliferation of in-situ imaging methods and the need to constrain relationships between particle size and carbon content or sinking

velocity, numerous studies have highlighted how diversity in particle chemical and taxonomic composition, or particle morphology can influence the efficiency of particle transfer to depth (Durkin et al. 2021; Giering et al. 2020b). For instance, though particle size remains an important control on BCP function (Lacour et al. 2024), size-sinking velocity relationships vary widely in time and space owing to differences in other particle characteristics (Iversen et al. 2010; McDonnell and Buesseler, 2012) and the importance of particle size as a control on particle sinking velocity has been shown to be dependent on additional particle traits (Laurenceau-Cornec et al. 2015b). Morphological diversity associated with different taxonomic groups of plankton which comprise particle- for instance diatoms- have also been implicated in determining particle sinking velocities (Laurenceau-Cornec et al. 2015b; Omand et al. 2020), whilst aside from sinking velocities, variations in particle lability are likewise an important factor in determining the balance between particle sinking and remineralisation that determines flux attenuation (Stephens et al. 2024). Taken together, particle characteristics have been identified as highly important in regulating BCP, yet an area of uncertainty that must be resolved to further mechanistic understanding (Henson et al. 2024).

1.8 Thesis Aims, Outline, and Hypotheses

The response of transfer efficiency to climate change is one of the largest sources of uncertainty in forecasting how the BCP will respond to changes in climate (Wilson et al. 2022). The below table, adapted from Henson et al. (2024), outlines properties and processes influencing these properties that are rated as "high importance" yet "uncertain" in setting the degree of interior respiration to which sinking particles are exposed (hence highly important in setting transfer efficiency). Many of these properties and processes are interlinked.

Table 1.1 Particle properties and particle alteration processes rated as highly important in determining the efficiency of particle transfer to depth during particle sinking. Adapted from Henson et al. (2024).

Feature	Property or	Definition
	Process	
Particle types	Property	The type of particle (faecal pellet, aggregate, larvacean
		houses) determines features of particles that influence their
		sinking velocity and susceptibility to remineralisation, and
		influences the likelihood and type of plankton-particle
		interactions.

Chapter 1

Particle characteristics	Property	Influenced by particle type and processes altering particles within the water column, particle characteristics such as size, morphology, porosity, shape, and ballast content act to influence particle sinking velocities and degree of exposure to remineralisation.
Biotic fragmentation	Process	Fragmentation of particles into smaller pieces by zooplankton or turbulence, with implications for particle structure, size and sinking velocity.
Aggregation	Process	The formation of larger particles via the aggregation of smaller particles, which influences particle sizes and sinking velocity. The role of turbulence and exopolymeric substances both influence particle aggregation.
Microbial solubilisation	Process	Microbial respiration of dissolved and particulate material. The degree of particle remineralisation is influenced by the above particle properties, which can determine particle lability and sinking velocity, hence setting the length of time during which particles are exposed to remineralisation. Environmental factors also play a major role.

The aim of this thesis is to address uncertainty in the role of particle characteristics in determining sinking velocity and transfer efficiency. It is important to understand the influence of particle characteristics on sinking velocity and transfer efficiency in order to understand how ecological changes arising from climate change will impact the biological pump. This thesis focuses on these particle characteristics as they are not only mechanistically important, but also practically important for the conversion of particle image data into fluxes.

The structure of this thesis, and associated hypotheses are as follows:

Chapter 2: I investigate the extent to which particle size effectively predicts sinking-velocity for in situ marine particles.

H1: Size is a strong predictor of particle sinking velocity for in situ marine particles.

Size-based parameterisations are commonly used to represent particle pools with differing transfer efficiencies in biogeochemical models, and to estimate sinking velocities or fluxes from in situ image measurements. I assess the extent to which this holds true for in situ and ex-situ studies which measured particle size and sinking velocity.

Chapter 3: I assess the extent to which diatoms drive the efficient transfer of carbon through the mesopelagic in sinking particles.

H2: Diatoms promote the efficient transfer of carbon through the subpolar Southern Ocean twilight zone.

Due to their biogenic silica exoskeletons, diatoms have been posed to be efficient vectors for sinking carbon to depth due to the "ballast" provided by these dense skeletons; the validity of this hypothesis is debated, however.

Chapter 4: I examine vertical and spatial patterns in marine snow morphology across a transect of the Atlantic Ocean.

H3: Marine snow morphology varies with latitude and with depth, and influences efficiency of particle transfer to depth.

Morphological characteristics of particles are thought to play a role in dictating the efficiency of particle transfer to depth on the regional scale, but whether local mesopelagic communities or particle characteristics sinking from the surface play a larger role in shaping particle properties at depth is unclear.

Chapter 5: I present results from flow-modelling, shore-based trials, and field trials of a novel marine snow catcher design developed at the NOC. Such tools to reliably sample marine particulates and measure sinking fluxes are vital for the calibration of optical flux estimates and to gain a mechanistic understanding of the BCP.

Chapter 6: In this chapter, I discuss implications of the results presented within this thesis and suggest avenues for future work.

Chapter 2 In Situ Particle Measurements Deemphasize the Role of Size in Governing the Sinking Velocity of Marine Particles

This chapter has been published in Geophysical Research Letters as:

Williams, J.R. and Giering, S.L.C., 2022. In situ particle measurements deemphasize the role of size in governing the sinking velocity of marine particles. Geophysical Research Letters, 49(21), p.e2022GL099563. Methods have been integrated into the main discussion section.

JRW carried out conceptualization, data curation, formal analysis, investigation, methodology, visualisation, and writing of the manuscript. SLCG carried out conceptualisation, funding acquisition, methodology, project administration, supervision, and writing.

2.1 Abstract

Sinking particles are important in delivering carbon to the deep ocean, where it may be stored out of contact with the atmosphere. Whilst particle sinking velocities are known to be influenced by a multitude of factors, size-based parameterizations remain common in biogeochemical models and in the methods used to determine particulate fluxes from autonomous platforms. Here, I carried out an extensive literature review (62 data sets) into the size-sinking velocity relationship, and find the relationship is much weaker for studies examining particles in situ (median $R^2 = 0.09$) compared with ex situ studies (median $R^2 = 0.35$). This discrepancy may be because particles examined in the laboratory have more uniform properties than those studied in situ. This review highlights the shortcomings of using a simple relationship between size and sinking velocity to calculate sinking particulate fluxes in the ocean; considering additional particle characteristics will enable more accurate calculations of particulate fluxes.

2.2 Introduction

In the ocean, the production, transfer to depth, and remineralization of organic particles provide a major pathway for the export of carbon from the ocean's surface to the ocean interior (Volk and Hoffert 1985). Collectively termed the Biological Carbon Pump (BCP), these processes act to maintain atmospheric CO_2 approximately 200 ppm lower than they would otherwise be (Maier-Reimer et al. 1996; Parekh et al. 2006b). Although several processes contribute to the

BCP, the gravitational settling of organic particles are thought to result in ~1000 Pg of ocean carbon storage (Boyd et al. 2019), up to 90% of the carbon sequestered by the BCP (Boyd et al., 2019; Buesseler et al., 2020; Sarmiento & Gruber, 2006).

As particulate organic carbon (POC) sinks, proportions of this downward flux are reworked by metazoans such as zooplankton, and eventually remineralised back into CO₂, through both microbial and zooplankton respiration (Giering et al., 2014; Steinberg et al., 2008; van der Jagt et al., 2020). As a result of this particle remineralisation and reworking, sinking POC fluxes are observed to decrease with depth. The rate of flux attenuation (and hence the proportion of sinking carbon reaching the deep ocean) is determined by the balance between particle sinking velocities and remineralisation rates (Marsay et al. 2015; Bach et al. 2019). Since particle sinking velocities determine the length of time during which a particle is exposed to metazoan and microbial remineralisation, sinking velocity is a crucial determinant in the degree of attenuation of POC fluxes and BCP efficiency (Laurenceau-Cornec et al. 2015b) (Figure 2.1).

In recent years, the use of in situ optical methods has emerged as an important tool in the study of the BCP (Giering et al. 2020a). Increasingly able to be deployed autonomously (Lombard et al. 2019; Picheral et al. 2022), these methods can provide far greater spatiotemporal resolution and coverage than traditional ship-based sampling methods (Lombard et al. 2019; Giering et al. 2020a). Given also the considerable effort that has focused on improving the utility of in situ imaging devices, in situ cameras are now capable of providing quantitative particle information on particles from 1 – 10,000 µm in diameter (Lombard et al., 2019). Using the particle size distributions obtained by in situ imaging methods, particle fluxes within a given size class can be calculated if sinking velocities of particles within the size class can also be estimated (McDonnell and Buesseler 2010; McDonnell and Buesseler 2012), or, more commonly, through directly relating particle size to flux via an empirical relationship (Guidi et al. 2008; Iversen et al. 2010). A robust understanding of the factors that govern particle sinking rate is therefore crucial in the implementation of these cutting-edge methods for estimating particulate fluxes and studying the BCP.

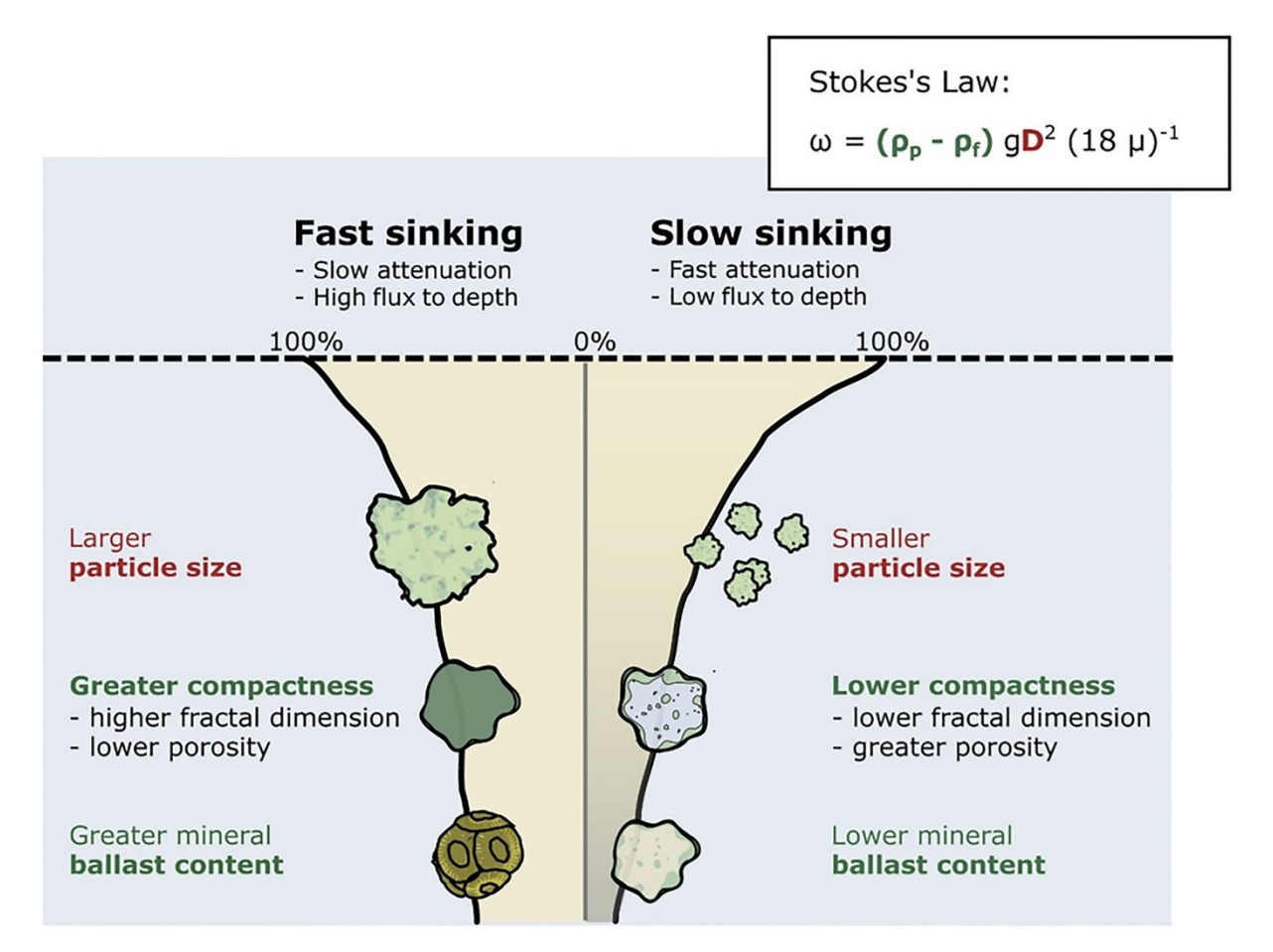


Figure 2.1 Schematic illustrating factors posed to influence particle sinking velocity, their relation to size (red) or density (green) as described in Stokes's law, and the effect of fast and slow sinking particles on particulate flux attenuation rates and particle fluxes reaching depth. Illustrative flux attenuation curves are shown for fast-sinking (left) and slow-sinking (right) particles. Fast-sinking particles experience slower rates of flux attenuation due to decreased duration of exposure to remineralisation whilst they sink.

Whilst the use of particle size spectra provides the means to calculate particulate fluxes with unprecedented resolution, the prevailing methods used to empirically relate size to fluxes assume that mass and sinking velocity as functions of particle size remain constant (Guidi et al. 2008; Iversen et al. 2010). Further, relying on a single relationship to describe sinking velocity in terms of particle size implies that larger particles should always sink faster than smaller ones (McDonnell and Buesseler 2010). Although several studies have observed size to exert a strong control on sinking velocities (Alldredge and Gotschalk 1988; Iversen et al. 2010), considering size as a key predictor of sinking velocity assumes relative constancy of other particle properties such as particle composition, porosity and biomineral content. In recent years, empirical studies have indicated that this assumption of constancy cannot be applied in situ (Iversen and Ploug 2010; Iversen and Lampitt 2020; Laurenceau-Cornec et al. 2020) and that size alone is often a poor predictor of sinking velocity (Diercks and Asper 1997; Iversen and Lampitt 2020).

Nevertheless, size-based methods remain a commonly used approach to estimate fluxes from in situ image data (Guidi et al. 2016; Ramondenc et al. 2016a; Fender et al. 2019; Kiko et al. 2020; Cram et al. 2022) and size-based parameterisations of vertical carbon fluxes remain common in biogeochemical models (Kriest and Oschlies 2008; Aumont et al. 2015; Swart et al. 2019; Leung et al. 2021; Yool et al. 2021).

Here, I first outline the theoretical basis underpinning commonly used size-based approaches. I then highlight the lack of evidence suggesting size can represent a strong predictor of marine particle sinking velocities in situ, and assess the reasons for differences between studies. I recommend avenues for further study that will facilitate improved mechanistic understanding of particle sinking velocities and broaden the applicability of in situ image-based estimations of particle flux.

2.2.1 The Theoretical Basis for Size-Based Methods

In recent decades, derivations such as Stokes's law have been widely used to estimate particle sinking velocity (Laurenceau-Cornec et al., 2020). Assuming that particle drag coefficients can be calculated as a simple function of Reynolds number for low Reynolds numbers (in laminar flow conditions), and balancing drag and gravitational forces on a particle, these derivations pose size to be a key determinant of sinking velocity. Stokes's Law says that

$$w = \left(\rho_p - \rho_f\right) \frac{gD^2}{18\mu} \tag{2.1}$$

where w is the sinking velocity of a sphere (m s⁻¹), ρ_P and ρ_f are the sphere and fluid densities (kg m⁻³), g is the acceleration due to gravity (9.81 m s⁻²), D is the sphere diameter (m), and μ is the fluid dynamic viscosity in kg m⁻¹s⁻¹. Power law functions based on Stokes's Law have been used to relate particle size to sinking velocity for decades (Alldredge & Gotschalk, 1988; Smayda, 1970) and more recently to parameterise modelled particle sinking velocities (Aumont et al., 2015; DeVries et al., 2014; Kriest & Evans, 1999; Leung et al., 2021). Other biogeochemical models simply incorporate size through discrete size classes, with a large, fast-sinking fraction and a small, slow-sinking fraction (Aumont et al., 2015; Swart et al., 2019; Yool et al., 2021). The lack of mechanistic understanding as to how well size constrains sinking velocity has resulted in a variety of size-sinking relationships in earth system models, which yield up to order of magnitude differences in sinking velocity for particles of the same size, and introduce uncertainty into flux prediction and biogeochemical models (Cael et al., 2021; Niemeyer et al., 2019). Since plankton models additionally suggest a decrease in cell size with warming,

constraining sinking velocities in an accurate mechanistic fashion is of importance for the accurate modelling of climate change projections (Cael et al., 2021; Finkel et al., 2010).

Power law functions have more recently also been used to directly estimate particulate fluxes from particle size distributions. Since both sinking velocity (w) and particle mass (m), and hence flux for a given particle i (F_i) can be expressed as power law functions of the form ($y = ax^b$), their product can be expressed in the same form:

$$F_i = wm = AD^B (2.2)$$

where D is particle diameter, and A and B are constants (Guidi et al. 2008). If A and B are known, size spectra can be used to calculate total mass fluxes, F. A and B may be estimated through a minimisation procedure (Cram et al., 2022; Fender et al., 2019; Guidi et al., 2008; Iversen et al., 2010; Nowald et al., 2015) if alternative measurements of particulate fluxes can be made, and assuming that mass and particle size as a function of depth are constant for all depths (Iversen et al. 2010). Alternatively, when additional flux measurements have not been made (such as on autonomous deployments on moorings, gliders, or floats), prior studies can be used to estimate global values for A and B (Guidi et al., 2008; 2016; Kiko et al., 2020; Ramondenc et al., 2016). The above approaches assume that particle mass and sinking velocity as functions of size are constant with depth and, in the latter instance, universally constant; hence both methods represent size as a strong control of sinking velocity.

2.3 Empirical Evidence on the Size-Sinking Velocity Relationship

2.3.1 Methods

To direct discussion in the most constructive fashion towards particle characteristics commonly discussed in the literature, I focused analysis on four of the most commonly studied characteristics. It should, however, be noted that the frequency with which characteristics are discussed in the literature does not necessarily indicate that they are the most important four drivers of sinking velocity. To identify these characteristics, I carried out a literature search into studies measuring particle sinking velocity and associated particle characteristics using both in situ and ex situ methods, and commonly used key terms to describe marine particle characteristics ("Size", "Ballast", "Morphology", "Composition", "Type", "Shape", "Compactness", "Fractal" [Dimension]). Restricting results to within Earth and Planetary Sciences, I searched for abstracts, titles, and keywords containing the words "Particle" and "Sinking" and "Velocity" as well as a given particle characteristic. Size returned the greatest

number of studies (79), followed by parameters relating to chemical and taxonomic composition (Composition: 37; Type: 22; Ballast: 18). Searches relating to other morphological properties typically returned the fewest results ("Shape": 17; "Fractal" [Dimension]: 5; "Compactness": 1; "Permeability": 1; "Morphology": 1).

Using the four most commonly studied particle attributes from the literature search (size, particle type, ballast, and shape), I identified 62 datasets from 38 studies and examined the degree of correlation between sinking velocity and each of the above attributes (Figure 2.2)- as outlined in more detail below.

2.3.1.1 Data compilation

We compiled observations of particle sinking velocity and associated particle characteristics from 62 data sets from 38 studies (see Supplementary Table S2.1, Supplementary Table S2.2). These data had previously been compiled by (Cael et al. 2021b) and (Laurenceau-Cornec et al. 2015b; Laurenceau-Cornec et al. 2020); all original data sets were validated and, if needed, redigitized using Plot Digitizer (https://automeris.io/WebPlotDigitizer/). Studies not relating to marine particles were excluded from this analysis. In the small number of cases where particle size and sinking velocity data had been fitted to a power law function in original studies (n = 10), published R^2 values in the literature were used. Data were assigned to "in situ" and "ex situ" groups for measurement type, based on whether sinking velocity measurements were made ex situ (e.g. in roller tanks, FlowCam) or in situ (e.g. scuba/ in situ camera system). The particle types examined in each study were assigned to one of nine particle types (e.g., natural aggregates, mixed diatom culture; for full list Figure 2.2, Supplementary Table S2.2), with the method used to measure particle sinking velocities also described through one of nine groups (e.g., Scuba photography, Vertical flow system; for full list, see legend of Figure 2.2, Supplementary Table S2.2). Note that in some studies, particles may have in situ origin but are classed as ex situ studies since sinking velocity measurements were made in situ (for example, naturally formed marine aggregates collected, stored and sinking velocities measured in roller tanks).

2.3.1.2 Sinking Velocity/Particle Characteristic Analyses

To assess the variability in sinking velocity explained by particle size in each study, a power law function (in the form $w = Ad^B$, where w is the sinking velocity, d the diameter, and A and B are scaling coefficients) was fitted to the data. A power law function was chosen over a linear relationship since sinking velocity is thought to scale with particle diameter according to a power law function according to Stokes's Law and empirically modified versions incorporating porosity (Guidi et al. 2008; Laurenceau-Cornec et al. 2020; Xiang et al. 2022).

For studies where more than one particle type, degree of ballast, and particle shape were recorded, R^2 values were recorded either from performing linear regressions or ANOVAs, depending on whether the particle characteristic was described in terms of continuous or categorical data. For example, in some studies particle type was analyzed as a categorical variable with discrete groups such as S. costatum or E. huxleyi aggregates- sinking velocity was compared between these groups by means of an ANOVA, and the R^2 value of this ANOVA was reported. In another study, particle type was expressed as a percentage of aggregate composition of one diatom morphotype (Laurenceau-Cornec et al. 2015b). In this case, a linear regression was performed between percentage of total composition and particle sinking velocity, and the R^2 value of this linear regression reported. Lastly, once R^2 values had been calculated for all individual studies, a Wilcoxon rank sum test with continuity correction was performed to assess whether the distribution of R^2 values differed significantly between studies which made particle measurements in situ and those which made particle measurements ex situ.

2.3.1.3 Methodological comparison

To represent the advantages and disadvantages of in situ and ex situ methods for sinking velocity measurement, methods were ranked in terms of their ability to measure particle characteristics, and in terms of particle realism. Although these assertions are subjective rankings, a scoring system was devised to standardize rankings and criteria by which methods were judged. For measurement capability score, particle characteristics (Size, Ballast, Taxonomic composition/Particle type, Chemical composition, Shape, Dry weight, Porosity, Fractal dimension, Density, and Sinking velocity) were assigned a score from 0 to 4, describing the comprehensiveness with which a particle characteristic could be studied with a given method (0 lowest, 4 highest; (see Supplementary Table S2.3). Measurement capability scores of individual characteristics were summed to give an overall score. Where a range of measurement scores was given for a particle characteristic, the mean value was used when summing scores to calculate (e.g., 2–3 scored as 2.5).

For the particle realism score, each method was assigned a score from 0 to 4, based on the extent to which the particles measured had been influenced by sampling and measurement procedures, that is, the extent to which particle communities measured could be expected to reflect natural marine particle communities in situ. A brief explanation for assigned scores and evidence supporting these assertions is outlined in Supplementary Table S2.3).

2.3.2 Discussion

Despite particle size having received the most interest, my review suggests the dependency of sinking velocity on size is not well constrained (Figure 2.2). Taking all studies (both in situ and ex situ) together, size explains between 0-88% of the variation in particle sinking velocity (as determined by the coefficient of determination (R^2) with a median value of 31%. The strongest correlation between size and sinking velocity was observed for intact salp faecal pellets from the Southern Ocean (Iversen et al. 2017). However, in 26% of the datasets, particle size was observed to be a poor predictor of sinking velocity, explaining less than 10% of the variation in particle sinking velocity (Figure 2.2). Particle size did not appear to be a stronger predictor of sinking velocity than particle type or particle ballast content (Wilcoxon rank tests, p > 0.8). The median percentage of variance in sinking velocity explained by particle type and ballast content was 26% and 30%, respectively. It is noteworthy, however, that only four ex situ datasets examined the influence of particle type (i.e. differences in both taxonomic composition, i.e. aggregates made of different phytoplankton species, or particle shape, e.g. faecal pellets vs aggregates) or ballast content. Likewise, for particle shape, only one ex situ (Laurenceau-Cornec et al. 2015b) and one in situ (Iversen and Lampitt 2020) study directly measured a particle shape characteristic (aspect ratio) and sinking velocity, with neither of these studies finding sinking velocity to be explained by particle shape alone.

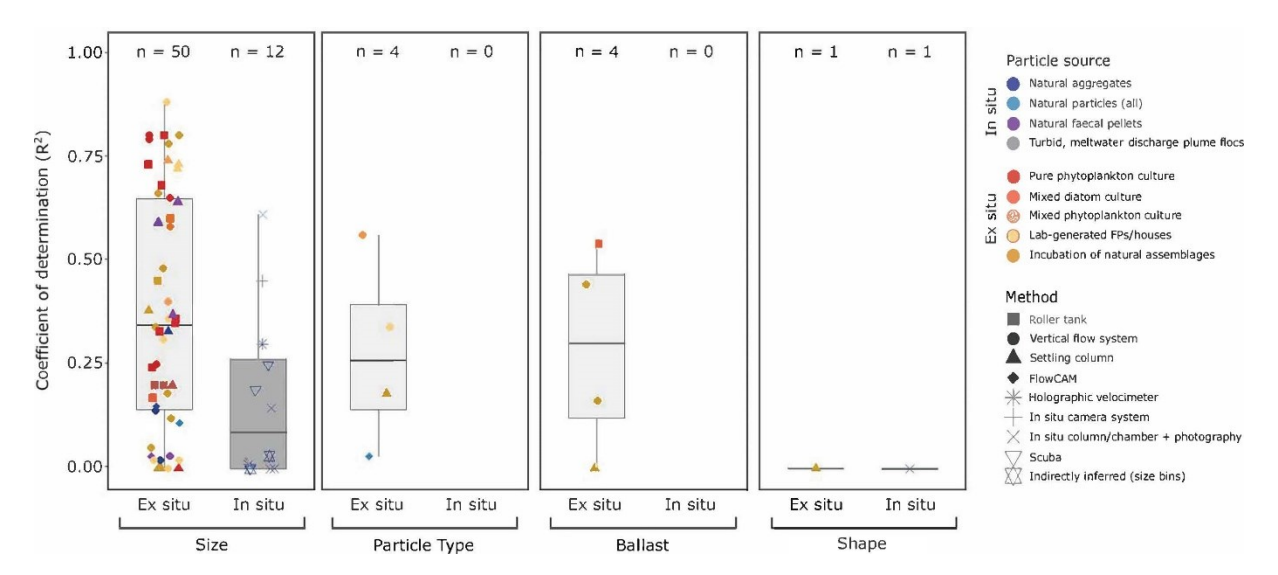


Figure 2.2 Boxplot comparing the proportion of variance in sinking velocity explained by particle characteristics. Coefficients of determination (R^2) from linear models and analyses of variance performed between particle characteristics (size, type, ballast content, shape) and sinking velocities directly measured in previous studies (see Supplementary Table S2.2). Colours of boxplots indicate whether sinking velocity measurements were made in situ (dark grey) or ex situ (light grey), and how

particles were generated (in situ: natural particles observed in situ or measured immediately ex situ without prior incubation; ex situ: cultured or incubated ex situ prior to measurement. Shapes of the points indicate method used to measure sinking velocity.

For the data sets focusing on particle size as a predictor, I found strong differences between measurements made in situ and ex situ. The distribution of R^2 values were significantly higher for ex situ studies than in situ studies (Wilcoxon rank test, p < 0.05; Figure 2.2), suggesting that the strength of the size-sinking velocity relationship may be influenced by whether measurements are made in or ex situ. For in situ particles, the median percentage of variance in sinking velocity explained by particle size was 9%, contrasting with 35% for particles measured ex situ (Figure 2.2). In addition, for in situ data sets (n = 12), size explained more than 30% of variability in sinking velocity in just two studies, which respectively examined flocs from meltwater discharge plumes and resuspended near-bottom sediment. By contrast, for ex situ datasets (n = 50), particle size explained more than 30% of variance in sinking velocity in the majority (27 out of 50) datasets. As a result, while weak correlations between size and sinking velocity were observed in both situ and ex situ data sets, strong dependencies of sinking velocity on particle size were only observed ex situ.

However, when combining all ex situ data sets, a clear lack of a "global" size-to-sinking velocity relationship becomes apparent (SV = 176*Size $^{0.477}$; n = 4,138, p = <0.001, R^2 = 0.017) (Figure 2.3a), though note that this weak relationship combines studies which used different methods, and so may forego a direct comparison (Giering et al. 2020b). A global relationship between size and sinking velocity for all particles from in situ studies was even weaker, and sinking velocities in situ were typically also lower than ex situ (SV = 98*Size $^{0.061}$; n = 485, p = 0.050, R^2 = 0.0004) (Figure 2.3a). Overall, these findings suggest that the strong relationships often observed ex situ between individual particle characteristics and sinking velocity rarely hold true in situ, and that strong relationships ex situ may dissolve if heterogeneous groups of particles are examined together. As such, the methodological biases outlined below should be taken into consideration before extrapolating relationships observed in ex situ studies to natural marine particles in situ.

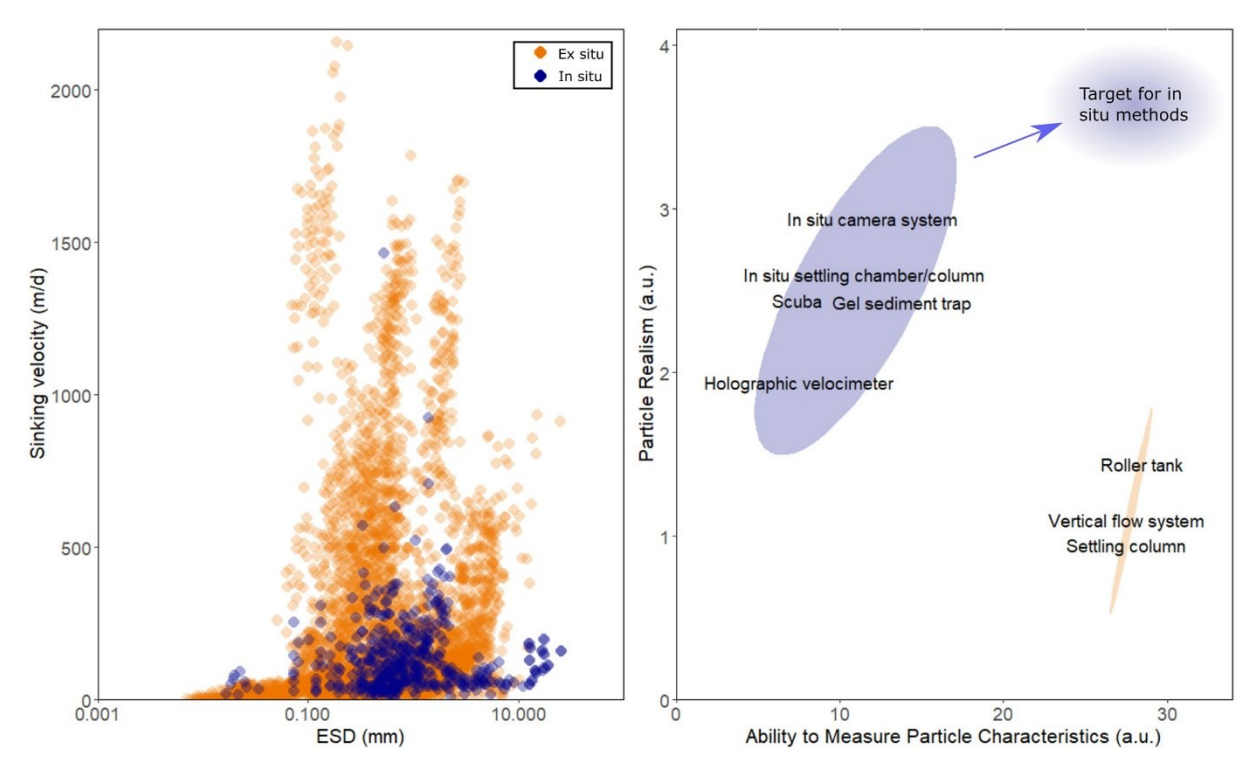


Figure 2.3 (a) Particle size (equivalent spherical diameter [ESD]) against sinking velocity for all particles in this study, from both in situ (blue) and ex situ (orange) studies (raw data within Supplementary Table S2.1). (b) Relative advantages of in situ and ex situ methods (blue and orange respectively) in terms of ability to measure particle characteristics and particle realism, when investigating the relationship between particle sinking velocity and particle characteristics. Position of each method relates to an assigned "Particle Realism score" and "Measurement Capability score" as described in 2.3.1.3; explanations of assertions used for scoring these methods are available in Supplementary Table S2.3.

2.3.2.1 Ex Situ Versus in Situ: Methodological Compromises

Methodological differences between in situ and ex situ studies can explain both the predominance of ex situ studies examining the size-sinking velocity relationship, and why size is seen to more tightly constrain sinking velocities ex situ than in situ.

In situ methods hold the major advantage of observing particles in their natural environment. Any measurements made are therefore acquired without the need for handling particles, decreasing (but not eliminating (Briggs et al. 2011; Cetinić et al. 2012)) the potential alteration and disturbance to particle properties (Giering et al. 2020a; Iversen and Lampitt 2020), and thus maximizing the realism of any interactions between sinking velocity and particle characteristics. However, a major drawback of in situ optical devices is that these methods lack the capability to provide direct information on a number of particle characteristics, such as particle density and composition (Giering et al. 2020b). These methods must hence rely on additional data or

assumptions to estimate particle sinking velocities and calculate particulate fluxes. Given these uncertainties, the expensive nature of in situ camera systems, and a lack of standardization in analysis routines for in situ image data sets (Giering et al. 2020b), in situ studies into particle sinking velocities remain sparse compared with more traditional ex situ methods. In summary, in situ studies lack the capacity to study particle characteristics which may be measured ex situ, but maximize realism (Figure 2.3b).

Most studies into factors constraining sinking velocity involve incubating particles ex situ prior to or during measurements. By examining particles in a laboratory, detailed measurements of a wide number of particle characteristics can be made, such as chemical and taxonomic composition, removing the need for estimates of these parameters (Mantovanelli and Ridd 2006). In addition, studies where particles are generated ex situ also allow for manipulation of particle characteristics, to test for effects of specific particle characteristics on sinking velocities (Giering et al. 2020a). However, ex situ particles are likely not reflective of in situ particle dynamics, partly owing to ex situ particles being more homogenous. Three aspects contribute to this discrepancy: (1) Homogeneity in the 'source' particle pool; (2) homogenization of particles during particle collection; (3) homogenization of particles during the incubation for measuring sinking velocities.

Firstly, particles for ex situ incubations are often sourced from "artificial," laboratory-produced particles, for example, incubating homogenous particle pools such as phytoplankton cultures in roller tanks, whilst in the natural environment, a heterogeneous pool of particles of varied age, composition, density, structure, and porosity exists (Alldredge and Gotschalk 1988; Alldredge 1998; Iversen and Lampitt 2020). The unnatural homogeneity of ex situ particles sourced in this way reduces the variability in sinking velocity introduced by factors other than size, thus allowing size to exert a dominant control over sinking velocity.

An alternative approach to sourcing particles for incubations involves the collection of natural marine particles. Whilst this approach allows for collection of a more diverse particle pool, highly fragile marine aggregates are susceptible to damage, alteration, and compaction or disaggregation during sampling for ex situ incubations (Kajihara 1971; Alldredge and Gotschalk 1988; Alldredge and Silver 1988; Takeuchi et al. 2019; Giering et al. 2020a; Iversen and Lampitt 2020). Particles measured in the laboratory are able to withstand higher turbulences than those observed in the ocean (Alldredge et al. 1990; Riebesell 1992), and also typically exhibit increased sinking velocities compared with measurements made in situ (Figure 2.3a) (Shanks and Trent 1980; Alldredge et al. 1990). These observations indicate that, despite the more heterogeneous nature of naturally occurring particles compared to cultured particles, sampling

in this way tends to alter particles (and/or particle populations) such that they are no longer fully representative of marine particles in situ.

Lastly, particles incubated ex situ are exposed to a far more limited set of processes influencing their formation and composition. In situ, a number of biological and physical processes contribute to the aggregation of particles. For physical processes, mechanisms such as Brownian motion, differential settling (in which faster sinking particles scavenge slower sinking or suspended particles upon collision), and turbulent shear (McCave 1984) influence aggregate formation, with the importance of these processes varying depending on particle size (McCave 1984; Jackson 1994; Takeuchi et al. 2019). By contrast, in roller tanks, turbulent shear is negligible in aggregate formation once the initial spin-up period is over (Engel et al. 2009; Laurenceau-Cornec et al. 2015b), whilst in Couette chambers the influence of shear is amplified relative to in situ (Lick et al. 1993; Jackson 2015). Ex situ incubations also typically lack the diversity of biologically mediated processes that aggregate or disaggregate particles. In situ, aggregation processes in situ can include compaction into faecal pellets, the accretion of particles onto mucous houses and other exuded exopolymers (Hamner et al. 1975; Hansen et al. 1996; Kiørboe 2001) and aggregation due to organisms' feeding currents (Fukuda & Koike, 2000). Particle disaggregation as a result of zooplankton feeding can also occur in situ, a process which may not be included in ex situ incubations (Dilling and Alldredge 2000; Iversen and Poulsen 2007). Given that in situ studies cannot replicate the diversity of in situ processes involved in forming and transforming particles, it is unsurprising that ex situ particle pools are more homogenous than those in situ, and hence exhibit stronger size-scaling relationships. Overall, ex situ studies favour the ability to measure and examine particle dynamics in detail, whilst sacrificing realism (Figure 2.3b).

2.4 An Outlook for the Use of In Situ Methods

This review highlights the discrepancy in the extent to which size controls sinking velocity between in situ and ex situ studies (Alldredge and Gotschalk 1988), and that—despite this discrepancy—size-based methods remain common for estimating fluxes from in situ data or representing marine particles in models.

While there is clear merit in using simple size-to-sinking velocity relationships for autonomous methods (e.g., Guidi et al., 2008; Iversen et al., 2010; Fender et al., 2019), these approaches provide limited mechanistic understanding of the size-flux relationship, limiting the certainty with which relationships can be spatiotemporally extrapolated. As suggested by McDonnell and Buesseler (2010), taking into account particle types will increase the range of spatiotemporal scales over which size-scaling relationships can be applied. Recognizing individual size-scaling

relationships for varying particle types will enable more accurate sinking velocity and flux estimates for each particle type. In turn, considering the weighted contribution of each particle type will maintain the accuracy of optical methods even under varied ecological and biogeochemical settings, when contributions from each particle type may vary. Alternatively, the inclusion of additional particle characteristics, such as compactness or bulk particle composition, into a unified equation (e.g., Giering et al., 2020b) may provide more accurate predictions of particle sinking velocities. Some information of these characteristics can be obtained from optical measurements, such as porosity (Bach et al. 2019), bulk density (Neukermans et al. 2012; Hurley et al. 2016), and bulk particle composition (inorganic/organic ratios, (Twardowski et al. 2001; Loisel et al. 2007)).

Yet, at present, the uncertainties associated with these proxies are large or unconstrained. Simultaneous measurements of particle type (or characteristics), size and sinking velocity will enable the development of these methods, and is likely to be expedited by advances in machine learning (Giering et al. 2020b; Iversen and Lampitt 2020). Moving away from purely size-based velocity and flux relationships to incorporate these additional particle properties will not only facilitate improved mechanistic understanding of particle sinking and the BCP, but also promote increased spatio-temporal resolution of methods used to the study the BCP, through the use of autonomous platforms and in biogeochemical models.

Chapter 3 Inefficient transfer of diatoms through the subpolar Southern Ocean twilight zone

This chapter has been published in Nature Geoscience as:

Williams, J.R. et al. (2024) "Inefficient transfer of diatoms through the subpolar Southern Ocean twilight zone," Nature Geoscience 2024 18:1, 18(1), pp. 72–77. Available at: https://doi.org/10.1038/s41561-024-01602-2.

The methodology has been moved into the main text to give a more traditional "Introduction-Methods-Results and Discussion" layout to the chapter; some material from the Supplementary Information has also been added to the appendices.

MSC, SAPS, and CTD data was collected by members of the CUSTARD cruise DY111 and COMICS cruise DY086. JRW did not analyse filters in the laboratory; data was taken from Baker et al. (2024)'s data submission https://doi.org/10.5285/1f3cccfc-3e11-acbf-e063-7086abc0ad53; and from Major et al. (2024): https://doi.org/10.5285/1f3cccfc-3e11-acbf-e063-7086abc0ad53. JRW developed methodology, carried out formal analysis to calculate molar ratios, fluxes, flux attenuation rates of the above measurements. JRW also carried out validation, data curation, and writing. A CRediT author statement for all authors is available at https://doi.org/10.1038/s41561-024-01602-2. Figure 3.1b was previously submitted as a standalone figure during my undergraduate degree.

3.1 Abstract

The Southern Ocean, a region highly vulnerable to climate change, plays a vital role in regulating global nutrient cycles and atmospheric CO2 via the biological carbon pump. Diatoms, photosynthetically active plankton with dense opal skeletons, are key to this process as their exoskeletons are thought to enhance the transfer of particulate organic carbon to depth, positioning them as major vectors of carbon storage. Yet conflicting observations obscure the mechanistic link between diatoms, opal, and particulate organic carbon fluxes, especially in the twilight zone where greatest flux losses occur. Here, I present direct springtime flux measurements from different sectors of the subpolar Southern Ocean, demonstrating that across large areas of the subpolar twilight zone, carbon is efficiently transferred to depth, albeit not by diatoms. Rather, opal is retained near the surface ocean, indicating that processes such as diatom buoyancy regulation and grazer repackaging can negate ballast effects of diatoms' skeletons. These results highlight that the presence of diatoms in surface waters of the Southern Ocean's largest biome does not guarantee their importance as vectors for efficient

carbon transfer through the subpolar twilight zone. Climate change-driven shifts in phytoplankton community composition may affect biologically sequestered carbon pools less than currently predicted.

3.2 Introduction

The Southern Ocean biological carbon pump plays a vital role in ocean carbon storage and global nutrient cycling. It removes ~3Pg carbon from the surface ocean annually, accounting for ~30% of global biological carbon pump export (Arteaga et al. 2018), and influences the vertical distribution of nutrients and their subsequent supply to the thermocline of the global ocean (Sarmiento et al. 2004). A key player in the Southern Ocean biological carbon pump are diatoms, a diverse group of ubiquitous and photosynthetically active plankton with armoured skeletons made of the biomineral opal (biogenic Silica; BSi). Owing to their dominance of primary production (Tréguer et al. 1995) in the Southern Ocean (where surface silicic acid concentrations are the highest throughout the global ocean (Matsumoto et al. 2002)), their large size relative to other phytoplankton and the role of their dense siliceous frustules which enhance particle sinking rates (Tréguer et al. 2017), diatoms are thought to play a major role in efficiently transferring carbon to the deep ocean, sequestering it out of contact with the atmosphere (Tréguer et al. 2017).

The implied importance of diatoms for particle transport is in large part based on observations in deep sediment traps (typically >2,000 m depth), which suggest that a relatively higher amount of BSi compared to POC reaches these depths (Ragueneau et al. 2002; Buesseler et al. 2006). Further, diatom frustules are present in both sedimented material in traps and sediments themselves. As these observations can be mechanistically explained (slow chemical dissolution, high density and hence sinking velocity of BSi vs high microbial and metazoan consumption of POC), the resulting "ballast hypothesis" (Armstrong et al. 2001; Klaas and Archer 2002) has been widely employed in models (Henson et al. 2022) and led to the concept that diatoms are an indicator of efficient POC transport.

A vital region in shaping the overall efficiency of POC transport to the deep ocean is the zone between the sunlit surface ocean (~100 m) and the deep ocean (>1000 m) – called the twilight zone. Forming a gateway between the surface and deep ocean (Martin et al. 2020), the twilight zone constitutes a major zone of sinking flux loss and heavily influences the efficiency of particle transfer (Steinberg et al. 2008; Martin et al. 2020). While numerous studies, including global syntheses (Wiedmann et al. 2020), have observed pulses of sinking carbon to be exported from surface waters following diatom blooms, sometimes propagating to the deep ocean (Martin et al. 2011; Smetacek et al. 2012), others have found that sinking carbon is transferred

to the deep ocean least efficiently in diatom-dominated high-latitude regions (Henson et al. 2012; Le Moigne et al. 2012; Le Moigne et al. 2014). As such, the efficiency with which diatoms transfer carbon through the twilight zone to the deep ocean (that is, diatoms' "transfer efficiency") is highly uncertain. Improving mechanistic understanding of carbon transfer efficiency is vital; in the most recent CMIP6 (Coupled Model Intercomparison Project Phase 6) global models, the response of transfer efficiency to climate change is the largest source of uncertainty (excluding primary production-induced changes) when projecting changes to biological carbon pump strength (Wilson et al. 2022).

Here, I identify a process in which BSi is transferred much slower than POC through the Southern Ocean twilight zone. I combine direct, high-resolution measurements of sinking fluxes from the field campaigns of two international collaborative projects studying the biological carbon pump in the Atlantic and Pacific sectors of the Southern Ocean (Figure 3.1a). In the Atlantic, we occupied two British Antarctic Survey (BAS) stations in the Scotia Sea in contrasting regimes (naturally iron-fertilized station 'P3' and HNLC control station 'P2') during the Controls over Ocean Mesopelagic Interior Carbon Storage (COMICS) cruise DY086 (12 November–19 December 2017). In the Pacific, we occupied three biogeochemically distinct stations (hereon referred to as 'OOI' (Ocean Observatories Initiative), 'TN' (Transect North) and 'TS' (Transect South)) during the Carbon Uptake and Seasonal Traits in Antarctic Remineralization Depth (CUSTARD) cruise DY111 (2 December 2019–9 January 2020). Our field campaigns covered a range of productivities and bloom progression (Appendix A.1), with peaks in net primary production (satellite-derived and using the Vertically Generalized Production Model (Behrenfeld and Falkowski 1997); Figure 3.1b-c) ranging from 328 mg C m⁻² d⁻¹ to 1,365 mg C m⁻² d⁻¹.

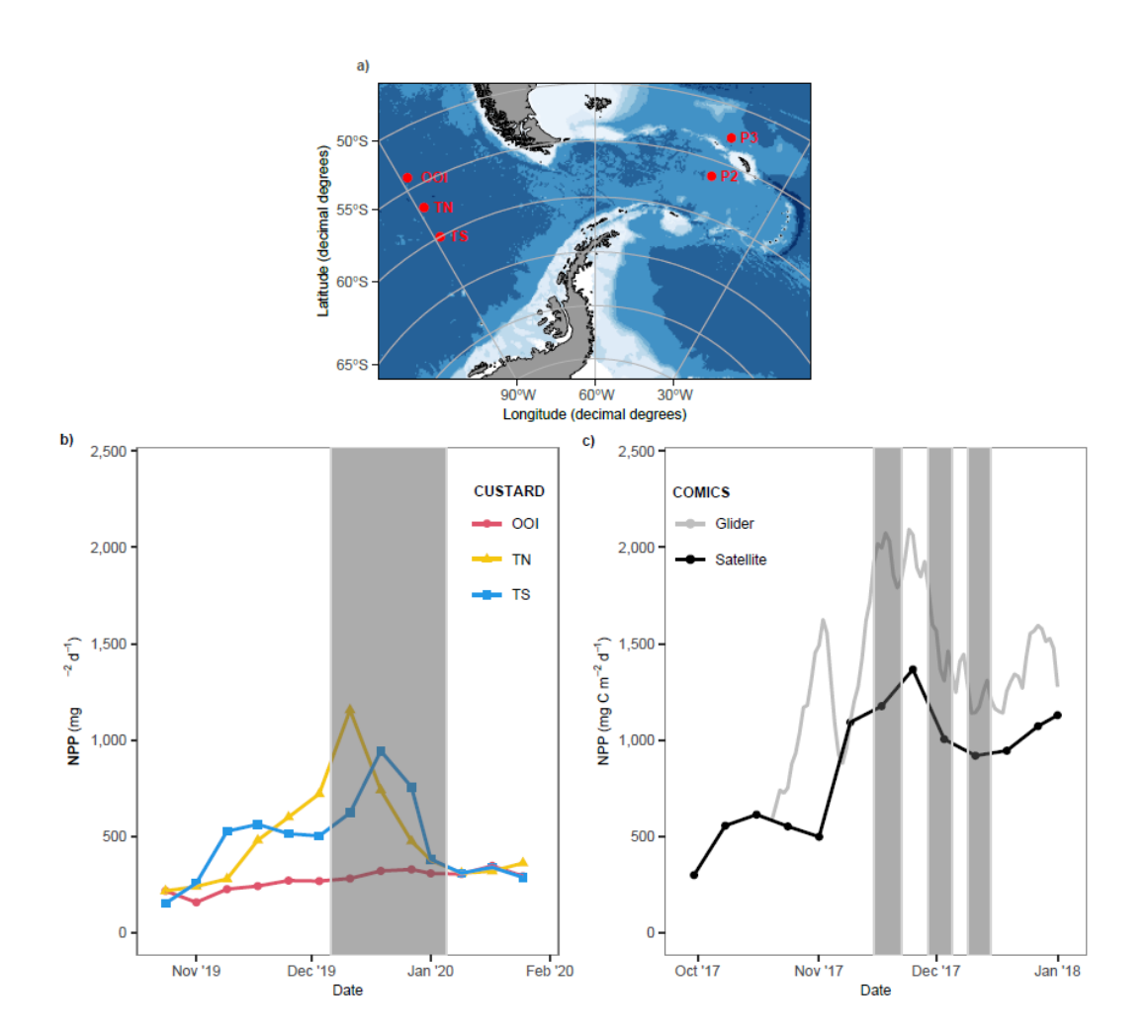


Figure 3.1 Study region and Net Primary Production (NPP) at the study sites. Location of stations shown by red markers (OOI, 54° S, 89° W; TN, 57° S, 89° W; TS, 60° S, 89° W; P3, 52.7° S, 40.1° W; P2, 56.4° S, 41.0° W). The OOI (Ocean Observatories Initiative) station was located at the site of the OOI Global Southern Ocean Array (https://oceanobservatories.org/array/global-southern-ocean-array/), but no data from the array are used in this study. Figure created with ggoceanmaps (Vihtakari, 2024) using bathymetric data from the ETOPO 2022 15 Arc-Second Global Relief Model distributed by the National Center for Environmental Information (https://www.ncei.noaa.gov/products/etopo-global-relief-model). (b) MODIS surface Chl-derived estimates of NPP calculated using the mean VGPM (Behrenfeld & Falkowski, 1997) outputs for 0.2-degree boxes around each of the CUSTARD sites (OOI, 54.4°S 89.1°W, red circles; TN, 57.0°S 89.1°W, yellow triangles; TS 60.0°S 89.1°W, blue squares) and (c) around the COMICS P3 site (P3, 52.7°S, 40.1°W). Glider-derived estimates of NPP are also shown for P3 site (grey line). For both projects (CUSTARD, 2019/20; COMICS, 2017) study periods are highlighted in grey.

Sinking fluxes of POC, BSi, and Chlorophyll-a (Chl) were directly measured using Marine Snow Catchers (MSCs) (Riley et al. 2012) deployed at 4-5 depths from just below the mixed layer (MLD + 10 m) (Baker et al. 2017) down to 750 m. For Pacific stations, 44 flux measurements were pooled into one profile per site (Appendix Figure A.2a-c). For Atlantic stations, 56 flux measurements were pooled into profiles for each of the three iron-fertilized-station occupations and one for the iron-limited station (Appendix Figure A.2d-f). Flux loss rates were quantified for each profile through fitting a power law(Martin et al. 1987), with a higher exponent 'b' indicating faster loss with depth. As diatoms are the main silicifying organisms in the Southern Ocean (Llopis Monferrer et al. 2021; Ainsworth et al. 2023), BSi:POC molar ratios were used to approximate the contribution of diatom-derived BSi in particulate material, with higher values indicating a larger contribution of diatoms. BSi:POC molar ratios were estimated from each MSC for time-zero (total), suspended, slow- and fast-sinking fractions, and total ratios compared with trends in molar ratios measured in samples collected via Niskin bottles and in situ pumps to ensure trends observed were not reflective of an instrumental bias.

3.3 Methods

3.3.1 Net Primary Production

To characterize productivity throughout the study period, satellite-derived estimates of net primary production (NPP) were downloaded from the Ocean Productivity website (http://www.science.oregonstate.edu/ocean.productivity/) using the mean Vertically Generalised Production model (VGPM) (1/12° grid resolution) (Behrenfeld and Falkowski 1997) outputs for 8-day composites of 0.2-degree boxes around each station. Glider-derived primary production was estimated in Henson et al. (2023), from glider-derived chlorophyll and light data coupled with a bio-optical model (Mignot et al. 2018). Region-specific photosynthetic parameters (chlorophyll-specific initial slope of the photosynthesis-irradiance curve, and the maximum chlorophyll-specific light-saturated photosynthesis) were measured during on-board incubation experiments as described in Poulton et al. (2019)..

3.3.2 Particulate molar ratios

Alongside Marine Snow Catcher samples, in situ pumps (Stand Alone Pumping Systems–SAPS, Challenger Oceanic®, hereon SAPS) and CTD Niskin bottle samples were used to assess particulate molar ratios. CTD Niskin samples were taken from 12 depths between the near surface down to approximately 1000 m. POC and BSi were analysed from all depths for DY086 but only for the upper 200 m for DY111. The latter are hence only discussed in Appendix A.3. For

POC, 1000 mL seawater was filtered onto pre-combusted (12 hours, 400 °C) GF/F filters (nominal pore size 0.7 μ m, 25 mm diameter, Whatman). Filters were placed into centrifuge tubes, dried (overnight, 50°C) and stored for analysis on land using the MSC protocol described below. For BSi, 500 mL seawater were filtered, rinsed, and analysed onboard using the MSC protocol below.

During DY111, SAPS filtered seawater (53-µm mesh, 293-mm diameter, NITEX) for one hour. Particles were rinsed from the mesh using Milli-Q water, and split for POC, BSi, and Thorium analyses using a Folsom® splitter (Le Moigne et al. 2013). For POC/N, a ¼-split was filtered onto precombusted GF/F filters (25-mm diameter, 0.7-µm nominal pore size, Whatman) and stored frozen and analysed on land (Poulton et al. 2006). For BSi, a 1/8-split was filtered onto polycarbonate filters (25-mm diameter, 0.8-µm pore size, Whatman) and analysed onboard as described below for MSC analyses. For ²³⁴Thorium-derived bulk sinking velocities, a ¼-split was filtered onto polycarbonate filters (142-mm diameter, 0.8-µm pore size, Whatman) was analysed to derive bulk sinking velocities using the radioactive pair-disequilibria methods of Villa-Alfageme et al. (2014) and Villa-Alfageme et al. (2016).

3.3.3 Marine Snow Catchers (MSCs)

For both cruises, MSCs were deployed to quantify particle fluxes below the mixed layer depth (MLD). During DY086, MSCs were typically deployed to MLD+10 m, MLD+50 m, MLD+100 m, 250 m and 500 m depth. During DY111, MSCs were typically deployed to MLD+10 m, MLD+110 m, 400 m, and 700 m depth. Detailed descriptions of the MSC and full sampling protocol are available in refs (Riley et al. 2012; Giering et al. 2016). Concentrations and fluxes are recorded in Supplementary Table S3.3 and S3.4, respectively.

3.3.3.1 MSC biogeochemical analysis

For Chlorophyll-a, 100 mL samples were filtered onto GF/F filters (0.7-µm nominal pore size, 25-mm diameter, Whatman), placed in 6 mL acetone (90%, HPLC), and pigments extracted for 24 hours at 4 °C. Fluorescence was measured onboard using a Turner Designs Trilogy fluorometer with a non-acidification module and calibrated using a solid and pure Chlorophyll-a standard.

For Biogenic Silica (BSi), 500 mL (time-zero, top and bottom samples) or 100 mL (tray samples) were filtered onto polycarbonate filters (0.8-µm, 25-mm diameter, Whatman) and rinsed with pH-adjusted (using ammonium) Milli-Q water. Blanks were prepared by filtering 500 mL of Milli-Q water through a filter and preparing the filter as described above. Filters were placed in 15-mL centrifuge tubes, dried (overnight, 50°C), digested in 5-mL 0.2-M sodium hydroxide solution, and incubated at 85°C for 2 hours. Cooled samples were then neutralized with 0.2-M hydrochloric

acid solution, shaken vigorously and analysed using standard colorimetric technique for silicate analysis onboard using a QuAAtro 39 segmented flow autoanalyzer.

For Particulate Organic Carbon (POC), 1000 mL (time-zero, top and bottom samples) or 200 mL (tray samples) were filtered onto pre-combusted (24 hours, 450°C) GF/F filters (0.7-µm nominal pore size, 25-mm diameter, Whatman), rinsed with pH-adjusted (using ammonium) Milli-Q water (pH 8.5), dried in an oven (overnight, 50 °C), and stored in the dark for analysis back onshore. Analytical procedures back on shore differed between DY086 and DY111.

For DY086, filters were fumed onshore with 35% hydrochloric acid for 24 hours, dried (>24 hours, 50°C), pelleted in tin disks (elemental microanalysis), and analysed using a Thermo Fisher Scientific FLASH 2000 Organic Elemental Analyser coupled to a Delta V Advantage Isotope Ratio Mass Spectrometer. POC calibration was performed using a series of caffeine standards of varying weights (1 – 5 mg) with known percentage content of carbon at the beginning of each batch. All samples were blank corrected.

For DY111, two ¼-filters were analysed on a Thermo Scientific Flash Smart Organic Elemental Analyser (Sabena Blackbird, University of Liverpool). Daily two-point calibration was performed using High Organic Sediment Standard OAS (Elemental Microanalysis Ltd) which was then analysed twice as an 'unknown'. Results for the 'unknown' were within uncertainty limits of certified values which were 7.17 ± 0.09%. Certified values were determined by elemental analyser calibrated to Cystine 143d from National Institute of Standards and Technology (NIST), Maryland, USA. Blanks were prepared by filtering 1000 mL Milli-Q water and preparing the filter as described above. Standard deviation of POC concentrations (from the two quarters of each filter) was calculated to provide an estimate of analytical uncertainty and sample heterogeneity. Standard deviations were propagated using standard error propagation equations to yield combined standard uncertainty (C.S.U.) estimates for both concentrations and fluxes.

3.3.3.2 MSC concentrations and fluxes

Concentrations (μ g L⁻¹ for Chl and POC, μ mol L⁻¹ for BSi), and fluxes (mg m⁻² d⁻¹; mmol m⁻² d⁻¹ for BSi) of fast and slow-sinking fractions were calculated according to the method of (Giering et al. 2016). Briefly, the concentration of the suspended particles (P_{susp}) is assumed equal to the concentration of material from the top sample after settling (P_{top}):

$$P_{susp} = P_{top} \tag{3.1}$$

Slow-sinking particle concentrations are calculated as the differences between the concentrations of top (P_{top}) and base (P_{base}) fractions, adjusted for volume of the MSC and base section (V_{MSC} = 95 L and V_{base} = 8 L, respectively):

$$P_{slow} = (P_{base} - P_{top}) \frac{V_{base}}{V_{MSG}}$$
 (3.2)

Fast-sinking material is calculated as the difference between the concentrations in the tray and base fractions and adjusted to the area of the particle collection tray ($A_{tray} = 0.026 \text{ m}^2$), volume of the tray ($V_{tray} \sim 1 \text{ L}$), and height of the MSC (h = 1.58 m) (note that 1000 (L m⁻³) in denominator here is to keep concentration in units of $\mu g L^{-1}$ rather than $\mu g m^{-3}$):

$$P_{fast} = (P_{tray} - P_{base}) \frac{V_{tray}}{A_{tray} \times h \times 1000}$$
(3.3)

During DY111, in a small number of instances, water was required for respiration measurements. In these cases, a larger time-zero volume was samples (10 L) and water was siphoned from around the particle collection tray to provide a larger tray volume (V_{tray^*}). For these instances, the equation used to calculate fast-sinking concentrations is as follows:

$$P_{fast} = (P_{tray^*} - P_{base}) \frac{V_{tray^*}}{V_{MSC}}$$
(3.4)

where P_{tray^*} is the concentration of particles siphoned from the tray and area surrounding the tray, and V_{tray^*} the volume of this siphoned water. All MSC deployments that use this altered sampling method are marked with a P_{tray^*} flag in Supplementary Table S3.1. Whenever both P_{tray} and P_{tray^*} were measured at the same depth, the concentrations fall within the range of concentrations measured via the P_{tray^*} method, so concentrations derived from the two methods appear comparable.

Slow-sinking fluxes were calculated by taking into account the dimensions of the MSC and length of settling period (t = 2 h) (note the 1000 in denominator here is to adjust flux units from $\mu \text{g m}^{-2} \text{ d}^{-1}$ to $\mu \text{m}^{-2} \text{ d}^{-1}$):

$$F_{slow} = P_{slow} \times \frac{V_{MSC}}{A_{MSC} \times t \times 1000}$$
 (3.5)

Fast-sinking fluxes were calculated from concentrations by multiplying fast-sinking concentrations by an assumed bulk sinking velocity (v_{fast}) for fast-sinking material:

$$F_{fast} = P_{fast} \times v_{fast} \tag{3.6}$$

The choice of v_{fast} used is a critical factor determining the magnitude of fast-sinking fluxes, and by extension, potentially influencing attenuation rates. Since this choice of value represents a source of potential uncertainty for the flux estimations, v_{fast} must be tailored to be most appropriate for each study.

For DY086, v_{fast} of 60 m d⁻¹ was chosen based on two independent measurements: particle-specific *in situ* sinking velocity measurements at 500 m depth (66 ± 47 m d⁻¹; particle diameter of 0.5–2.3 mm) (Giering et al. 2023) and Polonium-derived bulk sinking velocities of 44 – 58 m d⁻¹ at 60 m depth (Villa-Alfageme et al. 2023). Whilst these estimations constitute a best estimate, they also contribute an upper bound, with absolute lower bounds discussed by Giering et al. (2023).

For DY111, a v_{tast} of 40 m d⁻¹ was selected based on Thorium-derived bulk sinking velocities (discussed below), from comparison with mixed-layer nutrient budgets derived from nutrient uptake between occupations of each station, and comparison of export fluxes to NPP at each site (discussed below). I selected a higher v_{fast} than the theoretical minimum of 20 m d⁻¹ given previously tracked sinking velocities using in situ optical data for large backscattering or fluorescing particles (Briggs et al. 2020) and the export efficiencies which would be needed to explain the fluxes measured at depth if particles were to sink this slowly (Appendix A.4). Conversely, a very fast estimate for v_{fast} has the potential to artificially inflate fluxes to implausibly high levels. Existing direct, in situ flux measurements from 100 m depth by sediment trap and ²³⁴Th-²³⁸U disequilibrium measurements made north of the polar front reach up to 528 mg m⁻² d⁻¹ (Roca-Martí et al. 2017; Henson et al. 2019; Fan et al. 2020). Using a v_{fast} of 40 m d⁻¹, three of our export fluxes exceed this value (570 mg m^{-2} d^{-1} at TN3 30 m; 626 mg m^{-2} d^{-1} at TN4 80 m; and 601 mg ${\rm m}^{\text{-}2}\,{\rm d}^{\text{-}1}$ at TS4 50 m). However, all values exceeding previous measurements were from depths shallower (30-80 m) than the published export fluxes (at 100 m) (Henson et al. 2019; Fan et al. 2020). All fluxes that were measured at 100 m or deeper fall within previously measured estimates when using a v_{fast} of 40 m d⁻¹. By contrast, a v_{fast} of 60 m d⁻¹ would result in half (6 of 12) export flux estimates exceeding previously measured values, including a

measurement from 100 m. Further, bulk sinking velocities derived from 234Th-238U pair disequilibria using the method of (Villa-Alfageme et al. 2023) were 22 ± 20 m d⁻¹, 43 ± 25 m d⁻¹, and 47 ± 24 m d⁻¹ at OOI, TN, and TS Pacific stations respectively (Le Moigne et al., *in review*). Comparison of MSC fluxes with fluxes determined via other methods also suggests a $v_{\rm fast}$ of no higher than 40 m d⁻¹ should be used; MSC flux estimates are higher compared to Thorium-derived flux estimates, but show good agreement with mixed layer nutrient budget calculations derived from nutrient uptake and changes between occupations. So, an intermediate value of 40 m d⁻¹ appears most appropriate.

Since the choice of v_{fast} is a source of uncertainty in flux calculations, I test the sensitivity of b-values to changes in v_{fast} . The analysis is outlined below in the b-values methods section.

Molar ratios of BSi:POC concentrations were calculated for both time-zero and total-sinking particulate fractions. For total-sinking material, concentrations of fast and slow-sinking material were summed together prior to calculation. Where calculated concentrations were negative (indicating an upwards flux of material) as was the case for some slow-sinking concentrations, the magnitude of this concentration was used and summed to fast-sinking concentration. Regardless, negative concentrations were very low and likely resulted from measurement uncertainty and sample heterogeneity in both top and bottom samples. Trends in molar ratios within a depth profile did not change with or without these negative concentrations.

3.3.3.3 Flux attenuation coefficients (b-values)

Particle flux attenuation was assessed by fitting a power law function (Martin's *b*, (Martin et al. 1987)) to total fluxes of Chl, BSi, and POC:

$$F_z = F_0 \times (\frac{z}{z_0})^{-b} \tag{3.7}$$

Where F_0 flux at a given reference depth z_0 , F_z is the flux at a given depth, z, below the reference depth, and b the flux attenuation coefficient (wherein a higher value of b indicates more rapid attenuation). Reference depths chosen were the shallowest MSC deployment for each station (i.e. MLD+ 10 m). For DY086, a Martin's b power law function was fitted to total fluxes pooled for each occupation of the P3 station (P3A, P3B, P3C), as well as the P2 control station. For DY111, all occupations of each station were pooled, resulting in a single b-value for each station. The decision to pool several occupations of each station on the DY111 cruise was made for several reasons. Firstly, since reference depths chosen for each occupation were chosen to target MLD+ 10 m, the depth of the shallowest MSC within each individual occupation differed between occupations. b-values are highly sensitive to the choice of reference depth (Buesseler

& Boyd, 2009; Olli, 2015), and so temporal changes in *b*-values within successive occupations of each station the low number would have been confounded by changes in reference depth, diminishing the use of individual *b*-values for each occupation of the stations. Furthermore, the number of MSC deployments within individual occupations of each station was typically four, and sometimes as low as two due to misfires. *B*-values derived from so few data points would not be statistically robust and would be more susceptible to the influence of random variability; in pooling data we aimed to reduce the influence of random variability in our *b*-values, and capture the general patterns in flux attenuation at each study site during the productive study period sampled by the cruise.

3.3.3.4 V_{fast} sensitivity analysis

Since the choice of v_{fast} is a source of uncertainty for fast-sinking and total fluxes, altering v_{fast} also shifts the weighting of these fluxes for the calculation of total fluxes, and hence b-values. In order to test whether more rapid attenuation of POC relative to BSi is robust to changes in v_{fast} , I calculated b using a v_{fast} of 20 m d⁻¹ (close to the theoretical lower limit for fast-sinking material, as defined by MSC dimensions), a v_{fast} of 60 m d⁻¹, and a v_{fast} of 100 m d⁻¹. b-values determined in this analysis are shown in Appendix Table A.2 (also in Supplementary Table S3.5) and confirm these results are robust to variations in v_{fast} .

Further, whilst I have used constant v_{fast} for both POC and BSi when calculating fluxes, v_{fast} may differ between chemical groups and even vary with depth throughout the water column (Villa-Alfageme et al. 2016). Hence, I also calculated "maximized b-values" for POC and "minimized b-values" for BSi and POC to test whether varying v_{tast} with depth for each of these parameters could result in quicker attenuation of POC than BSi. For this the estimation of "minimized bvalues", I utilized a v_{fast} of 40 m d⁻¹ to calculate MSC fluxes from the upper MSC deployments (shallower than halfway down the profile), and a v_{tast} of 60 m d⁻¹ for MSCs deployed deeper than halfway down the profile. This approach exaggerates fluxes at depth relative to the surface and assumes increasing sinking velocity with depth, decreasing apparent rates of attenuation and hence b-values. For "maximized b-values", I did the opposite: inflating fluxes at the surface, assuming a decrease in sinking velocity with depth. The minimized attenuation rates are always lower for POC than BSi, indicating these results are robust even if sinking velocity increases throughout the water column (Appendix Table A.2, Supplementary Table S3.5). In most cases, even the maximized POC flux attenuation coefficients are lower than the minimized BSi flux attenuation coefficients, representing a situation where POC sinking velocity decreases yet BSi velocity increases with depth. In the Pacific sector, our results are robust to increasing sinking velocities with depth for BSi yet decreasing sinking velocities with depth for POC; in the latter

occupations of the Atlantic sector site, such changes could result in the usual situation occurring wherein BSi fluxes are attenuated more slowly than POC.

3.3.4 Uncertainties, limitations, and caveats

Our observations were collected by MSCs, CTD, and *in situ* pump deployments. Whilst these methods allow for direct measurements of sinking fluxes and characterization of chemical and morphological traits of marine particles, they are all, by nature, spatially and temporally limited as they are Eulerian point measurements representing particle fields at a given snapshot in time. Whilst our results are consistent between five biogeochemically distinct study sites, suggesting they may be applicable over large regions, they remain point measurements made over approximately one-month process cruises studying the productive bloom phase of the annual cycle. Uncertainty therefore remains over the extent to which these results apply to the wider Southern and global ocean, and throughout the year (Appendix A.5). Previous work has suggested BSi may be remineralized preferentially relative to POC in the Atlantic surface ocean (Brown et al. 2006), yet high-resolution chemical studies in the Southern Ocean mesopelagic remain scarce. Such studies must constitute an area of scientific interest for the purposes of mechanistically understanding the Biological Carbon Pump in the twilight zone of this understudied region.

Another limitation of assessing flux attenuation through Eulerian measurements is the potential for lateral advection to confound interpretation of flux profiles (Martin 2005). For the Pacific station OOI, surface particle back-trajectories suggest a stable environment with minimal advection (Appendix A.6). Whilst the stations TN and TS were dynamic sites situated near the subantarctic and polar fronts, and I cannot hence completely rule out the influence of advection at these sites, back-trajectories remain consistent throughout the study period (Appendix A.6). Atlantic stations fall within an area known for low current speeds and weak mesoscale activity, and no strong evidence for lateral advection was observed during the study period (satellite-derived surface current speed measurements, shipboard ADCP measurements, and satellite chlorophyll observations, discussed in detail in (Henson et al. 2023)). Given these observations and the consistency of our findings, I do not hold lateral advection to be a major confounding factor in interpretation of our results.

The choice of reference depth when fitting of fluxes to a "Martin's b" power law function also has the potential to introduce error into attenuation coefficients (b-values). If the reference depth used is too shallow, estimates of attenuation can encompass flux loss within the euphotic zone and hence overestimate attenuation (the opposite situation is true for a choice of reference depth deeper than the euphotic zone) (Buesseler et al. 2020). Reference depths used

in this study were not fixed; rather, the shallowest MSC deployments, targeted at MLD+10m, were used as a reference depth at each station. Changes in euphotic depth or mixed layer depth within our pooled profiles could mean that estimates of flux attenuation could be influenced by production of sinking particles beneath the MLD+10m reference depth. However, the same reference depths were used for BSi and POC flux profiles, and so any confounding effect will not influence comparison of flux attenuation rates for BSi and POC.

3.4 Results and Discussion

3.4.1 Preferential Losses of BSi Relative to POC

Total BSi fluxes decreased more rapidly with depth (b = 0.67 - 1.37) than total POC fluxes (b = 0.67 - 1.37) 0.25 – 0.90) at all stations (Figure 3.2 Flux attenuation coefficients for Chl, BSi and POCb-c), a finding which opposes the idea that BSi dissolves more slowly than POC is converted back into dissolved inorganic carbon (remineralized) (Nelson et al. 1996; Nelson et al. 2002; Ragueneau et al. 2002) or dissolved organic carbon. It also contradicts previous sediment trap observations of increasing BSi:POC ratios with increasing depth (Nelson et al. 1996; Nelson et al. 2002; Ragueneau et al. 2002). The patterns observed were not sensitive to the choice of flux parameterization and associated transfer efficiency metric (e.g. remineralisation length scale for exponential fits), nor assumed bulk sinking velocity applied to fast-sinking material in order to calculate fluxes (see v_{fast} sensitivity analysis in methods, results reported in main text use 40 m d⁻¹ for CUSTARD sites and 60 m d⁻¹ for COMICS sites). Differences in b between POC and BSi were only significant (ANCOVA, p < 0.05) at the P3A station, whilst at other stations, b-values were lower for POC than for BSi albeit not significantly so, owing to relatively large standard error in the linear models used to compute b-values (Appendix Table A.2). This error indicates high variability within each profile, which may be high due to the pooling of several occupations of each station during period of changing flux, so introducing variability into each profile. Nonetheless, the consistent pattern of higher b for BSi than POC suggests that while differences in attenuation at individual sites may be slight, and not statistically significant against a backdrop of rapid flux changes, the trend we observe is indeed systematic and certainly, BSi is not transferred more efficiently than POC. Indeed, when comparing overall differences in our bvalue estimates between all stations together, b-values for POC were significantly lower than for BSi (Paired sample t-test, p = 0.004, t = 4.54, d.f. = 6). At all stations, POC was attenuated more slowly than the median b-value (b = 0.96) from a recent Southern Ocean compilation (b = 0.25 -1.97) (Bach et al. 2023), suggesting efficient POC transfer through the upper twilight zone at our sites. Total POC flux attenuation was slowest at the lowest productivity station (OOI), though

fluxes at 750 m depth still exceeded 100 mg C m^{-2} d^{-1} . Chl fluxes were attenuated faster than both BSi and POC at all stations.

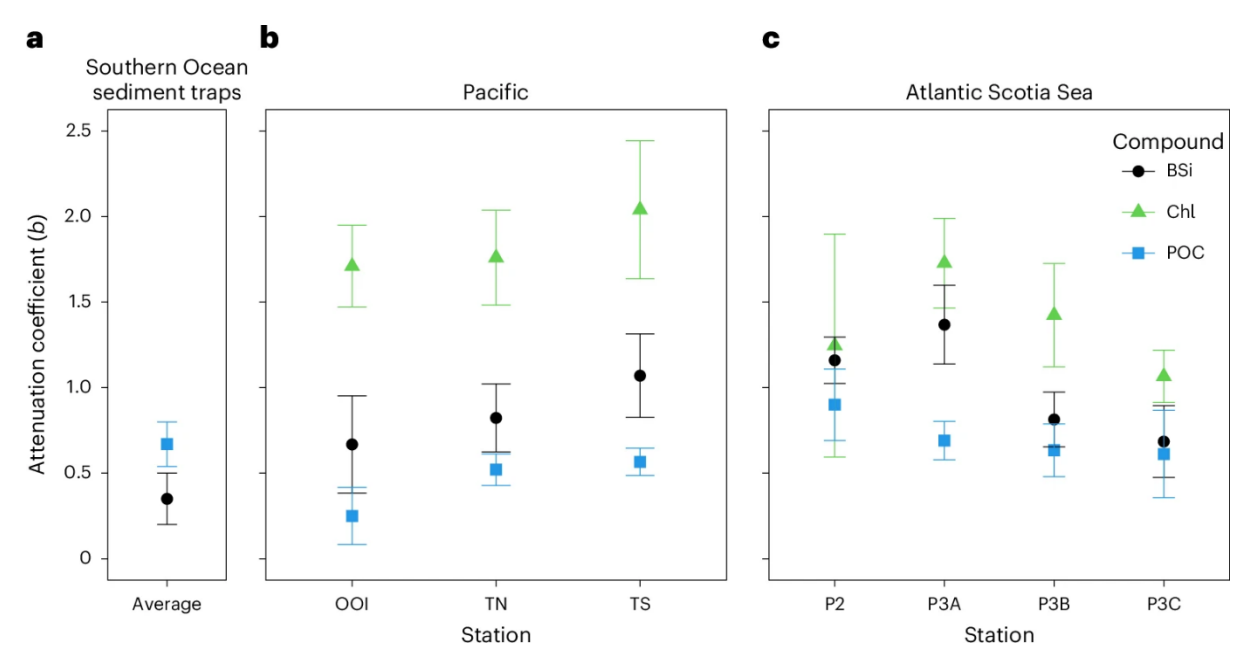


Figure 3.2 Flux attenuation coefficients for Chl, BSi and POC. (a) Illustrative Southern Ocean *b* values for POC and BSi, computed by collating all sediment trap fluxes (250–4,556 m) south of 40° S from the data compilation of Torres Valdés et al. (2014) (Appendix A.7). (b,c) Flux attenuation coefficients (*b* values) for total fluxes of Chl (green triangles), BSi (black circles) and POC (blue squares) measured at our Pacific (b) and Atlantic (c) stations. Coefficients were computed by fitting a power law function (Martin et al. 1987) to total fluxes of each compound, with errors bars depicting standard errors of the linear models used to compute *b* values.

We also observed a decrease in BSi:POC molar ratios in both the total particulate material (measured by MSC, in situ pumps and Niskin bottles samples; Appendix A.8), and total sinking fraction (measured by MSC) with depth, indicating a reduced contribution of diatoms to particulate material with increasing depth throughout the upper twilight zone. This trend is most visible shallower than 500 m at the Atlantic stations and shallower than 750 m at Pacific stations, before stabilising between these depths and 1000 m (Appendix A.8). For the Pacific stations, in situ pump measurements from the same depth as MSC deployments generally estimate higher BSi:POC ratios relative to MSC measurements, but relative changes over time, with depth, and between stations show good agreement between methods (Appendix A.3). In situ pump molar ratio measurements were not made for Atlantic stations, but molar ratios measured from Niskin bottle samples support the trend of decreasing molar ratios over the upper 500 m observed by MSCs, albeit to a lesser degree (Appendix A.8).

Our estimates of flux attenuation coefficients and particulate molar ratios may be influenced by advection or by non-steady state dynamics (Martin 2005) that could integrate particle pools originating from communities with different composition and stoichiometry (Martin 2005). Regarding the former, we did not find strong evidence for lateral advection at our study sites based on surface particle back-trajectories (A.6), satellite derived surface current speed measurements, shipboard ADCP measurements, and satellite Chlorophyll observations (see methods, and Henson et al. (2023).

Non-steady state phytoplankton communities can alter the biogeochemical signal over time (Martin 2005). For example, increasing iron stress can lead to increasingly silicified diatoms in surface waters (Takeda 1998), confounding flux attenuation coefficients and depth-related trends in molar ratios. At the Atlantic P3 station, in situ dissolved iron concentrations increased (<0.11 – 0.17 nM, 20 – 40 m; 0.11 – 0.56 nM, 110 m) (Ainsworth et al. 2023) and BSi:POC ratios remained stable in surface waters throughout the study period (Ainsworth et al. 2023) so I rule out increasing silicification in surface waters as a confounding factor. At the Pacific stations, BSi:POC molar ratios just below the mixed layer increased progressively, and iron limitation was widespread (in situ concentrations < 0.1 nM throughout cruise) (Wyatt et al. 2023). However, changes in the molar ratios of particles sinking just below the mixed layer were less than the vertical decrease in molar ratios from the surface to depth (Appendix A.9). Therefore, while I cannot completely rule out that temporal changes in composition of exported material affected these sites, changes in surface communities alone were unlikely to explain the differences we observe in BSi and POC attenuation coefficients or vertical changes in particulate molar ratios. Rather, these patterns still require a more efficient transfer of POC fluxes to depth relative to BSi fluxes.

3.4.2 Reconciling Twilight Zone and Deep Ocean Measurements

Our observations of decreasing BSi:POC molar ratios in the upper twilight zone appear at odds with the widely held conviction that sinking BSi is more efficiently transferred to depth than POC (Ragueneau et al. 2002; Buesseler et al. 2006), yet I can reconcile our observations with deepsea sediment trap fluxes. At the Atlantic Ocean iron-fertilised site, flux peaks measured in a deep-sea traps deployed at 2000 m prior to and during our study period were dominated by faecal pellets (60-66% total POC flux) (Manno et al. 2022) which displayed BSi:POC molar ratios ranging from 0.17 - 0.50 mol mol⁻¹ (Manno et al. 2022), corresponding well with molar ratios of sinking material observed in MSCs at 500 m (averages per occupation: first, 0.30 ± 0.17 mol mol⁻¹; second, 0.34 ± 0.15 mol mol⁻¹; third, 0.44 mol mol⁻¹). At the Pacific sites, no deep-sea trap samples that coincided with our study period are available, so I calculated how our MSC molar ratios may change with depth based on a range of flux attenuation parameters (details, see

Appendix A.10), and compared the results with published values from the same frontal zones in the Southern Ocean. Our projected deep ratios (0.13 mol mol⁻¹ at 1000 m, 0.25 mol mol⁻¹ at 2000 m) fall towards the lower range of previous observations (Figure 3.3) (an order of magnitude lower than some Polar Frontal Zone measurements (Honjo et al. 2000; Nelson et al. 2002; Rigual-Hernández et al. 2016, Appendix A.10) but within the range of ratios measured in the same frontal zones (Subantarctic (Honjo et al. 2000; Rigual-Hernández et al. 2016), Polar Frontal Zones (Honjo et al. 2000; Nelson et al. 2002; Rutgers van der Loeff et al. 2002; Rigual-Hernández et al. 2016) Scotia Sea (Manno et al. 2022)) (Figure 3.3), suggesting that the more rapid attenuation of BSi fluxes relative to POC that we observe in the mesopelagic zone, whilst unexpected, can be reconciled with previous deep sediment trap observations from a range of locations in the Southern Ocean (Figure 3.3).

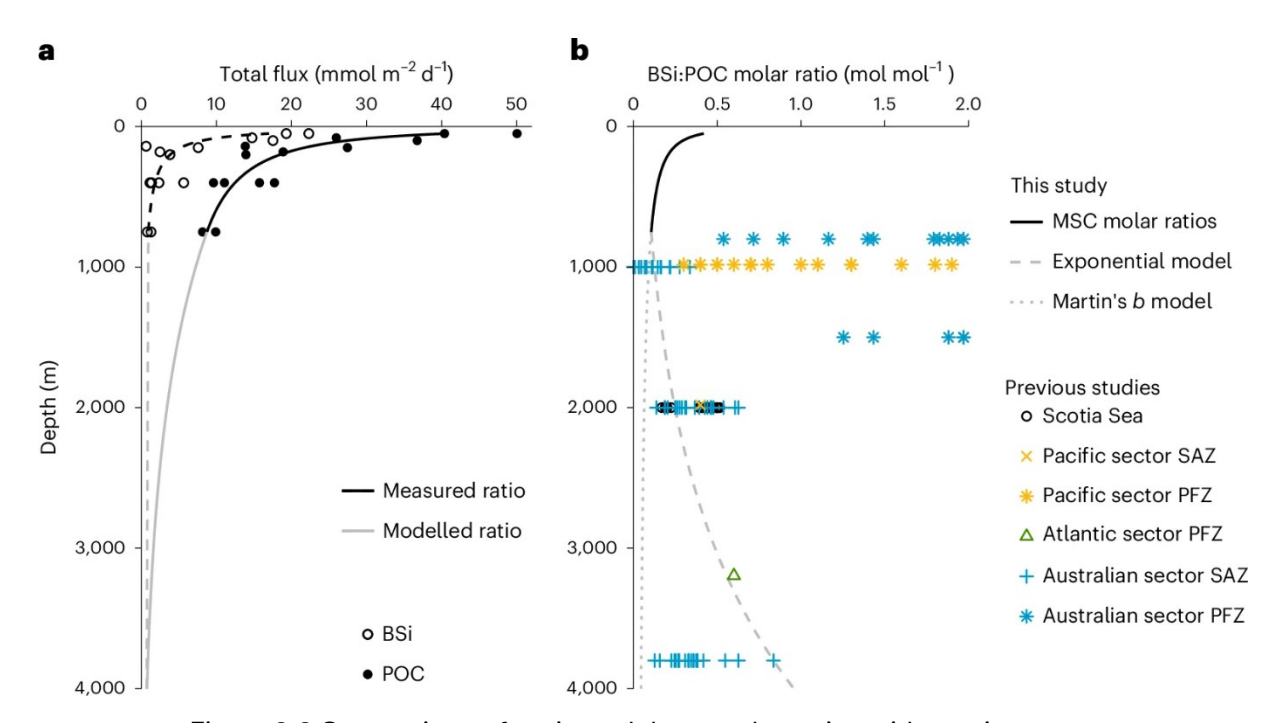


Figure 3.3 Comparison of projected deep molar ratios with previous measurements.

Flux profiles and attenuation curves (black lines) for Biogenic Silica (BSi) (dashed line, open circles) and Particulate Organic Carbon (POC) fluxes (solid line, full circles) at station TS in the upper 750 m. Fluxes below 750 m were modelled using an exponential fit ($F = F_{750} e^{-Z/V}$; grey lines, Appendix A.10 for attenuation parameters used). (b) Measured and projected molar ratios (mol mol⁻¹) compared with previously measured ratios. Ratios in the upper 750m (black line) are the ratio of BSi: POC attenuation curves derived from MSC measurements in panel a. Molar ratios below 750m are shown both for fluxes projected by Martin's b power law model derived in the upper 750m (grey dotted line), and by the exponential fit in panel a (grey dashed line). Previously measured molar ratios from deep sediment traps in similar frontal zones of the

ocean (Subantarctic (SAZ) and Polar Frontal Zones (PFZ) in Australian and Pacific sectors (Honjo et al. 2000; Nelson et al. 2002; Rigual-Hernández et al. 2016), Atlantic sector PFZ (Rutgers van der Loeff et al. 2002), iron-fertilised Atlantic station (Manno et al. 2022)) are shown by coloured points. Some of the deep molar ratios measured and estimated within the polar frontal and subantarctic zones (Honjo et al. 2000; Nelson et al. 2002; Rigual-Hernández et al. 2016) are up to an order of magnitude higher than our modelled estimates and are presented in Appendix A.10.

Our results show that across different sectors of the subpolar twilight zone, during times of peak export rates (i.e. blooms), BSi fluxes may be rapidly attenuated, retaining large portions of silica near the surface, whilst POC appears to be transferred to depth relatively efficiently. This observation is unexpected and challenges our current understanding that POC is remineralized more quickly than BSi due to heterotrophic consumption and the more rapid chemical degradation of POC (Nelson et al. 1996; Nelson et al. 2002; Ragueneau et al. 2002), and that diatoms are thought to be efficiently transferred to depth owing to biomineral ballast (Tréguer et al. 2017). Several mechanisms could underpin this observation. I first considered whether BSi dissolution could have occurred more rapidly than remineralization or solubilization of POC, as both BSi dissolution rates and POC-specific respiration rates can vary by orders of magnitude $(0.003 - > 1 d^{-1})$ (Bidle et al. 2002; Beucher et al. 2004) and $0.01 - 0.5 d^{-1}$ (Cavan et al. 2017b), respectively), and preferential remineralization of silica relative to carbon has been observed previously in the surface Atlantic Ocean (Brown et al. 2006; Thomalla et al. 2008). However, this mechanism is unlikely given that cold temperatures like those at our study sites (mean temperatures at 200 m: OOI site, 5.5 °C; TN, 5.0 °C; TS, 2.8 °C; P3, 1.3 °C) are thought to enhance preferential preservation of BSi over POC due to faster slowdown of BSi dissolution than POC remineralization (Bidle et al. 2002).

Next, I consider whether complex ecosystem interactions could decouple BSi and POC fluxes. For example, vertical fluxes can decline through both loss of material by remineralisation and a decrease in sinking rates of particulate material. Hence, the more rapid attenuation of BSi fluxes with depth without preferential BSi remineralisation requires two pathways for sinking particulate material: a slow-sinking BSi-rich pool and a fast-sinking POC-rich pool. BSi-rich particles – such as individual diatoms or diatom aggregates - may reduce sinking velocities or stop sinking all-together at density gradients in the water column (Arrieta et al. 2020; Lafond et al. 2020), for example through active buoyancy regulation (Arrieta et al. 2020) (perhaps associated with changes in life stage as resting spores acquire nutrients at depth and avoid predation in surface waters (Smetacek 1985) (Le Moigne et al., in review)). Additionally, feeding on and fragmentation of BSi-rich material- such as labile, nutritionally valuable diatom

aggregates- could act to reduce sinking velocities of BSi-rich particles (Mayor et al. 2014; Briggs et al. 2020).

Fast-sinking POC-rich particles may take the form of faecal pellets of large zooplankton, which are known to be fast-sinking and efficiently transferred (Turner 2002). Although faecal pellets are thought to be enriched in inorganic material relative to the zooplankton's food source, larger zooplankton have been observed to remove <30% of phytoplankton biomass directly in the Southern Ocean (Atkinson et al. 2012; Halfter et al. 2020) and may instead graze preferentially on protists (Smetacek et al. 2004; Atkinson et al. 2012) rather than on diatoms. Through grazing predominantly on small, non-silicified zooplankton (low-BSi food sources) or lightly-silicified diatoms (Assmy et al. 2013), faecal pellets of large zooplankton would exhibit relatively low BSi:POC ratios. At our Atlantic P3 site, significant flagellate concentrations at 350 m depth (almost 100% of identifiable cell type at this depth) (Cook et al. 2023) coupled with a lack of synchronized diel vertical migration (Cook et al. 2023) supports the idea that larger zooplankton may have been feeding on POC-rich prey. Faecal pellet molar ratios (0.17 – 0.51 mol mol⁻¹) in the deep-ocean sediment traps at the Atlantic station (Manno et al. 2022) additionally suggest faecal pellets can provide a POC-rich vector transferring POC to depth- even in times when diatoms are not transferred to depth effectively- in communities where a POC-rich food source is available.

3.4.3 Spatiotemporal Variation Obscures Nuanced Plankton Ecology

Whilst I consistently observe more rapid attenuation of BSi fluxes than POC fluxes throughout the upper twilight zone, these observations must be reconciled with previous observations of highly efficient diatom transfer to depth (Smetacek et al. 2012; Rigual-Hernández et al. 2016). Our study sites all fall (see Methods caveats, Appendix A.5) within the subpolar Southern Ocean biome (as per Fay and McKinley 2014), which encompasses 39% of the Southern Ocean and is hence its largest biome (Fay and McKinley, 2014). In the subpolar biome, I propose that the processes (buoyancy regulation, grazing and repackaging of carbon into faecal pellets) which attenuate BSi fluxes in the upper twilight zone act to temporally decouple POC and BSi fluxes in a way that permits efficient transfer of POC to depth whilst BSi is retained near the surface until transfer to depth at different times in the year, for example, by heavily silicified species. Temporal decoupling on annual scales has been observed during export (Assmy et al. 2013) and in shallow sediment traps on the Kerguelen Plateau (Rembauville et al. 2016). Similar annual decoupling in the twilight zone could act as a mechanism that both reconciles conflicting historical observations of transfer efficiency associated with diatom blooms and explains the order-of-magnitude variation in particulate BSi:POC ratios in deep traps (Appendix A.10). Our results do not, therefore, suggest that Silica is not efficiently transferred to depth in the

Southern Ocean on annual timescales. On the contrary, previous observations of highly efficient diatom transfer to depth (Smetacek et al. 2012; Rigual-Hernández et al. 2016), siliceous oozes in Southern Ocean sediments dominated by heavily silicified diatom species (Treguer et al. 1995; DeMaster, 2002), and low Si* in subantarctic Mode Water (SAMW) necessitate that Silica must be efficiently removed from the upper ocean each year. Rather, our results simply suggest a temporal decoupling between periods of maximum carbon and silica transfer through the mesopelagic, which implies the importance of silica ballasting in controlling the efficiency of carbon transfer may be less than previously thought.

This temporal effect can also partly explain why more rapid attenuation of BSi than POC fluxes has, until now, not been observed in the twilight zone. Sediment traps from deeper in the water column integrate not just over wider areas and time intervals than shallower measurements, but also integrate processes over the entire water column above these traps (Cael et al. 2021a). Deep-sea measurements may not reflect preferential BSi attenuation in the upper twilight zone due to convolution of this twilight-zone phenomenon with more efficient BSi transfer at greater depths or during Si-sinking (Assmy et al. 2013) export events. Our results highlight the importance of high-resolution biogeochemical studies (despite the temporal limitations of process cruises, see limitations section) focused on the twilight zone, where the greatest loss of sinking fluxes occur.

Here, I have found that BSi fluxes may be more rapidly attenuated than POC fluxes in the subpolar Southern Ocean twilight zone. This finding contrasts the prevailing view that BSi is more efficiently transferred to depth than POC and suggests that diatoms may not be as important as previously thought for transferring carbon to the deep ocean. Notably, I find this outcome likely arises from processes- such as buoyancy regulation and grazer repackaging of carbon- acting to negate opal ballast effects that may be present at other times of year or deeper in the water column. In attenuating BSi near to the surface whilst POC is transferred to depth by other vectors such as faecal pellets, these processes temporally decouple BSi and POC fluxes, a feature observed previously in the surface ocean but hitherto missed in the twilight zone. Our POC flux attenuation rates, relatively low in a global context, show good agreement with a global correlation (Wiedmann et al. 2020) that suggests relative diatom abundance may be used as a predictor of carbon flux attenuation. However, our results suggest this correlation may not arise simply from a straightforward causal relationship, and the presence of diatoms in surface water does not guarantee importance as a vector for sinking carbon in the twilight zone.

Taken together, these results highlight that diatoms may transfer carbon to depth less efficiently than previously thought, and that a more nuanced view may be required to accurately model the

Chapter 3

association between diatoms and silica and carbon cycles throughout the year, and the transit of sinking particles through the twilight zone. More broadly, these results have implications for predicting how climate change may impact the strength of the ocean's biological carbon pump. Climate change will impact net primary production, export efficiency, and phytoplankton community structure throughout the Southern and global ocean (Wilson et al. 2022; Henson et al. 2024), and the magnitude and even direction of this shift is uncertain (Hauck et al. 2015). Mechanistically understanding how efficiently large key phytoplankton such as diatoms transfer carbon to depth is therefore fundamental to predicting how the ocean's biological carbon pump may be changed in future climates (Wilson et al. 2022; Henson et al. 2024). If diatoms are less efficient in transferring sinking carbon to depth than thought previously, predicted changes to the size of the biologically sequestered carbon pool in the deep Southern Ocean-due to climate-driven shifts in phytoplankton community composition- may be less than currently anticipated.

Chapter 4 Patterns of Marine Snow Morphology and Sinking Throughout the Atlantic Ocean

This chapter is in preparation for submission to Limnology & Oceanography.

Williams, J.R., Couret, M., Contreras-Pacheco, Y., Elineau, A., Major, M., Masoudi, M., Takeuchi,

M., Giering, S.L.C., *in prep*. Patterns of Marine Snow Morphology and Sinking Throughout the

Atlantic Ocean. Limnology & Oceanography.

UVP deployments onboard DY157 were performed by myself and other members of the Sari Giering's ANTICS team (Yessica Contreras-Pacheco, Will Major, Mojtaba Masoudi, Marika Takeuchi). Expert manual validation of EcoTaxa vignettes was performed by Amanda Elineau.

4.1 Abstract

"Marine snow"-largely organic marine particles- are the dominant vector of carbon export in the ocean's biological carbon pump, which maintains atmospheric CO_2 100-200 ppm lower than it would otherwise be. It is thought that the morphological characteristics of marine snow (e.g. size, compactness, and shape) govern the efficiency with which sinking carbon is transferred to the deep ocean. As in situ imaging approaches become more widespread in the study of the BCP, classifying marine snow and relating marine snow morphology to biogeochemical functioning will form a crucial lens through which to view the BCP. Recently, the use of statistical techniques to classify marine snow particles have been adopted for regional time series studies, yet the scalability of this approach and conclusions from regional studies are unclear. Large gradients in environmental conditions and highly diverse plankton ecosystems across the Atlantic Ocean likely drive strong variations in particle morphologies across the Atlantic basin, with knock-on implications for the efficiency of carbon transfer via the BCP.

Here, I explore the vertical and spatial patterns in marine snow composition across an Atlantic meridional transect. I classified marine snow particles into eight morphological groups via a principal component analysis and k-means clustering approach, and find that particle brightness (indicative of compactness) provides a stronger constraint on efficiency of particle transfer than particle size, and that particle compactness is a prerequisite for size to influence efficiency of particle transfer. I observe that average particle compactness typically increases outside of the surface ocean, with the exception of particles coinciding with the DVM resting depth, which are likely influenced by diel vertical migrants. These results confirm the importance of particle morphology to particle transfer and the utility of statistical techniques to discriminate marine particles at the basin scale.

4.2 Introduction

The ocean's biological carbon pump (BCP) plays a vital role in the regulation of atmospheric CO_2 (Volk and Hoffert 1985), and the vertical transport of energy and nutrients throughout the water column (Sarmiento et al. 2004). Through the uptake of dissolved inorganic carbon by phytoplankton in surface waters, and the subsequent transport of organic material out of the surface ocean where it is remineralised out of contact with the atmosphere (Volk and Hoffert 1985), the BCP acts to maintain atmospheric CO_2 100 – 200 ppm lower than it would otherwise be (Maier-Reimer et al. 1996; Oschlies 2009). In general, the deeper organic carbon penetrates before remineralisation, the longer that carbon will be held out of contact with the atmosphere (Marsay et al. 2015), and the more carbon may be sequestered within the ocean, lowering atmospheric CO_2 (Kwon et al. 2009).

In recent years, various processes such as the diel (Steinberg and Landry 2017; Boyd et al. 2019) and seasonal (Jónasdóttir et al. 2015; Boyd et al. 2019) migration of zooplankton have been identified as important processes transporting organic carbon to depth. Yet, the passive sinking of organic particles, collectively termed "marine snow" (Alldredge and Gotschalk 1988; Alldredge and Silver 1988), still constitutes the dominant vector within the BCP, transporting carbon out of the surface ocean (Boyd et al. 2019). The term "marine snow" was originally coined to describe organic aggregates > 500 µm in size, though now it is typically used to refer to any marine organic particle including faecal pellets, detritus, or aggregated particles containing mixtures of these components and some inorganic material. The diverse origins and composition of marine snow have been posed to influence their particle sinking velocities (Laurenceau-Cornec et al. 2015b), which in turn determines the depth to which carbon penetrates before remineralisation and is, therefore, a critical factor in determining the size of the biologically sequestered carbon pool in the ocean (Sanders et al. 2014; Marsay et al. 2015). As such, there is a pressing need to study the patterns and processes shaping marine snow morphology both vertically and spatially throughout the global ocean.

In recent years, developments in in situ imaging technologies have opened a new avenue for study of the BCP. Such technologies not only provide far higher vertical resolution than traditional methods, but- through integration onto autonomous instruments- enable for higher temporal and spatial coverage of the ocean (Stemmann and Boss 2012; Giering et al. 2020a). In situ technologies also allow for examination of particle dynamics with minimal particle alteration (Giering et al. 2020a; Iversen and Lampitt 2020; Williams & Giering et al. 2022), and offer insights into processes causing particle transformation (Burd and Jackson 2009; Iversen et al. 2010; Takeuchi et al. 2019). Yet, despite the advantages of these methods, their utility is heavily reliant upon the conversion used to relate properties such as sinking velocity and carbon

content to particle size (Giering et al. 2020a). Size-sinking velocity and size-carbon relationships have been shown to vary widely in space and time as a result of particle heterogeneity (Kriest 2002; Guidi et al. 2008; Iversen et al. 2010; McDonnell and Buesseler 2010; Kiko et al. 2020; Cael et al. 2021b), preventing attempts to unify size-sinking velocity measurements into a quasi-global relationship (McDonnell and Buesseler 2010).

A posed solution to these issues has been to incorporate more ecological information, and hence use this particle heterogeneity to further mechanistic understanding and constrain estimates of carbon fluxes (Giering et al. 2020b; Trudnowska et al. 2021; Williams and Giering 2022; Ceballos Romero et al. 2024). For instance, sorting particles into categories based on morphology (Schröder et al. 2020) prior to sinking velocity or flux estimation will increase the spatiotemporal scales over which size-sinking velocity relationships can be applied (McDonnell and Buesseler 2010; Williams and Giering 2022; Ceballos Romero et al. 2024) (through weighting each relationship in accordance with changes in particle composition). A limiting factor to this approach, despite the importance of particle morphology, has been the ability to discriminate between ecologically meaningful groups of marine snow.

Standardising marine snow classifications is challenging owing to the high numbers of particle images, vast variety within and between particle classes, and continuous gradients in properties used to classify particles (Trudnowska et al. 2021; Alan Turing Institute Data Study Group, 2022). Across the Atlantic Ocean, large variations in environmental conditions likely result in extreme diversity of marine snow morphologies, potentially driving large variations in the efficient of sinking carbon transfer via the biological carbon pump. Here I apply a method for the statistical discrimination of particle morphological groups from UVP data (Trudnowska et al. 2021), which has successfully been used to examine changes in particle morphology for time series in highly productive Arctic regions (Trudnowska et al. 2021; Rogge et al. 2022), and during export events tracked by Lagrangian floats in the Angola basin (Soviadan et al. 2024), equatorial Atlantic (Habib et al. 2024), and Southern Ocean (Accardo et al. 2024). I present the first application of this method at the basin scale, to investigate patterns in marine snow morphology and processes driving vertical differences and across a latitudinal transect of the Atlantic Ocean.

4.3 Materials and Methods

4.3.1 Sample acquisition

As part of the 30th Atlantic Meridional Transect (AMT30) cruise DY157 (20 February – 30 March 2023) onboard RRS Discovery, 27 pre-dawn deployments of a UVP5 (Picheral et al. 2010) were

made along a latitudinal transect between Port Stanley (Islas Malvinas) and Southampton (UK) (Figure 4.1). The UVP is an imaging system designed to photograph, enumerate, and automatically extract morphological features of marine particles of a size range from ~0.1 – 16.4 mm, in an image volume of 1.02 L; full details of calibrations are outlined in Picheral et al. (2010). During the DY157 cruise, the UVP was mounted face-down on the "Red Camera Frame" (RCF), a purpose-built frame to allow the attachment of several in situ imaging devices in such a way that image volumes are minimally impacted by the bow-wave effect of the frame. The UVP obtained vertical profiles of particle abundance during the downcast of each deployment; the UVP was lowered to 600 m depth with a descent speed of 0.5 ms⁻¹ and an acquisition frequency of 20 Hz. In addition, at each station a Sea-Bird 911+ Conductivity, Temperature, Depth (CTD) system was deployed throughout the water column, equipped with a fluorescence sensor (Chelsea Technologies Group Aquatracka III fluorometer).

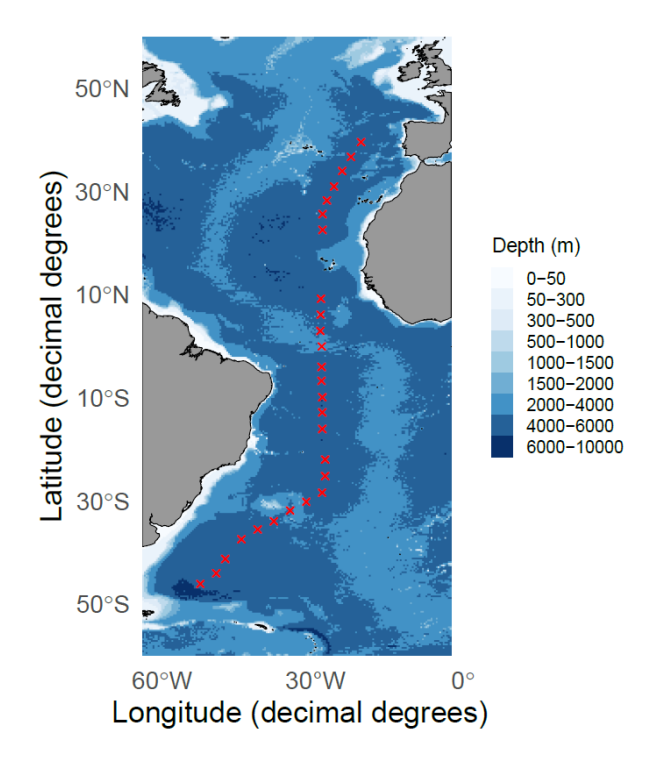


Figure 4.1 Map depicting the locations of 27 pre-dawn stations (red crosses) where the UVP5 was deployed.

4.3.2 Unsupervised morphological classification

The particle dataset contained 54,926 particle images, which were uploaded to the EcoTaxa web application (https://ecotaxa.obs-vlfr.fr/) with their associated metadata and morphological characteristics of each particle (measured automatically via the UVP Zooprocess software [https://sites.google.com/view/piqv/zooprocess]). Images were individually classified in the EcoTaxa web application with the assistance of machine learning classifiers, and all image classifications were manually validated. Artefacts and living organisms were then separated

from marine snow particles prior to analysis. Following the methods of Trudnowska et al., morphological properties were selected to represent size, brightness/shade intensity, shape, and structural complexity (Appendix Table B.1). For all properties, 0.1% most extreme values were removed to remove outliers, and some morphological properties were transformed to remove skewness (Appendix Table B.1). The 24 properties were then used to build a Principle Component Analysis (PCA) space with the "FactoMineR" and "factoextra" packages, to reduce dimensionality and represent the complexity of these 24 variables along four principal component axes. These four component axes explained 86.8% of total variation, with the first two axes explaining 71% (Appendix Figure B.1).

K-means clustering was applied to the first four PCA coordinates to distinguish marine snow morphotypes. Since an Atlantic transect would likely encompass a broader range of ecosystems and conditions than previous, more regionalised studies (Trudnowska et al. 2021), I wanted to capture a potentially broader diversity of marine snow morphotypes without compromising on resolution. I therefore settled on 8 clusters (k=8) as a trade-off: sufficiently high to avoid obscuring fine-scale changes in marine snow morphotypes, yet not so high as to become impractical or unwieldy.

4.3.3 Data analyses

4.3.3.1 Particle properties

Particle biovolume was computed for 20 m depth bins of each profile, as were total particle concentrations and individual cluster concentrations within these depth bins.

To compute biovolume, particle area in square pixels (Area_{pix}) was first converted to area in square millimetres (Area_{mm}) using a conversion factor specific to the calibration of our UVP (UVPsn223):

$$Area_{mm} = Area_{pix} * 0.094^2$$

Equivalent Spherical Diameter (ESD) was then calculated from particle area via the following equation:

$$ESD = \sqrt{4 * Area_{mm}/\pi}$$

, with ESD converted into Equivalent Spherical Volume (ESV) via:

$$ESV = ESD^3 * \frac{\pi}{6}$$

ESVs for each particle were then summed for each depth bin.

For each profile, an overall particle transfer efficiency (T_{100}) (Buesseler and Boyd 2009) for each profile was calculated, using the maximum concentration in the upper 150 m as a reference depth z_0 , and a depth 100 m below this z_{100} as a comparison. I then fitted a linear model between fluxes at z_0 and z_{100} to determine an average T_{100} across all profiles, such that the slope of the linear model represents a variance-weighted number concentration transfer efficiency (T_{100}) . Compared to calculating an arithmetic mean of T_{100} between stations, this approach downweights the random error in profiles with very few particles. I also selected stations with the largest (absolute) residuals from this linear model, to examine differences in particle composition between profiles with high and low transfer efficiencies, and related the residuals from this T_{100} linear model to mean particle area and brightness in each profile, to test whether these particle features influenced the efficiency of particle transfer during transit from z_0 to z_{100} .

4.3.3.2 Depth bin comparisons

Due to the small number of particles within the observable size range of the UVP (\sim 0.1 – 16.4 mm) for some profiles, I also binned particles into coarser depth bins to minimise the influence of random variability associated with small sample sizes when examining composition and transfer efficiency.

The first, and coarsest categorisation separated our profiles into three depth bins: a 0 – 100 m surface or productive layer, a 100 – 300 m "subsurface layer", and a 300 – 600 m "deep" layer. From this, I calculated the ratio of particle concentrations between the subsurface and surface bins for total particle concentrations and for all cluster concentrations, expressed as a percentage- which I henceforth term "Abundance Efficiency". Due to the coarser depth bins and higher particle counts, the ratio of particle concentrations between these two depth strata is less influenced by chance variation in particle abundance and thus provides a more accurate assessment of the transfer to depth than our 20 m depth bins. It should be noted that an abundance efficiency is not a true "transfer efficiency" (sensu Buesseler & Boyd). For instance, Cluster A particles could be completely removed from the water column during sinking (transfer efficiency of 0%), yet transformation of Cluster B particles inside the lower depth stratum could result in new generation of Cluster A particles at depth, potentially to greater numbers than in the surface. Thus "Abundance efficiency" is influenced not just by the efficiencies with which different particle morphologies sink between depth strata, but also by particle transformations between particle morphologies- I define our count-based metric here make this distinction from a true transfer efficiency.

The second coarse categorisation was defined dynamically based on 75kHz narrowband Acoustic Doppler Current Profiler (ADCP) data. I aimed to test whether inputs of particles from diel vertical migrants could explain a slight elevation in the proportion of larger particles within the 300 – 600 m depth bin of the above categorisation. UVP data could not be used to identify DVM resting depth due to our profiles being night-time profiles, so I visually selected a ~three-hour daytime window from ADCP scatter data and plotted average ADCP signal return with depth throughout this window. From this, I identified three depth strata: a "control" region of low acoustic signal above the diel vertical migration (DVM) resting depth; a "DVM" resting depth region characterised by a small peak in acoustic signal; and a "deep region encompassing a 60 m window 40 – 100 m beneath the base of the DVM region (for more explanation, see Appendix Figure B.7: ; depth horizons for each depth bin are reported in Appendix Table B.4 and shown in Appendix Figure B.8).

For both of the above categorisations, non-metric multidimensional scaling (NMDS) plots were used to represent the multivariate differences in particle community composition between depth strata and between sites, and visualise environmental factors (outlined below) driving these differences (see NMDS analyses section below).

4.3.4 NMDS analyses

Multivariate particle composition was investigated using NMDS using the vegan package on Rstudio (Oksanen et al., 2022). Cluster concentrations were converted to proportions of total concentration in each depth bin, and a Bray-Curtis dissimilarity matrix was calculated. Stress scores of each NMDS solution are shown on each figure and were all \sim 0.2, indicating weak links but nonetheless reliable conclusions. Significance of differences in particle composition between depth strata was assessed through permanova test using the *adonis* function in R, and pairwise tests through the RVAideMemoire package. I used the *envfit* function (Vegan package) to overlay internal variables (cluster proportions) and environmental parameters onto our NMDS ordination as vectors. Such vectors depict the correlation between projections of each sample and the corresponding variable; only vectors with a significant (p <0.05) correlation are shown. The environmental variables tested are described below.

4.3.4.1 Environmental variables

The influence of several environmental variables derived from Conductivity, Temperature, Depth (CTD) fluorescence measurements, ADCP data, UVP data, and metadata was assessed via the envfit function. Specifically, I tested the following parameters: Surface Chlorophyll (averaged 0 -100 m), Latitude, mesopelagic migrant strength, total zooplankton concentration,

sea surface temperature, and overall abundance efficiency- each term is defined in Appendix Table B.2 and data is shown in Supplementary Table S4.1.

4.4 Results

4.4.1 Particle morphotype classifications

The 24 morphological properties were used to define a PCA space, before k-means clustering was applied to distinguish 8 marine snow morphotypes (Figure 4.2). Particle greyness (mean grey level), rather than particle size, was the main driver of variability along our principle component axes (Appendix Figure B.1), in contrast with Soviadin et al. (2024). I described our morphotypes with up to three descriptors relating to size (small or large), intensity (dark, grey, light), and shape (round or elongated).

Cluster 1 comprised large, dark particles (LaDs, median perimeter 101 pixels, mean area 324 square pixels). Cluster 2 I refer to as elongated particles (Es)- these particles displayed the lowest median circularity (0.23), and were small if judged by area (134 square pixels) but large if judged by particle perimeter (median 87.4 pixels, boxplot for particle perimeter in Appendix Figure B.3). Cluster 3 comprised another group of large particles (median area 22 square pixels, median perimeter 96.4 pixels), yet in contrast to LaDs, these particles were large, light particles (LaLis, median "mean grey level" of 229 [0 = black particles, 255 = white]).

In contrast with the large particles, the smallest particle morphologies were also among the most circular. Clusters 8 and 6 respectively comprised small, dark, round particles (SDRs, median area 99 pixels, median "mean grey level" 118) and small, light, round particles (SLiRs, median area 99 pixels, median "mean grey level" 118).

Cluster 7 comprised large, dark, round LaDRs particles of intermediate size between LaDs and SDRs, the main distinguishing feature being their roundness (median circularity 0f 0.76, in contrast with LaDs 0.41). Cluster 4 was the most "average" cluster, falling in the centre of the PCA space, and are thus labelled "SGs"- small, grey particles of intermediate brightness (area 119 square pixels, median "mean grey level" of 147). Lastly, Cluster 5 comprised small, light particles (SLis, median area of 123 square pixels, median "mean grey level" of 229.)

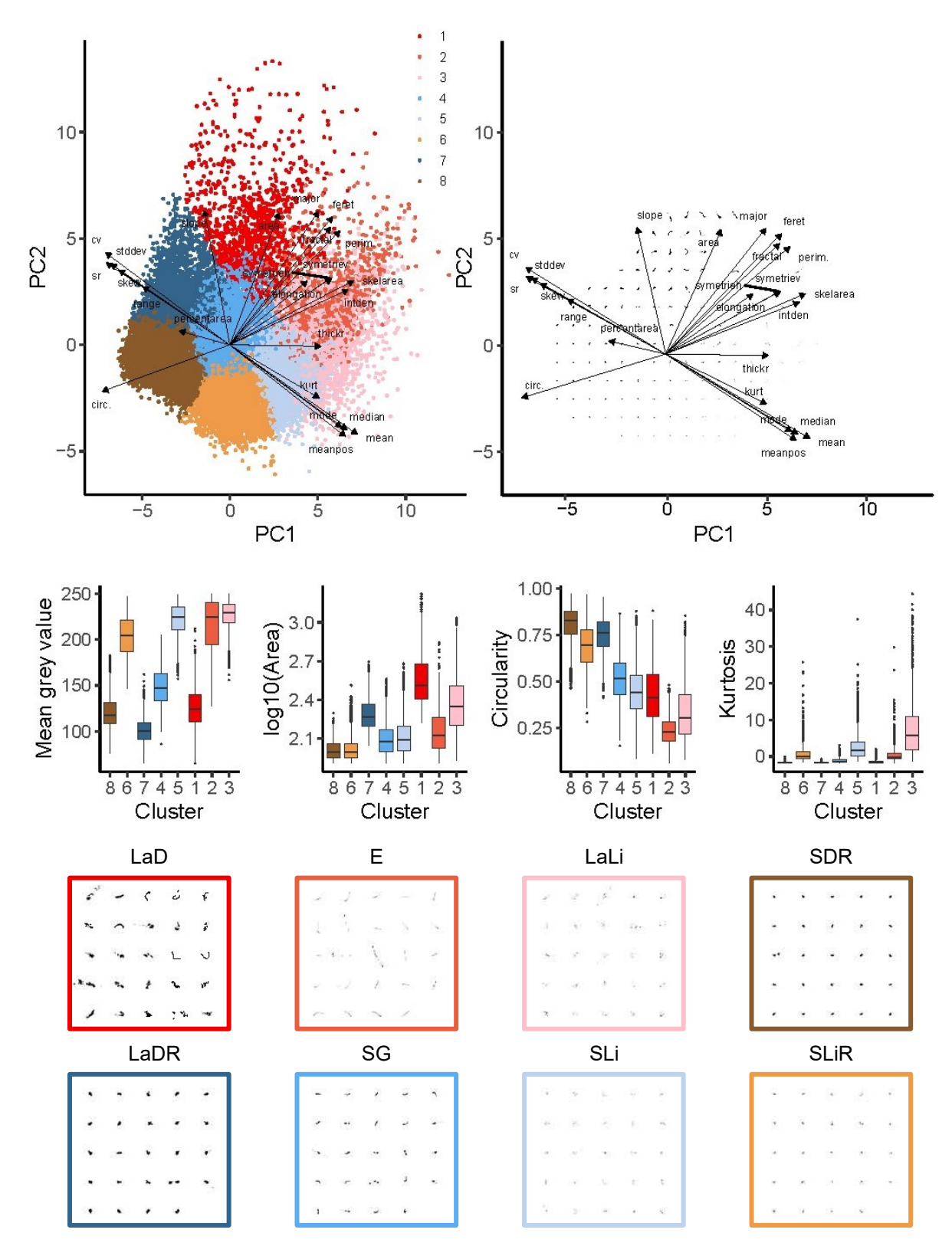


Figure 4.2 Assignation of marine snow into morphological groups via Principal Component Analysis (PCA) with k-means clustering. (a) K-means clusters represented on the first two dimensions of the PCA space, with eight particle morphological clusters shown by colour. Loading vectors for the 24 morphological characteristics are shown by arrows, depicting correlation between principal component axes and particle characteristics. (b) The same PCA space and loading vectors, with exemplar particle images showing particle properties in the PCA

space. (c) Boxplots depicting distributions of particle brightness (mean particle grey values), size (log-transformed particle area), particle shape (circularity), and particle structural uniformity (particle kurtosis). Boxplots depict median values, 25th and 75th percentiles. (d) Exemplar images of marine snow morphotypes within each cluster.

4.4.2 Latitudinal and vertical trends in particle distribution and morphology

The abundances of marine snow morphologies varied by orders of magnitude throughout the transect, and particle properties associated with some morphologies appeared to influence the efficiency of their attenuation. Maximum marine snow concentrations (0.78 particles L-1) and biovolume (1.10 mm³ L⁻¹) were observed between 40 – 60 m during our second station at 44 °S, whilst stations 11 – 14 in the South Atlantic gyre displayed biovolumes $< 0.02 \text{ mm}^3 \text{ L}^{-1}$ over the same depth range (Supplementary Table S4.2). In terms of latitudinal trends in particle morphology, our southernmost stations in the South Atlantic (south of 44 °S) contained the greatest proportion of dark particles (SDRs, LaDRs, LaDs), and mean particle brightness was lowest at these stations (Figure 4.3). Here SDRs and LaDRs were the primary dark particles by concentration (Figure 4.3), yet due to their large size LaDs dominated particle biovolume in the upper 300 m before being replaced by LaDRs below this depth (Appendix Figure B.3). Other stations with notably high biomass in surface waters differed starkly in their morphological composition. Second-highest biomass concentrations (0.91 mm³ L⁻¹) were observed at station 8 which was dominated numerically by light (largely SLi, also LaLis and SLiR) particles (Figure 4.3), whilst station 22 (0.87 mm³ L⁻¹) displayed a more even numerical composition of particle morphologies (Figure 4.3), biomass dominated by LaLi particles. Both stations 8 and 22 displayed the most rapid declines in particle biomass and number concentration with depth (Figure 4.3); I investigated the relationship between transfer efficiency and particle composition further.

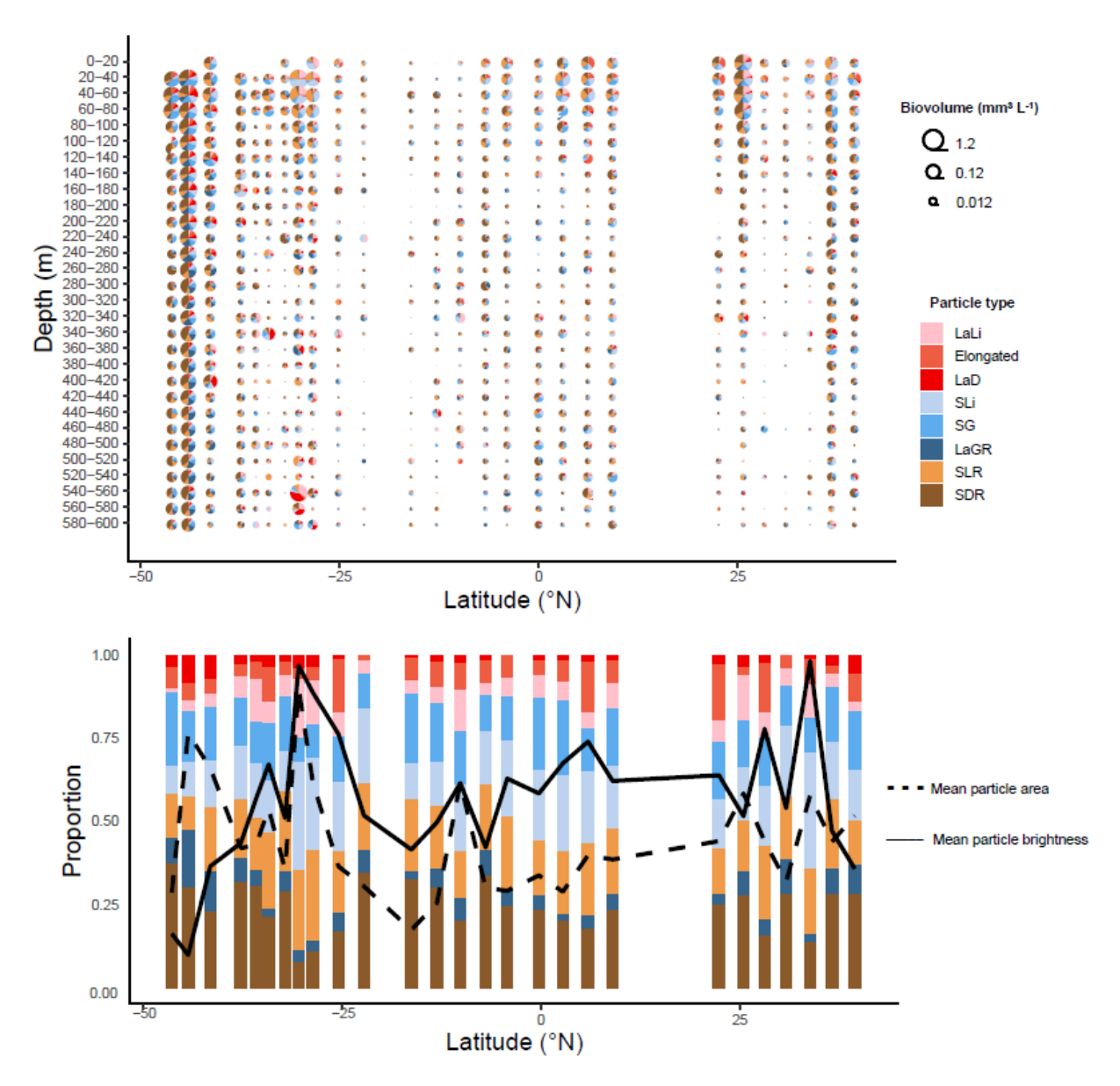


Figure 4.3 (a) Numerical proportions of marine snow morphologies across the entire transect and with depth. (b) The proportions of marine snow morphologies to particle assemblage throughout the entire particle profile for each station. Scaled mean particle area (dashed line) and scaled mean particle brightness (mean grey level [lower score, dark particles; higher score, light particles], solid black line) for each profile is overlaid.

4.4.3 Patterns in particle morphology associated with particle transfer

The linear model fitted between maximum particle concentrations in the upper 150 m at each station (depth z_0), and the particle concentrations 100 m below this depth, z_{100} , is shown in Figure 4.4. The slope of this linear model, representing a variance-weighted mean transfer efficiency (T_{100}), was 0.19 (T_{100} of 19%).

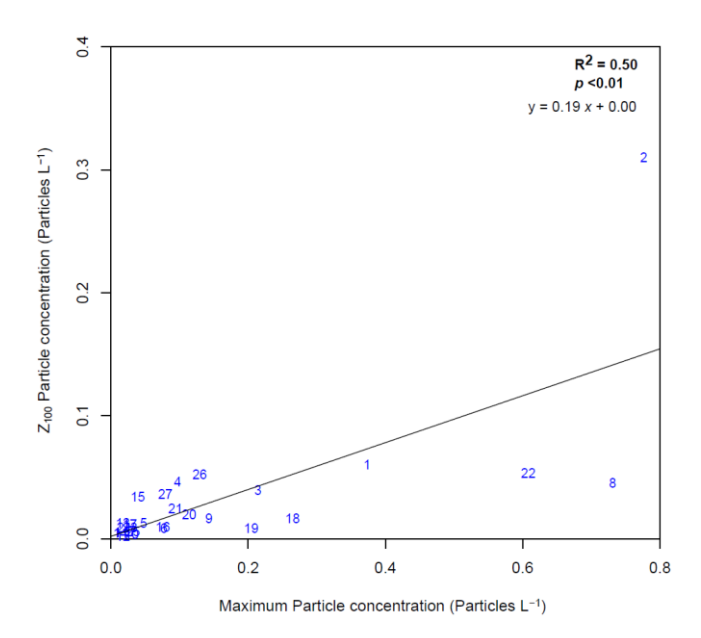


Figure 4.4 Linear regression between maximum particle number concentration in the upper 150 m of each profile, at a depth z, and the number concentration at depth z_{100} , 100 m beneath the maximum concentration. Solid black line shows the linear regression between these two concentrations, where the gradient represents a variance-weighted mean of T_{100} . Numbers plotted indicate station number.

From this linear model, I selected the stations with the most positive residuals (2, 4, 15, 26, 27) as examples of high particle transfer stations and those with the most negative residuals (Profiles, 8, 18, 19, 22) as examples of low particle transfer stations. Residuals from this linear model are hereon termed T_{100} residuals.

No clear trend linking particle morphology to high transfer efficiency stations emerged. These profiles were typically influenced by particle spikes (Appendix Figure B.5:), which likely masked any effects relating changes in particle morphology to transfer efficiency. Station 2 - the station with highest T_{100} residual- however, was characterised by the lowest particle brightness of all stations across our transect, and also second highest mean particle size.

In the low particle transfer group (stations 8, 18, 19, 22), total particle biomass at the depth z of particle maxima was generally dominated by light (LaLi, SLi, SLiR) particles (St8, 87%; St18, 64%, St19, 60%; St22, 57% of total particle biomass). Strong reductions in number and biomass concentrations of particles during sinking to z_{100} appeared to be driven by preferential losses of these light particles (Figure 4.3a; Appendix Figure B.3), with the contribution of light particles to z_{100} total particle biomass strongly reduced (from 87% to 2% at St2; 64% to 12% at St18, 60% to 5% at St19, 57% to 35% at St22). Changes in the proportion of large (LaDR, LaD, LaL) particles showed no clear trends between these depths, increasing from 44% to 46% at St8, from 11% to 44% at St18, 17% to 35% at St19, yet decreasing from 56% to 29% at St22. With the exception of St22, average particle brightness throughout the water column at these stations was higher than

the mean (Figure 4.3b). Slight increases in the proportion of large particles with depth, and strong decreases in particle brightness, suggests the efficiency with which dark (SDR, LaD, LaDR) particles are transferred to depth is far greater than that of light (LaLi, SLi, SLiR) particles. In isolation, mean particle brightness was significantly negatively correlated with T_{100} residuals $(p=0.001,R^2=0.33,df=25;$ Appendix Table B.3), but mean particle area was not $(p=0.98,R^2=-0.03,df=25;$ Appendix Table B.3). However, when accounting for particle brightness, mean particle area became significantly positively correlated (p<0.001) with T_{100} residuals, and a significant interaction (p<0.001) between particle area and brightness was observed (Appendix Figure B.7: , Appendix Table B.3).

4.4.4 Broad scale particle transfer and transformation

The ratio of particle concentrations in the "surface" (0-100 m) to particle concentrations in the subsurface (100-300 m), aka "Abundance efficiency" (Supplementary Table S4.3) varied by particle morphological group (Figure 4.5). Mean particle abundance efficiency was 32 % (Figure 4.5); this figure does not represent a measure of transfer efficiency and is presented only for comparison. The figure is also higher than our 19% T100 estimate due to the equal weightings of all ratios calculated (regardless of particle concentration at each station), and only serves as a baseline with which to compare abundance efficiencies of other particle groups.

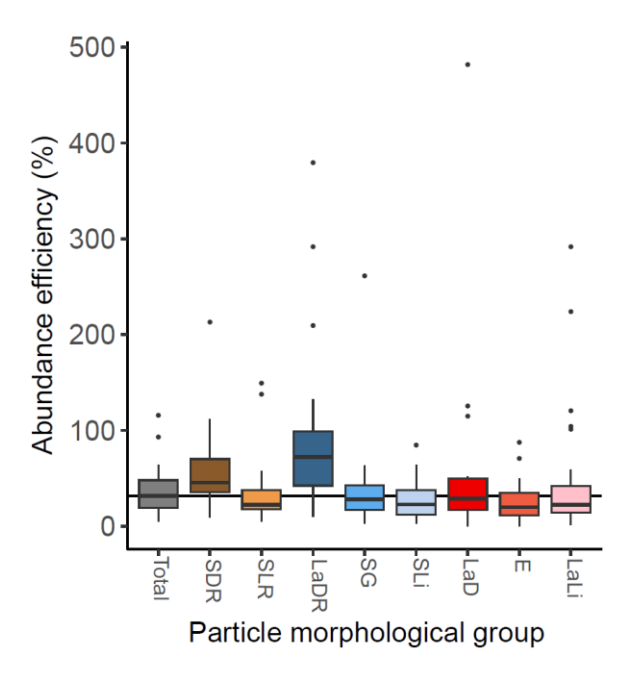


Figure 4.5 Distribution of total particle abundance efficiencies and particle abundance efficiencies for each particle morphology, calculated between 0 – 100 m and 100 – 300 m bins.

LaDR particles had the highest median abundance efficiency of 72%, whilst SDR particles had a median abundance efficiency of 45%. Regardless of light particles (SLiR, Sli, LaLi) all had a median abundance efficiency of 22%, whilst elongated particles (also with high mean greyness) had a median abundance efficiency of 20%, further implying some relationship between of particle brightness and efficiency of transfer to depth. LaD particles were the only dark particles with a median abundance efficiency (29%) less than the overall average, yet given the high abundance efficiency of LaDRs, this low value is likely heavily influenced by particle transformations as well as losses during sinking.

Particle composition differed significantly (PERMANOVA, p = 0.001) between these coarse depth bins (Figure 4.6b). Surface (0-100 m) particle communities tended to contain higher proportions of light SLiR and SLi particles (Figure 4.6a) than subsurface (100 – 300 m) and deep (300 – 600 m) communities, which contained higher proportions of dark SDR, LaDR and LaD particles. Pairwise comparisons indicated surface particle communities differed significantly from both deeper depth bins (PERMANOVA, p_{adj} < 0.01 for both, BH correction) (Figure 4.6b). Deep particle communities interestingly exhibited a slight shift towards higher proportions of larger LaD, Lali, and elongated particles (clusters 1-3) compared to subsurface particle communities (Figure 4.6a) but differences between subsurface and deep particles communities were not significant (PERMANOVA, p = 0.15, BH correction). Surface particle communities were also fractionally more similar to deep particle communities than they were to subsurface particle communities (Figure 4.6b). In terms of environmental drivers, SST were significantly correlated (p = 0.001, $R^2 = 0.42$, df = 25) and thus both significantly correlated with particle composition (Chlorophyll: p = 0.001, $R^2 = 0.18$, df = 25; SST: p = 0.007, $R^2 = 0.11$, df = 25 (Figure 4.6a). Colder, higher chlorophyll waters tended to contain higher proportions of dark (SDR, LaDR, and LaD) particles, whilst higher SST and lower Chl stations were correlated with higher proportions of small, lightly coloured SLiR and SLi particles (Figure 4.6b).

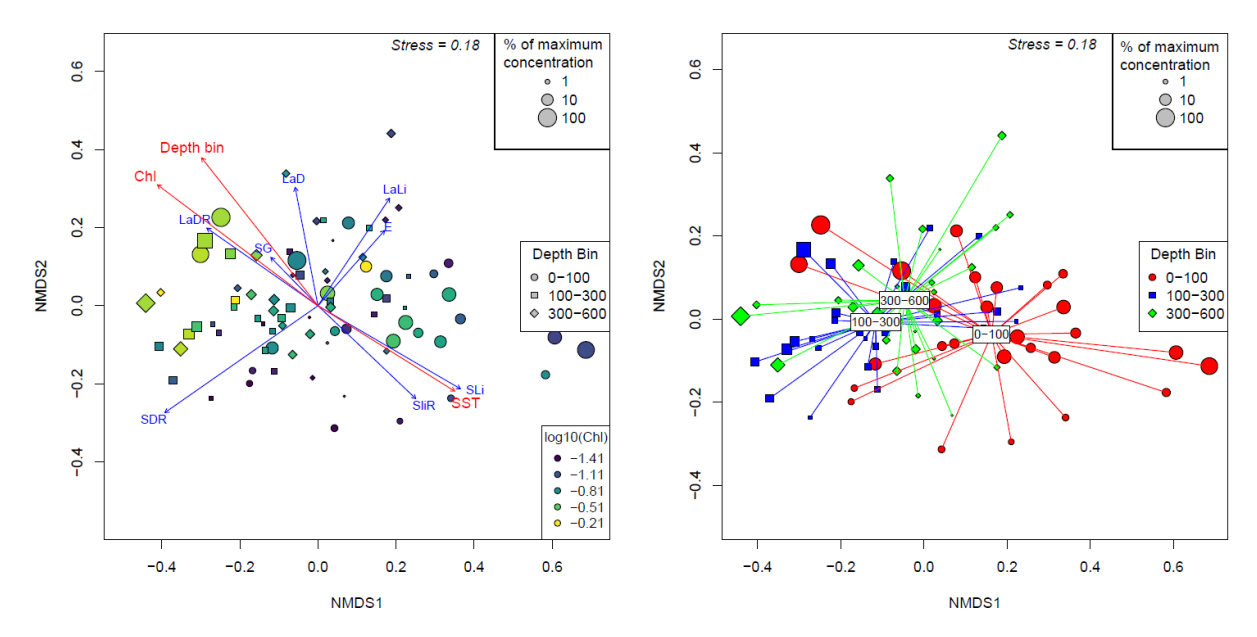


Figure 4.6 Non-metric multidimensional scaling (NMDS) ordination of particle community composition. (a) Points are coloured by mean Chlorophyll concentration ($\mu g \, L^{-1}$) in the upper 100 m, their shape dictated by depth bin (circles, 0 – 100 m; squares, 100 – 300 m; diamonds, 300 – 600 m), and size dictated by percentage of maximum particle concentration observed across the transect in these depth bins. Blue arrows depict loading vectors for proportions of different particle clusters to community composition (see Figure 4.2), and red arrows depict environmental variables (Chl, mean surface chlorophyll; SST, sea surface temperature) significantly correlated with NMDS ordination. (b) "Ordispider" depicting NMDS centroids and distributions within the NMDS ordination for the three depth bins red circles, 0 – 100 m; blue squares, 100 – 300 m; green diamonds, 300 – 600 m). Sizing of point is as in panel (a).

4.4.5 The influence of diel vertical migration

Overall differences between the three depth strata above, at, and below the DVM resting depth ("control, "DVM", "deep") were not significant (PERMANOVA, p = 0.067), though pairwise comparisons of the three depth strata indicated particle communities at the DVM resting depth differed significantly from the particle communities in the control stratum overlying them (PERMANOVA, p = 0.027, BH correction) (Figure 4.7b). Control communities typically displayed increased proportions of SDR particles, with DVM particle communities associated with a greater proportion of LaD, SG, and SLi particles. Deep particle communities were intermediate between the control and DVM particle communities, significantly different from neither (both p > 0.5, BH correction), but displaying a slight shift back towards SDR particles. In terms of environmental drivers of particle community composition between profiles, surface Chlorophyll was again a significant (p = 0.003) driver despite the distance of the three depth strata from the

surface. Migrant strength was also significantly correlated (*p* = 0.001) with differences in particle communities between profiles; in general, control, DVM, and deep particle communities had a smaller proportion of LaD, LaLi, and SLiR particles when migrant strength was higher.

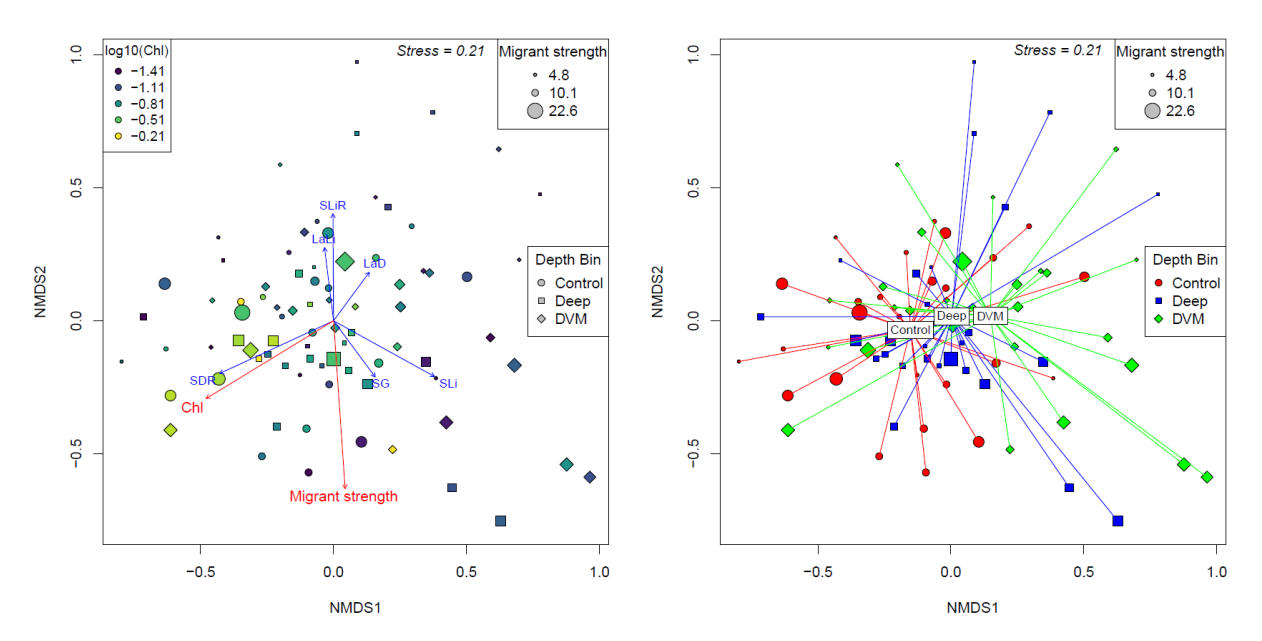


Figure 4.7 Non-metric multidimensional scaling (NMDS) ordination of particle community composition. (a) Points are coloured by log(mean Chlorophyll concentration (µg L⁻¹)) in the upper 100 m, their shape dictated by depth bin (circles, control; diamonds, DVM; squares, Deep), and size dictated migrant strength calculated from night – day ADCP signal strength in the epipelagic layer. Blue arrows depict loading vectors for proportions of different particle clusters, and red arrows depict environmental variables (Chl, mean surface chlorophyll) significantly correlated with NMDS ordination. (b) "Ordispider" depicting NMDS centroids and distributions within the NMDS ordination for the three depth bins (red circles, control; green diamonds, DVM resting depth, blue squares, deep layer). Sizing of point is as in panel (a).

4.5 Discussion

4.5.1 Vertical changes in particle morphology

Vertical changes in particle morphologies I observe at basin scales largely echo those of regional studies (Trudnowska et al. 2021; Accardo et al. 2024; Habib et al. 2024; Soviadan et al. 2024): I find that the proportion of small, dark, round particles generally increases with depth while elongated, fibre-like particles are generally restricted to the surface. Despite a confounding influence of particle transformation (see below discussion in 4.5.4), higher abundance efficiencies for small, dark, round particles than small, light, round particles add to

the growing body of evidence highlighting the importance of particle compactness in dictating the efficiency of particle transfer to depth (Laurenceau-Cornec et al. 2015b; Iversen and Lampitt 2020; Williams and Giering 2022). Our observations that (i) higher T100 was significantly correlated but with decreases in particle brightness but not increases in particle size, and (ii) that low particle brightness was a prerequisite for particle size to significantly influence T100, are strikingly similar to the observations of Laurenceau-Cornec et al., (2015b), and suggest a dominant control of particle compactness over size on particle sinking velocities. Our results also appear to support on the basin scale claims that size alone is not an efficient predictor of particle sinking velocities in situ (Laurenceau-Cornec et al. 2015b; Iversen and Lampitt 2020; Williams and Giering 2022). Yet, without sinking velocity estimates for our particle morphologies from pulse tracking as in regional previous studies (Trudnowska et al. 2021; Accardo et al. 2024; Habib et al. 2024; Soviadan et al. 2024), I caveat this conclusion due to the possible influence of particle transformation on abundance efficiencies of each morphological group (see 4.5.4 below).

4.5.2 Deep changes in particle morphology

Throughout our latitudinal transect, I observed marine snow particles to undergo transformations or selective losses such that smaller darker particles became increasingly common between the surface and subsurface (100 - 300 m) depths. Whilst such particle transformations resulted in significant differences between particle communities between these depth strata, I also observe that for to mid-mesopelagic particle communities ("control", "DVM" and "deep" depth strata), surface chlorophyll a concentrations remained a significant driver of particle morphological composition. This observation suggests that the influence of source particle composition driven by variations in surface chlorophyll concentrations can be observed to propagate down even to mid-mesopelagic particle communities; vertical changes in particle composition remain relative to surface communities rather than changing to a global mesopelagic particle community. Our results thus highlight the importance of depth-related (Trudnowska et al. 2021) and productivity-driven (Kiko et al. 2022) changes in particle community composition. Kiko et al. additionally highlight a productivity-driven effect on the slope of the particle size spectrum. Our observations of the increasing dominance of darker particles in more productive stations suggests primary production also influences over particle compactness, in addition to Kiko et al.'s observation of a productivity-driven effect on the slope of particle size spectrum.

Shifts towards darker, more compact particles with increasing depth did not usually occur throughout the entire profile, however. Significant differences in communities at the DVM resting depth to overlying control communities dominated by SDR particles suggest an

important role for diel vertical migrants in shaping morphological properties of deep particle communities. The processes introducing a diversity of larger or lighter particles in the DVM layer remain unclear, but may arise from deep production of relatively larger faecal pellets (Suzuki et al. 2003; Belcher et al. 2017; Tarrant et al. 2021), or incomplete fragmentation of particles into larger, looser bodies via microbial gardening (Mayor et al. 2014) or small-scale turbulence generated by swimming organisms (Dilling and Alldredge 2000; Ziervogel et al. 2025). Losses in proportions of larger, lighter particles as they sink out of the DVM layer suggests new particles originating in the DVM may be selectively subject to similar transformation and consumption processes as particles sinking out of the surface ocean-for instance, consumption by zooplankton. Particles produced in the DVM layer by diel vertical migrants may be a vital source of energy for deep Rhizarian communities along our transect (Couret et al., in prep) and in a broader sense, shifts in particle community composition associated with the DVM layer highlight the mutual and bidirectional relationship between deep plankton and particle communities.

4.5.3 Productivity and particle compactness

Our observation of increasingly dark, compact particles at more productive stations appear, at first, at odds with previous studies relating phytodetrital particle size to particle porosity. The coupling between zooplankton grazers and phytoplankton communities likely plays a key role in reconciling these differences, and driving the productivity-driven effects on particle community composition that we observe. In general, porosity of phytodetrital aggregates is thought to increase with particle size (Logan & Wilkinson, 1990; Laurenceau-Cornec et al. 2015; 2020), and more productive, diatom-dominated communities at higher latitudes have been posed to produce loosely packaged aggregates that may not sink efficiently (Henson et al. 2012; Williams et al. 2025). Thus, changes in phytoplankton community composition alone may therefore be unlikely to explain our results. Zooplankton, however, are known to play an important role in repackaging loose aggregates into more densely packed particles (Steinberg et al. 2008; Belcher et al. 2017), and so increases in zooplankton abundances coupled to increases in primary production could result in the high numbers of dark, compact particle that we observe. This explanation agrees well with the observations of Bach et al. (2019) that highly porous aggregates are enabled by a lack of zooplankton grazers, and more broadly supports the model of Lam et al. (2011) that the degree of coupling between zooplankton and phytoplankton communities is a major determinant of BCP efficiency. None of our stations likely sampled major blooms; mid latitude stations in the South Atlantic sampled the end of austral summer or start of autumn, whilst our final station in the North Atlantic did not exhibit high particle concentrations (0.10 L⁻¹ within UVP observable size range) and was sampled before the typical onset of the spring bloom

at this latitude (Henson et al. 2018). As a result, phytoplankton growth is unlikely to outpace zooplankton growth and become decoupled from grazing at our stations, meaning that zooplankton were likely to be able to keep pace with phytoplankton growth, selectively graze on porous and loose aggregates, and repackage material into more compact particles (Lam et al. 2011; Bach et al. 2019). Establishing how phytoplankton-zooplankton coupling varies throughout the course of the year may therefore be an important goal in order to understand the controls on particle morphology, and by extension transfer efficiency of the BCP.

A further effect explaining darker particles at more productive stations could be from relatively higher levels of transparent exopolymeric substance (TEP) production at nutrient-limited sites with lower productivity. TEP production throughout the world's oceans is poorly constrained and many factors have been posed to influence TEP production and consumption (Zamanillo et al. 2019), yet TEP production of *Synechococcus* cyanobacteria has been observed to increase under nutrient stress (Deng et al. 2016). Particles at oligotrophic, nutrient-limited stations may therefore be expected to contain more TEP, which is transparent and with low excess density (Engel and Schartau, 1999), contributing to the relatively (optically) lighter particles observed at low Chl stations. Since we did not measure TEP production across the transect, we cannot verify this hypothesis.

4.5.4 Morphological changes: transfer or transformation?

A key metric within BCP research is the "transfer efficiency" of the BCP- the efficiency with which exported organic carbon is transferred to a given depth (Buesseler and Boyd, 2009). Quantifying this efficiency for POC is intuitive and directly linked to losses in carbon fluxes originating in the upper ocean. Applying such a metric to particle concentrations as I have done here ("abundance efficiency") is useful, but also experiences the confounding effect due to particle transformations. For instance, LaD particles being broken up into several smaller particles would artificially inflate the abundance efficiency of daughter LaDR or SDR particles. Use of biovolume rather than counts would be a similarly imperfect metric given that larger particle broken into smaller particles would still attribute daughter biovolume into the SDR or LaDR class, regardless of whether the particle sank and was then fragmented, or vice-versa.

Abundance efficiencies as I have calculated them can nonetheless offer meaningful results but should only be taken as qualitative indicators rather than a quantitative measure of transfer efficiency for each morphological group. For instance, comparison of the abundance efficiency of SLiR and SDR particles highlights the importance of particle brightness/compactness for particle transfer and flux losses, given that fragmentation of these particle morphologies would only result in daughter particles of the same particle type. Low abundance efficiencies of LaD

particles, by contrast, can not be taken to definitively indicate low transfer efficiencies of these particles, given the broad spectrum of potential daughter particles types that LaD particles could conceivably be broken into. Until directions of transformations between particles are better understood, even if sinking velocity measurements will become available, I anticipate that transfer vs transformation will remain an important caveat when interpreting vertical changes in particle morphology.

4.5.5 Outlook for large scale studies into particle morphology

Understanding the role of particle properties in shaping the downward transfer of marine snow is essential for in situ image measurements, and mechanistic understanding of passive particle sinking within the BCP (Giering et al. 2020b; Omand et al. 2020; Trudnowska et al. 2021). A practical step, therefore, in incorporating more ecological information about marine snow particles is the ability to objectively classify a broad spectrum of marine snow into groups using functionally important traits.

Here I have shown that Trudnowska et al. (2021)'s method maybe successfully applied to large basin-scale studies as well as regional time-series, and demonstrated that prior observations at regional and local scales (discussed below) are generally scalable and coherent with our observations across an Atlantic transect. However, I also realise an important limitation of applying this method to broad scale transects as opposed regional time-series. In contrast to regional studies, broad-scale transects do not permit "flux pulse" tracking of particle concentration maxima during sinking (Trudnowska et al. 2021; Accardo et al. 2024; Habib et al. 2024; Soviadan et al. 2024), preventing estimation of sinking velocities for particle morphologies. Without these sinking velocities, parsing the simultaneous effects of particle transformation and transfer during sinking becomes much more difficult, especially for larger particle morphologies (see Transfer and Transformation section above). This is not a limitation of global-scale studies per se, rather a limitation of transects.

The scalability of processes that I observe between regional and basin scales is highly encouraging, and, given sufficient spatial coverage of autonomous floats, suggests methods employed by Accardo et al. 2024; Habib et al. 2024 and Soviadan et al. 2024 could be used to discriminate particle morphologies and assign sinking velocities to these particle morphologies on large scales. Our results also support increasing calls for incorporation of more ecological information into image-based flux estimates (Giering et al. 2020a; Iversen and Lampitt 2020). Specifically, studies simultaneously measuring sinking velocities and morphological properties of individual particles in tandem would enable size-sinking velocities for different particle morphological groups to be determined. If particle morphologies were defined from a large, global morphospace of particles, a range of size-sinking velocity relationships for these groups

Chapter 4

could allow for accurate flux estimations in biogeochemically diverse locations throughout the world's oceans through separate calculation and summation of fluxes from each of these morphological groups.

Chapter 5 A Tool for the Collection of Water Samples and Sampling of Marine Particulates with Minimal Particle Alteration: A Novel Marine Snow Catcher Design

In this chapter I present the design of a novel Marine Snow Catcher (MSC) designed developed at the National Oceanography Centre (NOC) and assess how the new model compares to the old model.

This chapter is currently undergoing revisions after submission to Limnology & Oceanography: Methods.

Williams, J.R., Giering, S.L.C., Brown, R., Contreras-Pacheco, Y., Major, W., Saw, K., Shorter, S., Takeuchi, T., Lampitt, R. S. *in prep*. A Tool for the Collection of Water Samples and Sampling of Marine Particulates with Minimal Particle Alteration: A Novel Marine Snow Catcher Design.

Limnology & Oceanography: Methods

The new MSC design was developed and built by the Ocean Technology & Engineering (OTE) group at the NOC, principally Kevin Saw, Steven Shorter, and Robin Brown. Conceptualization was carried out by myself and Sari Giering. Field trial MSC deployments were carried out by myself, Sari Giering, and Marika Takeuchi. POC samples were run by Sabena Blackbird. Myself and Kevin Saw carried out flow modelling in Autodesk CFD.

5.1 Abstract

Marine particles play crucial roles in biogeochemical and ecological processes throughout the world's oceans. They form the largest component of ocean's Biological Carbon Pump, regulating atmospheric CO2, and are essential in distributing chemical elements, energy, macro-, and micronutrients throughout the water column. The importance of marine particles has led to their study on a variety of scales, from bulk particle fluxes to microscale studies examining particle properties. One instrument widely used to study marine particles across a range of scales in recent decades is the Marine Snow Catcher (MSC), yet this design of instrument has remained largely unchanged since its development. Here I present results from flow modelling, shore-based trials, and field trials, outlining the design of a new MSC model that is faster and safer to deploy, is flushed more completely during deployment, and minimizes turbulence, potentially lessening alteration to particles. This new model will allow for accurate

measurements of fluxes and particle properties whilst preserving particle realism, facilitating improved mechanistic understanding of the Biological Carbon Pump and provision of direct measurements to calibrate flux estimates from novel imaging technologies.

5.2 Introduction

Marine particles play crucial roles in biogeochemical and ecological processes throughout the world's oceans. They are essential in the distributing chemical elements, energy, macro-, and micronutrients throughout the world's oceans, and are thus fundamental to life in the oceans and global nutrient cycles. The importance of marine particles has led to their study on a variety of scales. Research on bulk particulate fluxes and vertical material transfer has advanced our understanding of the Biological Carbon Pump (Volk & Hoffert, 1985). Microscale studies have focused on individual particles measurements of particle microstructure (Flintrop et al., 2018), sinking velocity, and chemical concentrations (Belcher et al., 2016; Iversen & Ploug, 2010; Ploug et al., 2008), and also examined microbial communities associated with different particle types (Duret et al., 2019). Crucial to the utility of the above analyses is the assumption that particles sampled are reflective of those found in situ, and relatively unaltered during sampling prior to analysis. Whilst ex situ generation of particles allow for the testing of specific hypotheses in mesocosm experiments, conclusions drawn from particles generated ex-situ often differ from those observed in situ (Williams & Giering, 2022), and in situ particles provide a gold-standard for the study of real marine particles and their properties. The Marine Snow Catcher (MSC) is an integral instrument allows for simultaneous bulk flux measurements and examination of individual particles, and has been widely used over the last decade (Baker et al., 2017; Belcher et al., 2016; Duret et al., 2019; Flintrop et al., 2018; Giering et al., 2016; Karthäuser et al., 2021; Riley et al., 2012). It is a large-volume, column-shaped water container with two terminal openings and several taps down the side of the column. Once lowered through the water column to the desired depth, the MSC is 'fired' by means of a messenger, closing the terminal apertures, and the sample recovered to deck. After collection of an initial "time-zero" sample, the apparatus is left on deck for particles to settle over a consistent settling period, typically two hours. After settling, samples may be drawn from the upper tap of the MSC, bottom tap, or from a particle collection tray on the floor of the column. Depending on the study purpose, fluxes may be calculated from the concentration gradient established with the column, and individual particles may be extracted from the particle collection tray for analysis.

The currently operational model ('Mk1') is an early design developed to collect marine snow (Lampitt et al., 1993) and has been broadly unchanged since. This design has several deficiencies: whether or not the MSC misfires is highly sensitive to position of release

mechanism on wire; the MSC opens and close via a plunger mechanism which reduces and alters flow into the MSC; the MSC requires crew and crane support to assemble and take samples on deck.

Here I provide structural details and description of operations for a new MSC model (named "Yuki", after the Japanese word for snow) designed to improve safety, enhance deployment speed, improve sampling accuracy, and preserve particle realism. I present results from turbulence modelling of the new model compared to a previous MSC version, which illustrate greatly improved flushing whilst minimizing turbulence that may alter particle properties. Lastly, I present results from field trials of the Yuki design, assessing the quality of the data by comparing these results with paired deployments with the Mk1 version, and present shore-based assessments of measurement variability. This new model will allow for accurate measurements of fluxes and particle properties, facilitating improved mechanistic understanding of the Biological Carbon Pump and provision of direct measurements to calibrate flux estimates from novel imaging technologies.

5.3 Materials and procedures

5.3.1 Materials

The purpose and operating principle of all MSC versions are principally the same: to enable the sampling of large water volumes whilst preserving marine particulates, and to enable the separation of sinking from non-sinking particles. As described previously (Riley et al., 2012), the MSC is in principle a large volume water sampler deployed at a target depth by means of a messenger-operated closure release. The MSC is lowered throughout the water column with terminal apertures open, allowing water to enter and pass through the MSC. Once the target depth is reached, the MSC is closed using the messenger, capturing water and particles within this water from the target depth. Upon recovery to deck, the MSC is secured upright on deck for a settling period, during which particles sink throughout the device. After the settling period, suspended particulates are sampled from the upper unit of the MSC, whilst sinking fractions are sampled from a base unit and particle collection tray at the bottom of the MSC.

The modification to new design of the MSC (named "Yuki", after the Japanese word for snow) are designed to (1) improve ease of operation, (2) improve safety, (3) reduce reliance on ship's crew involvement, and (4) improve scientific quality. In this "Materials" section I describe the key structural differences between the Yuki MSC and Mk1 model; associated improvements to ease of set up and scientific quality are outlined in "Procedures" and "Assessment", respectively.

5.3.1.1 Structure of MSC Yuki

The new Yuki model consists of a large cylindrical PVC upper section, a detachable PVC base section attached to the upper section by means of four clamps, and a messenger-operated lid closure system which seals the upper end of the MSC when fired. These sections are contained within a stainless-steel frame which may be shackled directly to a wire for deployment. The metal frame is equipped with four lead weights around the base of the frame to ensure the MSC has sufficient ballast to flood with water when first entering the water.

The upper section comprises the main body of the MSC and is 123 cm in length. The upper section is held free-standing, suspended, 28 cm off the ground, by the stainless-steel frame. Two taps are situated 12 cm and 75 cm from the top of the column to enable sample collection and draining of the MSC column. An O-ring is positioned at top of the upper section to provide a secure seal with the MSC lid, with four J-hook type toggle clamps placed around the bottom of the upper section to attach the MSC base section.

The base section (Figure 5.1) comprises a 21-L PVC container with a tap 12 cm from the base of the MSC, permitting drainage down to 8 L for sampling of the base material. The floor of the base section allows a white PVC particle collection tray to be secured to the bottom of it on the inside surface (Figure 5.1). A crucial feature (and modification to the previous version) is that the floor of the MSC now constitutes a giant butterfly valve, such that the floor may be lifted inside the base and secured in an open position, allowing water to flow into the MSC (Figure 5.1b). A metal wire connected to a cocking arm via an R-pin runs up the exterior of the MSC passes over a pulley system to the release mechanism of the MSC (Figure 5.2).

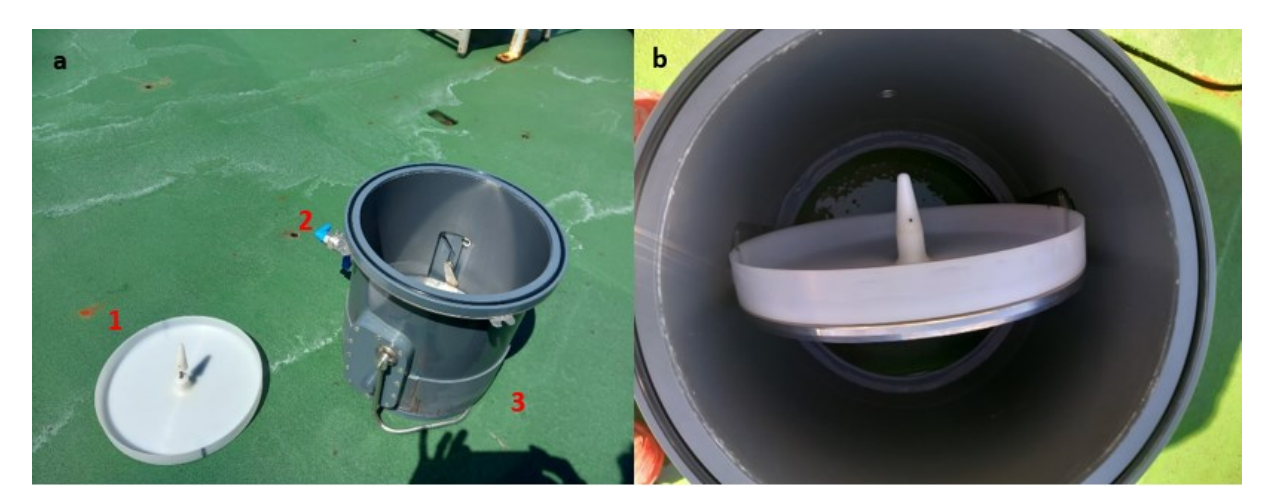


Figure 5.1 Base section of MSC Yuki. (a) Constituent parts of Yuki base section: (1) PVC particle collection tray; (2) tap for draining base section; (3) Cocking arm used to secure floor of the MSC in the upright position. (b) MSC base compartment with floor of the MSC base, ready for water to flow into the MSC.

The release mechanism of Yuki is incorporated into the structure of the MSC, rather than attached to the wire. The lid on top of the MSC houses a screw-shut air valve, and a metal pole which slides upwards to open the MSC prior to deployment. The metal pole contains a groove, into which a pivot is inserted to hold the lid open (Figure 5.2). When a messenger hits a rod connected to the pivot, the pivot rotates away from the metal pole and out of the latch. The weight of the lid causes the lid to fall, pulling on the wire which is connected to the cocking arm. As this arm is pulled, the floor of the MSC bases closes simultaneously to the lid.

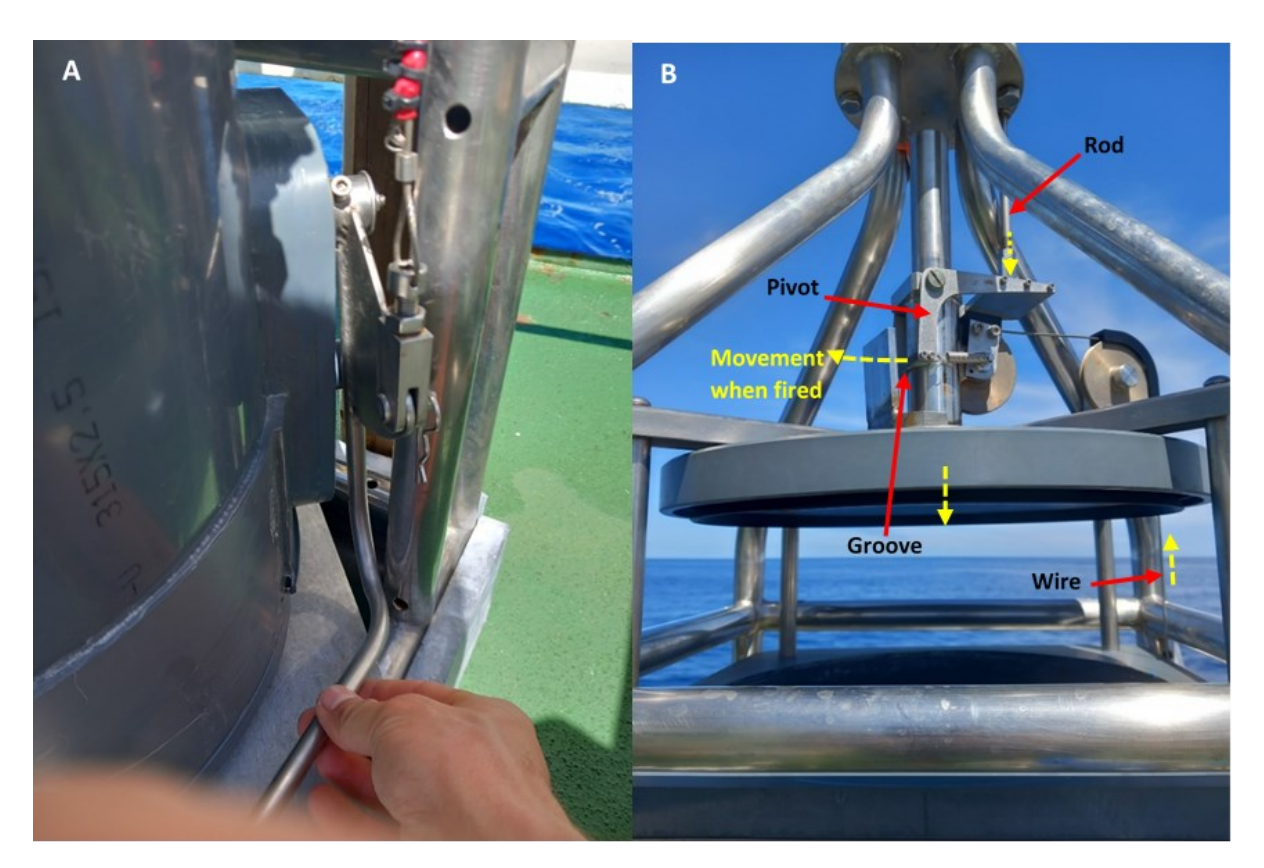


Figure 5.2 Closure mechanisms of MSC Yuki. (a) R-pin used to attach metal wire to the cocking arm of MSC base. (b) The release mechanism on MSC Yuki. When the rod is struck by a messenger, the pivot rotates out of the groove in the central pole. The lid then falls, pulling the wire over the pulley system to simultaneously close the base section via the cocking arm in (a). Yellow arrows indicate moving parts when MSC fired.

5.3.1.2 Key structural differences to Mk1 MSC model

The novel Yuki MSC version described above has a number of key structural differences relative to the Mk1 model (Figure 5.3). The release mechanism is now integrated onto the MSC rather than requiring attachment to the ship's wire, reducing the capacity for misfires when the release is incorrectly positioned on the release wire. To make it easier to separate top and base sections of the MSC and reduce reliance on ship's crew, the internal pole has now been removed from Yuki, and the upper section is now freestanding, permitting the base unit to be placed beneath it

without suspending the upper section by crane. The Yuki model also features an external frame which not only allows the MSC to be assembled upright on deck, but also offers protection to the MSC body should it come into contact with the side of the vessel whilst suspended from the wire during deployments. The closure mechanism in the base unit of Yuki has been changed from a spring-mechanism plunger system to a butterfly valve to improve flushing and reduce turbulence that could alter particle structure.

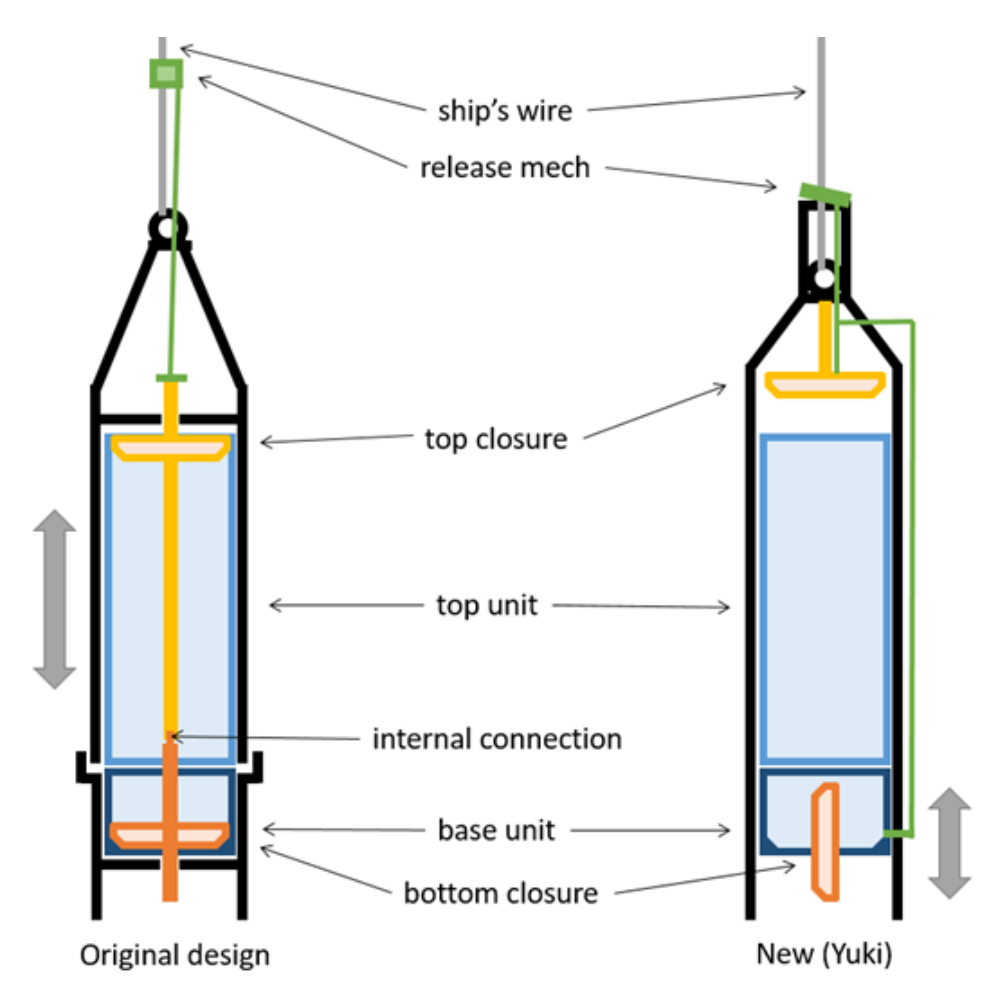


Figure 5.3 Schematic illustrating structural differences between the MSC designs: original MSC design (left, shown in closed state), and Yuki (right, shown in open state). Note the absence of internal pole for Yuki, bottom closure modified to butterfly valve system on Yuki model, and differences in assembly (old design, raising and lowering upper section with no external frame; Yuki design, lowering and raising base section with external frame present).

5.3.2 Procedures

5.3.2.1 Pre-deployment

Yuki should be rinsed with fresh water prior to deployment, taking particular care to wet the pulley system central pole on top of the lid, enabling it to more easily slide in and out of its sheath with less friction. As with all MSCs, all taps should be closed prior to set-up for deployment. For Yuki, the valve on top of the lid should also be screwed shut, to ensure a vacuum seal and prevent leakage once recovered to deck.

The MSC base should be set up by screwing the white PVC collection tray into the base section of the MSC. The floor should then be secured in the upright open position by lifting the cocking arm and raising the floor of the MSC inside the base section. Once the floor is lifted and the MSC floor vertical inside the base, the cocking arm is lowered, securing the floor in the upright position until the MSC fires. It is crucial that from this point, the cocking arm is not raised from the lowered position, in order to prevent premature closure of the MSC. At this point, the base can be slid underneath the upper section of the MSC on a metal support (Figure 5.4a), ensuring the O-ring seated on the base section is well seated. The base should be aligned with all four J-hooks of the clamps on the upper section of the MSC prior to fastening these clips and securing the base and upper sections of the MSC together.

The lid on top of the MSC is raised by pulling downwards on the wire (Figure 5.4b) and secured in the upright position by inserting the plate of the pivot into the groove on the central pole above the lid (Figure 5.4c-d). It is advisable when doing this to place a block beneath the lid when setting this up, in case the wire is accidentally released and the lid drops, to prevent the lid falling onto the operator's fingers. With the lid then secured in the open position, the wire on the side of the MSC should now extend down to the level of the cocking arm and can be carefully attached to the cocking arm using the small R-pin, ensuring not to raise this arm which would fire the MSC.

Lastly, the wire is attached to the MSC via a shackle. During this step it is possible that the release arms mechanism could be triggered by the individual attaching the shackle, but this is easily prevented through i) advising the individual to take caution and ii) placing fingers or a small wooden wedge behind the pivot (Figure 5.4d). With these mitigation steps, even if the release mechanism is jarred, the pivot will not rotate out of the groove on the central pole. Once the shackle is secured, and valves and taps are double-checked to be closed, the MSC is now ready for deployment.

5.3.2.2 Deployment and post-deployment

The MSC is lowered to the required depth as quickly as conditions allow, to maximize flushing. At the required depth, a messenger is thrown down the wire, and the scientist must keep their arm on the wire until they feel a vibration or ping, indicating the MSC has fired. After this, the MSC is recovered to deck. Once secured, the MSC may be drained or samples may be taken from the MSC according to standard MSC sampling procedures (Baker et al., 2017; Giering et al., 2016; Riley et al., 2012)- the valve on top of the MSC must be opened to do this, and closed once samples have been drained to ensure the vacuum seal is formed once more.

5.3.2.3 Improvements to ease and safety of deployment

Compared to the previous MSC model, we observed a number of key differences in the ease of use of model Yuki. Whilst previous models require at least two scientists, and the support of ship's crew to operate the winch during assembly and disassembly of the MSC, Yuki can be prepared, assembled and disassembled by a single scientist. We also found speed of set-up to be quicker for MSC Yuki, typically 5-10 minutes in contrast with ~15 minutes for the Mk1 version. Additionally, during disassembly of previous models, an R-pin had to be removed from the central internal pole of the MSC while the upper section was suspended on a winch. Despite mitigation measures in place, a small risk remains of trapping limbs between the upper and base sections of the previous MSC during this step- removal of the internal pole removes this hazard. Lastly, integration of the release mechanism onto the MSC structure reduces the capacity for human error arising from positioning the release mechanism on the MSC wire as with previous MSC model).



Figure 5.4 Key steps during preparation of MSC Yuki for deployment (a) Inserting the base section of Yuki beneath the upper section using the sliding tray; (b) Pulling down on the metal wire to raise the lid of Yuki; (c) The lid held (by hand) in the raised position, with the pivot plate not inserted into the central pole slot. If released in this position, the lid would fall; (d) lid secured in the upper position with the pivot plate inserted into the groove of the central pole. Holding the pivot in position as shown may also be used when attaching shackle to MSC if not using a wooden wedge, to ensure MSC is not fired accidentally.

5.3.3 General maintenance

The central exterior pole attached to the lid, along with the pulley system, should be rinsed thoroughly with fresh water at the end of deployments each day. The inside of both the upper and base sections should also be rinsed at the end of each day to remove residual organic material. On one occasion in rough seas, Yuki misfired because the wire running down the side

of the MSC had become caught on the red clamps which run hold the upper and base sections of Yuki together. This was easily rectified through the use of cable ties on the frame to hold the wire vertically and prevent it being washed to one side; we recommend the use of cable ties to maintain the track of the wire and prevent this issue.

5.4 Assessment

5.4.1 Flow modelling simulations

Prior to field trials, we performed computational fluid dynamics (CFD) model simulations using Autodesk Simulation CFD 2015 (Autodesk Inc., San Rafael, CA, USA) to characterize flow fields through and around both Mk1 and Yuki MSC versions. Geometries for three-dimensional model simulations were created within Autodesk, with ABS (Molded) used as the material for MSCs. Sea Water (Liquid Phase) was used to simulate flow past the MSC, with a volumetric flow rate set to 1 m s⁻¹ to simulate fluid flow relative to the MSCs at typical descent speeds.

Flow modelling simulations suggest Yuki demonstrates higher flow velocities through the MSC, with reduced flow alteration, turbulence, and vorticity around MSC flow entrance and exits relative to the Mk1 model (Figure 5.5). Flow velocities 60 cm above the opening of the Mk1 MSC were as low as 3 cm s⁻¹ near to the central pole, and highest (22 cm s⁻¹) close to the MSC walls where flow was most unimpeded by the inlet plunger (Figure 5.5a). By contrast, flow velocities 60 cm above the Yuki MSC opening were lowest (44 cm s⁻¹) nearer MSC walls (due to a lip near the inlet where the base plate rests), and peaked at 70 cm s⁻¹ (Figure 5.5b). Closer to the MSC inlet, differences in flow were most stark. In the new Yuki model, median flow velocity through the MSC 10cm above the inlet exceeded 80 cm s⁻¹, with flow generally uniform along the MSC axis (Figure 5.5c). In the Mk1 MSC, fluid flow into the MSC was inhibited by the MSC plunger, resulting in slower and more turbulent flow. Fluid velocities 10cm above the plunger floor were highest in jets (42 cm s⁻¹) close to the MSC walls, with turbulent vortices generated by these jets resulting in negative velocities (i.e. backwards flow towards the MSC inlet) near the central pole of the MSC (Figure 5.5d). Thus, the Yuki model demonstrates a clear reduction in turbulence relative to the Mk1 version, as shown by higher and more uniform flow velocities and the vector fields around MSC openings (Figure 5.5c-d).

Chapter 5

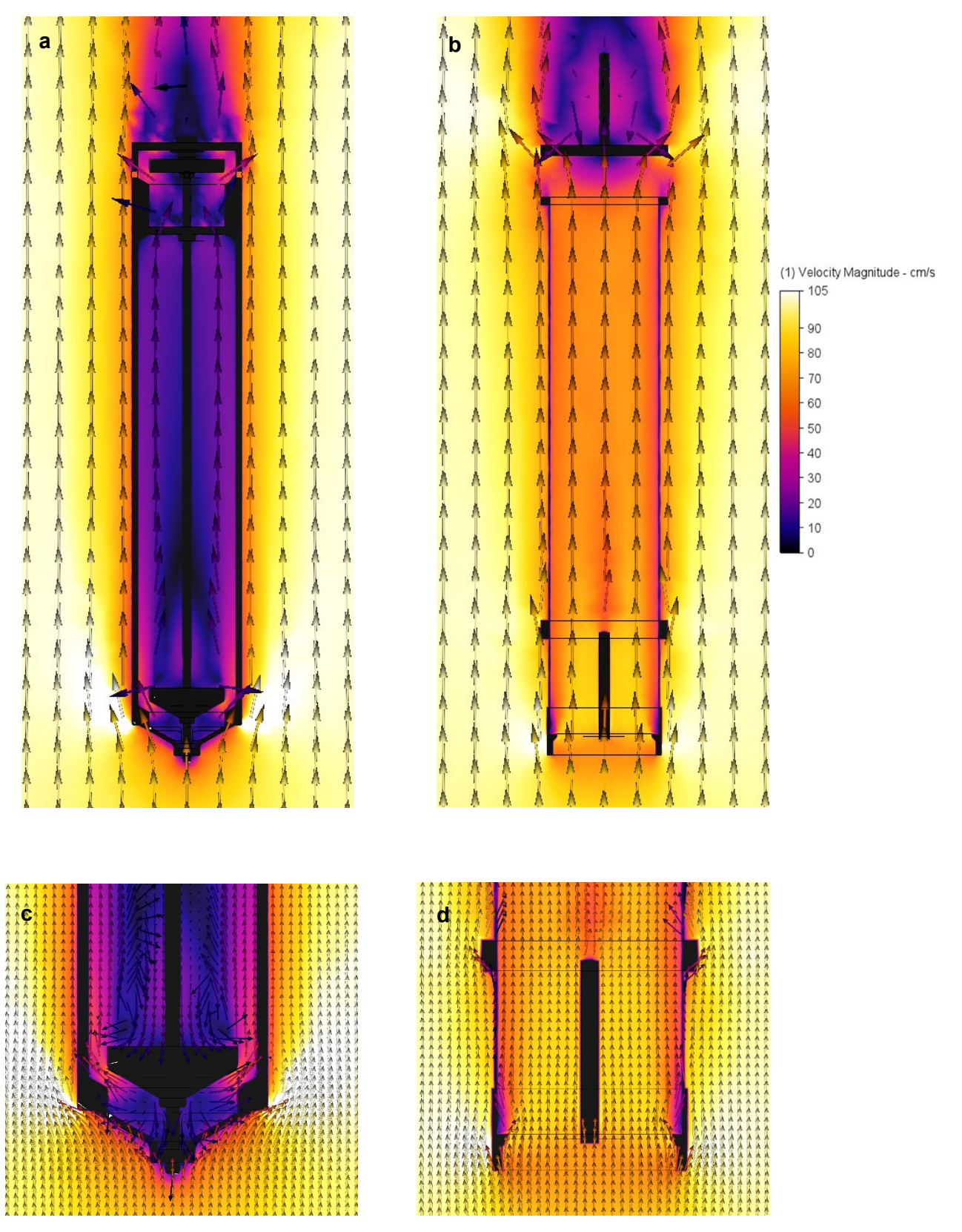


Figure 5.5 Simulation of flow fields fields through MSCs. (a) Mk1 MSC version, and (b) new Yuki MSC. Flow simulation was performed using Autodesk Simulation CFD 2015 (Autodesk, Inc., San Rafael, CA, USA) for initial flow velocities of 1 m s⁻¹, a typical descent speed when deploying MSCs. Colours indicate flow velocity magnitude, arrows depict velocity vectors.

5.4.2 Field trials: MSC version comparison

To test where scientific results from the Mk1 and Yuki MSC models were comparable, I compared several paired deployments of Yuki and Mk1 MSC versions. Both Yuki and Mk1 MSC designs were deployed to the same depth as part of an annual cruise (JC231) to the Porcupine Abyssal Plain (PAP) time-series site (48°50' N 16°30' W). MSCs were deployed back-to-back, typically within 30 minutes of each other, either to 50 m (just below the mixed layer) or 150 m depth.

Nine MSC deployment pairs were made during fields trials (Table 5.1). I directly compared the concentrations of Chlorophyll and POC in the initial sample ("Time-zero", equivalent to a typical water sample taken from a Niskin rosette) and "top" sample (i.e. the suspended particles), and when possible, I compared total fluxes, calculated using the same equations, for Chlorophyll (five paired deployments) and POC (six paired deployments). MSC samples were processed, and fluxes calculated in our comparisons were calculated according to standard procedures (Baker et al., 2017; Giering et al., 2016). For some MSCs, additional water was required from each fraction for additional analyses and so different sampling procedures and calculations were used to determine fluxes from these MSCs. MSC pairs where fluxes were not calculated using the same method were excluded from our comparison.

Table 5.1 List of MSC deployments from field trials. Chl and POC refer to Chlorophyll and Particulate Organic Carbon, respectively. Fluxes directly comparable and used in our assessment are shown here- some MSC pairs were not directly comparable because of slight deviations in the methods used to sample and calculate fluxes (see text above) For fluxes and concentrations from MSCs used in assessment, see 149

Date	MSC	Mk1 MSC	Yuki MSC	Depth	Time-zero	Тор	Fluxes directly
	Pair	Deploymen	Deploymen	(m)	fraction	fraction	comparable
		t no.	t no.		measured	measured	
					?	?	
4 May	1	2	1	50	Chl, POC	Chl, POC	Chl, POC
5 May	2	4	3	150	Chl, POC	Chl, POC	
5 May	3	6	5	50	Chl, POC	Chl, POC	Chl, POC
6 May	4	10	11	50	Chl, POC	Chl, POC	
6 May	5	12	14	150	Chl, POC	Chl, POC	
7 May	6	16	18	50	Chl, POC	Chl, POC	Chl, POC
9 May	7	19	20	50	Chl, POC	Chl, POC	Chl, POC
10 May	8	26	28*	50	Chl, POC	Chl, POC	POC
10 May	9	29	28*	50	Chl, POC	Chl, POC	Chl, POC

Chlorophyll concentrations are a useful tool to compare sampling efficiency as they typically have a pronounced vertical profile with high concentrations near the surface and a pronounced decrease below. When sampling just below this Chlorophyll maximum – as we did here - the MSC is lowered through a strong concentration gradient. Poor flushing would result in higher measured Chlorophyll concentrations, because water sampled by the MSC would in fact reflect shallower, more particle-rich water than that at the targeted sampling depth. Whilst flow modelling suggests improved flushing in the new Yuki model, total (time-zero) chlorophyll concentrations sampled by the Mk1 and Yuki MSC did not significantly differ (Paired t-test, t = 1.00, p = 0.35, d.f. = 8), with just six out of nine paired deployments displaying higher concentrations in the Mk1 MSC than in MSC Yuki (Figure 5.6a).



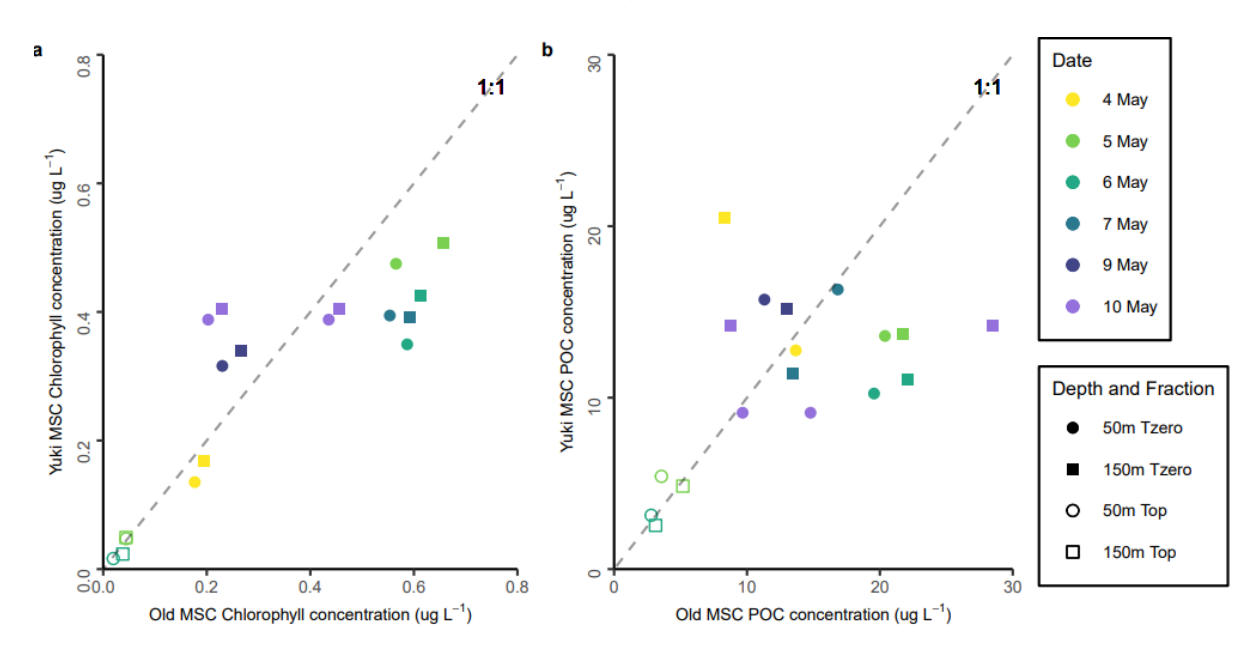


Figure 5.6 Time-zero and top fraction concentrations measured by Mk1 and Yuki MSCs. (a) Comparison of (a) Chlorophyll and (b) POC concentrations measured in the "time-zero" (squares) and "top" (circles) fractions of Yuki and Mk1 model MSCs, with Mk1 MSC on the x-axis and MSC Yuki on the y-axis, and colour indicating the date of paired deployments of Yuki and Mk1 MSCs. Sample fractions from MSCs deployed to 50 m are shown by closed symbols, with samples from 150 m shown by open symbols.

Due to the three deployment pairs where concentrations were higher in MSC Yuki, improvements to flushing do not seem to have resulted in significant differences in Chlorophyll concentrations between the Mk1 and Yuki models, leading me to conclude that measurements of chlorophyll concentrations by MSC Yuki and the Mk1 MSC models are comparable when set against natural variability. I must caveat this conclusion, however, as inspection of CTD fluorescence profiles reveal that these three elevated instances where Yuki measured higher concentrations than the Mk1 MSC may have been the result of irregular Chlorophyll profiles, wherein poor flushing by the Mk1 MSC could result in lower concentrations. Such instances could arise if MSC Yuki sampled a deep Chlorophyll spike correctly (owing to efficient flushing), while the Mk1 MSC still integrated relatively Chlorophyll poor waters from shallower depth (owing to inefficient flushing) (Figure 5.7).

I demonstrate the potential relationship between elevated Chlorophyll concentrations in MSC Yuki and irregular Chlorophyll profiles using these three paired deployments. The first pair where Yuki measured higher Chlorophyll concentrations (Pair 2), was deployed to 150 m depth on 5th May, below >50 m of near-constant Chlorophyll concentrations (Figure 5.6a). These two MSCs give almost identical concentration estimates (they fall directly on the 1:1 line; Figure 5.7a). The other two pairs where we observed higher Chlorophyll concentrations in MSC Yuki

(Pair 7 and Pair 8) were deployed on the 9th May and 10th May respectively, to 50 m depth. I plot MSC-derived concentrations over the profile for CTD 6, which was deployed on 10th February (no CTD deployment on the 9th February). The Chlorophyll profiles reveal several large peaks in concentrations (around 20 m, 30 m and, crucially, 40 m depth). Given the dynamic nature of the water column at the PAP site and rapid changes in Chlorophyll profiles (Appendix Figure C.1), it is possible that comparisons of these paired MSC deployments may have been confounded by transient Chlorophyll peaks. Chlorophyll peaks sampled by Yuki MSC may have been missed by the Mk1 MSC due to the poorer flushing, with the Mk1 MSC sampling (integrated) lower concentrations above the Chlorophyll peak. I cannot rule out that differences in the two MSCs were caused by the challenge of precisely targeting the desired sampling depth: close to a rapid vertical change in Chlorophyll concentrations, small differences in deployment depths could result in considerable concentrations differences. However, given the improved flushing of the Yuki MSC and added ballast weight on the Yuki frame, the Yuki model is less easily swayed by strong currents and more likely to sample deeper (hence lower Chl concentrations in a typical vertical profile) than the Mk1 model. I therefore conclude that whilst improved flushing may not lead to statistically significant differences between Chlorophyll concentrations between Yuki and Mk1 MSC models, that is not to rule out that this influences measurements. Merely, the direction of influence may be variable and dependent on variations in vertical chlorophyll profiles.

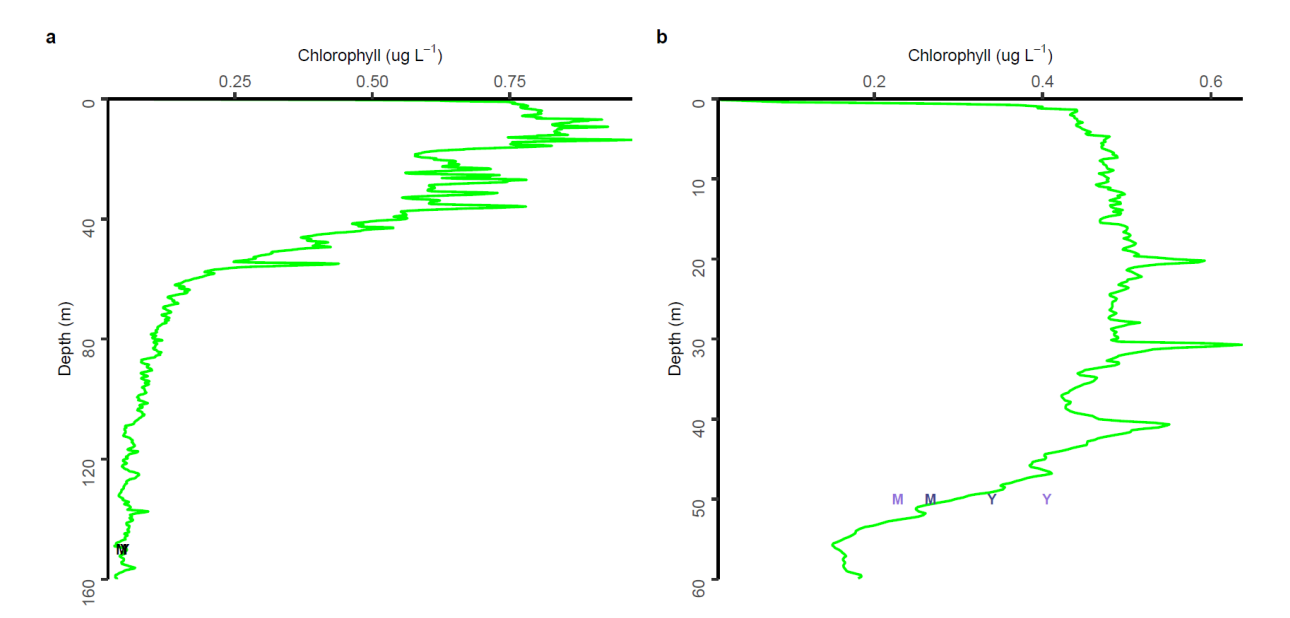


Figure 5.7 CTD chlorophyll fluorescence profiles with MSC time-zero Chlorophyll concentrations superimposed. (a) CTD Cast 3 with MSC 3 (Yuki, Y) and 4 (Mk1, M) concentrations shown in black. (b) CTD Cast 6 with MSC pair 7 (Mk1, navy blue M; Yuki, navy blue Y) and MSC pair 8 (Mk1, purple M; Yuki, purple Y) overlaid.

POC concentrations likewise showed no systematic difference in time-zero nor top concentrations between Mk1 and Yuki MSCs (p = 0.52 and p = 0.23 respectively; Figure 5.6b); POC concentrations were also more variable than Chlorophyll concentrations, a trend mirrored in the fluxes. Neither fluxes of Chlorophyll (Figure 5.8a) nor POC (Figure 5.8b) showed consistent differences between Mk1 and Yuki MSCs, with three out of five MSC pairs measuring higher Chlorophyll fluxes in MSC Yuki, and four of six pairs measuring higher POC fluxes in MSC Yuki. This finding either indicates that reductions to turbulence do not influence particle fluxes within the MSC, and hence flux measurements between the two MSCs are comparable, or alternatively that the lack of a consistent response may in part be down to variable responses of particles to increased turbulence. Turbulence can either result in particle compaction and aggregation, which increase particle density or size and hence increase sinking velocities and fluxes, or in particle disaggregation, reducing particle size and hence sinking velocities and fluxes (Burd & Jackson, 2009; Takeuchi et al., 2019; Williams & Giering, 2022). Given also the dependence of a particle's response to turbulence is highly sensitive to particle composition and type (Alldredge & Gotschalk, 1988; Takeuchi et al., 2019), different particle pools in different MSCs would be differently affected, and hence result in differing alterations to particle fluxes even under the increase in turbulence. The latter explanation would suggest that the reduction in turbulence associated with the new MSC model has the potential to influence MSC fluxes through reduced impact to particle characteristics during sampling, yet the magnitude and even sign of this change is variable and dependent on characteristics of the particle field.

Our field trials additionally serve as a useful proof of concept for ecological insights that can come from MSC studies, and highlight the importance of meticulous notetaking and recording of metadata. For each of the five pairs where both POC and Chlorophyll fluxes were measured, POC and Chlorophyll fluxes agreed in terms of whether Yuki or Mk1 MSC measured higher fluxes in each pair, yet variability was far greater for POC than for Chlorophyll (Figure 5.8). Such variability present in POC but not Chlorophyll is likely the result of large, rare, particles rich in POC but not containing Chlorophyll, such as gelatinous particles or exopolymeric substances, which we frequently observed at the PAP site throughout the course of the cruise. Chance sampling of such material could result in either fraction being enriched in POC; an issue that remains inherent in both MSCs and other gear when sampling rare or patchily distributed particles. When comparing POC export fluxes at 50 m from our paired deployments, export fluxes range from 37 - 134 mg m⁻² d⁻¹ across Mk1 MSCs and 71 - 121 mg m⁻² d⁻¹ for Yuki MSC deployments, with the exception of two MSC deployments which stand out: 573 mg m⁻² d⁻¹ in MSC 20 (Yuki) and 376 mg m⁻² d⁻¹ in MSC 29 (Mk1). Processing filters on 9th May (MSCs 19 & 20), we observed a jellyfish in MSC 19, which was removed, and unusually slow filtration for MSC 20, which we speculated might be due to high transparent exopolymer particles that clogged the

we observed the highest percentage of nitrogen and carbon as a percentage of dry weight in the dataset (around an order of magnitude higher than most), further suggesting anomalous environmental conditions potentially linked to jellyfish and transparent exopolymer particles. A similar anomalous percentage of nitrogen and carbon relative to dry weight was observed in MSC 29 (Mk1) and a jellyfish was observed on one of the filters, again potentially explaining the unusually high flux estimates. Note that the presence of jellyfish and TEP did not appear to affect the Chl estimates, likely reflecting the absence of Chl in jellyfish, jellyfish mucous and TEP as well as the smaller filtration volume (typically 200 mL for Chl vs 1000 mL for POC). Hence, I conclude that the presence of jellyfish appears to affect the sampling of both Mk1 and Yuki MSCs, which – at times – affects the direct comparison of the two MSC models. Through our deployments we have also been able to identify the important contribution of large, rare, gelatinous or exopolymeric particles to POC export fluxes. Lastly, it highlights the importance of carefully assessing the raw data, meticulous note taking, metadata recording and replicate deployments if possible, to accurately sample and interpret the marine environment.

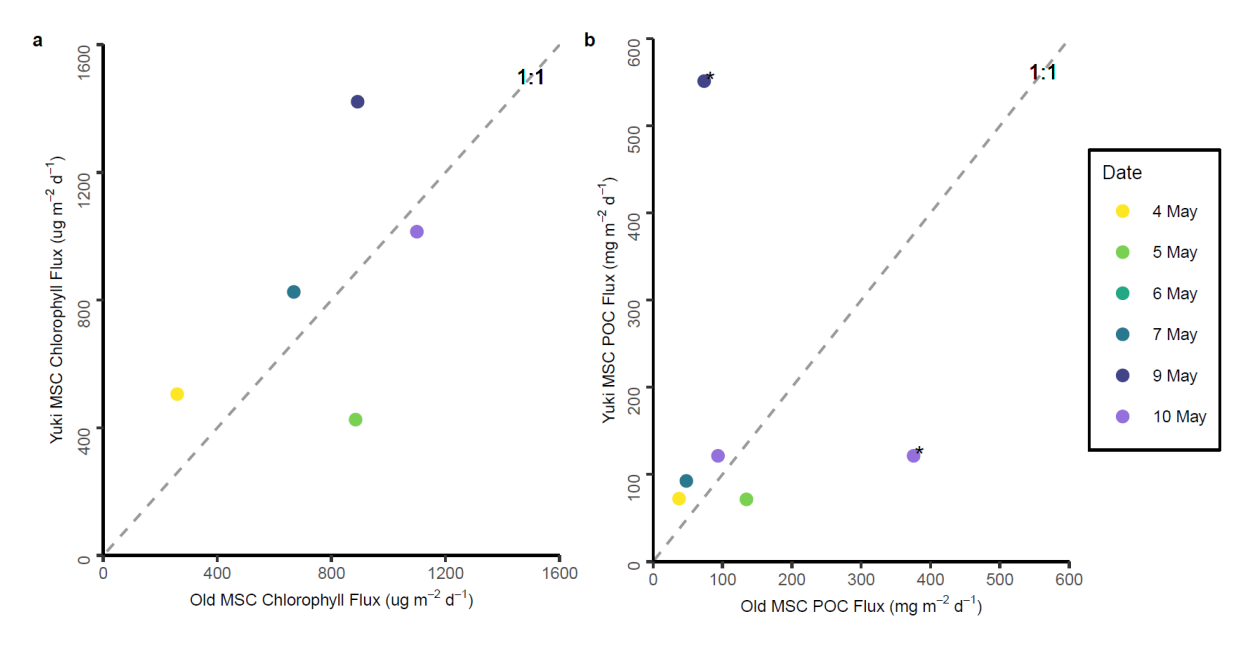


Figure 5.8 MSC measured fluxes of Chlorophyll and Particulate Organic carbon (POC): (a) Comparison of total (a) Chlorophyll flux and (b) POC flux measurements for Yuki and Mk1 model MSCs, with Mk1 MSC on the x-axis and MSC Yuki on the y-axis, with colour and text indicating the date of paired deployments of Yuki and Mk1 MSCs. Pairs marked with an asterix (*) for POC show anomalously high fluxes, likely influenced by the presence of gelatinous or exopolymeric substances (see text).

5.4.3 Shore-based variability study

Due to sampling constraints on the JC231 cruise, we were unable to deploy the new MSC model several times in quick succession to test sampling variability. Instead, I carried out shore-based trials to assess reproducibility of flux measurements.

Using a suspension of cornflour and olive stone particles to represent slow-sinking or suspended and fast-sinking particles respectively, we repeatedly sampled the MSC following established protocols (Baker et al., 2017; Giering et al., 2016; Riley et al., 2012), before measuring particle concentrations using a FlowCAM and calculating fluxes (for full description of method, see 147, for concentrations and fluxes see Table C.2). Total fluxes showed similar variability (%SD = 22%) to in situ/natural variability in MSC flux measurements (%SD), though when that outlying replicate (Replicate 2) that differed significantly from other replicates (Onesample t-test, p = 0.0046, t = 14.7, d.f. = 2) was removed, total flux reproducibility was excellent (%SD = 4.6%) (Figure 5.9). Propagated uncertainties from sample replicates gave rise to percentage combined standard uncertainties (%C.S.U.) for total particles fluxes ranging from 4.7 - 12.5%, highlighting the role of random error from sampling heterogeneity in introducing uncertainty to total flux estimates. I hesitate to put pose an exact value for percentage uncertainty of total flux measurements from the Marine Snow Catcher but, if bulk sinking velocities are correctly assigned (see limitations discussion below), it should range from ~5% as we observe here in a controlled system to ~25%. when variability of the natural system comes into play. Limits of detection will not differ from the original MSC model as both depend on analytical procedures used to measure concentrations on sample filters.

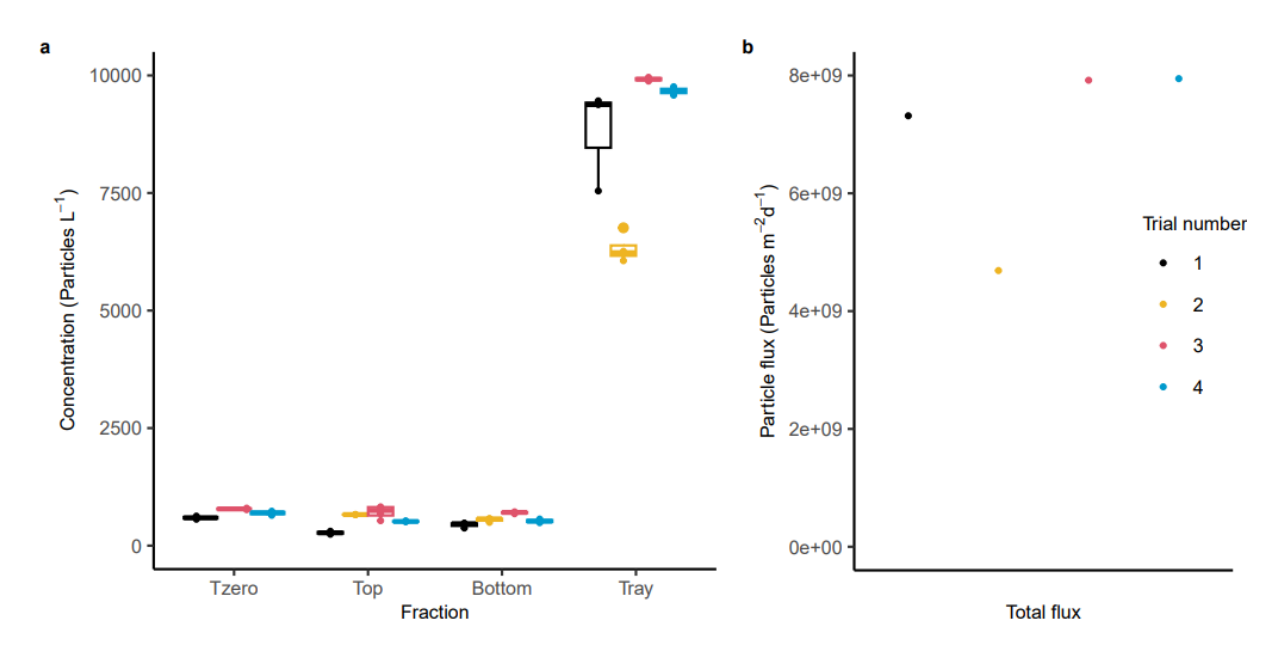


Figure 5.9 Boxplots showing variability in replicates of particle concentrations. (Particles L⁻¹) for each sample fraction (Tzero, Top, Bottom, Tray) within each of the four MSC trial replicates (1-4: black, yellow, red, blue); (b) Total particle flux

(Particles $m^{-2} d^{-1}$) calculated for each of the four MSC trial replicates (1-4: black, yellow, red, blue).

5.5 Discussion

5.5.1 Future improvements

Motivated by the need to sample marine particles and particulate fluxes unaltered in the marine environment, we sought to create an improved MSC model that would allow for safer, more rapid, and more accurate, true-to-life measurements of marine particulates. Results from the assessments illustrate the new "Yuki" MSC demonstrates improved flushing, allowing more accurate targeting of specific depth horizons, and generates reduced turbulence, allowing for collection of marine particles and particulate flux measurements with minimal particle alteration, representative of the marine environment. Whilst also meeting design targets in terms of ease and safety of operation, we acknowledge that as a first prototype long-term testing is also needed and further improvements can be made.

As a new instrument, durability of the device and its continued performance over time remains a question and will need to be addressed in future studies. For example, whilst the body of Yuki is protected by a steel frame, the release mechanism is necessarily housed above the frame to allow the messenger to reach the release unimpeded. Maintenance and constant rinsing of the release mechanism has been sufficient to ensure the release operates smoothly during initial tests of the Yuki MSC, but long-term maintenance of this part of the MSC is likely to be essential in ensuring its continued use.

The cost (~£15,000 at the time of writing) is another drawback of the MSC. Whilst not prohibitive to anyone with funds to purchase the original MSC model, these costs could be prohibitive to enabling broader access to MSC use in developing countries. Coupled to the already large costs of seagoing research, MSC access may be limited without subsequent capacity building and equipment-sharing programs.

When using the MSC to determine sinking fluxes, one limitation of the MSC that persists with MSC Yuki is the need to correctly assign a bulk-fast-sinking velocity to fast-sinking material, representing a potential source of error in flux estimations. Several methods are available to estimate sinking velocity, such as measurements in a settling cylinder (Baker et al., 2017; Belcher et al., 2016; Ploug et al., 2010), flow chamber (Baker et al., 2017; Ploug & Jørgensen, 1999), radioisotope-derived measurements (Villa-Alfageme et al., 2023), or image-based in situ measurements (Giering et al., 2023; Iversen & Lampitt, 2020), yet many of these methods

involve measuring particle sinking velocities on different temporal and spatial scales to those used in MSC measurements. Integrating a camera system or optical sensor into the MSC to determine the sinking velocity of large particles could be one route to reducing this uncertainty. This integration would likely greatly increase the cost, time, and specialist knowledge needed to deploy MSCs however, restricting the accessibility of this equipment.

Alongside minimizing the limitations outlined above, MSCs must, at present, be deployed one after the other, necessitating numerous different MSCs to be deployed one after the other in order to sample a profile of the water column. A potential avenue for further improvement would be to develop an MSC rosette, allowing for multiple MSC closures at different depths in the water column, akin to closing Niskin bottles on a CTD. This innovation would speed up deployments several-fold and reduce the time gaps between measurements in a profile. Whilst such MSCs do not yet exist, flow modelling of a conceptual MSC with a hinged lid closure designed for deployment on a rosette suggests an MSC could be developed to operate effectively when deployed on a rosette. This constitutes an avenue for future investigation.

5.5.2 Insight and applications

Here we have presented a novel MSC design, an instrument widely used for the collection of marine particles and measurements of sinking particulate fluxes. As well as advancing the ease and speed of deployment, measurements from the Yuki MSC appear comparable with the Mk1 model, whilst improved flushing and reductions to turbulent flow into the MSC have important implications for the utility and conclusions drawn from MSC studies. Firstly, improved flushing enables more accurate sampling of a given sampling depth, ensuring particles captured here by the MSC are representative of the desired depth rather than a few meters higher in the water column. Although a seemingly straightforward improvement, accurate sampling of target depth is pivotal to central questions in ocean biogeochemistry commonly investigated using MSCs. For instance, widely used metrics "export efficiency" and "transfer efficiency" are critically dependent on the choice of reference depth to which sinking fluxes deeper in the water column are compared (Buesseler et al., 2020), with the potential either overestimate or underestimate these values based on whether reference depth used is shallower or deeper respectively than euphotic depth (Buesseler et al., 2020). If MSC samples forming a reference depth for flux profiles are representative of depths shallower than their intended deployment, BCP efficiencies may therefore be overestimated. In addition, several ecologically and biogeochemically relevant features such as subsurface chlorophyll thin layers may be less than 5 m thick (Barnett et al., 2019; Dekshenieks et al., 2001), so flushing is also vital ensure validity of conclusions drawn when attempting to sample these features. Minimising turbulence is critical to accurately assessing both bulk particulate fluxes and individual particle

Chapter 5

characteristics. Although the manner which particles are affected by turbulence varies (Alldredge & Gotschalk, 1988; Takeuchi et al., 2019), and we do not see significant differences in flux measurements between MSC models, particles may undergo compaction, aggregation, disaggregation, or some combination of these processes, with implications for both individual particle-scale studies of particle characteristics and studies examining bulk particulate fluxes. As image-based methods for sinking flux estimation develop, correctly capturing particle properties as they exist in situ is essential in constraining size-sinking velocity relationships upon which size-spectrum-based methods depend (Giering et al., 2020; Guidi et al., 2008; Williams & Giering, 2022). We hope our new MSC will broadly enable more accurate characterization of particle characteristics and particulate fluxes in situ, to further mechanistic understanding of particles processes involved in the BCP and constrain relationships on which image-based flux estimations depend.

Chapter 6 Conclusions and Synthesis

The aim of this work was to address uncertainties in the role of particle characteristics in influencing particle sinking velocities, and hence efficiency of the Biological Carbon Pump. The role of particle characteristics have previously been identified as key source of uncertainty in future projections of the Biological Carbon Pump (Henson et al. 2024), and are often inextricably linked with ecological processes

In this thesis I have explored the paradigm that size exerts an important control on particle sinking velocities through a large-scale metanalysis and basin-scale analysis of particle image data, exploring methodological biases that have informed this paradigm and examining the importance of particle size across an Atlantic transect. I have also presented high-resolution flux measurements from the subpolar Southern Ocean to investigate the role of diatoms and particle ballasting in an understudied region, and presented field trials of a novel sampling apparatus designed to minimises biases due to particle alteration during sampling.

6.1 Key findings

This work produced four major findings, which are discussed in detail in below sections:

- 1) In contrast with H1, particle size alone is typical a poor predictor of particle sinking velocities, and hence a poor predictor of particle transfer efficiency. Other morphological traits such as particle compactness may be at least as important as particle size in shaping particle sinking velocity and transfer at large scales (Chapters 2 and 4).
- 2) In contrast with **H2**, diatoms may not (always) be efficient vectors for sinking carbon through the twilight zone, even if they dominate in surface waters. Ecological processes can decouple sinking fluxes of silica and carbon and negate the influence of biomineral ballast (Chapter 3).
- 3) In support of **H3**, particle morphological composition varies significantly both with productivity and depth across the Atlantic Ocean; particle compactness is a key morphological trait in setting the efficiency of particle transfer to depth and a prerequisite for particle size to exert significant control on particle transfer (Chapter 4).
- 4) A novel Marine Snow Catcher design is faster and safer to operate than the original design. It provides comparable flux estimates and minimises turbulence which can alter particles during sampling. In the near-term, methods to accurately measure particulate fluxes are essential for the validation of in situ optical flux estimates (chapters 2 and 5).

6.1.1 Particle size, morphology, and sinking velocity

In recent decades, particle size has come to be recognised as key parameter governing sinking velocity and transfer efficiency both in biogeochemical models (Yool et al. 2013; Aumont et al. 2015; Swart et al. 2019) and for the estimation of sinking fluxes from particle image datasets (Guidi et al. 2008). Such methods are clearly of merit for their utility, are underpinned by a theoretical basis in Stokes's Law, and have also been supported by numerous observations which observe strong size-sinking velocity relationships for marine particles (Engel et al. 2009; Iversen et al. 2017; van der Jagt et al. 2018). However, numerous studies have also called the strength of this relationship into question (Laurenceau-Cornec et al. 2015b; Iversen and Lampitt 2020).

In this thesis I highlighted a methodological bias underpinning this paradigm- that the majority of studies supporting a size-sinking velocity of relationship utilise ex-situ measurements, which typically display far stronger relationships than the few studies measuring particles in situ. This may occur due to particle alteration during sampling and incubation, or simply that particles have been generated ex-situ and exposed to fewer processes, resulting in a more homogenous particle pool.

I also highlighted the shortcomings of purely size-based flux estimations across an Atlantic transect examining particle morphologies. No significant difference effect of particle size alone was observed in driving more efficient particle transfer out of the upper ocean, and at basinscale, and particle compactness was found to be a prerequisite for a size-sinking velocity relationship. In addition, I found the two stations with largest mean particle area displayed completely contrasting efficiencies of particle transfer. The station dominated by dark particles displaying far greater than average particle transfer out of the surface ocean whilst the station dominated by light, loose particles displayed the lowest efficiency. A single size-based parameterisation would fail to reflect the stark contrast in transfer efficiency we observe here, highlighting that the incorporation of additional morphological traits is vital. As a result, I advise against using size-sinking velocity relationships compiled in Chapter 2- or more broadly, any previously published size-sinking velocity relationships- to estimate sinking fluxes from particle image data, unless directly tuned against direct flux measurements, such as in Kiko et al. (2020). And, whilst tuning flux estimates with direct flux measurements would enable errors resulting from particle heterogeneity to be avoided, I provide an outlook for future approaches that will enable autonomous methodologies in "Future outlook" below.

6.1.2 Diatoms and particle ballasting in the Southern Ocean

Another particle characteristic that has been posed to influence transfer efficiency is the presence of biomineral "ballast" minerals- dense minerals that increase the density and hence sinking velocities of marine particles (Armstrong et al. 2001; Klaas and Archer 2002). For this reason, and because of their substantial contribution to marine primary production, diatoms-diverse, siliceous phytoplankton- are often thought and observed to represent important and highly efficient vectors for transferring carbon from the upper ocean to the deep ocean (Ragueneau et al. 2002).

In this thesis I presented high-resolution direct flux measurements across the subpolar Southern ocean twilight zone, from disparate sites with varying levels of productivity and in varying stages of bloom progression. Carbon at these stations was consistently transferred relatively efficiently through the mesopelagic but, owing to high-resolution chemical measurements, I was able to identify diatoms as playing a relatively small role in this efficient transfer of carbon; diatom silica transferred was less efficiently to depth than carbon. These findings highlight that whilst ballast undoubtably plays an important role in some locations and times of year, even at our study sites (Rembauville et al. 2015), ecological processes-for instance buoyancy regulation or grazer repackaging of carbon- can negate the role of balance in some circumstances. Equally, the co-occurence of diatoms and the efficient transfer of carbon to the deep ocean does not necessarily imply a causative relationship. More broadly, this result highlights the importance of ecological processes such as grazing and buoyancy regulation in decoupling POC and BSi, the importance of faecal pellets to efficient flux transfer, and deemphasises the importance of diatoms for transfer of carbon through the Southern Ocean. If POC and BSi fluxes are decoupled and diatoms are less important in efficiently transferring carbon to depth than thought previously, then projected shifts towards communities dominated by smaller phytoplankton (Cabré et al. 2015) may not impact BCP- and ocean carbon storage- as much as previously thought.

Yet, in highlighting the important role of grazers in repackaging carbon, there is a need to establish how shifts in phytoplankton community structure will alter food webs and potentially impact repackaging of carbon via the BCP. For instance, shifts towards smaller phytoplankton could result in fewer large microzooplankton such as krill or large copepods which graze on large diatoms (Cavan et al. 2019) and produce the fastest sinking faecal pellets. Changes in food quality may also impact zooplankton grazing efficiencies, resulting in changes to upper ocean nutrient cycling and impact transfer of sinking fluxes (Richon and Tagliabue, 2021). Further work is therefore needed to constrain how zooplankton grazing may be altered under climate change.

6.1.2.1 Balancing ballast and decoupling processes

Amongst our study sites, we consistently observed attenuation of chlorophyll fluxes to be far more rapid than BSi fluxes in the Pacific sector, whilst in the Atlantic sector, chlorophyll flux attenuation was only moderately faster. This discrepancy may highlight mechanistic differences in the processes attenuating BSi fluxes between these regions. In the Pacific sector where Chlorophyll fluxes were attenuated very rapidly, we observed at the TN site large numbers of neutrally buoyant diatom resting spores (Le Moigne et al. in prep). If buoyancy regulation associated with these spores- or more widely diatoms- were the primary mechanism attenuating BSi and chlorophyll fluxes at these stations, then chlorophyll fluxes may be expected to be attenuated very rapidly at density gradients where live phytoplankton rest, regulating buoyancy (Lafond et al. 2020). By contrast, if grazing were to attenuate chlorophyll fluxes, chlorophyll attenuation would be expected to be more diffuse as grazing occurs over a larger depth range than the depth covered by a pycnocline, and fresh faecal pellets are known to carry chlorophyll (Cavan et al. 2021)- which would result in low chlorophyll flux attenuation. This mechanism may explain the lower rates of chlorophyll flux attenuation in the latter occupations of the productive Atlantic sector site and at the iron-limited Atlantic site, as zooplankton grazers keep pace with phytoplankton growth. Understanding the balance between these processes decoupling POC and BSi fluxes, as well as ballasting, is crucial to establishing the full temporal and spatial extent to which the patterns we observed may be found throughout the world's oceans and their implications for ocean carbon storage.

6.1.3 A new tool for sampling particles without alteration

The ability to sample marine particulates with minimal alteration is crucial to the utility of mechanistic studies investigating the role of particle properties in influencing particle dynamics. In addition, image-based flux estimations typically require calibration from direct flux measurement co-located in time and space (Ceballos Romero et al. 2024). In recent years, the Marine Snow Catcher (Lampitt et al. 1993; Riley et al. 2012) has formed an important tool with which to measure sinking fluxes (Giering et al. 2016; Cavan et al. 2017b; Romanelli et al. 2024) and capture individual particles for analysis (Belcher et al. 2016b; Flintrop et al. 2018; Karthäuser et al. 2021).

In this thesis I presented results from field trials, flow-based modelling, and land-based tests of a new Marine Snow Catcher model that is both safer and easier to prepare for deployment.

Results from the novel MSC design appear comparable with those from the old design, and can offer similar ecological insights, yet improvements to flushing and reduced turbulent flow into the MSC suggest the newer design is better equipped to study fine-scale features and may be

capable of capturing particles with less particle alteration due to turbulence. The importance of the MSC and similar direct flux measurements is discussed in *Future Outlook* below.

6.2 Future outlook

A key theme running through this thesis is the need to incorporate sufficient levels of ecological complexity into the mechanistic understanding underpinning flux models or flux estimations from image datasets. Rather than a single size-sinking velocity relationship or binary view of whether biominerals enhance transfer efficiency, including additional information regarding particle type or composition will facilitate a move towards a more sound and broadly applicable understanding of the Biological Carbon Pump. Ideally, incorporating additional measurements, rather than simple grouping based on a priori particle classifications (such as a "diatom" or "detritus" category), would enable more finer tuning of models or flux estimations to encompass regional or temporal variability. Incorporating such changes into models or flux estimation routines present different challenges, discussed below.

6.2.1 Models and in situ flux estimation

Incorporating nuance and complexity of ecological processes are likely easier to do for flux estimations from in situ datasets than for biogeochemical models. With flux estimations, calculations are largely independent from other outputs, and computationally less demanding than biogeochemical models. Thus, increases in complexity with additional variables or particle classifications are likely to be feasible to incorporate into flux calculations (given that it is possible to sample the desired characteristics in tandem).

Choosing to incorporate new processes into biogeochemical models poses more of a challenge: factors to be taken into account are numerous (Martin et al. 2024), and modifications to models should ideally be computationally tractable, significantly impact carbon storage on centennial and global scales, and be supported by a solid body of observational data (Henson et al. 2024). A diminished role for ballasting and particle size in dictating particle sinking velocities could certainly impact carbon storage on centennial scales given predicted shifts in phytoplankton community composition and size structure (Cabré et al. 2015; Tagliabue et al. 2021). However, certainly in the case of the diminished role for ballast, further work is needed to assess the temporal and spatial extent of our findings before incorporation into models. Taking into account additional parameters such as particle morphology as well as particle size is perhaps an idea with stronger observational support that could sooner be considered for representation in models. An optimal number of computationally tractable particle groups will vary from model to model, but at least two (e.g. small and large/ compact and loose) would

enable some mechanistic understanding, and, if changes to particle compactness under future climates are predicted to differ to changes in particle size, then at least four particle groups (small and compact, large and compact, small and loose, large and loose) should be considered for representation. If changes to particle compactness and particle size under future climates are predicted to respond in similar fashion, then including both characteristics separately may not be necessary, assuming that covarying changes are adequately represented by a two-group model.

For incorporating additional particle characteristics into flux estimation from in situ image data, there are numerous methods which have already been posed. One method already in use that could be said to represent a "current best practice" is to calibrate image-based flux estimates using concurrent in situ flux measurements from traps, MSCs, or radionuclide measurements (Iversen et al. 2010; Fender et al. 2019; Ceballos Romero et al. 2024). In ensuring fluxes are calibrated with local rather than global estimates, flux estimates are implicitly tuned to accurately represent particle dynamics in that location, rather than with a general approximation which may not be appropriate. This approach, however, requires calibration from traditional ship-base deployments, and is therefore not appropriate for use with developing autonomous technologies. In addition, it serves to empirically, rather than mechanistically tune image-based fluxes.

One alternative approach would be to directly incorporate additional particle information such as morphological measurements, into a unified equation for sinking velocity (Giering et al. 2020b). Some information about some morphological properties, such as particle compactness or porosity, can already be obtained from particle image datasets (Bach et al. 2019; Giering et al. 2020b). Another alternative approach is to statistically discriminate several morphological particle groups and determine size-sinking velocity relationships for each of these groups. Weighting of flux size-sinking velocity relationships by abundance of each morphological groups would then allow for a flexible and specific size-sinking velocity parameterization which is tuned to particle characteristics in any given set of conditions.

For both of the latter approaches which hold more promise for autonomous deployments, the challenge to progress here is a practical one. A gold standard for future measurements must be the simultaneous measurements in situ of particle sinking velocities and numerous morphological characteristics which can be used to statistically discriminate morphological groups of particles. The capacity to make such measurements are starting to become possible with custom set ups such as that used by Iversen & Lampitt (2020), but instrumentation that combines the automated calculation of many morphological characteristics (such as the UVP) and particle-tracking to calculate sinking velocities would greatly enhance the ease of

Chapter 6

simultaneous measurements and enable determination of distinct size-sinking velocity relationships for different particle morphologies. Regardless of automated calculation of parameters, preserving particle images so that future studies can extract and utilise morphological information will be paramount in maximising understanding which can be drawn from particle image datasets. In the coming years, high-resolution studies and accurate measurements from both shipboard and novel image-based techniques will both be essential to validating image-based flux estimations, and developing the mechanistic understanding of the BCP which underpins these methods and biogeochemical models.

Appendix A Inefficient transfer of diatoms through the subpolar Southern Ocean twilight zone

A.1 Biogeochemical setting and bloom progression of study sites

The five study sites we sampled were in various states of bloom progression during their respective sampling periods, and encompass both areas of low- and high-productivity. At the lowest productivity site, station OOI, we did not observe any bloom throughout the study period, with net primary production (NPP) remaining consistently low (Figure 3.1, max NPP = 328 mg C m⁻² d⁻¹). Sea surface temperature (SST) increased throughout the study period (Figure A.1:), with mean SST during each occupation increasing from 7.0 °C during the first occupation (OOI1, 06 Dec 2019) to 8.7 °C in the final occupation (OOI4, 03 Jan 2020). Surface chlorophyll concentrations also remained low (mean during each occupation: 0.43 - 0.57 ug L⁻¹) (Figure A.1:) and as with all Pacific sector stations, iron concentrations were <0.1nM in surface waters throughout the study period (Wyatt et al. 2023). Dissolved silicate concentrations declined (mean surface concentrations decreased from 4.7 to 2.6 uM between first and last occupation, Figure A.1:) but were not limiting (Wyatt et al. 2023).

The bloom at our central station, TN, peaked some time between our first (TN1, 11/12/2019), and second (TN2, 20 Dec 2019) occupations and we sampled its decline in latter occupations. NPP peaked around the time of this first occupation (Figure 3.1, max NPP = 1153 mg C m⁻² d⁻¹), whilst surface chlorophyll peaked during the second occupation (TN1 mean = 1.24 ug L⁻¹, TN2 mean = 1.43 ug L⁻¹, Figure A.1 :), with both declining throughout the subsequent occupations. Sea surface silicate declined throughout the study period (TN1 mean = 3.79, TN4 mean = 0.27 uM , Figure A.1 :) but incubation experiments did not indicate primary silicate limitation) (Wyatt et al. 2023).

At the southernmost Pacific station (TS), we sampled prior to the bloom peak in our first occupation (TS1, 09 Dec 2019), around the peak of the bloom during our second occupation (TS2, 17 Dec 2019), and bloom decline in latter occupations. Peaks in surface chlorophyll (Figure A.1:, 2.36 ug L⁻¹) and NPP (Figure 3.1, 943 mg C m⁻² d⁻¹) were both measured during the second TN occupation. Surface silicate concentrations, initially highest of anywhere in our study during the TS1 occupation (6.5 uM), declined to 0.18 uM in the final occupation. Despite low silicate concentrations by the end of the study period, iron was consistently the primary

limiting nutrient at the TS site (though incubation experiments did indicate Fe–Mn–Si serial limitation) (Wyatt et al. 2023).

In the Atlantic sector, the P2 station was only occupied on one occasion so we can only comment on the state of bloom at this site to a limited extent. Satellite NPP estimates indicate that we sampled close to the end of a bloom peak, with an NPP of 453 mg C m⁻² d⁻¹ during our visit to this site P2. Mixed layer chlorophyll concentrations from CTD Niskin measurements of 0.96 ug L⁻¹ further support the suggestion that this site was slightly more productive than the OOI site (mixed layer depth concentrations 0.37 - 0.90 ug L⁻¹).

At the naturally iron-fertilised P3 station, satellite and glider derived NPP estimates indicate the first occupation (P3A, 15-22 Nov 2017) sampled the height of a bloom, with declining NPP over subsequent occupations (Henson et al. 2023). Chlorophyll concentrations declined throughout the course of the cruise (calibrated chlorophyll fluorescence from glider data, Figure A.1:) throughout the mixed layer from 3.8 ug L⁻¹ during P3A to 1.3 ug L⁻¹ during P3C, as did silicate concentrations (5.03 μ M during P3A to 2.28 μ M during P3C) (Figure A.1:) (Ainsworth et al. 2023). Despite the naturally iron-fertilised regime, surface phytoplankton were iron-limited in the iron-depleted mixed layer, though recycling of Fe resulted in increasing dFe concentrations in the upper mesopelagic throughout the course of the cruise (Ainsworth et al. 2023).

Therefore, together our sampling of the different study sites have encompassed non-bloom, early bloom, bloom peak, and bloom decline phases of bloom development.

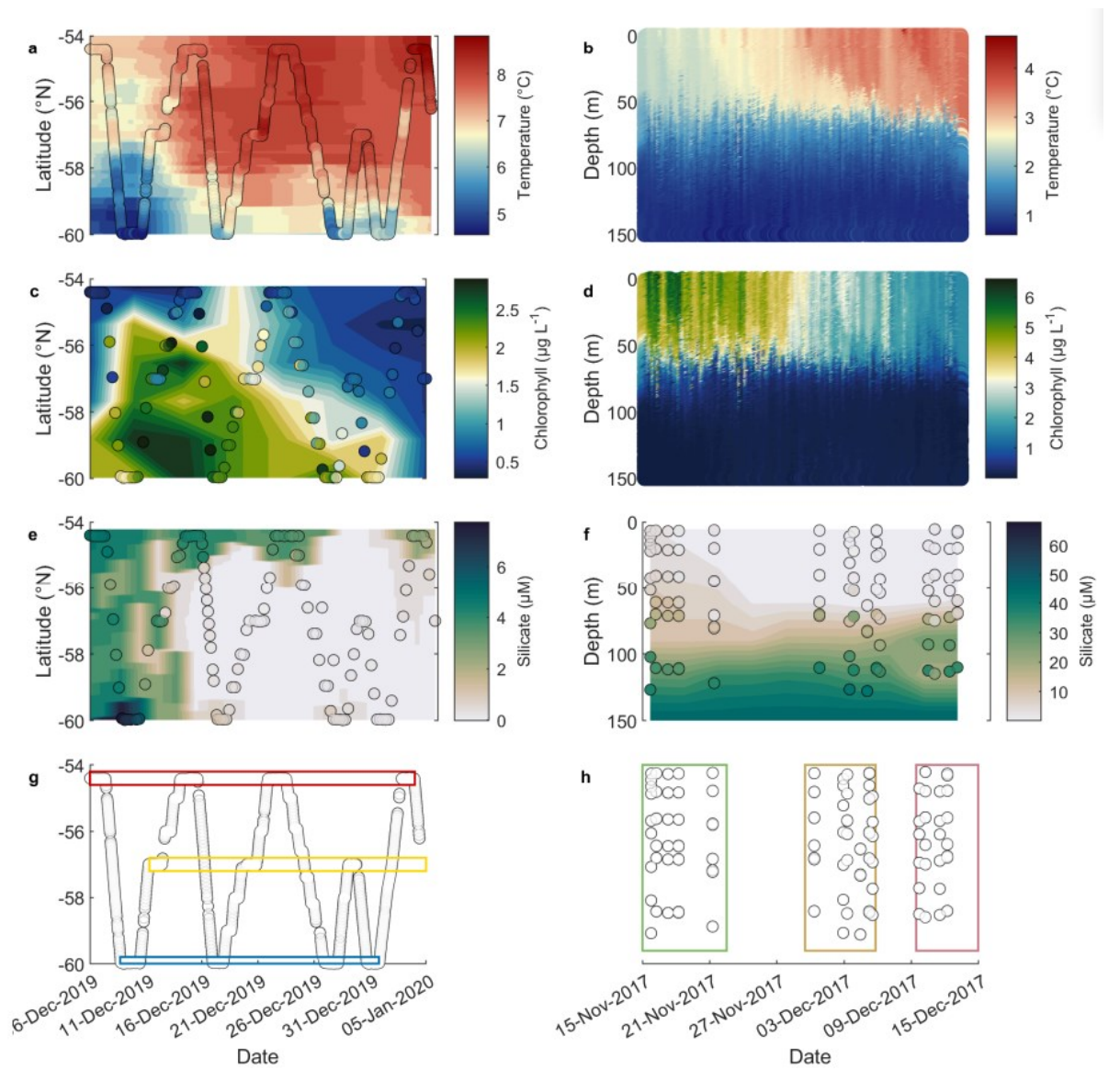


Figure A.1: Progression of bloom state at Pacific sector and Atlantic P3 station. Hovmöller plots (Time vs Latitude) of a) SST, c) Surface Chlorophyll, and e) Surface silicate from CTD and towed fish underway samples, at each of study sites in the Pacific sector study region (site latitude shown in g: OOI, red box; TN, yellow box; TS, blue box). Progression of b) glider-derived temperature measurements, d) glider-derived chlorophyll fluorescence (Henson et al. 2023), and f) discrete CTD Niskin dissolved silicate measurements are shown; dates of sampling period (P3A, green; P3B, yellow; P3C, red) shown in (h).

A.2 Total sinking flux profiles

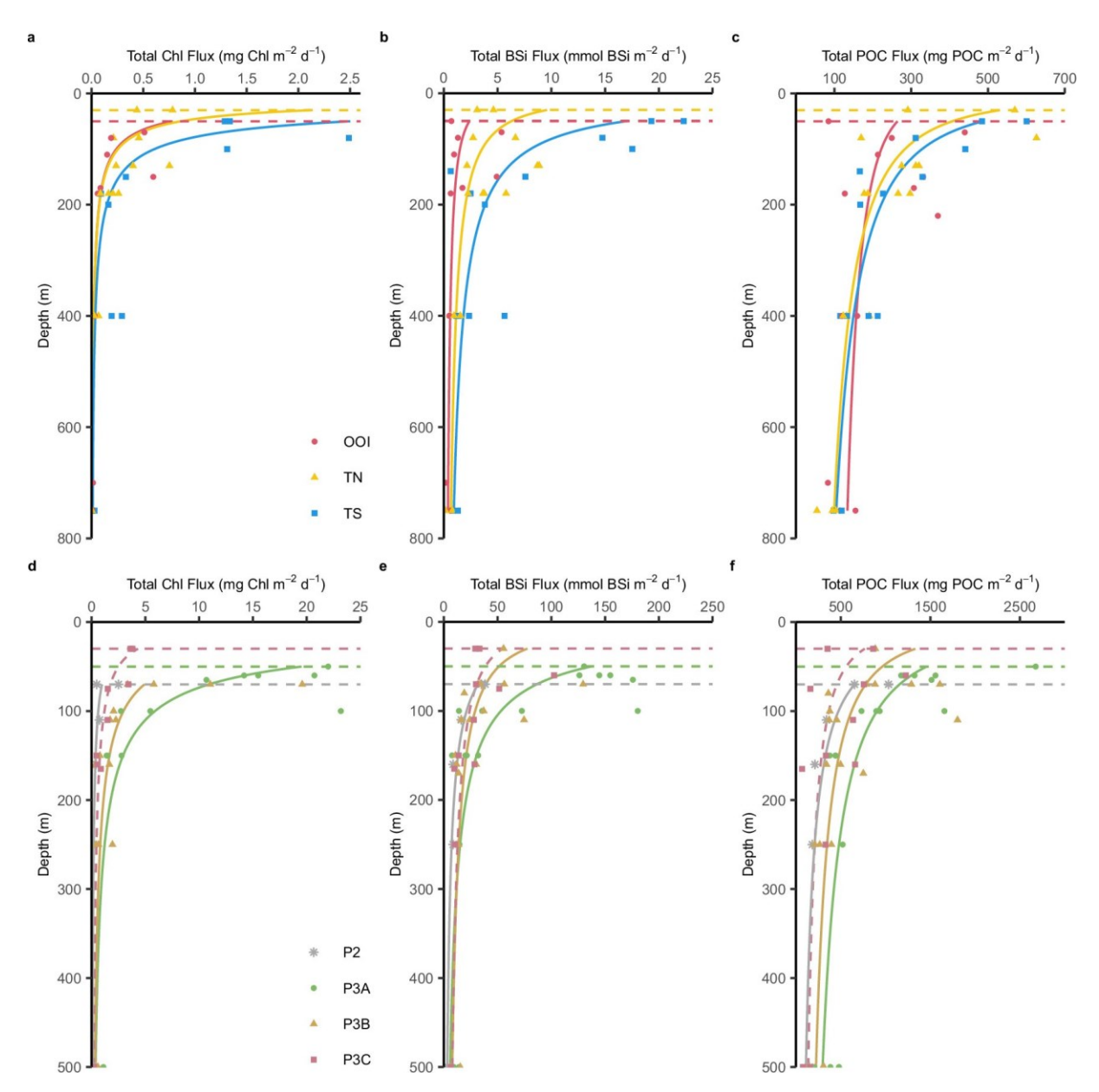


Figure A.2 Total fluxes of Chl, BSi, and POC (a–c respectively) at CUSTARD stations OOI, TN & TS, as well as at COMICS stations P3 and P2 (d–f respectively). Horizontal dashed lines depict the depth of the shallowest MSC deployment (MLD + 10 m) for each profile (OOI, 50 m, TN, 30 m; TS, 50 m; P2, 70 m; P3A, 50 m; P3B, 70 m, P3C, 30 m). For CUSTARD stations (a–c), all occupations of each station have been pooled (OOI, red circles; TN, yellow triangles; TS, blue squares). For COMICS stations (d–f), each occupation of P3 is presented separately (P3A, green circles; P3B, yellow triangles; P3C, red squares) along with P2 control station (grey stars). Flux profiles were calculated by fitting fluxes for all MSC deployments at each to a Martin curve (Martin et al., 1987), starting from z0 for each deployment the shallowest MSC deployment at each station.

A.3 DY111 molar ratios: MSC, SAPS, Niskin CTD measurements

Validation of trends in BSI:POC molar ratios during the CUSTARD project cruise DY111 was carried out primarily through comparison with SAPS and CTD measurements. CTD measurements of BSi and POC were typically only made throughout the upper 200m of the water column, precluding validation of decreasing BSi:POC ratios from this dataset, and so are not discussed in the main text but are instead discussed here.

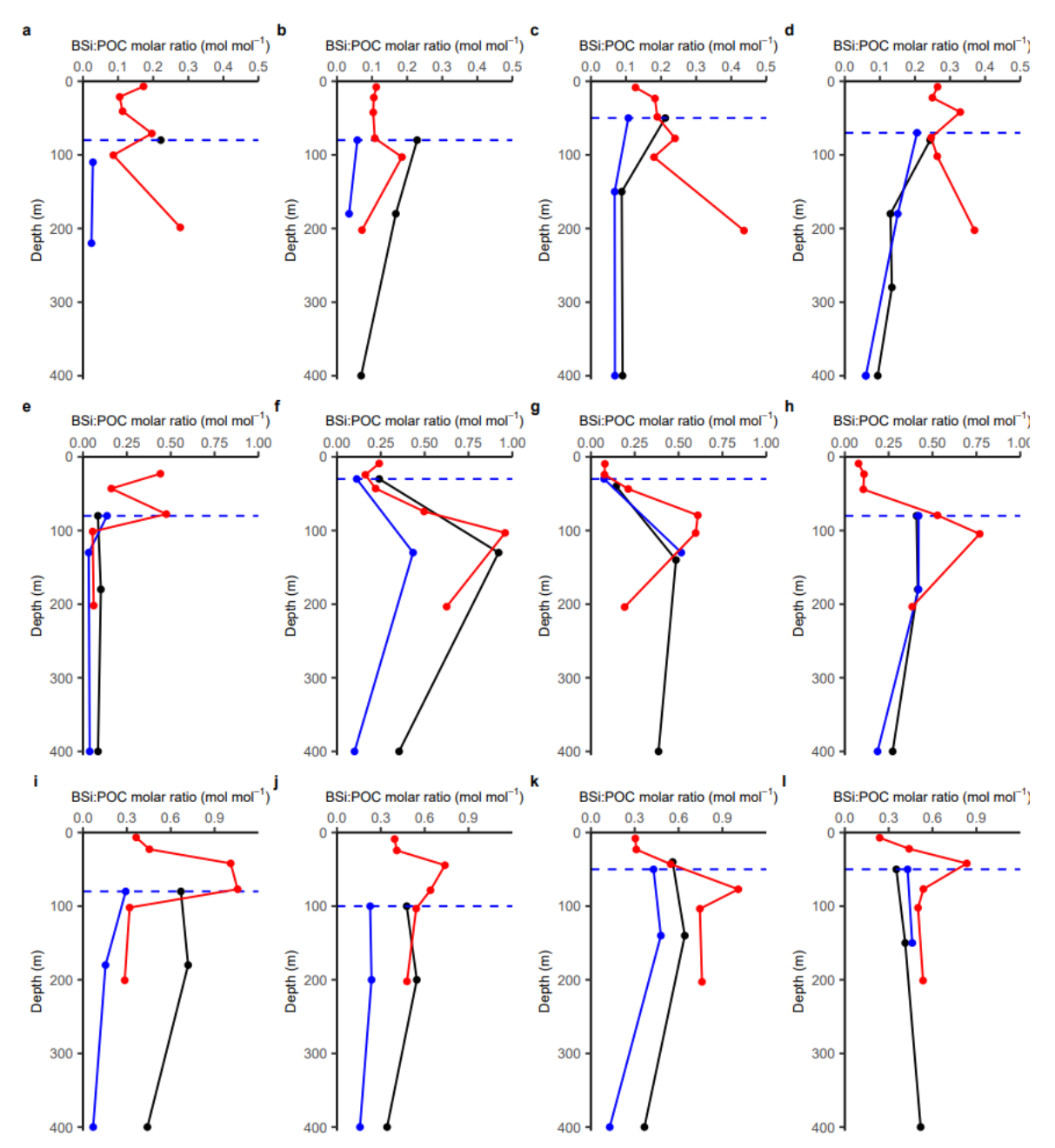


Figure A.3 Molar ratios of BSi:POC in each of the four visits to the northern Pacific station (OOI, a-d), central Pacific station (TN, e-h), and southern Pacific station (TS, i-l) measured from Marine Snow Catchers (black), in situ pumps (blue), and CTD Niskin bottles (red). Blue dashed lines indicate MLD+10 m during each occupation.

MSCs generally displayed lower absolute molar ratios than both SAPS and CTD, but relative changes in BSi:POC ratios with depth were generally congruent at all stations (Figure A.3 a-I).

From the comparisons we can make between MSCs and Niskin measurements in the upper 200m, we MSC molar ratios to fall consistently below those measure in Niskin samples at OOI (Figure A.3 a-d), yet at TN relative changes in molar ratios with depth are mirrored between CTDs and MSCs, generally increasing to an intermediate maximum between 100 m and 200m (Figure A.3 f-h) and then decreasing below this depth. At TS, the higher vertical resolution of CTD measurements meant a peak in molar ratios was observed in Niskin samples but not in SAPS nor MSC samples (Figure A.3 i-l). When taking into account the differences between depths sampled by each method, relative trends once again showed reasonable agreement between all three methods (Figure A.3 i-l).

A.4 Influence of v_{fast} on export efficiencies

In theory, the extreme minimum value of v_{fast} is set by the dimension of the MSC and settling period: material sinking 1.58m that takes the entire two hours to reach the particle tray would be sinking with a velocity of 19 m d⁻¹. However, sinking velocities this low are not only far lower than bloom pulses previously tracked using *in situ* optical data for large backscattering or fluorescing particles (Briggs et al. 2020), but would also require >30 days to sink from 100m to 750m. Given the sharp nature of peaks in production observed at the CUSTARD site, and the degree of remineralization that would be expected over a month of particle sinking through the water column, sinking velocities this low can in some cases result in export efficiencies greater than 100%.

Using a literature value for POC remineralization at $4 \, ^{\circ}$ C (carbon-specific respiration rate of 0.03 d⁻¹) (Iversen and Ploug 2013), we generated a conservative estimate of export fluxes needed to result in our measured fluxes at depth. Rearranging the below equation:

$$F_{750} = F_{export} e^{kt}$$

we arrived at:

$$ln(F_{export}) = ln(F_{750}) + kt$$

where F_{export} back-calculated export flux, F_{750} is measured flux at 700 or 750 m, k the carbon-specific respiration rate (0.03 d⁻¹), t is the time window over which particles sink from 100 m to the measured depth.

Note this estimate is conservative as it represents microbial remineralization only, and remineralization due to zooplankton consumption is thought to dominate remineralization in the Southern Ocean (Belcher et al. 2016b; Cavan et al. 2017a). If we also considered zooplankton remineralization, a greater degree of remineralization would occur during particle sinking and hence higher export fluxes would be required to produce our measured fluxes at depth. Dividing our estimate of back-calculated export efficiency by NPP (Supplementary Data Table S3.2, satellite-derived and using the Vertically Generalised Production Model (Behrenfeld and Falkowski 1997)), we can generate a conservative estimate of export efficiency required if fluxes were to sink as slowly as 20 m d⁻¹ and only experience microbial remineralization.

The table below shows back-calculated export efficiencies. Although some of these export efficiencies fall within the range expected from modelled (15 – 67% at 0 °C (Maiti et al. 2013), redigitized from Figure 2c) and observational measurements in the Southern Ocean (0 – 69% from sediment trap export fluxes; 2-85% from 234^{Th} derived export fluxes) (Maiti et al. 2013), they typically fall towards the upper end of this range, and some export efficiencies exceed 100%. Given that these estimates neglect the important influence of zooplankton remineralisation during transfer to depth, these export efficiencies suggest a v_{fast} higher than 20 m d⁻¹ is necessary. Taken alongside the other lines of evidence discussed in Methods (Thorium-derived bulk sinking velocities, comparison with mixed-layer nutrient budgets derived from nutrient uptake between occupations of each station, previously measured sinking velocities of bloom pulses measured from in situ optical data (Briggs et al. 2020)) we opt for a v_{fast} of 40 m d⁻¹.

Appendix Table A.1 Back-calculated export efficiencies.

Date of flux measurement	Occupation	Depth (m)	Total POC flux	Backcalculated export flux	NPP 1 month	Export efficiency
			(mg m ⁻² d ⁻¹)	(mg m ⁻² d ⁻¹)	Satellite NPP	(%)
					(mg C m ⁻² d ⁻¹)	
14/12/2019	0012	700	83.22	204.7	241.1	84.90253
22/12/2019	0013	750	115.05	305.02	269.9	113.0122
03/01/2020	0014	750	154.98	410.88	267.2	153.7725
20/12/2019	TN2	750	54.68	144.97	479.3	30.24619
29/12/2019	TN3	750	104.42	276.83	599	46.21536
04/01/2020	TN4	750	94.85	251.46	720.3	34.91045
17/12/2019	TS2	750	97.93	259.63	562.1	46.18929

30/12/2019	TS4	750	118.89	315.2	513.1	61.43052

A.5 Location of our study in relation to Fay & McKinley Biomes

Our study region encompasses five biogeochemically independent sites in the Southern Ocean, yet all of these stations fall within the Southern Ocean Subpolar Seasonally Stratified (SO SPSS) mean biome of (Fay and McKinley 2014) (Figure A.4), hereon the "subpolar Southern Ocean". Our sites in the subpolar biome span a broad range of conditions, including areas in the Subantarctic Zone north of the Subantarctic Front (sites OOI, TN), in the Polar Frontal Zone between the Subantartic and Polar Fronts (site TS), and even in the colder waters of the Antarctic Zone (sites P2, P3) due to the northward meander of the Polar Front near South Georgia. We therefore conclude that temporal decoupling of BSi and POC fluxes which we observe is likely representative of the subpolar biome, which covers 39 % the area encompassed by Southern Ocean biomes (mean SO SPSS biome area: 30.6 x 10⁶ km²).

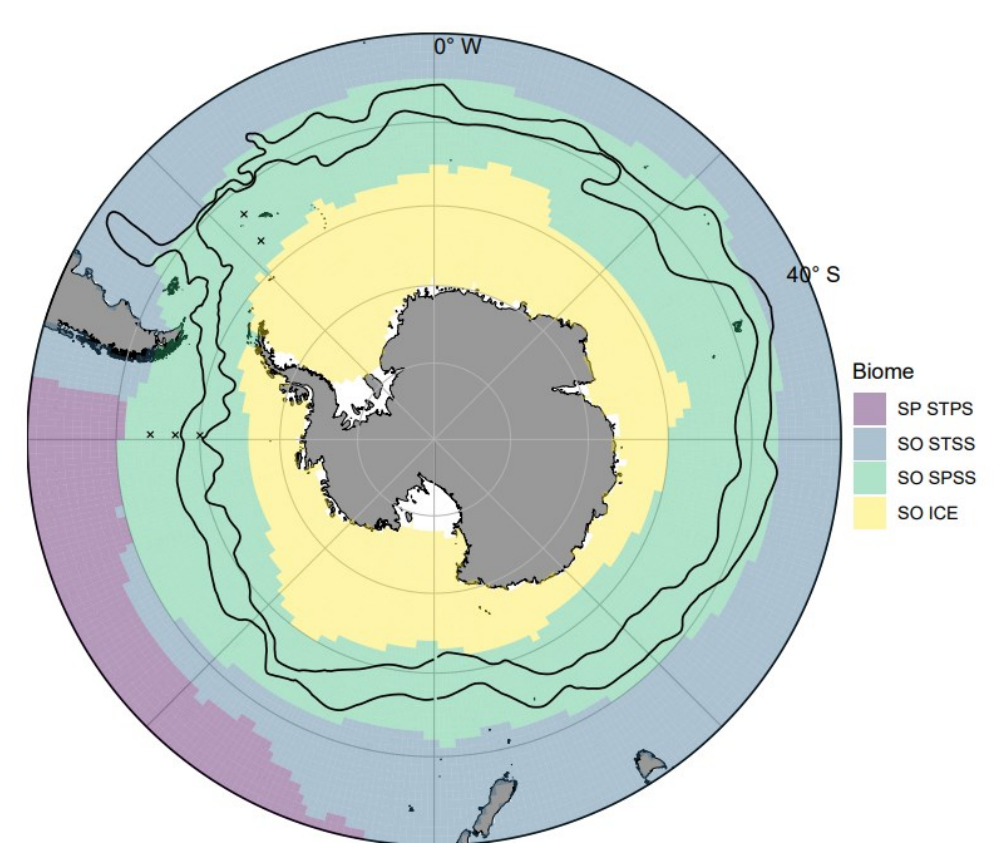


Figure A.4: Location of study sites (black crosses) in relation to Fay & McKinley biomes (South Pacific Subtropical Permanently Stratified (SP STPS), purple; Southern Ocean Subtropical Seasonally Stratified (SO STSS), purple; Southern Ocean Subpolar Seasonally Stratified (SO SPSS), green; Southern Ocean Ice (SO

ICE), yellow). Mean positions of Subantarctic and Polar Fronts (Orsi et al. 1995) are shown by black lines.

As we did not sample the Southern Ocean Ice (SO ICE) biome, we cannot so confidently conclude that our results extend to this region. However, we speculate that preferential attenuation of BSi fluxes to POC fluxes could extend to parts of this region, given that we observed this phenomenon at the Atlantic P3 and P2 stations, both which lie south of the polar front (in the Antarctic Zone). Throughout the course of the study period, phytoplankton standing stocks at these stations were dominated by species such as Fragilariopsis kerguelensis and Eucampia Antarctica (Ainsworth et al. 2023), heavily-silicified species typical of the iron-limited waters south of the polar front throughout much of the Antarctic Zone (Smetacek et al. 2012; Assmy et al. 2013). This observation suggests that even among more heavily ballasted phytoplankton assemblages such as those typical in the ice biome, processes such as buoyancy regulation may act to negate ballast effects, but further sampling of this region is needed to determine whether our findings extend here.

Similarly, our results may extend into the Southern Ocean Subtropical Seasonally Stratified Zone (SO STSS) to some extent, but we cannot conclusively say this without more extensive sampling. The subpolar biome as defined by Fay & McKinley is distinguished from the SO STSS by having a STT of < 8 °C. Whilst the OOI site falls within the mean subpolar biome, SST at the OOI site progressively increased throughout the study period and during the latter occupations exceed 8 °C (OOI3, 8.2 °C; OOI4, 8.7 °C); at these occupations, the OOI site is representative of criteria for the subtropical Southern Ocean rather than the subpolar biome. We cannot determine from these two measurements whether our results extend into a substantial portion of the Subtropical Southern Ocean biome, yet these results suggest the results we observe are not exclusive to waters colder than 8 °C and so could extend into warmer biomes. Preferential transfer of POC through the mesopelagic relative to BSi has not, to our knowledge, been observed previously, yet preferential export of POC relative to BSi has been observed in the Subtropical Southern Ocean and further afield (Thomalla et al. 2008). Processes that we pose decouple BSi and POC fluxes (diatom buoyancy regulation and grazer activity) could act in the both the surface ocean and twilight zone; further high-resolution studies in the subtropical Southern Ocean can determine whether our results are restricted to the subpolar Southern Ocean or observed elsewhere.

A.6 Surface particle back-trajectories

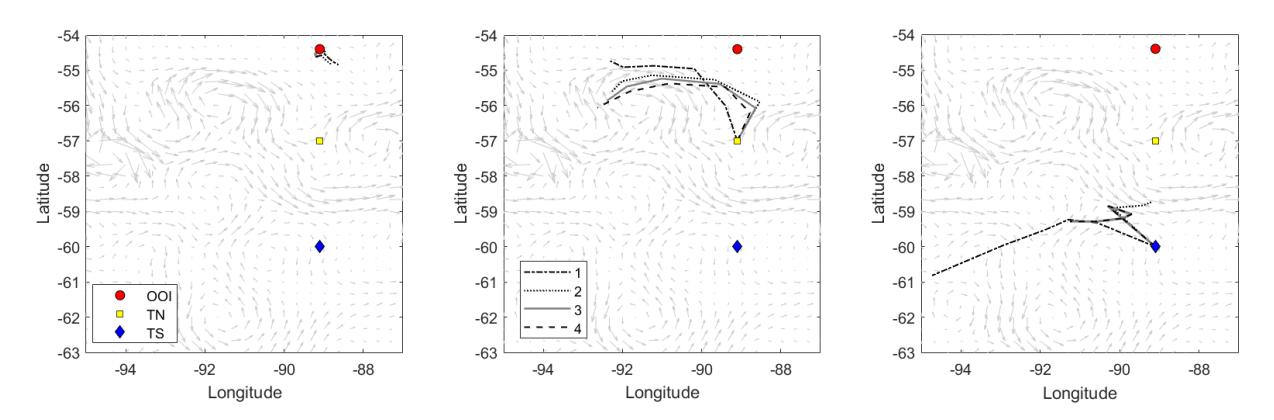


Figure A.5 Surface particle back-trajectories of water masses sampled at each occupation (1-4, line type) of CUSTARD Pacific stations (a) OOI, red circle; (b) TN, yellow square; (c) TS, blue diamond, calculated from satellite derived near-surface ocean current velocities over one month prior to each occupation. Back-trajectories are overlain over a quiver plot depicting *u* and *v* components of near-surface velocities from 20 December 2019. This figure was produced Dr. Chelsey Baker.

A.7 Torres-Valdes et al. sediment trap b-values

All sediment traps South of 40° S in the data complication of Torres Valdés et al. (2014) were used to generate illustrative Southern Ocean "averages" for attenuation coefficients for POC and BSi fluxes in the Southern Ocean. The purpose of this estimate was to visualise the widely accepted dogma and expectation that POC fluxes are typically attenuated more rapidly than BSi fluxes. Attenuation coefficients presented should in no way be taken as true attenuation rates; estimates presented here collate measurements from multiple disparate locations throughout the Southern Ocean (Figure A.6), from various parts of the seasonal cycle, and from different years. As such, many points in both the profile of POC and BSi are in no way connected to measurements elsewhere in the profile.

We opted to calculate attenuation coefficients in this way rather than presenting the commonly used "global" value of Martin et al. (1987) as Martin et al. do not present an attenuation rate for BSi for comparison. As a reference, a recent study compiling *b*-values from the literature south of 60 S observed a median b-value for POC of 0.96 (range: 0.25 – 1.97) (Bach et al. 2023). The median value falls only slightly higher than our illustrative "average", suggesting that whilst not

a true measure of attenuation, our computed *b*-value offers a reasonable estimate by which to compare generalised BSi and POC flux attenuation.

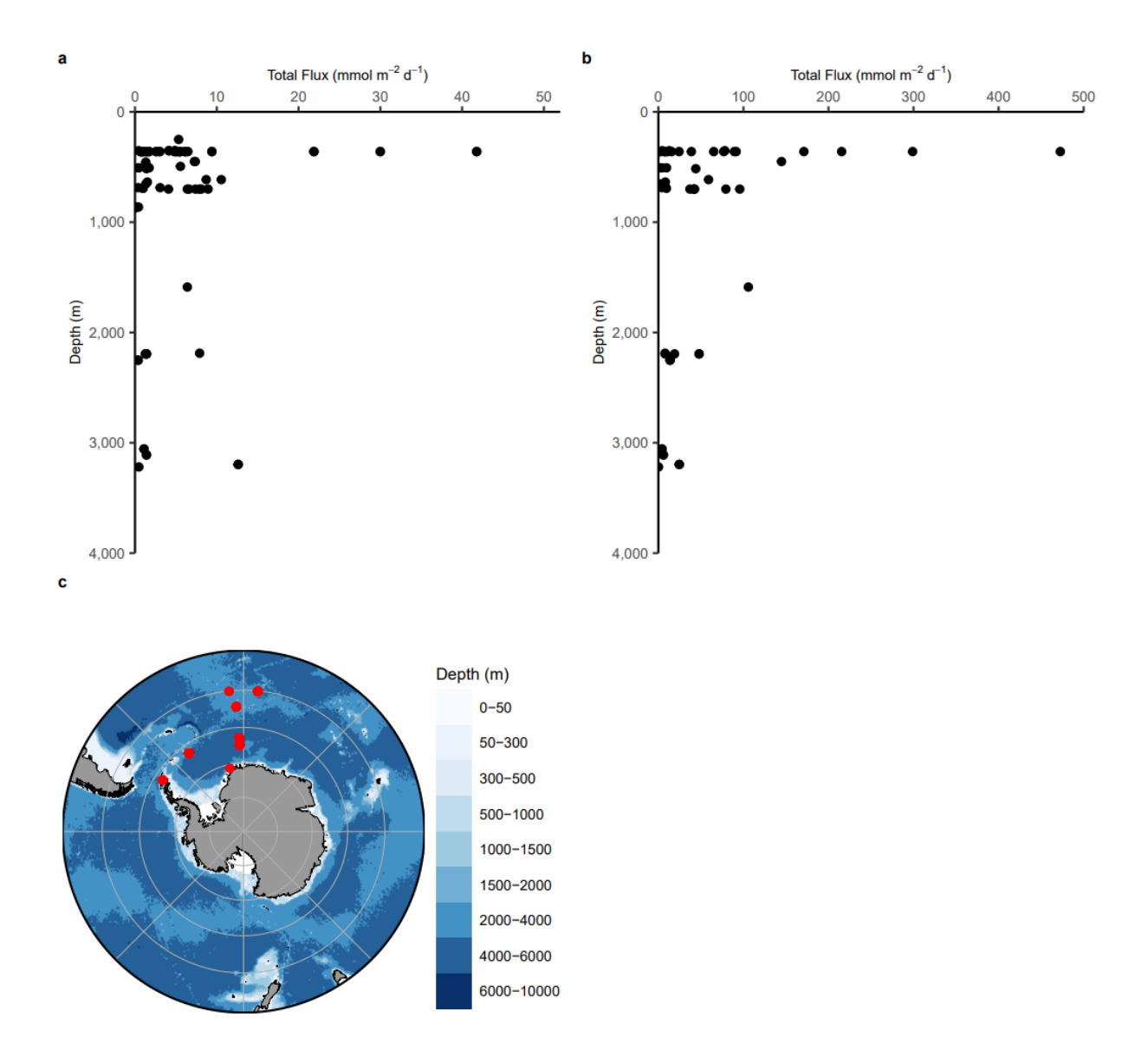


Figure A.6: Fluxes of (a) POC and (b) BSi measured in deep sediment traps south of 40° S from the compilation of (Torres Valdés et al. 2014), used to generate illustrative flux attenuation coefficients for POC and BSi in the Southern Ocean. c) Location of traps from compilation used to generate flux attenuation coefficients.

A.8 BSi:POC particulate molar ratios profiles during the CUSTARD and COMICS projects.

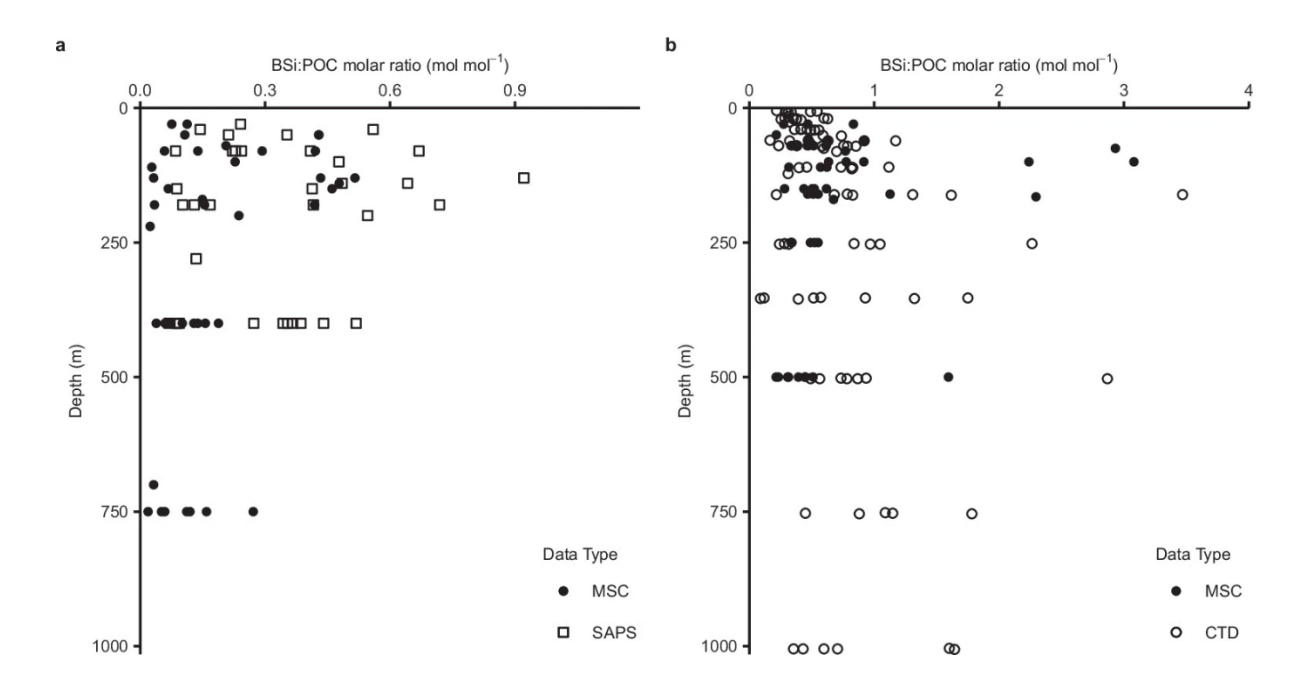


Figure A.7 (a) CUSTARD BSi:POC molar ratios measured from time-zero fraction of MSC deployments down to 750 m (filled circles) and in situ pump deployments (open squares) down to 400 m; (b) COMICS BSi:POC molar ratios measured from time-zero fraction of MSC deployments down to 500 m (filled circles) and CTD deployments (open circles) down to 1000 m.

A.9 Temporal changes to molar ratios during sinking

Increasing BSi:POC ratios of surface communities over time can confound interpretation of vertical profiles. If particles at depth reflect prior, low BSi:POC communities, vertical profiles would appear to suggest preferential loss of BSi with depth even if BSi and POC were transferred in equal measure.

To test whether these temporal changes alone could confound our results, we trace back to the date when our particles at depth should have left surface waters, and compare molar ratios of sinking particles from these dates to those we measured at depth.

Total sinking molar ratios are calculated as the ratio of the sum of slow and fast sinking BSi concentrations to the sum of slow and fast sinking POC concentrations (Supplementary Table S3.3)

At station TS, the molar ratio of total sinking material at 750 m during our final occupation (TS4, 30 Dec 2019) was 0.14 mol mol⁻¹. Using our sinking velocity of 40 m d⁻¹ we can estimate that this material sank from 100 m depth on 14 Dec 2019, in between our first two occupations of the TS station (TS1, 09 Dec 2019; TS2, 17 Dec 2019). The molar ratio of total material sinking from the surface ocean (80 m at TS1, 100 m at TS2) during both of these early occupations was 0.52 mol mol⁻¹, suggesting preferential losses of BSi during transit to 750 m depth at TS4. At 400 m depth during TS4, we also measured a molar ratio of 0.36 mol mol⁻¹ in total sinking material. This material would be expected to have sunk from 80 m on 22 Dec 2019, between our second and third occupations of the TS station (TS2, 17 Dec 2019; TS3, 27 Dec 2019), in which we measured molar ratios of 0.52 mol mol⁻¹ and 0.42 mol mol⁻¹ respectively. Thus, molar ratios at this depth additionally suggests preferential loss of BSi as particles sink to this depth.

At station TN, the molar ratios of total sinking material measured at 750 m during our final occupation (TN4, 05 Jan 2020) was 0.06 mol mol⁻¹. 16 days prior on the 20 Dec 2019, when this material should have sunk from 110 m d⁻¹, we occupied TN for the second time. Our nearest flux measurement to 110 m was at 130 m depth, where me measured a total sinking molar ratio of 0.25 mol mol⁻¹, again necessitating a preferential loss of BSi during sinking. It should be noted that this measurement at 130 m sampled an unusual feature with likely contained diatom resting spores (Le Moigne et al., in review), but measurements at 30 m depth also displayed higher molar ratios than were measured at 750 m in TN4.

At OOI, our deepest MSC analysed in the final occupation (OOI4, 03 Jan 2020) was from 400 m, where we measured a molar ratio 0.05 mol mol⁻¹ in total sinking material. Assuming a sinking velocity of 40 m d⁻¹, we can judge that this material will have sunk through 80 m on 26 Dec 2019. This date falls between our third and fourth occupation of OOI where we measured total sinking molar ratios of 0.19 mol mol⁻¹ at 50 m depth (OOI3, 22 Dec 2019) and 0.11 mol mol⁻¹ at 70 m depth (OOI4, 03 Jan 2020).

Thus, tracing our molar ratios back and comparing to surface value, we consistently observe the need for preferential loss of BSi relative to POC. Since microbial remineralization would be expected to preferentially remineralise POC relative to BSi, this necessitates a mechanism to attenuate BSi fluxes through decreases in sinking velocity, and a means to rapidly transfer POC to depth.

A.10 Projected deep molar ratios and comparison with previous measurements

In the Pacific sector, no deep-sea sediment trap samples that coincided with our study period are available, and so we extrapolate our molar ratios using a range of flux attenuation parameters and compare them to previously measured molar ratios in published literature from the same frontal zones of the Southern Ocean.

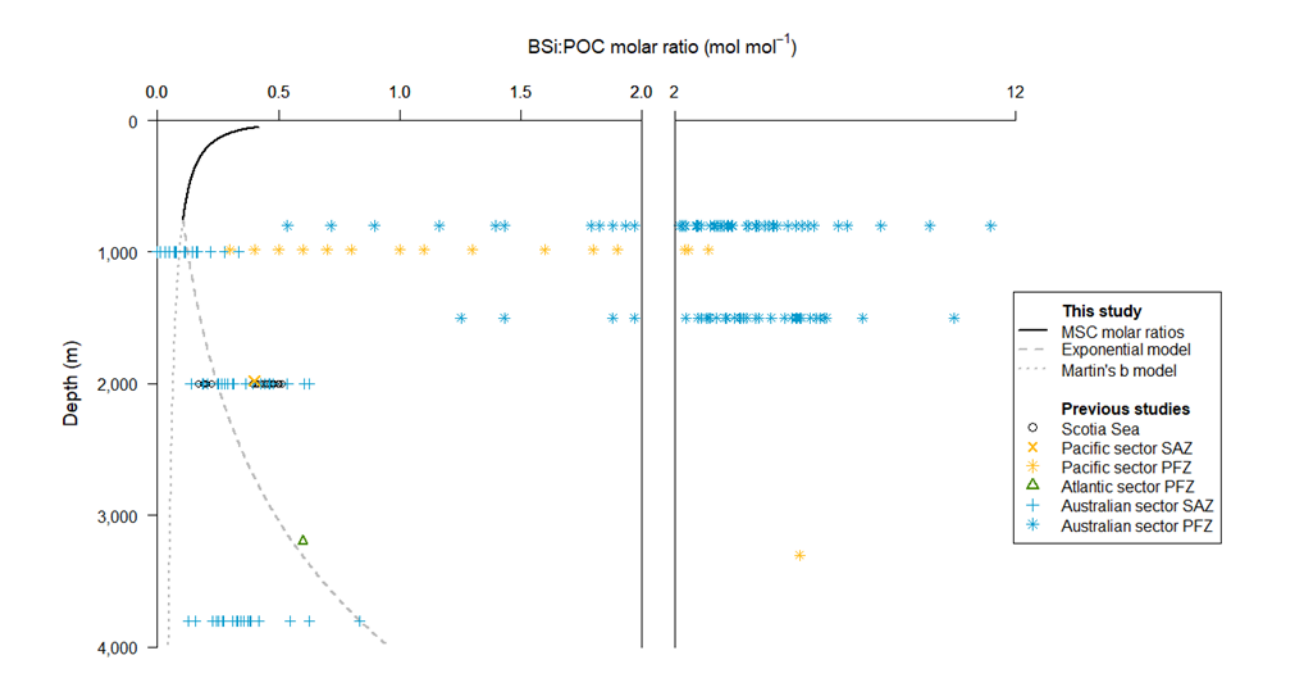
Molar ratios below 750 m at the southern Pacific station were projected both using the "Martin's b" power law curves derived from our MSC measurements in the upper 750 m, and using an exponential fit incorporating literature values for BSi dissolution rates (0.003 d⁻¹) (Tréguer et al. 1989; Bidle et al. 2002) and carbon specific respiration rates (0.03 d⁻¹) (Iversen and Ploug 2013) in diatoms at 4 °C. It should be noted that projecting fluxes from the OOI or TN Pacific stations did not influence whether or not our projections could be reconciled with previous measurements- that is to say, our projections fell towards the lower end, but within the range of previous measurements. We chose to present fluxes from the southern station (TS) as i) TS represented a bloom-forming site (unlike the northern station OOI), enabling comparison to the COMICS station; ii) at central station TN we observed an anomalous particle accumulation layer (Le Moigne et al., in review) and thus the TN site does not represent a good model for comparisons of a "usual" state.

First, we extrapolated molar ratios by applying the Martin's *b* attenuation rates measured in the upper ocean to the deep ocean. These projected ratios fell below even the lowest previous measurements deeper than 1000 m (dotted grey line, Appendix Figure A.8), highlighting the inapplicability of extrapolating attenuation rates derived from the upper ocean to the entire water column (Cael and Bisson 2018) (the majority of flux attenuation is known to occur in the mesopelagic and attenuation in the mesopelagic is faster more rapid than in the deep ocean (Boyd and Trull 2007; Belcher et al. 2016a)).

Next, rather than tune b-values to match our extrapolated fluxes to previous deep-sea measurements, we test whether our fluxes at 750 m depth can be reconciled with deep-sea measurements using accepted literature values for POC remineralization and BSi dissolution in diatom aggregates at 4 °C (carbon-specific respiration rate of 0.03 d⁻¹ (Iversen and Ploug 2013) and a specific dissolution rate of 0.003 d⁻¹ for BSi (Bidle et al. 2002) fluxes; temperatures at 200 m at our study sites range from 2.8 - 5.5 °C). We extrapolate our fluxes below 750 m depth (F) using an exponential fit ($F = F_{750}$ e^{-kz/v}), where F_{750} is flux at 750 m, z is depth below the 750 m reference depth, v is sinking velocity (40 m d⁻¹ for both BSi and POC), and k are the

aforementioned literature rates. Although choice of flux parameterization may have large implications for flux estimates at shallow depths, deep flux estimates generally converge (Cael and Bisson 2018) and so use of the exponential fit should not influence conclusions drawn. Our exponentially projected molar ratios fall within the range of previous measurements, yet some previously measurements in deep sediment traps exceed our projected estimates by an order of magnitude or greater (Appendix Figure A.8).

This large variation in the composition of sinking material may be explained by decoupling of fluxes resulting in different temporal and spatial patterns of transfer efficiency of POC and BSi. Whilst we have observed processes decoupling BSi and POC fluxes to allow efficient POC transfer to depth, BSi has been retained near the surface; other studies observing decoupling in the Southern Ocean have observed thickly-shelled "Si-sinking" species to preferentially export silica (Assmy et al. 2013). This hypothesis is further supported when considering the studies with highest molar ratios. All studies displaying molar ratios >2 mol mol⁻¹ were located in the Polar Frontal Zone of the Australian (Rigual-Hernández et al. 2016) or Pacific (Honjo et al. 2000; Nelson et al. 2002) sectors. Whilst Nelson et al. do not specifically describe diatom species present, Honjo et al. from the similar region describe "well-silicified diatom frustules", and Rigual-Hernandez et al. describe a diatom assemblage dominated by Fragilariopsis kerguelensis, the archetypal Si-sinking species identified by Assmy et al.. Therefore we hold the high BSi:POC measurements to be indicative of a "Si-sinking" phase of BSi:POC decoupling which transfers to depth great quantities of Si through "Si-sinking" species- in contrast to the efficient POC transfer to depth which we observe here, where BSi is not efficiently transferred to the deep ocean- and explaining the discrepancies between these measurements and our modelled molar ratios.



Appendix Figure A.8 Comparison of our projected molar ratios with previous measurements (coloured points). Extrapolating fluxes at 750 m to the deep ocean using the Martin's b model (grey dotted line) derived from the upper ocean (black line) underestimates molar ratios relative to previous measurements. When projecting using an exponential fit, our estimates fall within the range of previously measured values but an order of magnitude lower than some measurements.

A.11 Vfast sensitivity analysis

Appendix Table A.2: b-values and statistical outputs of linear models used to calculate these b-values, for different values of v_{fast} .

Compound	vfast	b	S.E.	p	R ²	n
Chl	20	1.54	0.317	<0.01	0.819	6
	40	1.36	0.47	<0.05	0.6	6
	60	1.25	0.652	0.128	0.347	6
	100	0.968	1.24	0.479	-0.08	6
BSi	20	1.41	0.132	<0.001	0.96	6
	40	1.23	0.134	<0.001	0.943	6
	60	1.16	0.136	<0.01	0.935	6
	100	1.11	0.138	<0.01	0.927	6
	minimised	0.974	0.197	<0.01	0.825	6
POC	20	0.89	0.226	<0.05	0.744	6
	40	0.9	0.211	<0.05	0.773	6
	60	0.9	0.209	<0.05	0.778	6
	100	0.9	0.209	<0.05	0.778	6
	minimised	0.72	0.242	<0.05	0.612	6
	maximised	1.08	0.184	<0.01	0.869	6

Compound	vfast	b	S.E.	p	R ²	n
Chl	20	1.9	0.246	<0.001	0.84	13
	40	1.79	0.254	<0.001	0.802	13
	60	1.73	0.262	<0.001	0.78	13
	100	1.68	0.27	<0.001	0.758	13
BSi	20	1.41	0.212	<0.001	0.732	17
	40	1.38	0.225	<0.001	0.7	17
	60	1.37	0.23	<0.001	0.682	17
	100	1.36	0.235	<0.001	0.67	17
	minimised	1.18	0.237	<0.001	0.596	17
POC	20	0.86	0.078	<0.001	0.875	18
	40	0.74	0.098	<0.001	0.767	18
	60	0.69	0.112	<0.001	0.688	18
	100	0.65	0.126	<0.001	0.596	18
	maximised	0.868	0.099	<0.001	0.817	18
Chl	20	1.5	0.341	<0.001	0.566	15
	40	1.44	0.309	<0.001	0.598	15
	60	1.42	0.302	<0.001	0.603	15
	100	1.41	0.297	<0.001	0.606	15
BSi	20	0.76	0.154	<0.001	0.553	20
	40	0.8	0.157	<0.001	0.567	20
	60	0.81	0.16	<0.001	0.577	20
	100	0.83	0.163	<0.001	0.567	20
	minimised	0.62	0.161	<0.01	0.419	20
POC	20	0.65	0.172	<0.001	0.441	18
	40	0.65	0.159	<0.001	0.458	18

Compound	vfast	b	S.E.	p	R ²	n
	60	0.62	0.16	<0.001	0.483	18
	100	0.65	0.316	<0.05	0.167	19
	minimised	0.48	0.15	<0.01	0.35	18
	maximised	0.76	0.173	<0.001	0.522	18
Chl	20	1.35	0.42	<0.05	0.539	9
	40	1.19	0.237	<0.01	0.752	9
	60	1.07	0.153	<0.001	0.856	9
	100	0.97	0.133	<0.001	0.881	8
BSi	20	0.77	0.21	<0.01	0.557	11
	40	0.71	0.201	<0.008	0.513	11
	60	0.69	0.21	<0.01	0.492	11
	100	0.67	0.211	<0.05	0.472	11
	minimised	0.58	0.202	<0.05	0.418	11
POC	20	0.76	0.292	<0.05	0.348	12
	40	0.66	0.267	<0.05	0.321	12
	60	0.61	0.255	<0.05	0.302	12
	100	0.55	0.247	<0.05	0.267	12
	minimised	0.529	0.269	0.077	0.207	12
	maximised	0.75	0.258	<0.05	0.403	12
Chl	20	1.82	0.29	<0.001	0.82	9
	40	1.71	0.24	<0.001	0.83	11
	60	1.53	0.24	<0.001	0.81	11
	100	1.38	0.25	<0.001	0.76	11
BSi	20	0.87	0.31	<0.05	0.44	10
	40	0.67	0.28	<0.05	0.31	11

Compound	vfast	b	S.E.	р	R ²	n
	60	0.74	0.27	<0.05	0.4	11
	100	0.78	0.26	<0.05	0.45	11
	minimised	0.48	0.28	0.12	0.17	11
POC	20	0.23	0.24	0.34	0	13
	40	0.25	0.17	0.16	0.1	13
	60	0.24	0.15	0.14	0.11	13
	100	0.22	0.14	0.16	0.1	13
	maximised	0.41	0.17	<0.05	0.3	13
Chl	20	1.32	0.24	<0.001	0.68	15
	40	1.76	0.28	<0.001	0.72	17
	60	1.65	0.24	<0.001	0.74	17
	100	1.6	0.24	<0.001	0.73	17
BSi	20	0.7	0.19	<0.01	0.46	16
	40	0.82	0.2	<0.001	0.5	17
	60	0.76	0.18	<0.001	0.51	17
	100	0.72	0.17	<0.001	0.5	17
	minimised	0.63	0.17	<0.01	0.45	17
POC	20	0.23	0.24	0.34	0	13
	40	0.52	0.09	<0.001	0.66	17
	60	0.48	0.1	<0.001	0.59	17
	100	0.45	0.11	<0.001	0.5	17
	maximised	0.62	0.11	<0.001	0.67	17
Chl	20	1.66	0.6	<0.05	0.38	12
	40	2.04	0.4	<0.001	0.67	13
	60	1.92	0.34	<0.001	0.72	13

Compound	vfast	b	S.E.	р	R ²	n
	100	1.88	0.31	<0.001	0.75	13
BSi	20	1.08	0.36	<0.001	0.64	14
	40	1.07	0.24	<0.001	0.59	14
	60	1.07	0.26	<0.001	0.55	14
	100	1.06	0.28	<0.01	0.51	14
	minimised	0.89	0.25	<0.01	0.46	14
POC	20	0.58	0.07	<0.001	0.84	14
	40	0.57	0.08	<0.001	0.79	14
	60	0.57	0.09	<0.001	0.73	14
	100	0.57	0.11	<0.001	0.66	14
	maximised	0.72	0.08	<0.001	0.87	14

Appendix B Patterns of Marine Snow Morphology and Sinking Throughout the Atlantic Ocean

B.1 Appendix Tables

Appendix Table B.1: 24 morphological properties used to create PCA morphospace, as well as their median value in each cluster, transformations applied, and definition of parameter.

Definitions of these morphological features are the standard definition of Zooprocess software, outlined in Gorsky et al. 2010).

Property	Туре	Transformation	Definition
area	Size	log10(trim())	Surface area of the object in square pixels
perim	Size	log10(trim())	The length of the outside boundary of the object
major	Size	log10(trim())	Primary axis of the best fitting ellipse for the object
feret	Size	log10(trim())	Maximum feret diameter, i.e. the longest distance between any two points along the object boundary
fractal	Size	trim()	Fractal dimension of object boundary (Berube and Jebrak, 1999)
skelarea	Size	log10(trim())	Surface area of skeleton in pixels. In a binary image, the skeleton is obtained by repeatedly removing pixels from the edges of objects until they are reduced to the width of a single pixel
mean	Intensity	trim()	Average grey value within the object; sum of the grey values of all pixels in the object divided by the number of pixels
mode	Intensity	trim()	Modal grey value within the object
intden	Intensity	log10(trim())	Integrated density. The sum of the grey values of the pixels in the object (i.e. ¼ Area*Mean)
median	Intensity	trim()	Median grey value within the object
range	Intensity	trim()	Range of grey values
stdev	Structure	trim()	Standard deviation of the grey value used to generate the mean grey value

Property	Туре	Transformation	Definition
skew	Structure	trim()	Skewness of the histogram of grey level values
kurt	Structure	trim()	Kurtosis of the histogram of grey level values
%area	Structure	log1p(trim())	Percentage of object's surface area that is comprised of holes, defined as the background grey level
slope	Structure	trim()	Slope of the grey level normalized cumulative histogram
meanpos	Structure	trim()	(max–mean)/range (of grey values)
cv	Structure	trim()	100*(stdv/mean) (of grey values)
sr	Structure	trim()	100*(stdv/(max-min)) (of grey values)
circ	Shape	trim()	Circularity = (4 * Pi * Area) / Perim2); a value of 1 indicates a perfect circle, a value approaching 0 indicates an increasingly elongated polygon
symetrieh	Shape	log10(trim())	Bilateral horizontal symmetry index
symetriev	Shape	log10(trim())	Bilateral vertical symmetry index
thickr	Shape	log1p(trim())	Thickness Ratio; relation between the maximum thickness of an object and the average thickness of the object excluding the maximum
elongation	Shape	log10(trim())	Major-minor axes

Appendix Table B.2: Environmental parameters fitted to a multiple regression against NMDS ordination coordinates, and how they were derived.

Parameter	Definition
Surface Chlorophyll	Average Chlorophyll concentration from the top 100 m (µg/L) from CTD fluorescence measurements
Latitude	Latitude (°N)
Migrant strength	Night minus Day acoustic backscatter signal strength in the upper 200 m.
Total zooplankton concentration	Total concentration of zooplankton in each depth bin (individuals/L) from UVP image data
Sea surface Temperature (SST)	SST (°C, upper metre of the water column) from CTD measurements.
Particle abundance efficiency	Total abundance efficiency (ratio of particle concentrations between 0-100 m and 100 – 300 m)

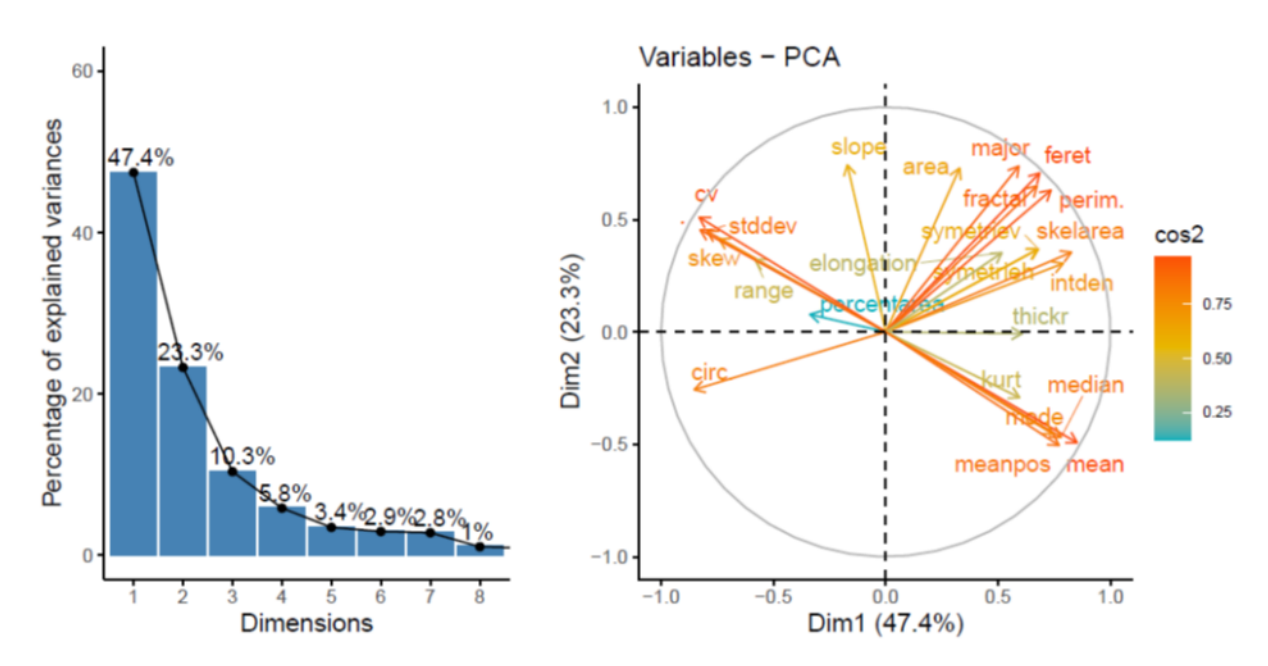
Appendix Table B.3: Outputs from simple and interactive linear models to investigate relationships between mean particle area and/or brightness from each station and the residuals of our T_{100} linear model in Figure 4.

Model call	Term	df	t	p
Residuals ~ Area R² = -0.03 F = 0.000836	Area	25	0.029	0.977
Residuals~Mean R² = 0.33 F = 13.78	Mean	25	-3.713	0.001
Residuals~Area * Mean R² = 0.57 F = 12.47	Area Mean Area*Mean	23	3.929 3.221 -3.847	<0.001 0.004 <0.001

Appendix Table B.4: Depth boundaries for "control", "DVM", and "deep" depth strata identified from ADCP backscatter data in each profile.

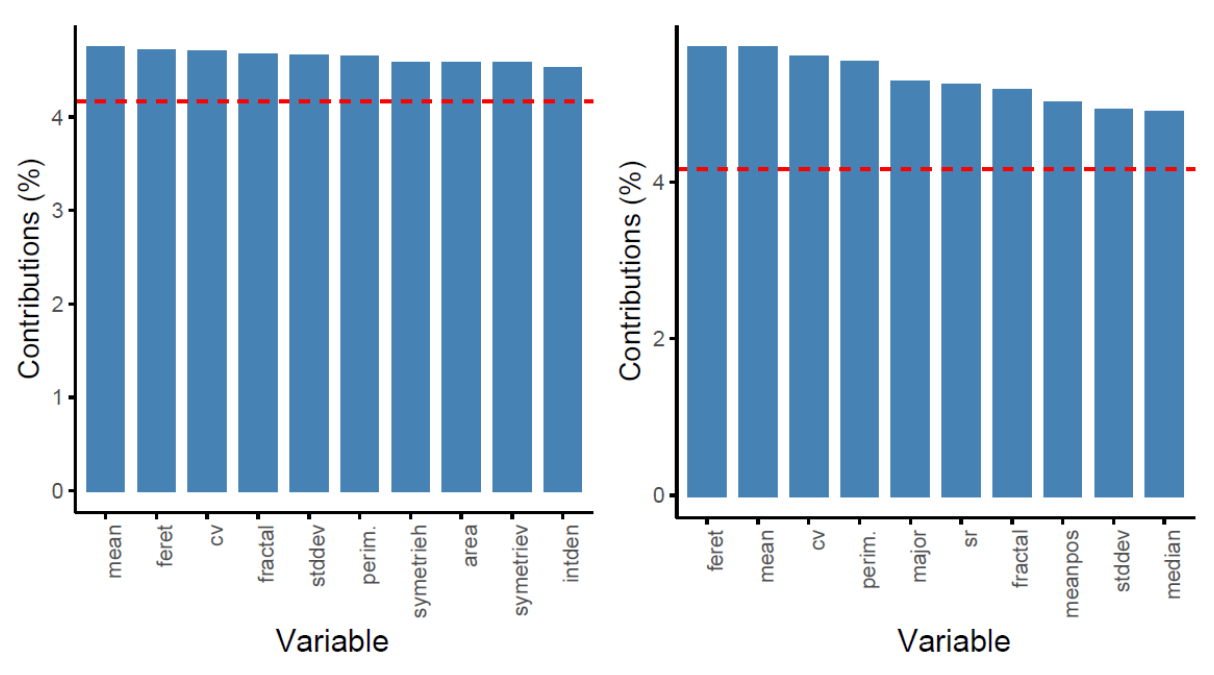
Profile	Date	Control lower	Control higher	DVM lower	DVM higher	Deep lower	Deep higher
1	23/02/2023	260	300	320	340	380	440
2	24/02/2023	300	320	340	400	440	500
3	25/02/2023	280	320	380	420	460	520
4	27/02/2023	280	360	400	440	480	540
5	28/02/2023	260	320	400	440	480	540
6	01/03/2023	280	320	460	500	540	600
7	02/03/2023	400	460	480	520	540	600
8	03/03/2023	400	460	500	540	540	600
9	04/03/2023	380	420	460	520	540	600
10	05/03/2023	380	440	460	520	540	600
11	06/03/2023	400	460	480	540	540	600
12	08/03/2023	300	360	360	400	440	500
13	09/03/2023	360	420	420	460	500	560
14	10/03/2023	360	400	420	460	500	560
15	11/03/2023	300	340	360	420	460	520
16	12/03/2023	300	340	360	420	460	520
17	13/03/2023	280	320	340	400	440	520
18	14/03/2023	280	320	320	360	400	460
19	15/03/2023	280	320	360	400	440	500
20	16/03/2023	280	320	360	420	460	520
21	20/03/2023	320	380	400	460	500	560
22	21/03/2023	380	420	460	500	520	560
23	22/03/2023	300	380	440	480	520	580
24	23/03/2023	320	400	420	460	500	560
25	24/03/2023	320	380	440	500	540	600
26	25/03/2023	280	340	400	440	480	540
27	26/03/2023	260	300	360	400	440	500

B.2 Appendix Figures

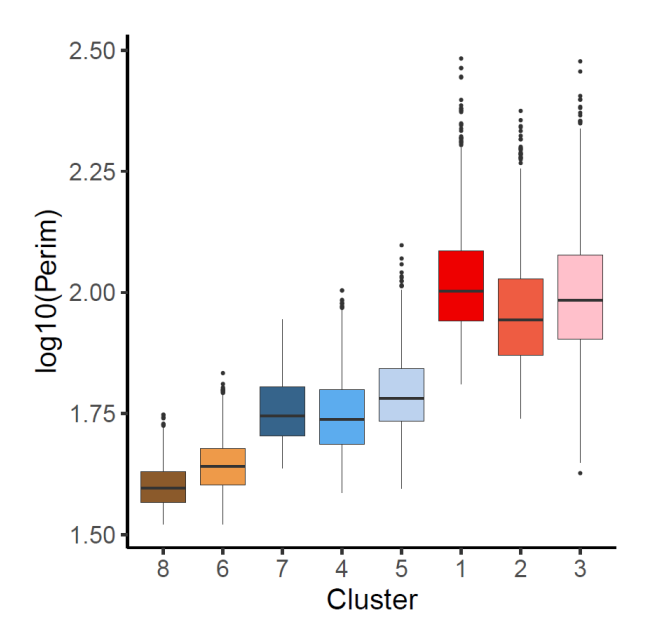


Appendix Figure B.1: Summary of outputs from PCA analysis. (a) Variance explained by each principle component dimension; (b) Variable correlation plot showing correlations between variables and the first two principal component axes.

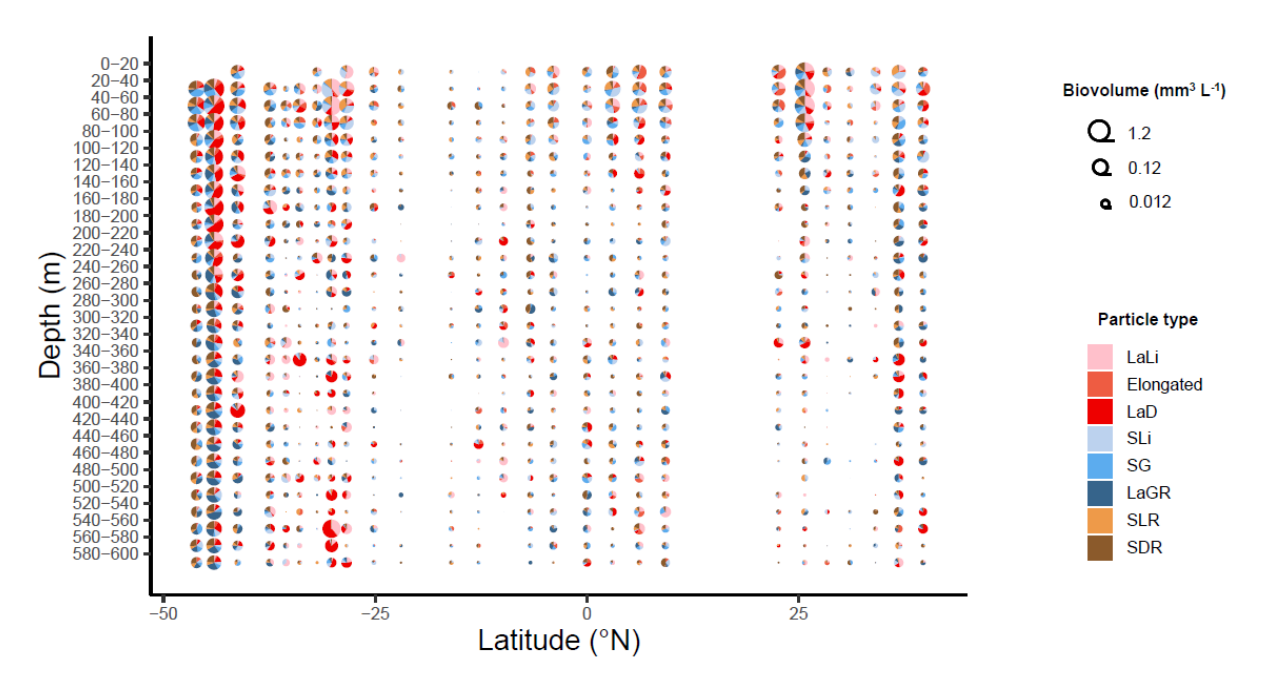
Variables are coloured by square cosine value.



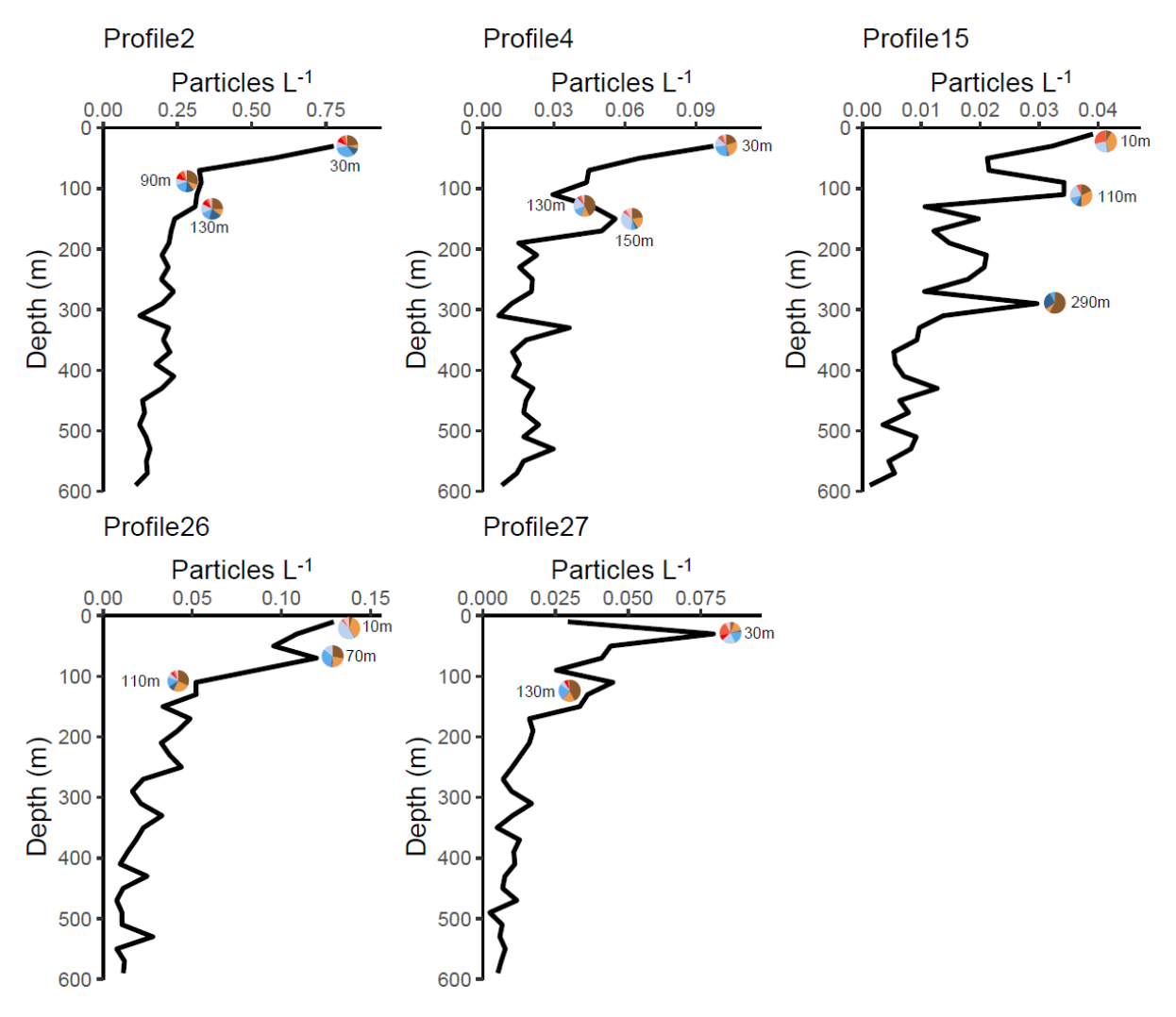
Appendix Figure B.2: The top 10 variables that contribute the most to the variability of (a) all principal component axes and (b) the first two principal component axes.



Appendix Figure B.3: Boxplot showing distributions of log-transformed particle perimeter for each particle cluster. Boxes depict median values, 25th and 75th percentiles. Area is shown as a representative measure of particle size in the main text as it is thought to be more directly linked to particle mass (via estimation of ESD), yet perimeter makes a larger contribution to the component axes (see Figure B.2 above).

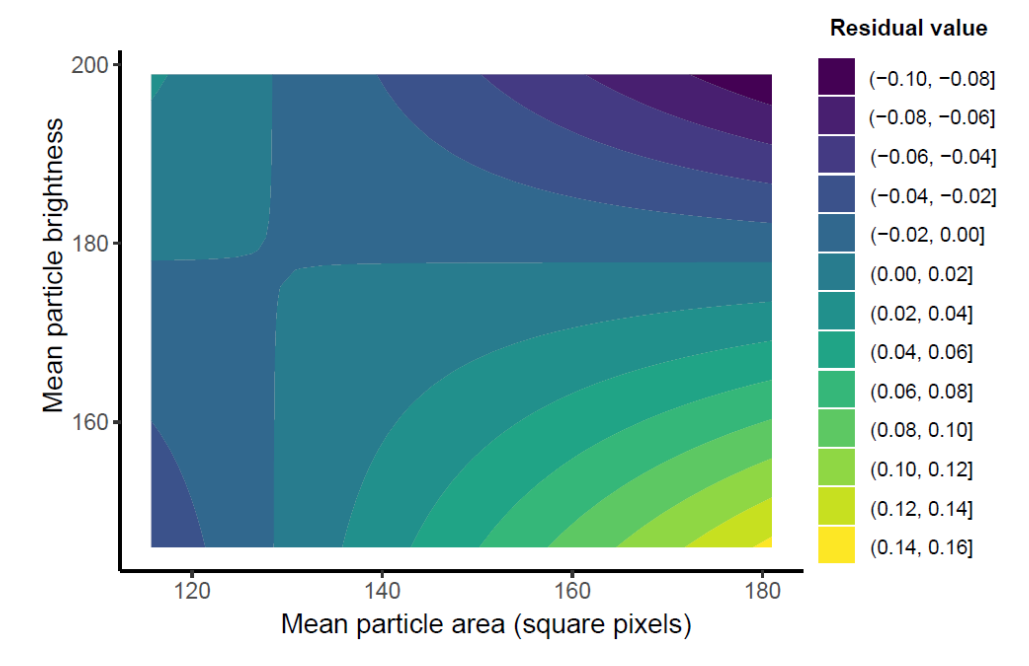


Appendix Figure B.4: Proportions of marine snow morphology biovolume across the entire transect and with depth in 20 m depth bins, with piechart size scaled by the log of particle biovolume concentration within each depth bin.

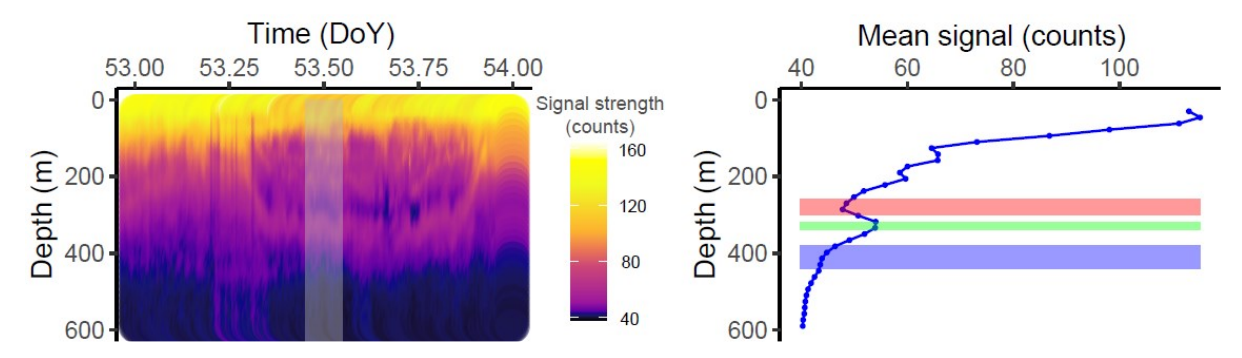


Appendix Figure B.5: Profiles of particle number concentration at the five "high $T_{\rm eff}$ " stations, as defined by residuals in Figure 4. Pie charts show the proportion of number concentration at the depth (z) of maximum particle concentrations, at a depth 100 m below this (z_{100}), and in some plots for any notable peaks in particle concentration, some of which impacted estimates of T_{100} .

Appendix B



Appendix Figure B.6: Contour plot showing interaction between mean particle brightness, mean particle area, and residuals of a linear model fitted between maximum particle concentrations in each profile and particle concentrations 100 m below this depth; higher residuals indicate a more efficient transfer of particles to depth than the covariance weighted mean T_{100} calculated across all stations.



Appendix Figure B.7: Example of the identification of "control" (red rectangle), "DVM" (green rectangle), and "deep" (blue rectangle) depth strata. (a) Shows ADCP signal strength throughout the course of the 54th day of year (DoY), with a light grey box indicating a daytime window over which signal strength was averaged. Mean signal strength from this window is plotted in panel b, with depths of control, DVM, and deep depth strata shown by red, green, and blue boxes respectively.

Appendix B 0-20 · 20-40 · 40-60 · 60-80 · 80-100 · 100-120 · 120-140 · 140-160 · 40-16 ********************************* Biovolume (mm3 L-1) Q 1.2 Q 0.12 140-160 · 160-180 · 180-200 · 200-220 · 220-240 · 240-260 · 260-280 · 300-320 · 320-340 · 340-360 · 360-380 · 400-420 · 400-420 · 400-420 · 160 **Q** 0.012 6 . 6 . Depth (m) Particle type LaLi Elongated 400-420 · 420-440 · 440-460 · LaD SLi 440-460 · 460-480 · 480-500 · 500-520 · 520-540 · 560-580 · 580-600 · SG LaGR • SLR SDR

Latitude (°N)

-25

-50

Appendix Figure B.8: Reproduction of Figure 4.3a, with depth boundaries for "control" (red rectangles), "DVM" (green rectangles), and "deep" (blue rectangles) depth strata overlaid for each profile.

25

Appendix C A Novel Marine Snow Catcher Design

C.1 Supplementary Discussion

C.1.1 Discrepancies in trends between POC and Chlorophyll

Chlorophyll concentrations consistently showed the expected pattern of higher concentrations in the time-zero fraction compared to the top fraction, and higher concentrations for each fraction in Mk1 MSC compared with the equivalent one in Yuki. However, these patterns were not clearly mirrored in POC concentrations, suggesting an additional source of variability influencing POC. We discuss possible sources of this variability in POC concentrations here.

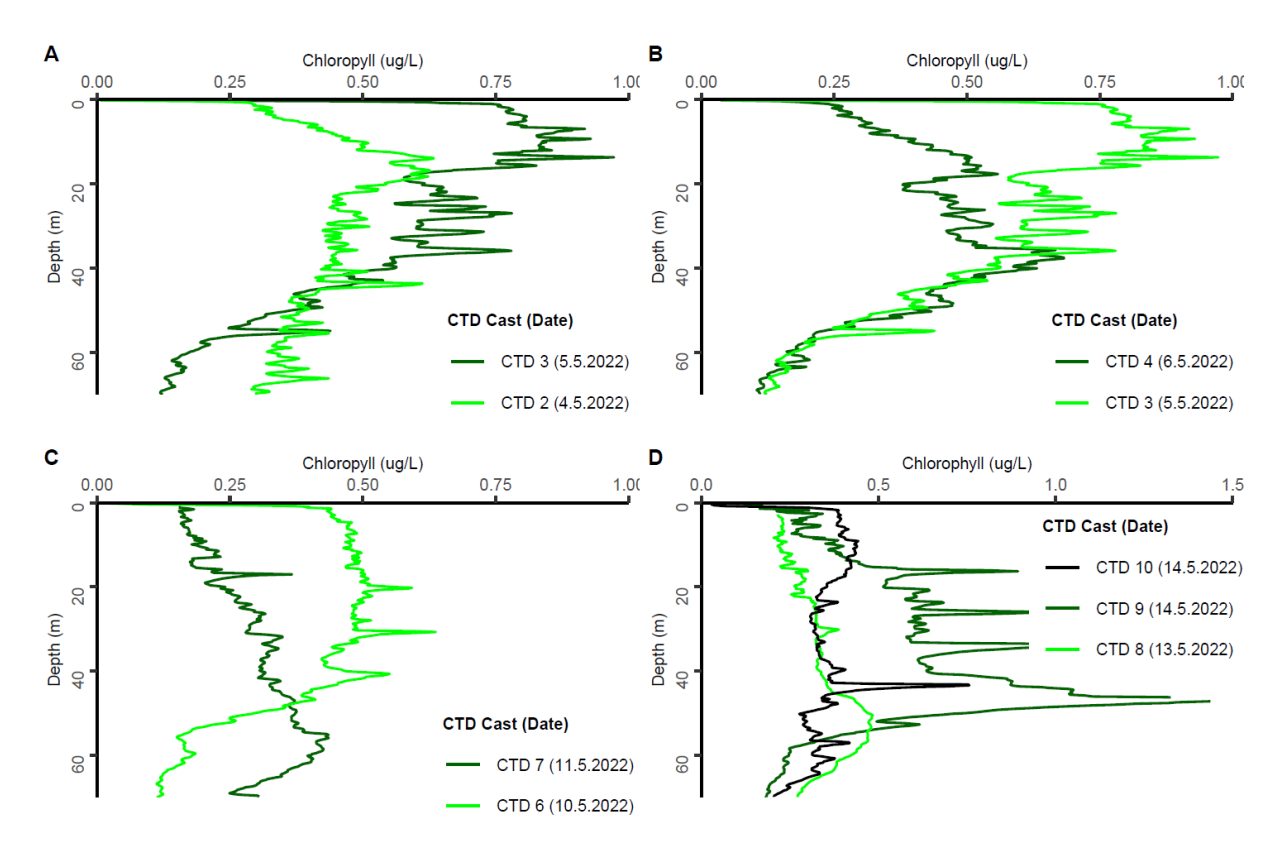
Contamination with organic matter during filtration, storage, and sample collection could introduce uncertainty into measurements (Gardner et al., 2003; Strubinger Sandoval et al., 2022) and result in contamination of POC measurements without observing a similar signal in Chlorophyll measurement. Whilst attempts were made to minimize this effect through combustion of filters prior to use, our open-funnel filtration setup could introduce contamination during filtration, and contamination during filter storage could amount to ~7 ug per filter (Strubinger Sandoval et al., 2022).

Another explanation is ecological: patchiness of rare, POC-rich particles could introduce variable POC concentrations. Patchiness is known to be ubiquitous in the ocean on various scales, yet the role of patchiness in introducing uncertainty to estimates of POC concentrations remain poorly constrained and may be substantial relative to measured concentrations (Bochdansky et al., 2016; Strubinger Sandoval et al., 2022; Wangersky, 1974). We aimed to homogenize samples at every step of the sampling and filtration process, yet - considering that our measurements constitute separate deployments and not replicate measurement from a single deployment - rare large particles could account for differences in paired deployments.

C.1.2 Day-to-day variability in chlorophyll profiles

A number of MSC deployment pairs showed the opposite trend in chlorophyll concentrations than what would be expected if chlorophyll profiles were stable and chlorophyll concentrations decreased below a single maximum. These anomalous results can perhaps be explained by one MSC (e.g. Yuki) per chance sampling a sharp peak in chlorophyll that was not sampled by the other model (e.g. Mk1). Alternatively, the shape of chlorophyll profiles could have changed between deployments. In order to explore this possibility, we investigated the variability in Chl

profiles. From day to day, the magnitude of chlorophyll peaks and shape of profiles often displayed drastic changes (Appendix Figure C.1). Moreover, several subsurface Chlorophyll Maximum Thin Layers (<5m)- often transient (may appear and be lost over timescale of hours, (Durham & Stocker, 2012)) yet widely observed in the Western English Channel and Celtic Sea (Barnett et al., 2019; Sharples et al., 2001)- were present in our CTD Chlorophyll profiles. Together, these features result in chlorophyll profiles far more variable than monotonically decreasing chlorophyll below a subsurface maximum, offering an explanation for anomalous paired deployments.



Appendix Figure C.1: CTD Chlorophyll profiles from successive days. Where CTD chlorophyll profiles are available from back-to-back days, they are shown here: (a) 4th and 5th May; (b) 5th and 6th May; (c) 10th and 11th May; (d) 8th – 10th May. First day in each series is shown in the lightest shade of green, with later days growing increasingly dark.

C.2 Supplementary Methods

C.2.1 Shore-based variability studies

We performed a series of lab-based 'deployments' with reference material to quantify the reproducibility of MSC sampling. The following protocol was carried out for four replicates.0.28 g of olive stone granules (0 – 50 μ m) and 0.55 g cornflour particles we added to a centrifuge tube, which was shaken vigorously to immerse all particles and ensure no particles were no

longer visibly stuck to the bottom of the centrifuge tube. It was noted that the mass reading on the balance for olive stone and cornflour tended to drift by ~ 0.03 g if the mass was left on the balance for more than a few seconds, and so whilst masses were measured as quickly as possible to maintain consistency, absolute masses may vary slightly between replicates and thus constitute a source of error.

The MSC Yuki model was assembled with the base section attached and lid closed and filled with water via a hosepipe. As soon as this process was started, the particle suspension was once again shaken vigorously to resuspend any particles and poured into the MSC body via the open lid. During initial trial runs, particle suspension had been added midway through the MSC filling process, but we found that the hosepipe did not sufficiently generate enough turbulence throughout the entire MSC to homogenously distribute particles. Thus, the protocol was amended to add the suspension at the start of filling, when turbulence could homogenously mix particles throughout a small volume of water, and the remainder of the filling process would simply dilute the concentration within the MSC.

Sampling of the MSC followed established protocols (Giering et al., 2016; Riley et al., 2012). Immediately after the MSC was filled, a 5-L sample was taken from the top tap of the MSC, representing a "time-zero" sample. After a two-hour settling period, a 5-L sample was taken from the top tap of the MSC ("top") sample. The MSC was drained with care taken to drain slowly from the bottom tap to avoid particle resuspension. The base section of the MSC was then removed cautiously (again, to minimize resuspending particles), and 5 L siphoned from the base to provide a "bottom" sample. The remaining water above the 2 L particle collection tray was then siphoned off, before the tray was then removed and its contents poured via a funnel into a 5-L carboy. Olive stone had a slight tendency to stick to the tray after 2 hours more than we have observed with real marine aggregates and particles; the tray was then rinsed with ~25 mL of water to ensure all particles entered the carboy and did not stick to the tray.

It should be noted that it is essential collect a large enough volume for each sample to average out heterogeneity and patchiness of particles within each MSC section, regardless of volume required for analysis. In earlier trial runs of the protocol, since we were running samples through the FlowCam instead of a filtration rig and thus required less sample volume, samples had been taken directly into 50-mL centrifuge tubes. We noticed this was introducing variability into our results due to heterogeneous concentrations within each MSC section (i.e in the base, at the top of the maim MSC body, etc.), but this variability was removed when we sampled larger 5-L volumes representative of the entire MSC section. This source of variability should not be a problem for previous studies since 5-L carboy samples are typical for MSC samples which would be filtered via filtration rig.

Particle concentrations were determined via FlowCam 8400 measurements, which also allowed us not only to determine concentrations but examine whether the olive stone and cornflour had been partitioned during the settling period as we would expect. For each time-zero, top and bottom sample, the 5-L carboy was inverted three times to homogenize particles that had sunk prior to analysis, and 50 mL transferred into a 50-mL centrifuge tube. Once the FlowCam had been set up (Flow rate 0.2 mL min-1, 20 fps, FOV100, 10x objective lens), the centrifuge tube was inverted to suspend particles, and a 1-L sample from the centrifuge tube was run through the FlowCam. For each sample from an MSC replicate, three 1-L samples were run through the FlowCam to provide sample replicates. Tray samples were analyzed exactly as above, only diluted by a factor of 10 or 20 with MilliQ prior to transfer into the 50-mL centrifuge tube in order to avoid clogging the FlowCam with this high concentration sample. Fluxes were then calculated as in Giering et al. (2016).

C.3 Appendix Tables

Table C.1 Table of Chlorophyll a and POC concentrations from Time-zero and Top fractions, and total fluxes of Chlorophyll and Particulate Organic Carbon

Date	MSC Pair	MSC Deployment no.	Yuki/Mk1	Depth (m)	Chlorophyll Tzero concentration (ug L ⁻¹)	Chlorophyll Top concentration (ug L ⁻¹)	Total Chlorophyll Flux (ug m² d¹1)	Particulate Organic Carbon (POC) Tzero concentration (ug L-1)	Particulate Organic Carbon (POC) Top concentration (ug L-1)	Total Particulate Organic Carbon (POC) Flux (mg m² d¹)
04- May	1	1	Yuki	50	0.168	0.135	505.4	20.49	12.76	72.14
04- May	1	2	Mk1	50	0.194	0.177	259.2	8.34	13.67	37.33
05- May	2	3	Yuki	150	0.049	0.047	NA	4.84	5.41	NA
05- May	2	4	Mk1	150	0.044	0.044	NA	5.17	3.56	NA
05- May	3	5	Yuki	50	0.507	0.479	425.5	13.73	13.6	71.32
05- May	3	6	Mk1	50	0.660	0.565	884.7	21.77	20.38	134.47
06- May	4	10	Mk1	50	0.612	0.587	NA	22.05	19.56	NA
06- May	4	11	Yuki	50	0.426	0.350	NA	11.03	10.24	NA

Date	MSC Pair	MSC Deployment no.	Yuki/Mk1	Depth (m)	Chlorophyll Tzero concentration (ug L ⁻¹)	Chlorophyll Top concentration (ug L ⁻¹)	Total Chlorophyll Flux (ug m² d¹1)	Particulate Organic Carbon (POC) Tzero concentration (ug L-1)	Particulate Organic Carbon (POC) Top concentration (ug L-1)	Total Particulate Organic Carbon (POC) Flux (mg m² d¹)
06- May	5	12	Mk1	150	0.038	0.020	NA	3.12	2.79	NA
06- May	5	14	Yuki	150	0.023	0.016	NA	2.55	3.14	NA
07- May	6	16	Mk1	50	0.592	0.553	668.1	13.48	16.83	47.85
07- May	6	18	Yuki	50	0.393	0.394	825.6	11.4	16.31	92.46
09- May	7	19	Mk1	50	0.267	0.230	891.9	13.03	11.31	73.52
09- May	7	20	Yuki	50	0.340	0.316	1421.7	15.17	15.72	572.99
10- May	8	26	Mk1	50	0.228	0.203	NA	8.8	9.67	93.47
10- May	8	28	Yuki	50	0.405	0.388	NA	14.18	9.12	121.29
10- May	9	28	Yuki	50	0.405	0.388	1014.4	14.18	9.12	121.29
10- May	9	29	Mk1	50	0.456	0.435	1099.7	28.45	14.78	375.57

Table C.2 Particle counts and concentrations in MSC fractions, as well as calculated slow-sinking and fast-sinking concentrations and fluxes, and total fluxes

MSC trial number	MSC Fraction	Sample Replicate no.	Vol measured (mL)	FlowCam count	FlowCam concentration (particles mL ⁻¹)	Dilution factor	Sample concentration (particles mL ⁻¹)	Replicate average (particles L ⁻¹)	Replicate SD (particles L ⁻¹)	Slow sinking concentration (Particles L ⁻¹)	Fast sinking concentration (Particles L ⁻¹)	Slow sinking flux (Particles m ⁻² d ⁻¹)	Fast sinking flux (Particles m ⁻ ² d ⁻¹)	Total sinking flux (Particles m- ² d ⁻¹)
1	Tzero	1	1	562	562	1	562	594000	33045.42	14007.02	176244.7	2.66E+08	7049789030	7315922363
1	Tzero	2	1	592	592	1	592							
1	Tzero	3	1	628	628	1	628							
1	Тор	1	1	307	307	1	307	274333.3	32020.83					
1	Тор	2	1	273	273	1	273							
1	Тор	3	1	243	243	1	243							
1	Bottomsiphon	1	1	375	375	1	375	440666.7	57239.26					
1	Bottomsiphon	2	1	480	480	1	480							
1	Bottomsiphon	3	1	467	467	1	467							
1	Tray	1	1	1886	1886	4	7544	8794667	1083847					
1	Tray	2	1	938	938	10	9380							
1	Tray	3	1	946	946	10	9460							
2	Tzero	1	NA	NA	NA	NA	NA	NA	NA	-9628.07	121793.2	-1.8E+08	4871729958	4688796624
2	Tzero	2	NA	NA	NA	NA	NA							
2	Tzero	3	NA	NA	NA	NA	NA							

MSC trial number	MSC Fraction	Sample Replicate no.	Vol measured (mL)	FlowCam count	FlowCam concentration (particles mL ⁻¹)	Dilution factor	Sample concentration (particles mL ⁻¹) 661	Replicate average (particles L ⁻¹)	Replicate SD (particles L-1)	Slow sinking concentration (Particles L ⁻¹)	Fast sinking concentration (Particles L ⁻¹)	Slow sinking flux (Particles m² d¹)	Fast sinking flux (Particles m ⁻ ² d ⁻¹)	Total sinking flux (Particles m- ² d ⁻¹)
2	Тор	3	1	662 661	662 661	1	662 661							
2	Bottomsiphon	1	1	569	569	1	569	547000	44305.76					
2		3	1	576 496	576 496	1	576 496	1						
2	Tray	1	1	606	606	10	6060	6320000	305068.3					
2	Tray	2	1	626	626	10	6260							
2	Tray	3	1	338	338	20	6760							
2	Tray	4	1	310	310	20	6200							
3	Tzero	1	1	781	781	1	781	781333.3	15502.69	-912.281	198417.7	-1.7E+07	7936708861	7919375527
3	Tzero	2	1	797	797	1	797							
3	Tzero	3	1	766	766	1	766							
3	Тор	1	1	531	531	1	531	712500	138064					
3	Тор	2	1	679	679	1	679							
3	Тор	3	1	818	818	1	818							
3	Тор	4	1	822	822	1	822							
3	Bottomsiphon	1	1	679	679	1	679	701666.7	20526.41					

MSC	MSC Fraction	Sample	Vol	FlowCam	FlowCam	Dilution	Sample	Replicate	Replicate	Slow sinking	Fast sinking	Slow	Fast sinking	Total sinking
trial		Replicate	measured	count	concentration	factor	concentration	average	SD	concentration	concentration	sinking	flux	flux
number		no.	(mL)		(particles mL ⁻¹)		(particles mL ⁻¹)	(particles L ⁻¹)	(particles	(Particles L ⁻¹)	(Particles L ⁻¹)	flux	(Particles m ⁻	(Particles m-
									L-1)			(Particles	² d ⁻¹)	² d ⁻¹)
												m ⁻² d ⁻¹)		
3	Bottomsiphon	2	1	719	719	1	719							
3	Bottomsiphon	3	1	707	707	1	707							
3	Tray	1	1	524	524	20	10480	10106667	325781.1					
3	Tray	2	1	498	498	20	9960							
3	Tray	3	1	494	494	20	9880							
4	Tzero	1	1	699	699	1	699	692666.7	43844.42	673.6842	198347.4	12800000	7933895921	7946695921
4	Tzero	2	1	733	733	1	733							
4	Tzero	3	1	646	646	1	646							
4	Тор	1	1	511	511	1	511	517000	8717.798					
4	Тор	2	1	527	527	1	527							
4	Тор	3	1	513	513	1	513							
4	Bottomsiphon	1	1	489	489	1	489	525000	38742.74					
4	Bottomsiphon	2	1	520	520	1	520							
4	Bottomsiphon	3	1	566	566	1	566							
4	Tray	1	1	522	522	20	10440	9926667	453578.4					
4	Tray	2	1	488	488	20	9760							
4	Tray	3	1	479	479	20	9580							

Accardo, A., Laxenaire, R., Baudena, A., Speich, S., Kiko, R. and Stemmann, L. 2024. Massive and localized export of selected marine snow types at eddy edges in the South Atlantic Ocean. Available at: https://egusphere.copernicus.org/preprints/2024/egusphere-2024-1558/ [Accessed: 14 February 2025].

Ainsworth, J., Poulton, A.J., Lohan, M.C., Stinchcombe, M.C., Lough, A.J.M. and Moore, C.M. 2023. Iron cycling during the decline of a South Georgia diatom bloom. *Deep-Sea Research Part II: Topical Studies in Oceanography* 208. doi: 10.1016/j.dsr2.2023.105269.

Alan Turing Institute Data Study Group team. 2022. Data Study Group Final Report: Centre for Environment, Fisheries and Aquaculture Science. Zenodo.

https://doi.org/10.5281/zenodo.6799166

Alldredge, A. 1998. The carbon, nitrogen and mass content of marine snow as a function of aggregate size. *Deep Sea Research Part I: Oceanographic Research Papers* 45(4–5), pp. 529–541. doi: 10.1016/S0967-0637(97)00048-4.

Alldredge, A.L. and Gotschalk, C. 1988. In situ settling behavior of marine snow'. *Limnology and Oceanography* 33(3), pp. 339–374. doi: https://doi.org/10.4319/lo.1988.33.3.0339.

Alldredge, A.L., Granata, T.C., Gotschalk, C.C. and Dickey, T.D. 1990. The physical strength of marine snow and its implications for particle disaggregation in the ocean. *Limnology and Oceanography* 35(7), pp. 1415–1428. Available at:

https://onlinelibrary.wiley.com/doi/full/10.4319/lo.1990.35.7.1415 [Accessed: 18 February 2025].

Alldredge, A.L. and Silver, M.W. 1988. Characteristics, dynamics and significance of marine snow. *Progress in Oceanography* 20(1), pp. 41–82. doi: 10.1016/0079-6611(88)90053-5.

Anderson, T.R., Gentleman, W.C., Cael, B.B., Hirschi, J.J.M., Eastwood, R.L. and Mayor, D.J. 2023. Proliferating particle surface area via microbial decay has profound consequences for remineralisation rate: a new approach to modelling the degradation of sinking detritus in the ocean. *Biogeochemistry* 164(2), pp. 335–347. Available at:

https://link.springer.com/article/10.1007/s10533-023-01055-6 [Accessed: 24 June 2024].

Armstrong, R.A., Lee, C., Hedges, J.I., Honjo, S. and Wakeham, S.G. 2001. A new, mechanistic model for organic carbon fluxes in the ocean based on the quantitative association of POC with

ballast minerals. *Deep Sea Research Part II: Topical Studies in Oceanography* 49(1–3), pp. 219–236. doi: 10.1016/S0967-0645(01)00101-1.

Arrieta, J., Jeanneret, R., Roig, P. and Tuval, I. 2020. On the fate of sinking diatoms: the transport of active buoyancy-regulating cells in the ocean. *Philosophical Transactions of the Royal Society A* 378(2179). Available at: https://royalsocietypublishing.org/doi/10.1098/rsta.2019.0529 [Accessed: 16 January 2023].

Arteaga, L., Haëntjens, N., Boss, E., Johnson, K.S. and Sarmiento, J.L. 2018. Assessment of Export Efficiency Equations in the Southern Ocean Applied to Satellite-Based Net Primary Production. *Journal of Geophysical Research: Oceans* 123(4), pp. 2945–2964. Available at: https://onlinelibrary.wiley.com/doi/full/10.1002/2018JC013787 [Accessed: 15 March 2024].

Assmy, P. et al. 2013. Thick-shelled, grazer-protected diatoms decouple ocean carbon and silicon cycles in the iron-limited Antarctic Circumpolar Current. *Proceedings of the National Academy of Sciences of the United States of America* 110(51), pp. 20633–20638. Available at: https://www.pnas.org/doi/abs/10.1073/pnas.1309345110 [Accessed: 13 April 2023].

Atkinson, A., Schmidt, K., Fielding, S., Kawaguchi, S. and Geissler, P.A. 2012. Variable food absorption by Antarctic krill: Relationships between diet, egestion rate and the composition and sinking rates of their fecal pellets. *Deep Sea Research Part II: Topical Studies in Oceanography* 59–60, pp. 147–158. doi: 10.1016/J.DSR2.2011.06.008.

Aumont, O., Ethé, C., Tagliabue, A., Bopp, L. and Gehlen, M. 2015. PISCES-v2: An ocean biogeochemical model for carbon and ecosystem studies. *Geoscientific Model Development* 8(8), pp. 2465–2513. doi: 10.5194/GMD-8-2465-2015.

Bach, L.T. et al. 2019. The Influence of Plankton Community Structure on Sinking Velocity and Remineralization Rate of Marine Aggregates. *Global Biogeochemical Cycles* 33(8), pp. 971–994. Available at: https://onlinelibrary.wiley.com/doi/full/10.1029/2019GB006256 [Accessed: 20 February 2022].

Bach, L.T. et al. 2023. Identifying the Most (Cost-)Efficient Regions for CO2 Removal With Iron Fertilization in the Southern Ocean. *Global Biogeochemical Cycles* 37(11), p. e2023GB007754. Available at: https://onlinelibrary.wiley.com/doi/full/10.1029/2023GB007754 [Accessed: 10 January 2024].

Bacon, M.P., Spencer, D.W. and Brewer, P.G. 1976. 210Pb/226Ra and 210Po/210Pb disequilibria in seawater and suspended particulate matter. *Earth and Planetary Science Letters* 32(2), pp. 277–296. doi: 10.1016/0012-821X(76)90068-6.

Baker, C.A. et al. 2017. Slow-sinking particulate organic carbon in the Atlantic Ocean: Magnitude, flux, and potential controls. *Global Biogeochemical Cycles* 31(7), pp. 1051–1065. Available at: https://onlinelibrary.wiley.com/doi/full/10.1002/2017GB005638 [Accessed: 3 June 2024].

Barnett, M. L., Kemp, A. E. S., Hickman, A. E., & Purdie, D. A. (2019). Shelf sea subsurface chlorophyll maximum thin layers have a distinct phytoplankton community structure.

Continental Shelf Research, 174, 140–157. https://doi.org/10.1016/J.CSR.2018.12.007

Baumann, M.S., Moran, S.B., Lomas, M.W., Kelly, R.P. and Bell, D.W. 2013. Seasonal decoupling of particulate organic carbon export and net primary production in relation to sea-ice at the shelf break of the eastern Bering Sea: Implications for off-shelf carbon export. *Journal of Geophysical Research: Oceans* 118(10), pp. 5504–5522. doi: 10.1002/JGRC.20366.

Baumas, C.M.J. et al. 2024. A novel method to sample individual marine snow particles for downstream molecular analyses. *Limnology and Oceanography: Methods* 22(1), pp. 34–46. Available at: https://onlinelibrary.wiley.com/doi/full/10.1002/lom3.10590 [Accessed: 28 January 2025].

Behrenfeld, M.J. et al. 2005. Carbon-based ocean productivity and phytoplankton physiology from space. *Global Biogeochemical Cycles* 19(1), pp. 1–14. Available at: https://onlinelibrary.wiley.com/doi/full/10.1029/2004GB002299 [Accessed: 12 June 2024].

Behrenfeld, M.J. and Falkowski, P.G. 1997. Photosynthetic rates derived from satellite-based chlorophyll concentration. *Limnology and Oceanography* 42(1), pp. 1–20. Available at: https://onlinelibrary.wiley.com/doi/full/10.4319/lo.1997.42.1.0001 [Accessed: 21 December 2022].

Belcher, A. et al. 2016a. Depth-resolved particle-associated microbial respiration in the northeast Atlantic. *Biogeosciences* 13, pp. 4927–4943. Available at: www.biogeosciences.net/13/4927/2016/ [Accessed: 22 February 2024].

Belcher, A., Iversen, M., Manno, C., Henson, S.A., Tarling, G.A. and Sanders, R. 2016b. The role of particle associated microbes in remineralization of fecal pellets in the upper mesopelagic of the Scotia Sea, Antarctica. *Limnology and Oceanography* 61(3), pp. 1049–1064. doi: 10.1002/LNO.10269.

Belcher, A., Manno, C., Ward, P., Henson, S.A., Sanders, R. and Tarling, G.A. 2017. Copepod faecal pellet transfer through the meso- and bathypelagic layers in the Southern Ocean in spring. *Biogeosciences* 14(6), pp. 1511–1525. doi: 10.5194/BG-14-1511-2017.

Bendtsen, J., Hilligsøe, K.M., Hansen, J.L.S. and Richardson, K. 2015. Analysis of remineralisation, lability, temperature sensitivity and structural composition of organic matter from the upper ocean. *Progress in Oceanography* 130, pp. 125–145. doi: 10.1016/J.POCEAN.2014.10.009.

Beucher, C., Tréguer, P., Corvaisier, R., Hapette, A.M. and Elskens, M. 2004. Production and dissolution of biosilica, and changing microphytoplankton dominance in the Bay of Brest (France). *Marine Ecology Progress Series* 267, pp. 57–69. doi: 10.3354/MEPS267057.

Bianchi, D., Stock, C., Galbraith, E.D. and Sarmiento, J.L., 2013. Diel vertical migration: Ecological controls and impacts on the biological pump in a one-dimensional ocean model. *Global Biogeochemical Cycles*, 27(2), pp.478-491.

Bidle, K.D., Manganelli, M. and Azam, F. 2002. Regulation of oceanic silicon and carbon preservation by temperature control on bacteria. *Science* 298(5600), pp. 1980–1984. Available at: https://www.science.org/doi/10.1126/science.1076076 [Accessed: 9 June 2023].

Billett, D.S.M., Lampitt, R.S., Rice, A.L. and Mantoura, R.F.C. 1983. Seasonal sedimentation of phytoplankton to the deep-sea benthos. *Nature 1983 302:5908* 302(5908), pp. 520–522. Available at: https://www.nature.com/articles/302520a0 [Accessed: 12 June 2024].

Bochdansky, A. B., Clouse, M. A., & Herndl, G. J. (2016). Dragon kings of the deep sea: marine particles deviate markedly from the common number-size spectrum. *Scientific Reports* 2016 6:1, 6(1), 1–7. https://doi.org/10.1038/srep22633

Boyd, P.W., Claustre, H., Levy, M., Siegel, D.A. and Weber, T. 2019. Multi-faceted particle pumps drive carbon sequestration in the ocean. *Nature* 568(7752), pp. 327–335. doi: 10.1038/s41586-019-1098-2.

Boyd, P.W. and Trull, T.W. 2007. Understanding the export of biogenic particles in oceanic waters: Is there consensus? *Progress in Oceanography* 72(4), pp. 276–312. doi: 10.1016/J.POCEAN.2006.10.007.

Bressac, M., Laurenceau-Cornec, E.C., Kennedy, F., Santoro, A.E., Paul, N.L., Briggs, N., Carvalho, F. and Boyd, P.W., 2024. Decoding drivers of carbon flux attenuation in the oceanic biological pump. *Nature*, 633(8030), pp.587-593.

Briggs, N., Dall'Olmo, G. and Claustre, H. 2020. Major role of particle fragmentation in regulating biological sequestration of CO2 by the oceans. *Science* 367(6479), pp. 791–793. Available at: https://www.science.org/doi/10.1126/science.aay1790 [Accessed: 16 January 2023].

Briggs, N., Perry, M.J., Cetinić, I., Lee, C., D'Asaro, E., Gray, A.M. and Rehm, E. 2011. High-resolution observations of aggregate flux during a sub-polar North Atlantic spring bloom. *Deep-Sea Research Part I: Oceanographic Research Papers* 58(10), pp. 1031–1039. doi: 10.1016/j.dsr.2011.07.007.

Brown, L., Sanders, R. and Savidge, G. 2006. Relative mineralisation of C and Si from biogenic particulate matter in the upper water column during the North East Atlantic diatom bloom in spring 2001. *Journal of Marine Systems* 63(1–2), pp. 79–90. doi: 10.1016/J.JMARSYS.2006.03.001.

Buesseler, K.O. et al. 2006. An assessment of particulate organic carbon to thorium-234 ratios in the ocean and their impact on the application of 234Th as a POC flux proxy. *Marine Chemistry* 100(3–4), pp. 213–233. doi: 10.1016/J.MARCHEM.2005.10.013.

Buesseler, K.O. et al. 2007a. An assessment of the use of sediment traps for estimating upper ocean particle fluxes. *Journal of Marine Research* 65(3), pp. 345–416. doi: 10.1357/002224007781567621.

Buesseler, K.O. et al. 2007b. Revisiting carbon flux through the ocean's twilight zone. *Science* 316(5824), pp. 567–570. Available at: https://www.science.org/doi/10.1126/science.1137959 [Accessed: 17 June 2024].

Buesseler, K.O. et al. 2008. Particle fluxes associated with mesoscale eddies in the Sargasso Sea. *Deep Sea Research Part II: Topical Studies in Oceanography* 55(10–13), pp. 1426–1444. doi: 10.1016/J.DSR2.2008.02.007.

Buesseler, K.O., Bacon, M.P., Kirk Cochran, J. and Livingston, H.D. 1992. Carbon and nitrogen export during the JGOFS North Atlantic Bloom experiment estimated from 234Th: 238U disequilibria. *Deep Sea Research Part A, Oceanographic Research Papers* 39(7–8), pp. 1115–1137. doi: 10.1016/0198-0149(92)90060-7.

Buesseler, K.O. and Boyd, P.W. 2009. Shedding light on processes that control particle export and flux attenuation in the twilight zone of the open ocean. *Limnology and Oceanography* 54(4), pp. 1210–1232. Available at: https://onlinelibrary.wiley.com/doi/full/10.4319/lo.2009.54.4.1210 [Accessed: 19 May 2023].

Buesseler, K.O., Boyd, P.W., Black, E.E. and Siegel, D.A. 2020. Metrics that matter for assessing the ocean biological carbon pump. *Proceedings of the National Academy of Sciences* 117(18), pp. 9679–9687. doi: 10.1073/pnas.1918114117/-/DCSupplemental.

Buesseler, K.O., Steinberg, D.K., Michaels, A.F., Johnson, R.J., Andrews, J.E., Valdes, J.R. and Price, J.F. 2000. A comparison of the quantity and composition of material caught in a neutrally buoyant versus surface-tethered sediment trap. *Deep Sea Research Part I: Oceanographic Research Papers* 47(2), pp. 277–294. doi: 10.1016/S0967-0637(99)00056-4.

Burd, A.B. and Jackson, G.A. 2009. Particle Aggregation.

https://doi.org/10.1146/annurev.marine.010908.163904 1, pp. 65–90. Available at: https://www.annualreviews.org/doi/abs/10.1146/annurev.marine.010908.163904 [Accessed: 2 January 2024].

Cabré, A., Marinov, I. and Leung, S. 2015. Consistent global responses of marine ecosystems to future climate change across the IPCC AR5 earth system models. *Climate Dynamics* 45(5–6), pp. 1253–1280. Available at: https://link.springer.com/article/10.1007/s00382-014-2374-3 [Accessed: 19 February 2024].

Cael, B.B. et al. 2021a. Open Ocean Particle Flux Variability From Surface to Seafloor.

Geophysical Research Letters 48(9), p. e2021GL092895. Available at:

https://onlinelibrary.wiley.com/doi/full/10.1029/2021GL092895 [Accessed: 6 February 2024].

Cael, B.B. and Bisson, K. 2018. Particle flux parameterizations: Quantitative and mechanistic similarities and differences. *Frontiers in Marine Science* 5(OCT). doi: 10.3389/fmars.2018.00395.

Cael, B.B., Cavan, E.L. and Britten, G.L. 2021b. Reconciling the Size-Dependence of Marine Particle Sinking Speed. *Geophysical Research Letters* 48(5), p. e2020GL091771. Available at: https://onlinelibrary.wiley.com/doi/full/10.1029/2020GL091771 [Accessed: 7 March 2022].

Calvin, M. and Benson, A.A. 1948. The path of carbon in photosynthesis. *Science* 107(2784), pp. 476–480. Available at: https://www.science.org/doi/10.1126/science.107.2784.476 [Accessed: 19 March 2024].

Canadell, J.G. et al. 2023. Global Carbon and Other Biogeochemical Cycles and Feedbacks. In: *Climate Change 2021 – The Physical Science Basis*. Cambridge University Press, pp. 673–816. doi: 10.1017/9781009157896.007.

Cavan, E.L. et al. 2019. The importance of Antarctic krill in biogeochemical cycles. *Nature communications*, 10(1), p.4742.

Cavan, E.L., Kawaguchi, S. and Boyd, P.W., 2021. Implications for the mesopelagic microbial gardening hypothesis as determined by experimental fragmentation of Antarctic krill fecal pellets. *Ecology and evolution*, 11(2), pp.1023-1036.

Cavan, E.L., Henson, S.A., Belcher, A. and Sanders, R. 2017a. Role of zooplankton in determining the efficiency of the biological carbon pump. *Biogeosciences* 14(1), pp. 177–186. doi: 10.5194/BG-14-177-2017.

Cavan, E.L., Le Moigne, F.A., Poulton, A.J., Tarling, G.A., Ward, P., Daniels, C.J., Fragoso, G.M. and Sanders, R.J., 2015. Attenuation of particulate organic carbon flux in the Scotia Sea, Southern Ocean, is controlled by zooplankton fecal pellets. Geophysical Research Letters, 42(3), pp.821-830.

Cavan, E.L., Trimmer, M., Shelley, F. and Sanders, R. 2017b. Remineralization of particulate organic carbon in an ocean oxygen minimum zone. *Nature Communications 2017 8:1* 8(1), pp. 1–9. Available at: https://www.nature.com/articles/ncomms14847 [Accessed: 19 July 2023].

Ceballos Romero, E. et al. 2024. On the assessment of sinking particle fluxes from in situ particle size distributions. Available at: https://eartharxiv.org/repository/view/8228/ [Accessed: 13 February 2025].

Ceballos-Romero, E., De Soto, F., Le Moigne, F.A.C., García-Tenorio, R. and Villa-Alfageme, M. 2018. 234Th-Derived Particle Fluxes and Seasonal Variability: When Is the SS Assumption Reliable? Insights From a Novel Approach for Carbon Flux Simulation. *Geophysical Research Letters* 45(24), pp. 13,414-13,426. Available at:

https://onlinelibrary.wiley.com/doi/full/10.1029/2018GL079968 [Accessed: 1 February 2025].

Cetinić, I. et al. 2012. Particulate organic carbon and inherent optical properties during 2008 North Atlantic Bloom Experiment. *Journal of Geophysical Research* 117(C6), p. 6028. Available at: http://osprey.bcodmo.

Ciais, P., Sabine, C., Bala, G., Bopp, L., Brovkin, V. and et al. 2013. *Carbon and Other Biogeochemical Cycles*. *Climate Change 2013: The Physical Science Basis*. *Contribution of Working Group I to the Fifth Assessment Report of the Intergovernmental Panel on Climate Change*. C. Available at:

https://www.climatechange2013.org/images/report/WG1AR5_Chapter06_FINAL.pdf [Accessed: 19 March 2024].

Cook, K.B. et al. 2023. Carbon budgets of Scotia Sea mesopelagic zooplankton and micronekton communities during austral spring. *Deep Sea Research Part II: Topical Studies in Oceanography* 210, p. 105296. doi: 10.1016/J.DSR2.2023.105296.

Cram, J.A. et al. 2022. Slow Particle Remineralization, Rather Than Suppressed Disaggregation, Drives Efficient Flux Transfer Through the Eastern Tropical North Pacific Oxygen Deficient Zone.

Global Biogeochemical Cycles 36(1), p. e2021GB007080. Available at:

https://onlinelibrary.wiley.com/doi/full/10.1029/2021GB007080 [Accessed: 15 February 2025].

Dall'Olmo, G., Dingle, J., Polimene, L., Brewin, R.J. and Claustre, H., 2016. Substantial energy input to the mesopelagic ecosystem from the seasonal mixed-layer pump. *Nature Geoscience*, 9(11), pp.820-823.

Dekshenieks, M. M., Donaghay, P. L., Sullivan, J. M., Rines, J. E. B., Osborn, T. R., & Twardowski, M. S. (2001). Temporal and spatial occurrence of thin phytoplankton layers in relation to physical processes. *Marine Ecology Progress Series*, *223*, 61–71. https://doi.org/10.3354/MEPS223061

DeMaster, D.J., 2002. The accumulation and cycling of biogenic silica in the Southern Ocean: revisiting the marine silica budget. *Deep Sea Research Part II: Topical Studies in Oceanography*, 49(16), pp.3155-3167.

Deng, W., Cruz, B.N. and Neuer, S., 2016. Effects of nutrient limitation on cell growth, TEP production and aggregate formation of marine Synechococcus. *Aquatic Microbial Ecology*, 78(1), pp.39-49.

Devries, T. 2022. The Ocean Carbon Cycle. https://doi.org/10.1146/annurev-environ-120920-11130747, pp. 317–341. Available at:

https://www.annualreviews.org/doi/abs/10.1146/annurev-environ-120920-111307 [Accessed: 27 February 2024].

Devries, T., Primeau, F. and Deutsch, C. 2012. The sequestration efficiency of the biological pump. *Geophysical Research Letters* 39(13). doi: 10.1029/2012GL051963.

Diercks, A.-R. and Asper, V.L. 1997. In situ settling speeds of marine snow aggregates below the mixed layer: Black Sea and Gulf of Mexico. *Deep Sea Research Part I: Oceanographic Research Papers* 44(3), pp. 385–398. Available at:

https://www.sciencedirect.com/science/article/pii/S0967063796001045.

Dilling, L. and Alldredge, A.L. 2000. Fragmentation of marine snow by swimming macrozooplankton: A new process impacting carbon cycling in the sea. *Deep Sea Research Part I: Oceanographic Research Papers* 47(7), pp. 1227–1245. doi: 10.1016/S0967-0637(99)00105-3.

Doney, S.C. et al. 2024. Observational and Numerical Modeling Constraints on the Global Ocean Biological Carbon Pump. *Global Biogeochemical Cycles* 38(7), p. e2024GB008156. Available at: https://onlinelibrary.wiley.com/doi/full/10.1029/2024GB008156 [Accessed: 11 September 2024].

Ducklow, H.W., Steinberg, D.K. and Buesseler, K.O., 2001. Upper ocean carbon export and the biological pump. *Oceanography*, 14(4), pp.50-58.

Duret, M.T., Lampitt, R.S. and Lam, P. 2019. Prokaryotic niche partitioning between suspended and sinking marine particles. *Environmental Microbiology Reports* 11(3), pp. 386–400. Available at: https://onlinelibrary.wiley.com/doi/full/10.1111/1758-2229.12692 [Accessed: 13 June 2023].

Durham, W. M., & Stocker, R. (2012). Thin phytoplankton layers: characteristics, mechanisms, and consequences. *Annual Review of Marine Science*, 4, 177–207. https://doi.org/10.1146/ANNUREV-MARINE-120710-100957

Durkin, C.A., Buesseler, K.O., Cetinić, I., Estapa, M.L., Kelly, R.P. and Omand, M. 2021. A Visual Tour of Carbon Export by Sinking Particles. *Global Biogeochemical Cycles* 35(10), p. e2021GB006985. Available at: https://onlinelibrary.wiley.com/doi/full/10.1029/2021GB006985 [Accessed: 14 August 2024].

Engel, A. and Schartau, M. 1999. Influence of transparent exopolymer particles (TEP) on sinking velocity of Nitzschia closterium aggregates. *Marine Ecology Progress Series* 182, pp. 69–76. Available at: https://www.int-res.com/abstracts/meps/v182/p69-76/ [Accessed: 22 February 2022].

Engel, A., Szlosek, J., Abramson, L., Liu, Z. and Lee, C. 2009. Investigating the effect of ballasting by CaCO3 in Emiliania huxleyi: I. Formation, settling velocities and physical properties of aggregates. *Deep Sea Research Part II: Topical Studies in Oceanography* 56(18), pp. 1396–1407. doi: 10.1016/J.DSR2.2008.11.027.

Estapa, M.L., Feen, M.L. and Breves, E. 2019. Direct Observations of Biological Carbon Export From Profiling Floats in the Subtropical North Atlantic. *Global Biogeochemical Cycles* 33(3), pp. 282–300. Available at: https://onlinelibrary.wiley.com/doi/full/10.1029/2018GB006098 [Accessed: 17 June 2024].

Falkowski, P. et al. 2000. The global carbon cycle: A test of our knowledge of earth as a system. Science 290(5490), pp. 291–296. Available at:

https://www.science.org/doi/10.1126/science.290.5490.291 [Accessed: 27 February 2024].

Fan, G. et al. 2020. Southern Ocean carbon export efficiency in relation to temperature and primary productivity. *Scientific Reports 2020 10:1* 10(1), pp. 1–11. Available at: https://www.nature.com/articles/s41598-020-70417-z [Accessed: 15 December 2022].

Fay, A.R. and McKinley, G.A. 2014. Global open-ocean biomes: Mean and temporal variability. Earth System Science Data 6(2), pp. 273–284. doi: 10.5194/ESSD-6-273-2014.

Fender, C.K., Kelly, T.B., Guidi, L., Ohman, M.D., Smith, M.C. and Stukel, M.R. 2019. Investigating Particle Size-Flux Relationships and the Biological Pump Across a Range of Plankton Ecosystem States From Coastal to Oligotrophic. *Frontiers in Marine Science* 6, p. 462997. Available at: www.frontiersin.org [Accessed: 15 February 2025].

Flintrop, C.M., Rogge, A., Miksch, S., Thiele, S., Waite, A.M. and Iversen, M.H. 2018. Embedding and slicing of intact in situ collected marine snow. *Limnology and Oceanography: Methods* 16(6), pp. 339–355. Available at: https://onlinelibrary.wiley.com/doi/full/10.1002/lom3.10251 [Accessed: 28 January 2025].

Francois, R., Honjo, S., Krishfield, R. and Manganini, S. 2002. Factors controlling the flux of organic carbon to the bathypelagic zone of the ocean. *Global Biogeochemical Cycles* 16(4), pp. 34-1-34–20. doi: 10.1029/2001GB001722.

Fukuda, H. and Koike, I., 2000. Feeding currents of particle-attached nanoflagellates a novel mechanism for aggregation of submicron particles. *Marine Ecology Progress Series*, 202, pp.101-112.

Gardner, W. 1980. Sediment trap dynamics and calibration: A laboratory evaluation. *Journal of Marine Research* 38(1). Available at:

https://elischolar.library.yale.edu/journal_of_marine_research/1497 [Accessed: 5 February 2025].

Gardner, W.D. 1985. The effect of tilt on sediment trap efficiency. *Deep Sea Research Part A. Oceanographic Research Papers* 32(3), pp. 349–361. doi: 10.1016/0198-0149(85)90083-4.

Gibbs, R.J. 1985. Estuarine flocs: Their size, settling velocity and density. *Journal of Geophysical Research: Oceans* 90(C2), pp. 3249–3251. Available at:

https://onlinelibrary.wiley.com/doi/full/10.1029/JC090iC02p03249 [Accessed: 25 June 2024].

Gardner, W. D., Richardson, M. J., Carlson, C. A., Hansell, D., & Mishonov, A. V. (2003). Determining true particulate organic carbon: bottles, pumps and methodologies. *Deep Sea Research Part II: Topical Studies in Oceanography*, 50(3–4), 655–674. https://doi.org/10.1016/S0967-0645(02)00589-1

Giering, S.L.C. et al. 2014. Reconciliation of the carbon budget in the ocean's twilight zone. *Nature* 507(7493), pp. 480–483. doi: 10.1038/nature13123.

Giering, S.L.C. et al. 2016. High export via small particles before the onset of the North Atlantic spring bloom. *Journal of Geophysical Research: Oceans* 121(9), pp. 6929–6945. Available at: https://onlinelibrary.wiley.com/doi/full/10.1002/2016JC012048 [Accessed: 25 April 2023].

Giering, S.L.C. et al. 2020a. Sinking Organic Particles in the Ocean—Flux Estimates From in situ Optical Devices. *Frontiers in Marine Science* 6, p. 834. doi: 10.3389/fmars.2019.00834.

Giering, S.L.C. et al. 2023. Vertical imbalance in organic carbon budgets is indicative of a missing vertical transfer during a phytoplankton bloom near South Georgia (COMICS). *Deep Sea Research Part II: Topical Studies in Oceanography* 209, p. 105277. doi: 10.1016/J.DSR2.2023.105277.

Giering, S.L.C., Hosking, B., Briggs, N. and Iversen, M.H. 2020b. The Interpretation of Particle Size, Shape, and Carbon Flux of Marine Particle Images Is Strongly Affected by the Choice of Particle Detection Algorithm. *Frontiers in Marine Science* 7, p. 564. doi: 10.3389/fmars.2020.00564.

Giering, S.L.C., Sanders, R., Martin, A.P., Henson, S.A., Riley, J.S., Marsay, C.M. and Johns, D.G. 2017. Particle flux in the oceans: Challenging the steady state assumption. *Global Biogeochemical Cycles* 31(1), pp. 159–171. Available at: https://onlinelibrary.wiley.com/doi/full/10.1002/2016GB005424 [Accessed: 12 December 2023].

Gloege, L., McKinley, G.A., Mouw, C.B. and Ciochetto, A.B., 2017. Global evaluation of particulate organic carbon flux parameterizations and implications for atmospheric pCO2. *Global Biogeochemical Cycles*, 31(7), pp.1192-1215.

Gorsky, G. et al. 2010. Digital zooplankton image analysis using the ZooScan integrated system. *Journal of Plankton Research* 32(3), pp. 285–303. Available at: https://dx.doi.org/10.1093/plankt/fbp124 [Accessed: 15 February 2025].

Guidi, L. et al. 2016. Plankton networks driving carbon export in the oligotrophic ocean. *Nature* 2016 532:7600 532(7600), pp. 465–470. Available at:

https://www.nature.com/articles/nature16942 [Accessed: 15 February 2025].

Guidi, L., Jackson, G.A., Stemmann, L., Miquel, J.C., Picheral, M. and Gorsky, G. 2008. Relationship between particle size distribution and flux in the mesopelagic zone. *Deep-Sea Research Part I: Oceanographic Research Papers* 55(10), pp. 1364–1374. doi: 10.1016/j.dsr.2008.05.014.

Habib, J., Stemmann, L., Accardo, A., Baudena, A., Tuchen, F.P., Brandt, P. and Kiko, R. 2024. Marine snow surface production and bathypelagic export at the Equatorial Atlantic from an imaging float. Available at: https://egusphere.copernicus.org/preprints/2024/egusphere-2024-3365/ [Accessed: 13 February 2025].

Halfter, S., Cavan, E.L., Swadling, K.M., Eriksen, R.S. and Boyd, P.W. 2020. The Role of Zooplankton in Establishing Carbon Export Regimes in the Southern Ocean – A Comparison of Two Representative Case Studies in the Subantarctic Region. *Frontiers in Marine Science* 7, p. 837. doi: 10.3389/FMARS.2020.567917/BIBTEX.

Hamner, W.M., Madin, L.P., Alldredge, A.L., Gilmer, R.W. and Hamner, P.P. 1975. Underwater observations of gelatinous zooplankton: Sampling problems, feeding biology, and behavior1. *Limnology and Oceanography* 20(6), pp. 907–917. Available at: https://onlinelibrary.wiley.com/doi/full/10.4319/lo.1975.20.6.0907 [Accessed: 18 February 2025].

Hansen, J.L.S., Kiørboe, T. and Alldredge, A.L. 1996. Marine snow derived from abandoned larvacean houses: sinking rates, particle content and mechanisms of aggregate formation. *Marine Ecology Progress Series* 141(1–3), pp. 205–215. Available at: https://www.intres.com/abstracts/meps/v141/p205-215/ [Accessed: 18 February 2025].

Hauck, J. et al. 2015. On the Southern Ocean CO2 uptake and the role of the biological carbon pump in the 21st century. *Global Biogeochemical Cycles* 29(9), pp. 1451–1470. Available at: https://onlinelibrary.wiley.com/doi/full/10.1002/2015GB005140 [Accessed: 12 May 2024].

Hedges, J.I., Baldock, J.A., Gélinas, Y., Lee, C., Peterson, M. and Wakeham, S.G. 2001. Evidence for non-selective preservation of organic matter in sinking marine particles. *Nature 2001* 409:6822 409(6822), pp. 801–804. Available at: https://www.nature.com/articles/35057247 [Accessed: 27 June 2024].

Henson, S.A., Briggs, N., Carvalho, F., Manno, C., Mignot, A. and Thomalla, S. 2023. A seasonal transition in biological carbon pump efficiency in the northern Scotia Sea, Southern Ocean.

Deep Sea Research Part II: Topical Studies in Oceanography 208, p. 105274. doi: 10.1016/J.DSR2.2023.105274.

Henson, S.A., Cole, H.S., Hopkins, J., Martin, A.P. and Yool, A., 2018. Detection of climate change-driven trends in phytoplankton phenology. *Global Change Biology*, 24(1), pp.e101-e111.

Henson, S.A., Laufkötter, C., Leung, S., Giering, S.L.C., Palevsky, H.I. and Cavan, E.L. 2022. Uncertain response of ocean biological carbon export in a changing world. *Nature Geoscience* 2022 15:4 15(4), pp. 248–254. Available at: https://www.nature.com/articles/s41561-022-00927-0 [Accessed: 13 May 2024].

Henson, S.A., Sanders, R. and Madsen, E. 2012. Global patterns in efficiency of particulate organic carbon export and transfer to the deep ocean. *Global Biogeochemical Cycles* 26(1).

Available at: https://onlinelibrary.wiley.com/doi/full/10.1029/2011GB004099 [Accessed: 19 May 2023].

Henson, S.A., Sanders, R., Madsen, E., Morris, P.J., Le Moigne, F. and Quartly, G.D. 2011. A reduced estimate of the strength of the ocean's biological carbon pump. *Geophysical Research Letters* 38(4). doi: 10.1029/2011GL046735.

Henson, S.A., Yool, A. and Sanders, R. 2015. Variability in efficiency of particulate organic carbon export: A model study. *Global Biogeochemical Cycles* 29(1), pp. 33–45. Available at: https://onlinelibrary.wiley.com/doi/full/10.1002/2014GB004965 [Accessed: 18 June 2024].

Henson, S., Baker, C.A., Halloran, P., McQuatters-Gollop, A., Painter, S., Planchat, A. and Tagliabue, A. 2024. Knowledge Gaps in Quantifying the Climate Change Response of Biological Storage of Carbon in the Ocean. *Earth's Future* 12(6), p. e2023EF004375. Available at: https://onlinelibrary.wiley.com/doi/full/10.1029/2023EF004375 [Accessed: 22 July 2024].

Henson, S., Le Moigne, F. and Giering, S. 2019. Drivers of Carbon Export Efficiency in the Global Ocean. *Global Biogeochemical Cycles* 33(7), pp. 891–903. doi: 10.1029/2018GB006158.

Hernández-León, S., Sarmiento-Lezcano, A., Couret, M., Armengol, L., Medina-Suárez, I., Fatira, E., Tuset, V., Limam, A., Sánchez Díez, A., Díaz-Pérez, J. and Landeira, J.M., 2024. Seasonality of zooplankton active flux in subtropical waters. *Limnology and Oceanography*, 69(11), pp.2564-2579.

Honjo, S., Francois, R., Manganini, S., Dymond, J. and Collier, R. 2000. Particle fluxes to the interior of the Southern Ocean in the Western Pacific sector along 170°W. *Deep Sea Research Part II: Topical Studies in Oceanography* 47(15–16), pp. 3521–3548. doi: 10.1016/S0967-0645(00)00077-1.

Hurley, A.J., Hill, P.S., Milligan, T.G. and Law, B.A. 2016. Optical methods for estimating apparent density of sediment in suspension. *Methods in Oceanography* 17, pp. 153–168. doi: 10.1016/J.MIO.2016.09.001.

Iversen, M.H. 2023. Carbon Export in the Ocean: A Biologist's Perspective. *Annual Review of Marine Science* 15(Volume 15, 2023), pp. 357–381. Available at:

https://www.annualreviews.org/content/journals/10.1146/annurev-marine-032122-035153 [Accessed: 11 June 2024].

Iversen, M.H. and Lampitt, R.S. 2020. Size does not matter after all: No evidence for a size-sinking relationship for marine snow. *Progress in Oceanography* 189, p. 102445. doi: 10.1016/j.pocean.2020.102445.

Iversen, M.H., Nowald, N., Ploug, H., Jackson, G.A. and Fischer, G. 2010. High resolution profiles of vertical particulate organic matter export off Cape Blanc, Mauritania: Degradation processes and ballasting effects. *Deep-Sea Research Part I: Oceanographic Research Papers* 57(6), pp. 771–784. doi: 10.1016/j.dsr.2010.03.007.

Iversen, M.H., Pakhomov, E.A., Hunt, B.P.V., van der Jagt, H., Wolf-Gladrow, D. and Klaas, C. 2017. Sinkers or floaters? Contribution from salp pellets to the export flux during a large bloom event in the Southern Ocean. *Deep Sea Research Part II: Topical Studies in Oceanography* 138, pp. 116–125. doi: 10.1016/J.DSR2.2016.12.004.

Iversen, M.H. and Ploug, H. 2010. Ballast minerals and the sinking carbon flux in the ocean: Carbon-specific respiration rates and sinking velocity of marine snow aggregates. *Biogeosciences* 7(9), pp. 2613–2624. doi: 10.5194/bg-7-2613-2010.

Iversen, M.H. and Ploug, H. 2013. Temperature effects on carbon-specific respiration rate and sinking velocity of diatom aggregates – potential implications for deep ocean export processes. *Biogeosciences* 10(6), pp. 4073–4085. doi: 10.5194/BG-10-4073-2013.

Iversen, M.H. and Poulsen, L.K. 2007. Coprorhexy, coprophagy, and coprochaly in the copepods Calanus helgolandicus, Pseudocalanus elongatus, and Oithona similis. *Marine Ecology Progress Series* 350, pp. 79–89. Available at: https://www.int-res.com/abstracts/meps/v350/p79-89/ [Accessed: 18 February 2025].

Iversen, M.H. and Robert, M.L. 2015. Ballasting effects of smectite on aggregate formation and export from a natural plankton community. *Marine Chemistry* 175, pp. 18–27. doi: 10.1016/J.MARCHEM.2015.04.009.

Jackson, G.A. 1994. Particle trajectories in a rotating cylinder: implications for aggregation incubations. *Deep Sea Research Part I: Oceanographic Research Papers* 41(3), pp. 429–437. doi: 10.1016/0967-0637(94)90089-2.

Jackson, G.A. 2015. Coagulation in a rotating cylinder. *Limnology and Oceanography: Methods* 13(4), pp. 194–201. Available at: https://onlinelibrary.wiley.com/doi/full/10.1002/lom3.10018 [Accessed: 18 February 2025].

van der Jagt, H., Friese, C., Stuut, J.B.W., Fischer, G. and Iversen, M.H. 2018. The ballasting effect of Saharan dust deposition on aggregate dynamics and carbon export: Aggregation, settling, and scavenging potential of marine snow. *Limnology and Oceanography* 63(3), pp. 1386–1394. Available at: https://onlinelibrary.wiley.com/doi/full/10.1002/lno.10779 [Accessed: 23 March 2022].

Jannasch, H.W., Zafiriou, O.C. and Farrington, J.W. 1980. A sequencing sediment trap for timeseries studies of fragile particles1,2. *Limnology and Oceanography* 25(5), pp. 939–943. Available at: https://onlinelibrary.wiley.com/doi/full/10.4319/lo.1980.25.5.0939 [Accessed: 28 January 2025].

J, O. 2022. _vegan: Community Ecology Package_. R package version 2.6–4. Available at: https://cir.nii.ac.jp/crid/1370584340724217483.bib?lang=en [Accessed: 25 February 2025].

Jónasdóttir, S.H., Visser, A.W., Richardson, K. and Heath, M.R. 2015. Seasonal copepod lipid pump promotes carbon sequestration in the deep North Atlantic. *Proceedings of the National Academy of Sciences* 112(39), pp. 12122–12126. Available at:

https://www.pnas.org/doi/abs/10.1073/pnas.1512110112 [Accessed: 30 October 2024].

Kajihara, M. 1971. Settling velocity and porosity of large suspended particle. *Journal of the Oceanographical Society of Japan* 27(4), pp. 158–162. Available at: https://link.springer.com/article/10.1007/BF02109135 [Accessed: 14 January 2022].

Karthäuser, C. et al. 2021. Small sinking particles control anammox rates in the Peruvian oxygen minimum zone. *Nature Communications 2021 12:1* 12(1), pp. 1–12. Available at: https://www.nature.com/articles/s41467-021-23340-4 [Accessed: 1 August 2023].

Kiko, R. et al. 2020. Zooplankton-Mediated Fluxes in the Eastern Tropical North Atlantic. Frontiers in Marine Science 7, p. 481716. Available at: www.frontiersin.org [Accessed: 13 February 2025].

Kiko, R. et al. 2022. A global marine particle size distribution dataset obtained with the Underwater Vision Profiler 5. *Earth System Science Data* 14(9), pp. 4315–4337. doi: 10.5194/ESSD-14-4315-2022.

Kiøorboe, T. 2001. Formation and fate of marine snow: small-scale processes with large- scale implications. *Scientia Marina* 65(S2), pp. 57–71. Available at:

https://scientiamarina.revistas.csic.es/index.php/scientiamarina/article/view/682 [Accessed: 18 February 2025].

Klaas, C. and Archer, D.E. 2002. Association of sinking organic matter with various types of mineral ballast in the deep sea: Implications for the rain ratio. *Global Biogeochemical Cycles* 16(4), pp. 63–1. Available at: https://onlinelibrary.wiley.com/doi/full/10.1029/2001GB001765 [Accessed: 14 December 2022].

Kriest, I. 2002. Different parameterizations of marine snow in a 1D-model and their influence on representation of marine snow, nitrogen budget and sedimentation. *Deep Sea Research Part I:*Oceanographic Research Papers 49(12), pp. 2133–2162. doi: 10.1016/S0967-0637(02)00127-9.

Kriest, I. and Oschlies, A. 2008. On the treatment of particulate organic matter sinking in large-scale models of marine biogeochemical cycles. *Biogeosciences* 5(1), pp. 55–72. Available at: https://bg.copernicus.org/articles/5/55/2008/ [Accessed: 1 January 2022].

Kulk, G. et al. 2020. Primary Production, an Index of Climate Change in the Ocean: Satellite-Based Estimates over Two Decades. *Remote Sensing 2020, Vol. 12, Page 826* 12(5), p. 826. Available at: https://www.mdpi.com/2072-4292/12/5/826/htm [Accessed: 12 June 2024].

Kump, L.R., Brantley, S.L. and Arthur, M.A. 2003. Chemical Weathering, Atmospheric CO2, and Climate. https://doi.org/10.1146/annurev.earth.28.1.611 28, pp. 611–667. Available at: https://www.annualreviews.org/doi/abs/10.1146/annurev.earth.28.1.611 [Accessed: 27 February 2024].

Kwon, E.Y., Primeau, F. and Sarmiento, J.L. 2009. The impact of remineralization depth on the air—sea carbon balance. *Nature Geoscience 2009 2*:9 2(9), pp. 630–635. Available at: https://www.nature.com/articles/ngeo612 [Accessed: 9 December 2022].

Lacour, L. al. Particle size sets the carbon penetration depth during ocean bloom export events, 05 June 2024, PREPRINT (Version 1) available at Research Square [https://doi.org/10.21203/rs.3.rs-4474302/v1]

Lafond, A., Leblanc, K., Legras, J., Cornet, V. and Quéguiner, B. 2020. The structure of diatom communities constrains biogeochemical properties in surface waters of the Southern Ocean (Kerguelen Plateau). *Journal of Marine Systems* 212, p. 103458. doi: 10.1016/J.JMARSYS.2020.103458.

Lam, P.J., Doney, S.C. and Bishop, J.K., 2011. The dynamic ocean biological pump: Insights from a global compilation of particulate organic carbon, CaCO3, and opal concentration profiles from the mesopelagic. *Global Biogeochemical Cycles*, 25(3).

Lamborg, C.H. et al. 2008. The flux of bio- and lithogenic material associated with sinking particles in the mesopelagic "twilight zone" of the northwest and North Central Pacific Ocean. Deep Sea Research Part II: Topical Studies in Oceanography 55(14–15), pp. 1540–1563. doi: 10.1016/J.DSR2.2008.04.011.

Lampitt, R.S. et al. 2008. Particle export from the euphotic zone: Estimates using a novel drifting sediment trap, 234Th and new production. *Deep Sea Research Part I: Oceanographic Research Papers* 55(11), pp. 1484–1502. doi: 10.1016/J.DSR.2008.07.002.

Lampitt, R.S. et al. 2023. Deep ocean particle flux in the Northeast Atlantic over the past 30 years: carbon sequestration is controlled by ecosystem structure in the upper ocean. *Frontiers in Earth Science* 11. Available at: https://munin.uit.no/handle/10037/31580 [Accessed: 19 December 2023].

Lampitt, R.S., Wishner, K.F., Turley, C.M. and Angel, M. V. 1993. Marine snow studies in the Northeast Atlantic Ocean: distribution, composition and role as a food source for migrating plankton. *Marine Biology: International Journal on Life in Oceans and Coastal Waters* 116(4), pp. 689–702. Available at: https://link.springer.com/article/10.1007/BF00355486 [Accessed: 5 June 2024].

Laufkötter, C., John, J.G., Stock, C.A. and Dunne, J.P. 2017. Temperature and oxygen dependence of the remineralization of organic matter. *Global Biogeochemical Cycles* 31(7), pp. 1038–1050. Available at: https://onlinelibrary.wiley.com/doi/full/10.1002/2017GB005643 [Accessed: 13 September 2024].

Laurenceau-Cornec, E.C. et al. 2015a. The relative importance of phytoplankton aggregates and zooplankton fecal pellets to carbon export: Insights from free-drifting sediment trap deployments in naturally iron-fertilised waters near the Kerguelen Plateau. *Biogeosciences* 12(4), pp. 1007–1027. doi: 10.5194/BG-12-1007-2015.

Laurenceau-Cornec, E.C. et al. 2020. New guidelines for the application of Stokes' models to the sinking velocity of marine aggregates. *Limnology and Oceanography* 65(6), pp. 1264–1285. doi: 10.1002/lno.11388.

Laurenceau-Cornec, E.C., Trull, T.W., Davies, D.M., De La Rocha, C.L. and Blain, S. 2015b. Phytoplankton morphology controls on marine snow sinking velocity. *Marine Ecology Progress Series* 520, pp. 35–56. doi: 10.3354/meps11116.

Laws, E.A., Falkowski, P.G., Smith, W.O., Ducklow, H. and McCarthy, J.J. 2000. Temperature effects on export production in the open ocean. *Global Biogeochemical Cycles* 14(4), pp. 1231–1246. Available at: https://onlinelibrary.wiley.com/doi/full/10.1029/1999GB001229 [Accessed: 18 June 2024].

Leblanc, K. et al. 2009. Distribution of calcifying and silicifying phytoplankton in relation to environmental and biogeochemical parameters during the late stages of the 2005 North East Atlantic Spring Bloom. *Biogeosciences* 6(10), pp. 2155–2179. doi: 10.5194/BG-6-2155-2009.

Ledley, T.S., Sundquist, E.T., Schwartz, S.E., Hall, D.K., Fellows, J.D. and Killeen, T.L. 1999. Climate change and greenhouse gases. *Eos* 80(39). doi: 10.1029/99EO00325.

Leung, S.W., Weber, T., Cram, J.A. and Deutsch, C. 2021. Variable particle size distributions reduce the sensitivity of global export flux to climate change. *Biogeosciences* 18(1), pp. 229–250. doi: 10.5194/BG-18-229-2021.

Lévy, M., Bopp, L., Karleskind, P., Resplandy, L., Éthé, C. and Pinsard, F., 2013. Physical pathways for carbon transfers between the surface mixed layer and the ocean interior. *Global Biogeochemical Cycles*, 27(4), pp.1001-1012.

Lick, W., Hening Huang and Jepsen, R. 1993. Flocculation of fine-grained sediments due to differential settling. *Journal of Geophysical Research: Oceans* 98(C6), pp. 10279–10288. Available at: https://onlinelibrary.wiley.com/doi/full/10.1029/93JC00519 [Accessed: 18 February 2025].

Llopis Monferrer, N. et al. 2021. Role of small Rhizaria and diatoms in the pelagic silica production of the Southern Ocean. *Limnology and Oceanography* 66(6), pp. 2187–2202. Available at: https://onlinelibrary.wiley.com/doi/full/10.1002/lno.11743 [Accessed: 18 July 2024].

Logan, B.E. and Wilkinson, D.B. 1990. Fractal geometry of marine snow and other biological aggregates. *Limnology and Oceanography* 35(1), pp. 130–136. Available at: https://onlinelibrary.wiley.com/doi/full/10.4319/lo.1990.35.1.0130 [Accessed: 25 June 2024].

Loisel, H., Mériaux, X., Berthon, J.F. and Poteau, A. 2007. Investigation of the optical backscattering to scattering ratio of marine particles in relation to their biogeochemical composition in the eastern English Channel and southern North Sea. *Limnology and Oceanography* 52(2), pp. 739–752. Available at:

https://onlinelibrary.wiley.com/doi/full/10.4319/lo.2007.52.2.0739 [Accessed: 19 February 2025].

Lombard, F. et al. 2019. Globally consistent quantitative observations of planktonic ecosystems. *Frontiers in Marine Science* 6(MAR). doi: 10.3389/fmars.2019.00196.

Lutz, M., Dunbar, R. and Caldeira, K. 2002. Regional variability in the vertical flux of particulate organic carbon in the ocean interior. *Global Biogeochemical Cycles* 16(3), pp. 11–1. Available at: https://onlinelibrary.wiley.com/doi/full/10.1029/2000GB001383 [Accessed: 17 June 2024].

Maier-Reimer, E., Mikolajewicz, U. and Winguth, A. 1996. Future ocean uptake of CO 2: interaction between ocean circulation and biology. *Climate Dynamics* 12, pp. 711–721.

Maiti, K., Charette, M.A., Buesseler, K.O. and Kahru, M. 2013. An inverse relationship between production and export efficiency in the Southern Ocean. *Geophysical Research Letters* 40(8), pp. 1557–1561. Available at: https://onlinelibrary.wiley.com/doi/full/10.1002/grl.50219 [Accessed: 17 July 2024].

Manno, C., Fielding, S., Stowasser, G., Murphy, E.J., Thorpe, S.E. and Tarling, G.A., 2020. Continuous moulting by Antarctic krill drives major pulses of carbon export in the north Scotia Sea, Southern Ocean. *Nature communications*, 11(1), p.6051.

Manno, C., Stowasser, G., Fielding, S., Apeland, B. and Tarling, G.A. 2022. Deep carbon export peaks are driven by different biological pathways during the extended Scotia Sea (Southern Ocean) bloom. *Deep Sea Research Part II: Topical Studies in Oceanography* 205, p. 105183. doi: 10.1016/J.DSR2.2022.105183.

Mantovanelli, A. and Ridd, P. V. 2006. Devices to measure settling velocities of cohesive sediment aggregates: A review of the in situ technology. *Journal of Sea Research* 56(3), pp. 199–226. doi: 10.1016/J.SEARES.2006.05.002.

Marsay, C.M., Sanders, R.J., Henson, S.A., Pabortsava, K., Achterberg, E.P. and Lampitt, R.S. 2015. Attenuation of sinking particulate organic carbon flux through the mesopelagic ocean. *Proceedings of the National Academy of Sciences of the United States of America* 112(4), pp. 1089–1094. doi: 10.1073/pnas.1415311112.

Martin, A. 2005. The kaleidoscope ocean. *Philosophical Transactions of the Royal Society A: Mathematical, Physical and Engineering Sciences* 363(1837), pp. 2873–2890. Available at: https://royalsocietypublishing.org/doi/10.1098/rsta.2005.1663 [Accessed: 3 October 2023].

Martin, A. et al. 2020. The oceans' twilight zone must be studied now, before it is too late. *Nature* 2021 580:7801 580(7801), pp. 26–28. Available at: https://www.nature.com/articles/d41586-020-00915-7 [Accessed: 23 April 2024].

Martin, A.P. et al. 2024. When to add a new process to a model – and when not: A marine biogeochemical perspective. *Ecological Modelling* 498, p. 110870. Available at: https://linkinghub.elsevier.com/retrieve/pii/S0304380024002588 [Accessed: 5 March 2025].

Martin, J.H., Knauer, G.A., Karl, D.M. and Broenkow, W.W. 1987. VERTEX: carbon cycling in the northeast Pacific. *Deep Sea Research Part A. Oceanographic Research Papers* 34(2), pp. 267–285. doi: 10.1016/0198-0149(87)90086-0.

Martin, P., Lampitt, R.S., Jane Perry, M., Sanders, R., Lee, C. and D'Asaro, E. 2011. Export and mesopelagic particle flux during a North Atlantic spring diatom bloom. *Deep Sea Research Part I: Oceanographic Research Papers* 58(4), pp. 338–349. doi: 10.1016/J.DSR.2011.01.006.

Matsumoto, K., Sarmiento, J.L. and Brzezinski, M.A. 2002. Silicic acid leakage from the Southern Ocean: A possible explanation for glacial atmospheric pCO2. *Global Biogeochemical Cycles* 16(3), pp. 5–1. Available at: https://onlinelibrary.wiley.com/doi/full/10.1029/2001GB001442 [Accessed: 17 July 2024].

Mayor, D.J., Sanders, R., Giering, S.L.C. and Anderson, T.R. 2014. Microbial gardening in the ocean's twilight zone: Detritivorous metazoans benefit from fragmenting, rather than ingesting, sinking detritus. *BioEssays* 36(12), pp. 1132–1137. Available at: https://onlinelibrary.wiley.com/doi/full/10.1002/bies.201400100 [Accessed: 16 January 2023].

McCave, I.N. 1984. Size spectra and aggregation of suspended particles in the deep ocean. Deep Sea Research Part A. Oceanographic Research Papers 31(4), pp. 329–352. doi: 10.1016/0198-0149(84)90088-8.

McDonnell, A.M.P. et al. 2015. The oceanographic toolbox for the collection of sinking and suspended marine particles. *Progress in Oceanography* 133, pp. 17–31. doi: 10.1016/J.POCEAN.2015.01.007.

McDonnell, A.M.P. and Buesseler, K.O. 2010. Variability in the average sinking velocity of marine particles. *Limnology and Oceanography* 55(5), pp. 2085–2096. doi: 10.4319/lo.2010.55.5.2085.

McDonnell, A.M.P. and Buesseler, K.O. 2012. A new method for the estimation of sinking particle fluxes from measurements of the particle size distribution, average sinking velocity, and carbon content. *Limnology and Oceanography: Methods* 10(5), pp. 329–346. Available at: https://onlinelibrary.wiley.com/doi/full/10.4319/lom.2012.10.329 [Accessed: 15 February 2025].

de Melo Viríssimo, F., Martin, A.P. and Henson, S.A. 2022. Influence of Seasonal Variability in Flux Attenuation on Global Organic Carbon Fluxes and Nutrient Distributions. *Global Biogeochemical Cycles* 36(2), p. e2021GB007101. Available at: https://onlinelibrary.wiley.com/doi/full/10.1029/2021GB007101 [Accessed: 17 June 2024].

Mignot, A., Ferrari, R. and Claustre, H. 2018. Floats with bio-optical sensors reveal what processes trigger the North Atlantic bloom. *Nature Communications 2017* 9:1 9(1), pp. 1–9. Available at: https://www.nature.com/articles/s41467-017-02143-6 [Accessed: 16 May 2023].

Miklasz, K.A. and Denny, M.W. 2010. Diatom sinking speeds: Improved predictions and insight from a modified Stoke's law. *Limnology and Oceanography* 55(6), pp. 2513–2525. doi: 10.4319/lo.2010.55.6.2513.

Millar, R.J. et al. 2017. Emission budgets and pathways consistent with limiting warming to 1.5 °C. *Nature Geoscience 2017 10:10* 10(10), pp. 741–747. Available at: https://www.nature.com/articles/ngeo3031 [Accessed: 19 March 2024].

Le Moigne, F.A.C. et al. 2012. On the proportion of ballast versus non-ballast associated carbon export in the surface ocean. *Geophysical Research Letters* 39(15). Available at: https://onlinelibrary.wiley.com/doi/full/10.1029/2012GL052980 [Accessed: 12 December 2022].

Le Moigne, F.A.C., Pabortsava, K., Marcinko, C.L.J., Martin, P. and Sanders, R.J. 2014. Where is mineral ballast important for surface export of particulate organic carbon in the ocean? Geophysical Research Letters 41(23), pp. 8460–8468. Available at: https://onlinelibrary.wiley.com/doi/full/10.1002/2014GL061678 [Accessed: 12 December 2022].

Le Moigne, F.A.C., Villa-Alfageme, M., Sanders, R.J., Marsay, C., Henson, S. and García-Tenorio, R. 2013. Export of organic carbon and biominerals derived from 234Th and 210Po at the Porcupine Abyssal Plain. *Deep Sea Research Part I: Oceanographic Research Papers* 72, pp. 88–101. doi: 10.1016/J.DSR.2012.10.010.

Nelson, D.M. et al. 2002. Vertical budgets for organic carbon and biogenic silica in the Pacific sector of the Southern Ocean, 1996-1998. *Deep-Sea Research Part II: Topical Studies in Oceanography* 49(9–10), pp. 1645–1674. doi: 10.1016/S0967-0645(02)00005-X.

Nelson, D.M., DeMaster, D.J., Dunbar, R.B. and Smith, W.O. 1996. Cycling of organic carbon and biogenic silica in the Southern Ocean: Estimates of water-column and sedimentary fluxes on the Ross Sea continental shelf. *Journal of Geophysical Research: Oceans* 101(C8), pp. 18519–18532. Available at: https://onlinelibrary.wiley.com/doi/full/10.1029/96JC01573 [Accessed: 3 January 2023].

Neukermans, G., Loisel, H., Mériaux, X., Astoreca, R. and McKee, D. 2012. In situ variability of mass-specific beam attenuation and backscattering of marine particles with respect to particle size, density, and composition. *Limnology and Oceanography* 57(1), pp. 124–144. Available at: https://onlinelibrary.wiley.com/doi/full/10.4319/lo.2012.57.1.0124 [Accessed: 19 February 2025].

Nowald, N., Iversen, M.H., Fischer, G., Ratmeyer, V. and Wefer, G. 2015. Time series of in situ particle properties and sediment trap fluxes in the coastal upwelling filament off Cape Blanc, Mauritania. *Progress in Oceanography* 137, pp. 1–11. doi: 10.1016/J.POCEAN.2014.12.015.

Nowicki, M., DeVries, T. and Siegel, D.A., 2022. Quantifying the carbon export and sequestration pathways of the ocean's biological carbon pump. *Global Biogeochemical Cycles*, 36(3), p.e2021GB007083.

Olli, K., 2015. Unraveling the uncertainty and error propagation in the vertical flux Martin curve. *Progress in Oceanography*, 135, pp.146-155.

Omand, M.M., D'Asaro, E.A., Lee, C.M., Perry, M.J., Briggs, N., Cetinić, I. and Mahadevan, A. 2015. Eddy-driven subduction exports particulate organic carbon from the spring bloom. *Science* 348(6231), pp. 222–225. Available at:

https://www.science.org/doi/10.1126/science.1260062 [Accessed: 6 November 2024].

Omand, M.M., Govindarajan, R., He, J. and Mahadevan, A. 2020. Sinking flux of particulate organic matter in the oceans: Sensitivity to particle characteristics. *Scientific Reports 2020 10:1* 10(1), pp. 1–16. Available at: https://www.nature.com/articles/s41598-020-60424-5 [Accessed: 25 June 2024].

Orsi, A.H., Whitworth, T. and Nowlin, W.D. 1995. On the meridional extent and fronts of the Antarctic Circumpolar Current. *Deep Sea Research Part I: Oceanographic Research Papers* 42(5), pp. 641–673. doi: 10.1016/0967-0637(95)00021-W.

Oschlies, A. 2009. Impact of atmospheric and terrestrial CO2 feedbacks on fertilization-induced marine carbon uptake. *Biogeosciences* 6(8), pp. 1603–1613. doi: 10.5194/BG-6-1603-2009.

Parekh, P., Dutkiewicz, S., Follows, M.J. and Ito, T. 2006a. Atmospheric carbon dioxide in a less dusty world. *Geophysical Research Letters* 33(3). Available at:

https://onlinelibrary.wiley.com/doi/full/10.1029/2005GL025098 [Accessed: 9 December 2022].

Parekh, P., Dutkiewicz, S., Follows, M.J. and Ito, T. 2006b. Atmospheric carbon dioxide in a less duty world. *Geophysical Research Letters* 33(3). doi: 10.1029/2005GL025098.

Peterson, M.L., Hernes, P.J., Thoreson, D.S., Ifedges, J.I., Lee, C. and Wakeham, S.G. 1993. Field evaluation of a valved sediment trap. *Limnology and Oceanography* 38(8), pp. 1741–1761. Available at: https://onlinelibrary.wiley.com/doi/full/10.4319/lo.1993.38.8.1741 [Accessed: 28 January 2025].

Picheral, M. et al. 2022. The Underwater Vision Profiler 6: an imaging sensor of particle size spectra and plankton, for autonomous and cabled platforms. *Limnology and Oceanography:*

Methods 20(2), pp. 115–129. Available at: https://onlinelibrary.wiley.com/doi/10.1002/lom3.10475.

Picheral, M., Guidi, L., Stemmann, L., Karl, D.M., Iddaoud, G. and Gorsky, G. 2010. The Underwater Vision Profiler 5: An advanced instrument for high spatial resolution studies of particle size spectra and zooplankton. *Limnology and Oceanography: Methods* 8(9), pp. 462–473. Available at: https://onlinelibrary.wiley.com/doi/full/10.4319/lom.2010.8.462 [Accessed: 14 February 2025].

Ploug, H., Iversen, M.H. and Fischer, G. 2008. Ballast, sinking velocity, and apparent diffusivity within marine snow and zooplankton fecal pellets: Implications for substrate turnover by attached bacteria. *Limnology and Oceanography* 53(5), pp. 1878–1886.

Ploug, H., & Jørgensen, B. B. (1999). A net-jet flow system for mass transfer and microsensor studies of sinking aggregates. *Marine Ecology Progress Series*, *176*, 279–290. https://doi.org/10.3354/MEPS176279

Pongratz, J., Reick, C.H., Raddatz, T. and Claussen, M. 2009. Effects of anthropogenic land cover change on the carbon cycle of the last millennium. *Global Biogeochemical Cycles* 23(4). Available at: https://onlinelibrary.wiley.com/doi/full/10.1029/2009GB003488 [Accessed: 19 March 2024].

Poulton, A.J. et al. 2019. Seasonal phosphorus and carbon dynamics in a temperate shelf sea (Celtic Sea). *Progress in Oceanography* 177, p. 101872. doi: 10.1016/J.POCEAN.2017.11.001.

Poulton, A.J., Sanders, R., Holligan, P.M., Stinchcombe, M.C., Adey, T.R., Brown, L. and Chamberlain, K. 2006. Phytoplankton mineralization in the tropical and subtropical Atlantic Ocean. *Global Biogeochemical Cycles* 20(4). Available at:

https://onlinelibrary.wiley.com/doi/full/10.1029/2006GB002712 [Accessed: 17 July 2024].

Primeau, F. 2006. On the variability of the exponent in the power law depth dependence of POC flux estimated from sediment traps. *Deep Sea Research Part I: Oceanographic Research Papers* 53(8), pp. 1335–1343. doi: 10.1016/J.DSR.2006.06.003.

Puigcorbé, V., Masqué, P. and Le Moigne, F.A.C. 2020. Global database of ratios of particulate organic carbon to thorium-234 in the ocean: improving estimates of the biological carbon pump. *Earth System Science Data* 12(2), pp. 1267–1285. doi: 10.5194/ESSD-12-1267-2020.

Ragueneau, O., Dittert, N., Pondaven, P., Tréguer, P. and Corrin, L. 2002. Si/C decoupling in the world ocean: is the Southern Ocean different? *Deep Sea Research Part II: Topical Studies in Oceanography* 49(16), pp. 3127–3154. doi: 10.1016/S0967-0645(02)00075-9.

Ramondenc, S., Madeleine, G., Lombard, F., Santinelli, C., Stemmann, L., Gorsky, G. and Guidi, L. 2016a. An initial carbon export assessment in the Mediterranean Sea based on drifting sediment traps and the Underwater Vision Profiler data sets. *Deep Sea Research Part I:*Oceanographic Research Papers 117, pp. 107–119. doi: 10.1016/J.DSR.2016.08.015.

Ramondenc, S., Madeleine, G., Lombard, F., Santinelli, C., Stemmann, L., Gorsky, G. and Guidi, L. 2016b. An initial carbon export assessment in the Mediterranean Sea based on drifting sediment traps and the Underwater Vision Profiler data sets. *Deep Sea Research Part I:*Oceanographic Research Papers 117, pp. 107–119. doi: 10.1016/J.DSR.2016.08.015.

Rembauville, M., Blain, S., Armand, L., Quéguiner, B. and Salter, I. 2015. Export fluxes in a naturally iron-fertilized area of the Southern Ocean - Part 2: Importance of diatom resting spores and faecal pellets for export. *Biogeosciences* 12(11), pp. 3171–3195. doi: 10.5194/BG-12-3171-2015.

Rembauville, M., Blain, S., Caparros, J. and Salter, I. 2016. Particulate matter stoichiometry driven by microplankton community structure in summer in the Indian sector of the Southern Ocean. *Limnology and Oceanography* 61(4), pp. 1301–1321. Available at: https://onlinelibrary.wiley.com/doi/full/10.1002/lno.10291 [Accessed: 13 April 2023].

Richon, C. and Tagliabue, A., 2021. Biogeochemical feedbacks associated with the response of micronutrient recycling by zooplankton to climate change. *Global change biology*, 27(19), pp.4758-4770.

Riebesell, U. 1992. The formation of large marine snow and its sustained residence in surface waters. *Limnology and Oceanography* 37(1), pp. 63–76. Available at: https://onlinelibrary.wiley.com/doi/full/10.4319/lo.1992.37.1.0063 [Accessed: 18 February 2025].

Rigual-Hernández, A.S., Trull, T.W., Bray, S.G. and Armand, L.K. 2016. The fate of diatom valves in the Subantarctic and Polar Frontal Zones of the Southern Ocean: Sediment trap versus surface sediment assemblages. *Palaeogeography, Palaeoclimatology, Palaeoecology* 457, pp. 129–143. doi: 10.1016/J.PALAEO.2016.06.004.

Riley, J.S., Sanders, R., Marsay, C., Le Moigne, F.A.C., Achterberg, E.P. and Poulton, A.J. 2012. The relative contribution of fast and slow sinking particles to ocean carbon export. *Global Biogeochemical Cycles* 26(1). Available at:

https://onlinelibrary.wiley.com/doi/full/10.1029/2011GB004085 [Accessed: 25 April 2023].

Robison, B.H., Reisenbichler, K.R. and Sherlock, R.E., 2005. Giant larvacean houses: rapid carbon transport to the deep sea floor. *Science*, 308(5728), pp.1609-1611.

Roca-Martí, M. et al. 2017. High particulate organic carbon export during the decline of a vast diatom bloom in the Atlantic sector of the Southern Ocean. *Deep Sea Research Part II: Topical Studies in Oceanography* 138, pp. 102–115. doi: 10.1016/J.DSR2.2015.12.007.

Roca-Martí, M. and Puigcorbé, V. 2024. Combined Use of Short-Lived Radionuclides (234Th and 210Po) as Tracers of Sinking Particles in the Ocean. *Annual Review of Marine Science* 16(Volume 16, 2024), pp. 551–575. Available at:

https://www.annualreviews.org/content/journals/10.1146/annurev-marine-041923-013807 [Accessed: 1 February 2025].

Rogge, A. et al. 2022. Carbon dioxide sink in the Arctic Ocean from cross-shelf transport of dense Barents Sea water. *Nature Geoscience 2022 16:1* 16(1), pp. 82–88. Available at: https://www.nature.com/articles/s41561-022-01069-z [Accessed: 13 February 2025].

Romanelli, E. et al. 2024. Can intense storms affect sinking particle dynamics after the North Atlantic spring bloom? *Limnology and Oceanography* 69(12), pp. 2963–2974. Available at: https://onlinelibrary.wiley.com/doi/full/10.1002/lno.12723 [Accessed: 5 March 2025].

Rutgers van der Loeff, M.M., Buesseler, K., Bathmann, U., Hense, I. and Andrews, J. 2002. Comparison of carbon and opal export rates between summer and spring bloom periods in the region of the Antarctic Polar Front, SE Atlantic. *Deep Sea Research Part II: Topical Studies in Oceanography* 49(18), pp. 3849–3869. doi: 10.1016/S0967-0645(02)00114-5.

Sanders, R. et al. 2014. The Biological Carbon Pump in the North Atlantic. *Progress in Oceanography* 129(PB), pp. 200–218. doi: 10.1016/J.POCEAN.2014.05.005.

Sanders, R.J. et al. 2016. Controls over ocean mesopelagic interior carbon storage (COMICS): Fieldwork, synthesis, and modeling efforts. *Frontiers in Marine Science* 3(AUG). doi: 10.3389/fmars.2016.00136.

Sanders, R., Morris, P.J., Poulton, A.J., Stinchcombe, M.C., Charalampopoulou, A., Lucas, M.I. and Thomalla, S.J. 2010. Does a ballast effect occur in the surface ocean? *Geophysical Research Letters* 37(8). Available at:

https://onlinelibrary.wiley.com/doi/full/10.1029/2010GL042574 [Accessed: 27 June 2024].

Sarmiento, J.L. and Gruber, N. 2006. Ocean Biogeochemical Dynamics. *Ocean Biogeochemical Dynamics*. doi: 10.2307/J.CTT3FGXQX.

Sarmiento, J.L., Gruber, N., Brzezinski, M.A. and Dunne, J.P. 2004. High-latitude controls of thermocline nutrients and low latitude biological productivity. *Nature 2003 427*:6969 427(6969),

pp. 56–60. Available at: https://www.nature.com/articles/nature02127 [Accessed: 17 April 2023].

Schröder, S.M., Kiko, R. and Koch, R., 2020. MorphoCluster: efficient annotation of plankton images by clustering. *Sensors*, 20(11), p.3060.

Séférian, R. et al. 2020. Tracking Improvement in Simulated Marine Biogeochemistry Between CMIP5 and CMIP6. *Current Climate Change Reports 2020* 6:3 6(3), pp. 95–119. Available at: https://link.springer.com/article/10.1007/s40641-020-00160-0 [Accessed: 12 June 2024].

Shanks, A.L. and Trent, J.D. 1980. Marine snow: sinking rates and potential role in vertical flux. Deep Sea Research Part A. Oceanographic Research Papers 27(2), pp. 137–143. doi: 10.1016/0198-0149(80)90092-8.

Sharples, J., Moore, C. M., Rippeth, T. P., Holligan, P. M., Hydes, D. J., Fisher, N. R., & Simpson, J. H. (2001). Phytoplankton distribution and survival in the thermocline. *Limnology and Oceanography*, 46(3), 486–496. https://doi.org/10.4319/LO.2001.46.3.0486

Smetacek, V. et al. 2012. Deep carbon export from a Southern Ocean iron-fertilized diatom bloom. *Nature 2012 487:7407* 487(7407), pp. 313–319. Available at: https://www.nature.com/articles/nature11229 [Accessed: 18 May 2023].

Smetacek, V., Assmy, P. and Henjes, J. 2004. The role of grazing in structuring Southern Ocean pelagic ecosystems and biogeochemical cycles. *Antarctic Science* 16(4), pp. 541–558. Available at: https://www.cambridge.org/core/journals/antarctic-science/article/role-of-grazing-in-structuring-southern-ocean-pelagic-ecosystems-and-biogeochemical-cycles/CCE77EF9DD26E90D37EB2BC9C230BE03 [Accessed: 13 April 2023].

Smetacek, V.S. 1985. Role of sinking in diatom life-history cycles: ecological, evolutionary and geological significance. *Marine Biology* 84(3), pp. 239–251. Available at: https://link.springer.com/article/10.1007/BF00392493 [Accessed: 18 July 2024].

Smith, K.L., Kaufmann, R.S., Baldwin, R.J. and Carlucci, A.F. 2001. Pelagic—benthic coupling in the abyssal eastern North Pacific: An 8-year time-series study of food supply and demand. Limnology and Oceanography 46(3), pp. 543–556. Available at: https://onlinelibrary.wiley.com/doi/full/10.4319/lo.2001.46.3.0543 [Accessed: 12 June 2024].

Soviadan, Y.D. et al. 2024. Marine snow morphology drives sinking and attenuation in the ocean interior. *EGUsphere*. Available at: https://archimer.ifremer.fr/doc/00918/103031/ [Accessed: 13 February 2025].

Spall, M.A., 1995. Frontogenesis, subduction, and cross-front exchange at upper ocean fronts. Journal of Geophysical Research: Oceans, 100(C2), pp.2543-2557.

Steinberg, D.K. and Landry, M.R. 2017. Zooplankton and the Ocean Carbon Cycle. *Annual Review of Marine Science* 9(1), pp. 413–444. Available at:

https://www.annualreviews.org/content/journals/10.1146/annurev-marine-010814-015924 [Accessed: 30 October 2024].

Steinberg, D.K., Carlson, C.A., Bates, N.R., Goldthwait, S.A., Madin, L.P. and Michaels, A.F., 2000. Zooplankton vertical migration and the active transport of dissolved organic and inorganic carbon in the Sargasso Sea. *Deep Sea Research Part I: Oceanographic Research Papers*, 47(1), pp.137-158.

Steinberg, D.K., Van Mooy, B.A.S., Buesseler, K.O., Boyd, P.W., Kobari, T. and Karl, D.M. 2008. Bacterial vs. zooplankton control of sinking particle flux in the ocean's twilight zone. *Limnology and Oceanography* 53(4), pp. 1327–1338. doi: 10.4319/LO.2008.53.4.1327.

Stemmann, L. and Boss, E. 2012. Plankton and particle size and packaging: from determining optical properties to driving the biological pump. *Annual review of marine science* 4, pp. 263–290. Available at: https://pubmed.ncbi.nlm.nih.gov/22457976/ [Accessed: 12 February 2025].

Stephens, B.M., Durkin, C.A., Sharpe, G., Nguyen, T.T., Albers, J., Estapa, M.L., Steinberg, D.K., Levine, N.M., Gifford, S.M., Carlson, C.A. and Boyd, P.W., 2024. Direct observations of microbial community succession on sinking marine particles. *The ISME Journal*, 18(1), p.wrad010.

Stock, C.A., Dunne, J.P. and John, J.G. 2014. Global-scale carbon and energy flows through the marine planktonic food web: An analysis with a coupled physical–biological model. *Progress in Oceanography* 120, pp. 1–28. doi: 10.1016/J.POCEAN.2013.07.001.

Stolpovsky, K., Dale, A.W. and Wallmann, K., 2018. A new look at the multi-G model for organic carbon degradation in surface marine sediments for coupled benthic–pelagic simulations of the global ocean. *Biogeosciences*, 15(11), pp.3391-3407.

Strubinger Sandoval, P., Dall'Olmo, G., Haines, K., Rasse, R., & Ross, J. (2022). Uncertainties of particulate organic carbon concentrations in the mesopelagic zone of the Atlantic ocean. *Open Research Europe*, 1. https://doi.org/10.12688/OPENRESEUROPE.13395.3

Stukel, M.R. et al. 2024. Relationships Between Plankton Size Spectra, Net Primary Production, and the Biological Carbon Pump. *Global Biogeochemical Cycles* 38(4), p. e2023GB007994. Available at: https://onlinelibrary.wiley.com/doi/full/10.1029/2023GB007994 [Accessed: 11 September 2024].

Stukel, M.R., Ohman, M.D., Kelly, T.B. and Biard, T., 2019. The roles of suspension-feeding and flux-feeding zooplankton as gatekeepers of particle flux into the mesopelagic ocean in the Northeast Pacific. *Frontiers in Marine Science*, 6, p.397.

Suzuki, H., Sasaki, H. and Fukuchi, M. 2003. Loss processes of sinking fecal pellets of zooplankton in the mesopelagic layers of the antarctic marginal ice zone. *Journal of Oceanography* 59(6), pp. 809–818. doi: 10.1023/B:JOCE.0000009572.08048.0D.

Swart, N.C. et al. 2019. The Canadian Earth System Model version 5 (CanESM5.0.3).

Geoscientific Model Development 12(11), pp. 4823–4873. doi: 10.5194/GMD-12-4823-2019.

Tagliabue, A., Kwiatkowski, L., Bopp, L., Butenschön, M., Cheung, W., Lengaigne, M. and Vialard, J. 2021. Persistent Uncertainties in Ocean Net Primary Production Climate Change Projections at Regional Scales Raise Challenges for Assessing Impacts on Ecosystem Services. *Frontiers in Climate* 3, p. 738224. Available at: www.frontiersin.org [Accessed: 31 October 2024].

Takeda, S. 1998. Influence of iron availability on nutrient consumption ratio of diatoms in oceanic waters. *Nature 1998 393:6687* 393(6687), pp. 774–777. Available at: https://www.nature.com/articles/31674 [Accessed: 23 January 2024].

Takeuchi, M., Doubell, M.J., Jackson, G.A., Yukawa, M., Sagara, Y. and Yamazaki, H. 2019. Turbulence mediates marine aggregate formation and destruction in the upper ocean. *Scientific Reports 2019 9:1* 9(1), pp. 1–8. Available at: https://www.nature.com/articles/s41598-019-52470-5 [Accessed: 2 January 2024].

Tarrant, A.M., McNamara-Bordewick, N., Blanco-Bercial, L., Miccoli, A. and Maas, A.E. 2021. Diel metabolic patterns in a migratory oceanic copepod. *Journal of Experimental Marine Biology and Ecology* 545, p. 151643. doi: 10.1016/J.JEMBE.2021.151643.

Taucher, J., Bach, L.T., Riebesell, U. and Oschlies, A. 2014. The viscosity effect on marine particle flux: A climate relevant feedback mechanism. *Global Biogeochemical Cycles* 28(4), pp. 415–422. Available at: https://onlinelibrary.wiley.com/doi/full/10.1002/2013GB004728 [Accessed: 13 September 2024].

Thomalla, S.J., Poulton, A.J., Sanders, R., Turnewitsch, R., Holligan, P.M. and Lucas, M.I. 2008. Variable export fluxes and efficiencies for calcite, opal, and organic carbon in the Atlantic Ocean: A ballast effect in action? *Global Biogeochemical Cycles* 22(1), p. 1010. Available at: https://onlinelibrary.wiley.com/doi/full/10.1029/2007GB002982 [Accessed: 27 January 2024].

Thomalla, S., Turnewitsch, R., Lucas, M. and Poulton, A. 2006. Particulate organic carbon export from the North and South Atlantic gyres: The 234Th/238U disequilibrium approach. *Deep Sea Research Part II: Topical Studies in Oceanography* 53(14–16), pp. 1629–1648. doi: 10.1016/J.DSR2.2006.05.018.

Torres Valdés, S., Painter, S.C., Martin, A.P., Sanders, R. and Felden, J. 2014. Data compilation of fluxes of sedimenting material from sediment traps in the Atlantic ocean. *Earth System Science Data* 6(1), pp. 123–145. doi: 10.5194/ESSD-6-123-2014.

Tréguer, P. et al. 2017. Influence of diatom diversity on the ocean biological carbon pump. Nature Geoscience 2017 11:1 11(1), pp. 27–37. Available at: https://www.nature.com/articles/s41561-017-0028-x [Accessed: 24 April 2023].

Treguer, P., Nelson, D.M., Van Bennekom, A.J., DeMaster, D.J., Leynaert, A. and Quéguiner, B., 1995. The silica balance in the world ocean: a reestimate. *Science*, 268(5209), pp.375-379.

Tréguer, P., Kamatani, A., Gueneley, S. and Quéguiner, B. 1989. Kinetics of dissolution of Antarctic diatom frustules and the biogeochemical cycle of silicon in the Southern Ocean. *Polar Biology* 9(6), pp. 397–403. Available at: https://link.springer.com/article/10.1007/BF00442531 [Accessed: 17 January 2023].

Tréguer, P., Nelson, D.M., Bennekom, A.J. Van, DeMaster, D.J., Leynaert, A. and Quéguiner, B. 1995. The Silica Balance in the World Ocean: A Reestimate. *Science* 268(5209), pp. 375–379. Available at: https://www.science.org/doi/10.1126/science.268.5209.375 [Accessed: 16 January 2024].

Trudnowska, E. et al. 2021. Marine snow morphology illuminates the evolution of phytoplankton blooms and determines their subsequent vertical export. *Nature Communications* 12(1). doi: 10.1038/s41467-021-22994-4.

Turner, J.T. 2002. Zooplankton fecal pellets, marine snow and sinking phytoplankton blooms. *Aquatic Microbial Ecology* 27(1), pp. 57–102. Available at:

https://www.researchgate.net/publication/200146940_Zooplankton_fecal_pellets_marine_sno w_and_sinking_phytoplankton_blooms [Accessed: 13 May 2024].

Twardowski, M.S., Boss, E., Macdonald, J.B., Pegau, W.S., Barnard, A.H. and Zaneveld, J.R. V. 2001. A model for estimating bulk refractive index from the optical backscattering ratio and the implications for understanding particle composition in case I and case II waters. *Journal of Geophysical Research: Oceans* 106(C7), pp. 14129–14142. Available at: https://onlinelibrary.wiley.com/doi/full/10.1029/2000JC000404 [Accessed: 19 February 2025].

Van der Jagt, H., Wiedmann, I., Hildebrandt, N., Niehoff, B. and Iversen, M.H., 2020. Aggregate feeding by the copepods Calanus and Pseudocalanus controls carbon flux attenuation in the Arctic shelf sea during the productive period. *Frontiers in Marine Science*, 7, p.543124.

Verdeny, E., Masqué, P., Garcia-Orellana, J., Hanfland, C., Kirk Cochran, J. and Stewart, G.M. 2009. POC export from ocean surface waters by means of 234Th/238U and 210Po/210Pb disequilibria: A review of the use of two radiotracer pairs. *Deep Sea Research Part II: Topical Studies in Oceanography* 56(18), pp. 1502–1518. doi: 10.1016/J.DSR2.2008.12.018.

Vihtakari, M. [no date]. ggOceanMaps: Plot data on oceanographic maps using "ggplot2". *R* package version 2.2.0, *R* package version 2.2.0, https://mikkovihtakari.github.io/ggOceanMaps/.

Villa-Alfageme, M. et al. 2016. Geographical, seasonal, and depth variation in sinking particle speeds in the North Atlantic. *Geophysical Research Letters* 43(16), pp. 8609–8616. Available at: https://onlinelibrary.wiley.com/doi/full/10.1002/2016GL069233 [Accessed: 13 February 2024].

Villa-Alfageme, M., Briggs, N., Ceballos-Romero, E., de Soto, F., Manno, C. and Giering, S.L.C. 2023. Seasonal variations of sinking velocities in Austral diatom blooms: Lessons learned from COMICS. *Deep Sea Research Part II: Topical Studies in Oceanography*, p. 105353. Available at: https://linkinghub.elsevier.com/retrieve/pii/S0967064523001030 [Accessed: 12 December 2023].

Villa-Alfageme, M., De Soto, F., Le Moigne, F.A.C., Giering, S.L.C., Sanders, R. and García-Tenorio, R. 2014. Observations and modeling of slow-sinking particles in the twilight zone. *Global Biogeochemical Cycles* 28(11), pp. 1327–1342. doi: 10.1002/2014GB004981.

Volk, T. and Hoffert, M.I. 1985. OCEAN CARBON PUMPS: ANALYSIS OF RELATIVE STRENGTHS AND EFFICIENCIES IN OCEAN-DRIVEN ATMOSPHERIC CO 2 CHANGES. Available at: https://agupubs.onlinelibrary.wiley.com/doi/10.1029/GM032p0099 [Accessed: 9 December 2022].

Wangersky, P. J. (1974). Particulate organic carbon: Sampling variability. *Limnology and Oceanography*, 19(6), 980–984. https://doi.org/10.4319/LO.1974.19.6.0980

Ward, B.A., Dutkiewicz, S., Jahn, O. and Follows, M.J. 2012. A size-structured food-web model for the global ocean. *Limnology and Oceanography* 57(6), pp. 1877–1891. Available at: https://onlinelibrary.wiley.com/doi/full/10.4319/lo.2012.57.6.1877 [Accessed: 11 September 2024].

Weber, T., Cram, J.A., Leung, S.W., DeVries, T. and Deutsch, C. 2016. Deep ocean nutrients imply large latitudinal variation in particle transfer efficiency. *Proceedings of the National*

Academy of Sciences of the United States of America 113(31), pp. 8606–8611. Available at: https://www.pnas.org/doi/abs/10.1073/pnas.1604414113 [Accessed: 15 December 2022].

Wiedmann, I. et al. 2020. Arctic Observations Identify Phytoplankton Community Composition as Driver of Carbon Flux Attenuation. *Geophysical Research Letters* 47(14), p. e2020GL087465. Available at: https://onlinelibrary.wiley.com/doi/full/10.1029/2020GL087465 [Accessed: 22 April 2024].

Williams, J.R. et al., 2025. Inefficient transfer of diatoms through the subpolar Southern Ocean twilight zone. *Nature Geoscience*, 18(1), pp.72-77.

Williams, J.R. and Giering, S.L.C. 2022. In Situ Particle Measurements Deemphasize the Role of Size in Governing the Sinking Velocity of Marine Particles. *Geophysical Research Letters* 49(21), p. e2022GL099563. Available at:

https://onlinelibrary.wiley.com/doi/full/10.1029/2022GL099563 [Accessed: 13 June 2023].

Wilson, J.D. et al. 2022. The biological carbon pump in CMIP6 models: 21st century trends and uncertainties. *Proceedings of the National Academy of Sciences of the United States of America* 119(29), p. e2204369119. Available at:

https://www.pnas.org/doi/abs/10.1073/pnas.2204369119 [Accessed: 9 May 2024].

Wilson, S.E., Ruhl, H.A. and Smith, K.L. 2013. Zooplankton fecal pellet flux in the abyssal northeast Pacific: A 15 year time-series study. *Limnology and Oceanography* 58(3), pp. 881–892. Available at: https://onlinelibrary.wiley.com/doi/full/10.4319/lo.2013.58.3.0881 [Accessed: 21 August 2024].

Wilson, S.E., Steinberg, D.K. and Buesseler, K.O. 2008. Changes in fecal pellet characteristics with depth as indicators of zooplankton repackaging of particles in the mesopelagic zone of the subtropical and subarctic North Pacific Ocean. *Deep Sea Research Part II: Topical Studies in Oceanography* 55(14–15), pp. 1636–1647. doi: 10.1016/J.DSR2.2008.04.019.

Wyatt, N.J. et al. 2023. Phytoplankton responses to dust addition in the Fe–Mn co-limited eastern Pacific sub-Antarctic differ by source region. *Proceedings of the National Academy of Sciences of the United States of America* 120(28), p. e2220111120. Available at: https://www.pnas.org/doi/abs/10.1073/pnas.2220111120 [Accessed: 21 March 2024].

Xiang, Y., Lam, P.J., Burd, A.B. and Hayes, C.T. 2022. Estimating Mass Flux From Size-Fractionated Filtered Particles: Insights Into Controls on Sinking Velocities and Mass Fluxes in Recent U.S. GEOTRACES Cruises. *Global Biogeochemical Cycles* 36(4). Available at: https://onlinelibrary.wiley.com/doi/10.1029/2021GB007292 [Accessed: 20 April 2022].

Yool, A. et al. 2021. Evaluating the physical and biogeochemical state of the global ocean component of UKESM1 in CMIP6 historical simulations. *Geoscientific Model Development* 14(6), pp. 3437–3472. doi: 10.5194/GMD-14-3437-2021.

Yool, A., Popova, E., Model, T.A.-G. and 2013, undefined. 2013. MEDUSA-2.0: an intermediate complexity biogeochemical model of the marine carbon cycle for climate change and ocean acidification studies. *gmd.copernicus.org* 6, pp. 1767–1811. Available at: https://gmd.copernicus.org/articles/6/1767/2013/ [Accessed: 14 December 2022].

Zamanillo, M., Ortega-Retuerta, E., Nunes, S., Estrada, M., Sala, M.M., Royer, S.J., López-Sandoval, D.C., Emelianov, M., Vaqué, D., Marrasé, C. and Simó, R., 2019. Distribution of transparent exopolymer particles (TEP) in distinct regions of the Southern Ocean. *Science of the Total Environment*, 691, pp.736-748.

Ziervogel, K., Sweet, J.A., Song, Y., Bretherton, L., Rau, M.J., Quigg, A. and Passow, U. 2025. Sink or break: Oil increases resistance of phytoplankton aggregates to fragmentation. *Limnology and Oceanography Letters* 10(1), pp. 73–81. Available at:

https://onlinelibrary.wiley.com/doi/full/10.1002/lol2.10454 [Accessed: 2 March 2025].